ANALYSIS OF DISTORTION-INDUCED FATIGUE CRACK AT THE WEB GAP OF I-BEAM IN STEEL BRIDGES

Mr. Hung The Dinh

A Thesis Submitted in Partial Fulfillment of the Requirements
for the Degree of Doctor of Engineering Program in Civil Engineering
Department of Civil Engineering
Faculty of Engineering
Chulalongkorn University
Academic Year 2012
Copyright of Chulalongkorn University

การวิเคราะห์ร้อยร้าวบริเวณช่องว่างของแผ่นเอวของคานสะพานเหล็กรูปตัวไอ

นาย ฮัง เดอะ ดินฮ

วิทยานิพนธ์นี้เป็นส่วนหนึ่งของการศึกษาตามหลักสูตรปริญญาวิศวกรรมศาสตรมหาบัณฑิต
สาขาวิชาวิศวกรรมโยธา ภาควิชาวิศวกรรมโยธา
คณะวิศวกรรมศาสตร์ จุฬาลงกรณ์มหาวิทยาลัย
ปีการศึกษา 2556

Thesis Title	ANALYSIS OF DISTORTION-INDUCED FATIGUE CRACK AT THE WEB GAP OF I-BEAM IN STEEL BRIDGES
By	Mr. Hung The Dinh
Field of Study	Civil Engineering
Thesis Advisor	Professor Teerapong Senjuntichai Associate Professor Akhrawat Lenwari Professor Toshiro Hayashikawa

---

Accepted by the Faculty of Engineering, Chulalongkorn University in Partial Fulfillment of the Requirements for the Doctor’s Degree

…………………………………………Dean of the Faculty of Engineering
(Associate Professor Boonsom Lerdhirunwong, Dr. Ing.)

THESIS COMMITTEE

……………………………………………….. Chairman
(Professor Thaksin Thepchatri, Ph.D.)

………………………………………………. Thesis Advisor
(Professor Teerapong Senjuntichai, Ph.D.)

………………………………………………. Thesis Co-Advisor
(Associate Professor Akhrawat Lenwari, Ph.D.)

………………………………………………. Thesis Co-Advisor
(Professor Toshiro Hayashikawa, Ph.D.)

……………………………………………….. Examiner
(Associate Professor Jaroon Rungamornrat, Ph.D.)

……………………………………………….. External Examiner
(Assitant Professor Arnon Wongkaew, Ph.D.)

สุงทิดิน:การวิเคราะห์ร้อยร้าวบริเวณช่องว่างของแผ่นเอวของคานสะพานเหล็กรูปตัวไอ (ANALYSIS OF DISTORTION-INDUCED FATIGUE CRACK AT THE WEB GAP OF I-BEAM IN STEEL BRIDGES) อ.ที่ปรึกษาวิทยานิพนธ์หลัก : ศ.ดร.ธีระพงศ์ เสนจันทร์ฒิไชย, อ.ที่ปรึกษาวิทยานิพนธ์ร่วม : รศ.ดร.อัครวัชร เล่นวารี,ศ.ดร.โตชิโร ฮาวาชิกาว่า, 170 หน้า.

รอยร้าวล้าเนื่องจากการบิดเกิดขึ้นกับโครงสร้างสะพานเหล็กหลายประเภทโดยเฉพาะโครงสร้างที่มีการเชื่อม เนื่องจากหน่วยแรงเฉพาะที่ที่สูงบริเวณรอยเชื่อม อย่างไรก็ตามข้อกำหนดการออกแบบของ AASHTO ยังไม่ได้มีรายละเอียดในการพิจารณาหน่วยแรงภายใต้การบิดนอกระนาบ งานวิจัยนี้ศึกษาพฤติกรรมรอยร้าวบริเวณช่องว่างของแผ่นเอวของคานเหล็กรูปตัวไอภายใต้แรงกระทำเป็นรอบและประยุกต์ใช้แนวคิดกลศาสตร์การแตกร้าวยืดหยุ่นเชิงเส้นในการทำนายพฤติกรรม และศึกษาผลกระทบของตัวแปรต่าง ๆ จากการทดสอบและวิเคราะห์ โดยจากผลการศึกษาพบว่า แบบจำลองไฟไนต์เอลิเมนต์ที่ใช้เกณฑ์ SED สามารถนำมาประยุกต์ใช้ทำนายการเติบโตของรอยร้าวได้ นอกจากนั้นโหมด 1 และ 3 มีผลต่อทิศทางและอัตราการเติบโตของรอยร้าว

ภาควิชา วิศวกรรมโยธา
สาขาวิชา วิศวกรรมโยธา
ปีการศึกษา 2555

ลายมือชื่อนิสิต ....
ลายมือชื่อ อ.ที่ปรึกษาวิทยานิพนธ์หลัก…………………..
ลายมือชื่อ อ.ที่ปรึกษาวิทยานิพนธ์ร่วม…………………..
ลายมือชื่อ อ.ที่ปรึกษาวิทยานิพนธ์ร่วม…………………..

5271876721: MAJOR CIVIL ENGINEERING

KEYWORDS: DISTORTION INDUCED, FATIGUE CRACK, FRACTURE MECHANICS, WEB GAP, STRAIN ENERGY DENSITY.

HUNG THE DINH: ANALYSIS OF DISTORTION-INDUCED FATIGUE CRACK AT THE WEB GAP OF I-BEAM IN STEEL BRIDGES. THESIS ADVISORS: PROF. TEERAPONG SENJUNTICHAI, Ph.D., CO ADVISOR: ASSOC PROF. AKHRAWAT LENWARI, Ph.D., PROF. TOSHIRO HAYASHIKAWA, Ph.D., 170 pp.

Distortion-induced fatigue cracking has occurred in many types of steel bridge structures, especially the welded structures where high local stresses exist. However, out-of-plane distortion-induced stresses have not been fully considered in the AASHTO design specifications. This research studies the behavior around web-gap of I-beam in steel bridges under cyclic loading and applies the linear elastic fracture mechanics concepts for prediction of fatigue cracking behavior. Besides, effects of various parameters on the distortion-induced fatigue cracking behavior are considered experimentally and numerically. The results show that finite element modeling with SED criterion is applicable for the crack path prediction. In addition, mode I and mode III affected the fatigue crack direction and fatigue crack growth rate.

Department : Civil Engineering

Field of Study : Civil Engineering

Academic Year : 2012

Student’s Signature

Advisor’s Signature

Co-advisor’s signature

ACKNOWLEDGEMENTS

This thesis is my greatest science work up to this time. I has acquired and improved myself during the time writing this thesis. I also got a good way to do science research. These achievements would be very useful for my career and teaching. Time of PhD study is not too long and not too short, but I have a great time to work with passion and excitement of science research. I would like to express my sincerest gratitude to those who all gave me the possibility to complete this thesis.

First, I would like to thank my supervisors, Prof. Teerapong Senjuntichai, Assoc Prof. Akhrawat Lenwari, and Prof Toshiro Hayashikawa for the continuous support of my PhD study, for their patience, motivation, enthusiasm, and immense knowledge. Their guidance helped me in all the time of researching and writing this thesis. I am so lucky having nice advisors and mentors for my PhD study.

Besides my advisors, I would like to thank the rest of my thesis committee: Prof. Thaksin Thepchatri, Assoc Prof. Jaroon Rungamornrat, and Assist Prof. Arnon Wongkaew for their encouragement, insightful comments, and hard questions.

An important man who I would like to show deep gratitude is Mr Bordin. He was with me for all experiments for all days and nights. We worked hardly and get great friendship during wonderful time. I greatly appreciate his helps in doing my researches.

Besides that, I also want to give my thanks to Assist. Prof. Jirapong Kasivitamnuay who helps me to inspect the micro cracks on crack surfaces. Without his help, this thesis would not have a strong evidence to express the main idea of research.

Furthermore, I really want to give special words of gratefulness to all AUN/Set-net scholarship and staffs for their great enthusiasm. Many thanks to Chulalongkon University, Civil Engineering Faculty, laboratory technicians have facilitated and helped me during the research and experiments.

Last but not the least, I would like to thank my family who always encourage and support me throughout all the time.

CONTENTS

Page

Page

LIST OF TABLES

Page

LIST OF FIGURES

Page

Page

CHAPTER I

INTRODUCTION

1.1 General

It is well-known that a bridge is usually subjected to a large number of cycles of significant live load. Therefore, if a bridge survives the construction phase without fracture occurring, fatigue will precede fracture. Generally, controlling fatigue is more important and difficult than controlling fracture. However, design for fracture resistance members plays an important play in construction design because fatigue cracks eventually can grow to a critical size at which the member fractures. Furthermore, the problem of having a poor detail in highly constrained points, such as the intersection point of two or three welds, fatigue may happen directly from weld discontinuities without the prior growth of a fatigue crack.

Distortion-induced fatigue is the dominant cracking problem found in welded steel bridges. This type of cracking has occurred in many types of bridge structures. Stringer webs have cracked in suspension bridges at the stringer-floor-beam connections. Floor-beam webs have cracked in tied arch bridges. The longitudinal girders in a girder-floor-beam bridge have experienced cracking in the girder web. Multiple beam bridges have experienced cracking in the girder webs at cross-frames and diaphragms, and at least one box girder structure has developed cracks in the girder web at interior cross-frames. Cracking has been most extensive in welded structures where a weld toe has commonly existed in the height cyclic stress region. The AASHTO bridge design specifications published before 1985 did not require positive attachment between the connection stiffener and the girder flange (Figure 1.1). Thus, an abrupt stiffness change occurred within the small segment of the girder web between the flange and the connection stiffener end. This web gap region experiences high secondary stress under traffic loading, leading to out-of-plane distortion-induced cracking (Fisher, 1984). Cracks either develop along the horizontal flange-to-web welds or initiate from the end of the vertical stiffener to web welds, and then propagate downward into horseshoes shapes. Since 1989, Kansas Department of Transportation has required welded or bolted attachment of connection stiffeners to girder flanges. This policy change has significantly reduced the frequency of out-of-plane fatigue cracking. However, many welded plate girder bridges designed prior to 1989 have developed web gap cracks to some extent.

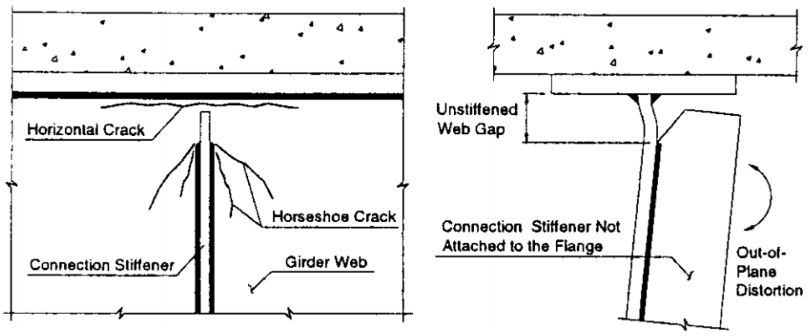

Figure 1.1 Out of plane distortion

Unlike load-induced fatigue, out-of-plane distortion-induced stresses are not quantified in the AASHTO design code. Unless appropriate finite element analysis or field testing is conducted, secondary stresses would not be determinable because the connection stiffener to girder flange and web intersection is under complex, three dimensional structural interactions, and the local geometry and relative stiffness of this detail are different for each individual bridge. Many experimental studies have been previously conducted to investigate the fatigue behavior and repair performance of the details subjected to out of plane distortion. Laboratory data obtained by Fisher et al. (1990) showed that un-stiffened web gaps can have fatigue resistance equivalent to an AASHTO Category C detail. Field tests performed by Koob et al. (1985), Fisher et al. (1987), and Stallings et al. (1993) all discovered web gap stresses higher than the fatigue limit for out of plane displacements of only about a tenth of a millimeter. Various repair strategies and implementations were also studied, and the details of available methods were summarized by Zhao and Roddis (2001). The three most commonly used retrofit approaches are (1) drilling stop holes at the crack ends; (2) attaching the connection stiffener to girder flange and (3) removing part of the connection stiffener to reduce the abrupt stiffness change at the web gap.

1.2 Motivation / Research Significance

Distortion-induced fatigue cracks appear as common in I-beam with web-gap of steel bridges. This phenomenon is the main reason for failures in a lot of steel bridge having web-gap left close to top or bottom flange. Beginning with the effort to prevent failures occurred in steel bridges originating from welds between connection stiffeners and girder tension flanges, common practice used to provide no positive attachment between connection stiffeners and girder flanges. Lack of connection creates a weak web gap region susceptible to out-of-plane distortions and fatigue. Although current AASHTO (2007) LRFD Bridge Design Specifications require positive attachment between transverse stiffeners and girder flanges, but they also allow the web gap with fixed length relative to girder thickness. Previous studies concentrated on analysis of the stresses at the web-gap under truck loading as well as methods to retrofit the I-beam to stop crack propagation. But the fracture mechanics of this problem are not understood. Some experiments have already been done on full scale testing with different definition on beam failure, as fixed critical deflection or fixed value of crack length increases. The typical beam failure with distortion-induced fatigue crack at web-gap is still not discovered with beam collapse. The questions on beam failure or distortion-induced fatigue crack behavior are still unanswered. So how is the fracture mechanics behavior in the web gap under effect of fatigue distortion-induced? How to predict the fatigue life in the web gap?

This study concentrates on analysis of distortion-induced fatigue crack at the web-gap of I-beam under cyclic loading. A rigorous study on this behavior in the content of fracture mechanics would be useful to prevent the crack as well as to extend fatigue life of I-beam. The typical beam failure is also considered to obtain critical fatigue crack of I-beam. With clear understanding on fracture behavior, the bridge parameters that influence the distortion-induced crack in web-gap are also investigated to get the better understanding on crack propagation. A propose method in predicting the distortion-induced fatigue crack base on fracture mechanics theory is also important to help capturing the crack growth. The full understanding of behavior of distortion-induced fatigue crack at web-gap and the effect of parameters to crack propagation would be useful to improve steel bridge’s resistance to unexpected out-of-plane affects.

1.3 Objectives

1) To study the behavior of distortion-induced cracks at the web gap of steel bridge.
2) To implement fracture mechanics concept for fatigue cracking in the web gap.
3) To study the influence from various parameters those are related to the distortion-induced fatigue cracks at the web-gap.

1.4 Methodology

1) Review on distortion-induced fatigue cracks at the web-gap of I-beam in steel bridges.
2) Implement fracture mechanics concept for crack initiating and propagating around the web-gap under cyclic loading.

3) Conduct an experiment of a stiffener – to – beam intersection with cyclic loads to simulate the actual cracking in the web gap of steel bridge.
4) Analysis the result in computation by using finite element analysis (ANSYS) which applying SED criterion to investigate the behavior of distortion-induced fatigue cracks in the web gap.
5) Study on effect parameters that relate to resistance for distortion-induced fatigue crack at the web-gap.

1.5 Scope of works

The research in this study would be limited to assumptions which simplify the computation as following:

1) Cyclic loading with constant amplitude.
2) Distortion-induced fatigue crack at web gap of composite I girder superstructure.
3) Linear elastic fracture mechanics.

CHAPTER II

LITERATURE SURVEY

2.1 General

Lateral bracings are installed in steel girder bridges to stabilize girders during construction to provide resistance to transverse loading, and to help distributing live loading laterally between girders (Tedesco et al., 1995). During the 1930's several failures occurred in steel bridges originating from welds between connection stiffeners and girder tension flanges (Fisher and Keating, 1989). In an effort to prevent this type of fatigue damage, common practice used to provide no positive attachment between connection stiffeners and girder flanges.

Lack of connection creates a weak web gap region susceptible to out-of-plane distortions and fatigue. Uneven loading of girders at equal stations along the bridge induces differential deflections between adjacent girders causing rotation of lateral bracing members. Because the girder top flange is restrained by the deck, out-of-plane displacement is concentrated in the flexible web gap region. Resulting secondary stresses in the web gap can lead to distortion-induced fatigue cracking. Although current AASHTO 2007 LRFD Bridge Design Specifications require positive attachment between transverse stiffeners and girder flanges, bridges constructed prior to the mid-1980s are at risk of experiencing damage due to distortion-induced fatigue.

Studies on distortion – induced fatigue crack in steel bridges have been conducted for many years due to damage found in the girder since 90s. There are two aspects of literature review undertaken in this thesis. The first deals with latest researches including field observation of the causes of distortional stress, type of fatigue damages and the factors influencing the cracking in I-beam of steel bridge. The second aspect is concerned with the fatigue cracking behavior in the web gap of structure I beam in steel bridge, and the application fracture mechanics model to solve the problem.

2.2 Distortion – induced fatigue cracking in the web gap of bridge girder

The most common types of fatigue cracking developed in bridge structures have been the result of secondary and/or displacement induced cyclic stresses. These problems have developed because of the unforeseen interaction between the longitudinal and transverse members. This interaction does not alter the in-plane behavior of the structure, and hence the design for in-plane loading and deflection is adequate when proportioning the individual components. Generally, the effects of the secondary and displacement – induced cyclic stresses are seen at connections. Often short gaps in a girder web or greater than expected restraint results in geometric amplification of the cyclic stress in the gap region, and this has resulted in cracking.

This type of cracking has occurred in many types of bridge structures. Stringer webs have cracked in suspension bridges at the stringer-floor-beam connections. Floor-beam webs have cracked in tied arch bridges. The longitudinal girders of girder-floor-beam bridges have experienced cracking in the girder web. Multiple beam bridges have experienced cracking in the girder webs at cross-frames and diaphragms, and at least one box girder structure has developed cracks in the girder web at interior cross-frames.

2.2.1 General background

The interaction of various components of a bridge structure under normal service loadings can result in cracking at unexpected locations in a relatively short time (Fisher, 1978). In multi-girder bridges, diaphragms members are present for construction purposes, to transfer lateral loads and to distribute live loads among girders. These diaphragms are commonly connected to the girders at the location of transverse stiffeners welded to the girder web. In bridge girders, fatigue cracks resulting from out of plane deformations are commonly found in webs where short gaps between the stiffener and the flange exist (Fisher and Keating, 1989). The differential displacement between adjacent girders under live loads causes a racking motion in the diaphragms as in figure 2.1, resulting in a concentration of deformation in the flexible web gap location (since the cross sectional shape of the stiff diaphragm is maintained). This problem is accentuated when diaphragms are placed on only one side of the girder web such as at exterior girders or in skewed bridges where diaphragms are staggered.

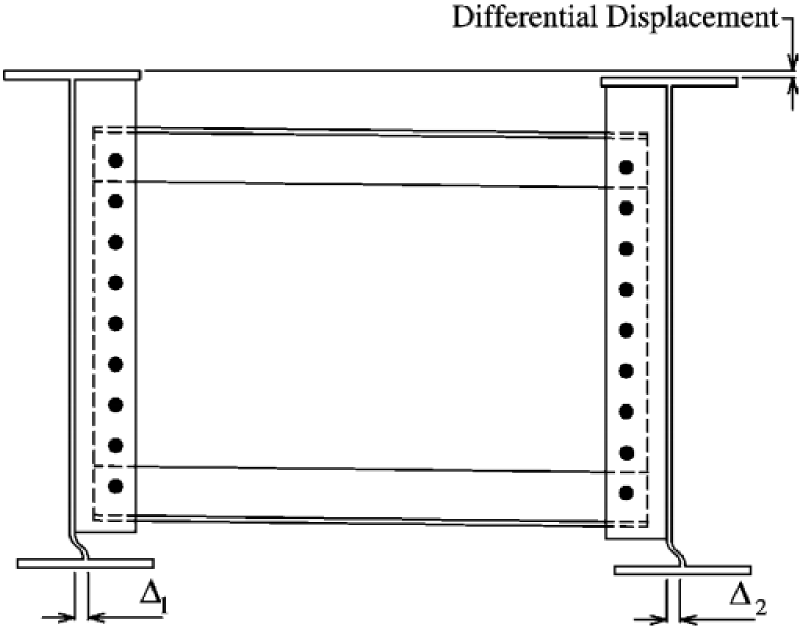

Figure 2.1 Typical out-of-plane distortions in web gap

The fatigue cracks, due to out-of-plane displacements, usually extend across the weld toe at the end of the transverse connection stiffener and grow into the web. Then, if the crack growth is allowed to continue, the crack would turn upward perpendicular to the primary stress field.

Because of the difficulty in estimating the stress range in the web gap, most displacement-induced secondary stress problems resulting in fatigue crack growth are difficult to predict at the design stage. Over the past few decades, understanding of distortion – induced fatigue cracking has improved significantly and detailing guidelines to prevent such problems have been developed. Both the use of full depth transverse stiffeners with positive connection to the flanges and the increase in the length of the web gap has both been shown to improve the fatigue life at diaphragm connections. Prior to the 1983 as guidelines in American Association of State Highway and Transportation Officials (AASHTO) Bridge Specifications (AASHTO, 1983), the transverse stiffeners were often cut short of the girder tension flange to facilitate fitting during fabrication to avoid a possible fatigue-prone detail resulting from wedding the transverse stiffeners to the tension flange. Subsequently, experience has shown that the fatigue life of this detail is independent of whether the stiffeners terminates in the web or is extended down to the flange (Fisher et al., 1998). A large number of bridges with fatigue-prone web gap details are still in service today.

Therefore, a research to determine the behavior and remaining life of these structures is important from both economic and safety-related points of view.

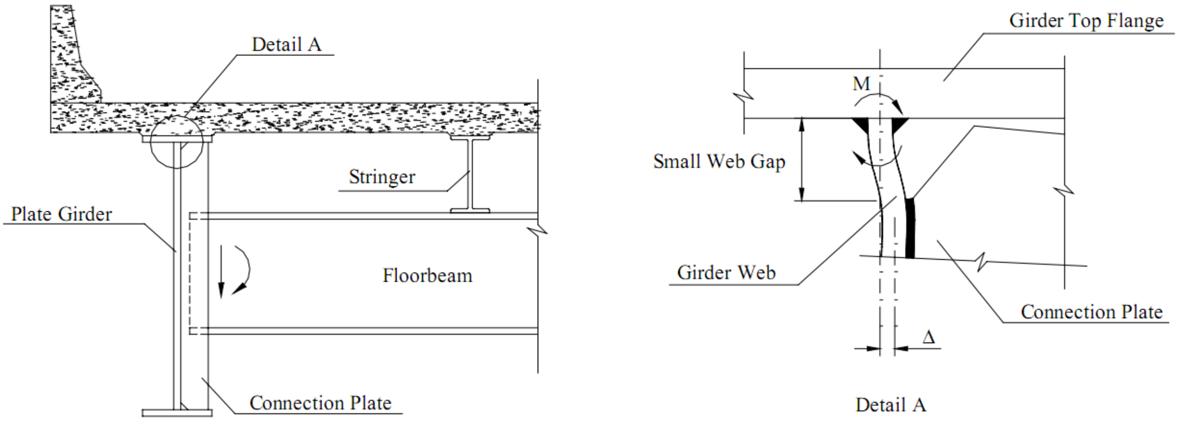

Figure 2.2 Out-of-plane distortions in small web gap at connection plate end (Fisher et al, 1990)

2.2.2 Study on distortion-induced fatigue cracking in steel I-beam of bridge

Fisher (1984) presented the investigation of seven cases of distortion – induced fatigue cracking resulting from out of plane displacement. These include: Cantilever floor – beam brackets, transverse stiffener web gaps, floor– beam connection plates, diaphragm connection plates, tied arch floor beams, stringer to floor beam (truss) brackets, and coped members. This study focus on two cases, which reveal the fatigue cracks in the web gaps, transverse stiffener web gaps and diaphragm connection plates.

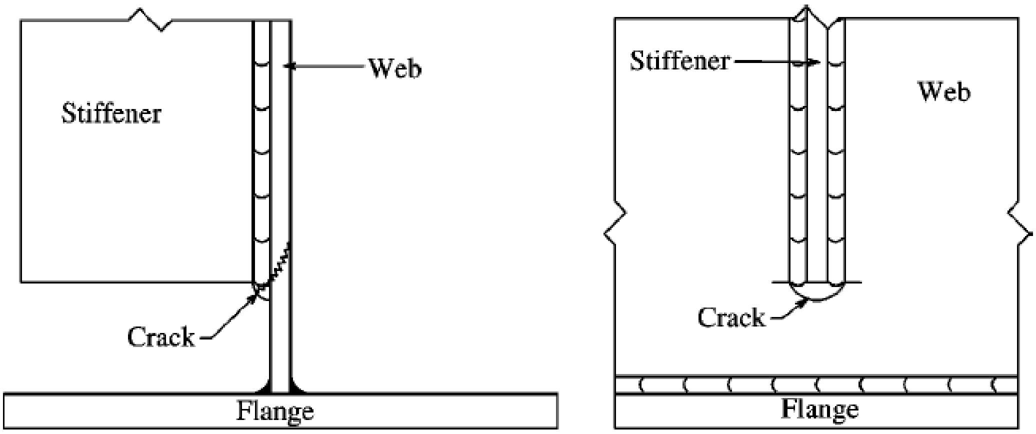

Figure 2.3 Schematic of Web Crack at End of Transverse Stiffener (Fisher, 1984)

The first case deals with cracks at the ends of transverse stiffeners that were cut short of the flanges in several plate girders. Most of the cracks were discovered either before the erection of girders or shortly after they were erected. Examination of these details indicated that cracks had formed at the weld toes at the end of stiffeners and had extended across the weld, into the web as shown in 2.3. In some cases, the cracks had started to turn upward, perpendicular to the primary bending stress field. Differential movements of the girder flanges, caused by the swaying motion of the train, likely induced sufficiently large strains in the web gap to initiate and propagate the cracks.

The second case involves fatigue cracks in the web gaps of longitudinal bridge girders at the connection of transverse beams. The cracks develop due to the end rotations of the transverse beams, which were bolted to stiffeners that had been welded to the web of the longitudinal girders. No connection was usually provided between the stiffener and the girder tension flange. Cracks develop in positive moment regions and adjacent to the top flange in the negative moment regions. In order to determine the magnitude of strains resulting from distortion of the web, strains were measured at the girder web near the web gap regions at several floor beam locations. These measurements showed that the strains in negative moment regions were larger than the stresses in the positive moment regions. Therefore the amount of lateral restraint to the tension flange seems to affect the web gap stresses, which demonstrates the difficulty in evaluating the maximum web gap stress.

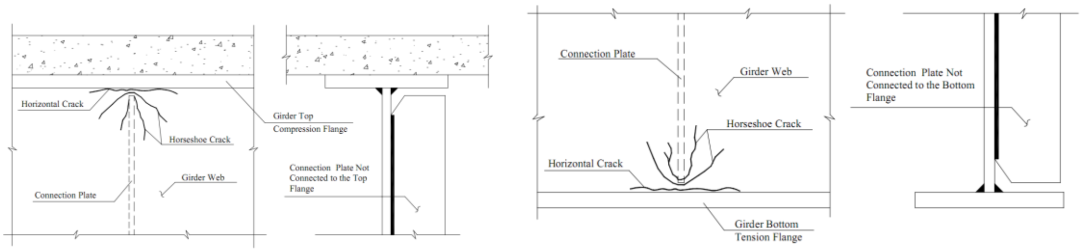

(a) Cracking in compression zone (b) Cracking in tension zone

Figure 2.4 Horizontal and horseshoe cracks developed in web gaps due to out of plane distortion.

Fisher (1984) also performed strain measurements to confirm that the web gap is subjected to double curvature. This was in agreement with Fisher and Keating (1989), and Fraser et al. (2000). The deformed shape of the web gap can be calculated as a fix-ended beam subject to a transverse support displacement. By using the moment-area theory, an approximate maximum stress in the web gap, assuming a unit width of web, is given as

$$\sigma = \frac{My}{I} = \frac{6EI\Delta}{L^2}\left(\frac{t}{2}\right)\left(\frac{1}{I}\right) = \frac{3E\Delta t}{L^2} \qquad (2.1)$$

where σ = maximum bending stress (*MPa*).
M = bending moment (*N mm*).
y = distance from neutral axis to extreme fibre (*mm*)
I = moment of inertia (*mm4*).
E = modulus of elasticity (*MPa*).
L = length of web gap (*mm*).
Δ = web thickness (*mm*).

When observing the distortion-induced fatigue cracking at the ends of transverse stiffeners, Fisher (1984) and Fraser *et al.* (2000) found that some cracks propagated further into the web and then turned upwards, perpendicular to the primary stress field. As the typical crack pattern in figure 2.3 and the idealized deformation of the web gap due to distortion-induced shown in figure 2.2, Fraser *et al.*(2000) suggested that fatigue cracks in the web gaps are the result of the combination of Mode I (crack opening mode) and Mode III (crack tearing mode). In the effective of Mode III, the top surface of the crack move further out of plane than bottom surface of the crack. Under in-plane loading conditions only (mode I), fatigue crack is just an opening crack.

Gross (1985), Tschegg and Stanzl (1988) conducted researches on Mode III fatigue crack propagation. The mode III loading causes the surfaces of a crack to rub against one another and this rubbing of the round crack surfaces causes energy to be dissipated through friction and abrasion. Because of the friction along the crack surfaces, the stresses at the crack tip are lower than would otherwise be expected. The increase of total amount of friction as the crack propagates results in the decreasing crack growth rate. When comparing the crack growth rate between one specimen subjected to "cyclic Mode III and static Mode I loading" and the other affected by "cyclic Mode III only", the first case increases the crack growth rate than the second case. When testing the crack propagation past the stop holes, Fraser *et al.* (2000) suggested that Mode III loading plays an important point in governing the distortion-induced fatigue crack. Therefore, the crack growth rate in the web gaps of bridge structure is the result of combined Mode I and Mode III fatigue loading.

In a research on behavior of distortion-induced fatigue crack in the bridge girder, Fraser *et al.* (2000) conducted an experiment on the full-scale bridge girders taken from the St. Albert Trail Mile 5.09, subdivision of bridge in Edmonton Alberta.

From the field test program, the distortions and stresses measured in the web gaps showed that the gaps are in double curvature: i.e. the top of the gap is pulled towards the end of the diaphragm and the bottom of the web gap is restrained by the relatively stiff bottom flange. It seems that rehabilitation of steel girders with distortion-induced fatigue cracks by the use of drilled holes at crack tips merely retards crack. Later, D'Andrea et al. (2001) compared the parameters between the field tests from St. Albert Trail Mile 5.09 Subdivision Bridge in Edmonton Alberta with the finite element analysis results, and confirmed that a combination of Mode I and Mode III loading was responsible for crack initiation past the stop hole. A drilled stop hole was found to be ineffective at arresting distortion-induced fatigue cracks. The stop hole drilling method can only be effective when the distortion of the web gap is prevented.

Dexter et al. (2004) also discussed about the retrofit the fatigue cracks in the web gaps by adding the rigid tee or angle together with high-strength bolts to the attachment plate and the tension flange. Holes must be drilled at the ends of short cracks as a temporary means of extending fatigue life.

2.2.3 Rehabilitation of girders with distortion-induced fatigue cracks at the web-gap

Out-of-plane fatigue cracks occur from the end of the stiffener to girder welding. Based on the observations of the Kansas Department of Transportation (KDOT) Special Inspection Team, cracking often begins with horizontal cracks at the weld-toe, and then curves into horseshoe (or U-shape) cracks in the girder under cyclic loading (Figure 2.4).

- *Cracking in compression zone:* In the investigation of KDOT, most girders were found to have horizontal and horseshoe cracks close to the girder compression flange due to pre-1989 details. Cracks often occurred at a negative moment zone and close to the top flange. As shown in figure 2.4(a), there is not possible weld or bolt to connect the stiffener to top flange, and there is only one stiffener on one side of the girder. The girder close to top flange is not restrained in out-of-plane side and the crack occurs in the compression zone. The crack grows larger as the number of cycles of load increase inside the compression zone.
- *Cracking in tension zone:* The second type of cracks effect by distortion-induced was found in bridge girders with stiffener members (diaphragms in one case, cross-frames in the other) which do not cover the full length of

girder and leave the space in tension zone. Cracks occur at the web close to the bottom flange of the positive moment region, or in tension zone. As shown in figure 2.4(b), the stiffener plates are not connected to the bottom flange, and there is only one stiffener on one side of the girder. The other side of web girder does not have stiffener to help resist out-of-plane distortion due to differential deflection between two girders of neighboring I-beams. The crack located at tension region is more common and serious when compared with the crack in compression zone. If no repair action is conducted to stop the crack propagation, the crack will grow larger and deeper into the main structural component.

Zhao and Roddis (2001) also reviewed and summarized the repairs of fatigue cracking due to out-of-plane distortion: holing drilling, stiffening the connection, cutting the connection plate short, diaphragm removal, bolt loosening, diaphragm repositioning, using composite materials. The most common methods are “Holing drilling”, Stiffening the connection and Cutting the connection plate short.

In measurement and analysis of distortion-induced fatigue in multi-girder steel bridges, Jajich and Schultz (2003) suggested that top web gap strains in negative movement regions should be considered for the bridge under investigation, and bottom web gap strains can generally be neglected. Web gap tresses during the truck tests were often much larger (as much as 20 times larger) than flange stresses in negative moment regions.

Zhao and Roddis (2003) continued using finite element analysis to calculate the web gap stresses. Both positive and negative moment region model analyses indicated severe stress concentration at the connection stiffeners ends close to the girder top flanges. The un-stiffened web gaps were exposed to stress ranges higher than the fatigue limit and were therefore vulnerable to fatigue cracking. For an un-cracked web gap detail, the area affected by out-of-plane distortion is within 125mm on each side of the connection stiffener. Using three retrofit methods: (1) add connecting welds as actually implemented in the bridge repair; (2) remove the upper truss chords; and (3) remove the truss members in addition to the current welded repair in both regions, the repairs show satisfactory to positive regions, but not successful to negative one.

In a study sponsored by the Minnesota Department of Transportation, Berglund and Schultz (2006) use the truck tests and finite element analysis of a diaphragm-girder sub-assemblage of the bridge to propose an equation for predicting web gap stresses assuming linear elastic behavior of this region.

$$\sigma_{wg} = 2E\left(\frac{t_w}{g}\right)\left(\frac{\Delta}{S}\right) \tag{2.2}$$

where E = modulus of elasticity

t_w = web thickness

g = web gap length

S = girder spacing and diaphragm length

Δ = girder differential deflection.

Also in this study, investigation of the differential deflection data from the finite element models at three girder spacing indicated that simple analytical functions could be used to represent the variation of differential deflection, Δ, with span length, *L*, and girder spacing, *S*. The schematic representation of web-gap rotation is performed in figure 2.5. The best-fit polynomial formulas offer a reasonably accurate representation of differential deflection and they are given by:

$$\frac{\Delta}{S} = \frac{aL^2 + \mathrm{bL} + \mathrm{c}}{L} \tag{2.3}$$

where L is in meters; and the coefficients *a, b,* and *c* are based on the values of skew angle, which can be obtained from linear interpolation.

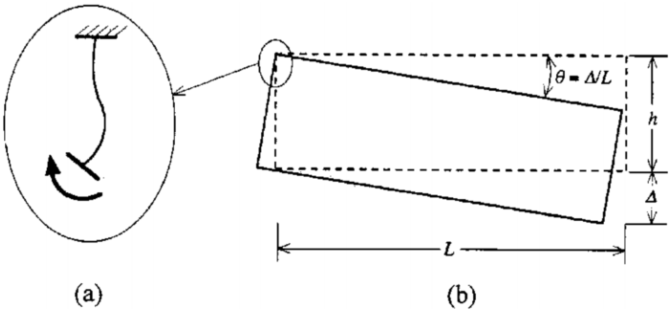

Figure 2.5 Schematic representation of web gap rotation: (a) web gap mechanism; (b) diaphragm rotation.

Berglund and Schultz (2006) also estimated the web gap length based on proportion between the girders thick, t_w, and the wep-gap length, *g*:

$$\frac{t_w}{g} = -0.00286L + 0.409 \tag{2.4}$$

Zhao and Roddis (2007) continue to investigate the fatigue behavior and retrofit distortion-induced web gap cracking with a studies in KDOT. In this study, Zhao and Roddis (2007) compared the effective of different retrofit fatigue cracking in the web gaps as shown in figure 2.6.

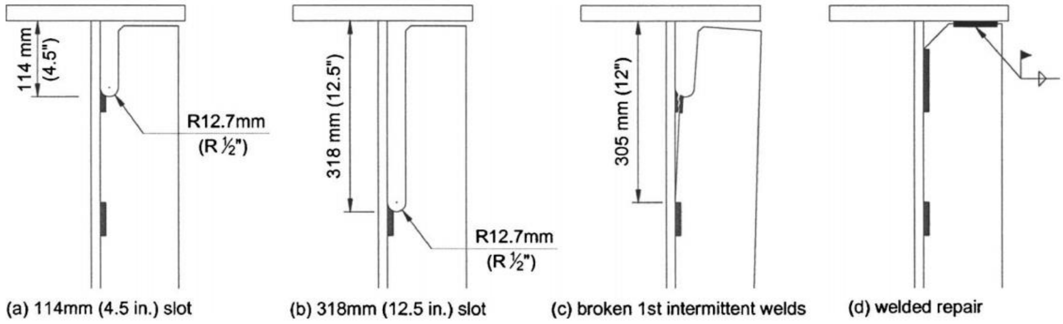

Figure 2.6 the cases investigation in Yuan Zhao (2007) study.

This study shows that the existing slot repair used in the bridge is ineffective. Increased web gap stresses are observed due to the insufficient cut-short length, which causes crack propagation and re-initiation at many of the repaired details. Use of a longer, 318 mm, (12.5in) slot could release the constraints and reduce the stress concentration to a certain degree, but would not guarantee a permanent repair as it is not able to decrease the fatigue stresses to the point below the constant amplitude fatigue threshold. The same conclusion is drawn for the condition of leaving the crack to propagate until the first intermittent welds broken. The most effective method is to stiffen the web gaps by providing positive attachment between the connection plates and girder flanges.

Hidayat and Lenwari (2009) used finite element analysis to study the effect of bridge parameters to web gap stresses, and concluded that the maximum relative displacement increases as the bridge length and girder spacing increase. In contrast, it decreases with increasing slab thickness and girder stiffness. The maximum vertical web gap stress occurred in the end of stiffener in one truck case and two truck cases implies that the stress in near the bottom flanges is more critical.

2.2.4 Current design practice

The AASHTO (1983) required that transverse stiffeners, which were connected to lateral bracing, be connected to both flanges. This requirement is partially based on the work of Fisher (1978), which included the investigation of cracking at the ends of transverse stiffeners cut short of the bottom flange of bridge girders. Current design standards AASHTO (1998) and Canadian Highway Bridge Design Code (CHBDC) (CSA, 2000) require that the transverse stiffeners be connected to both the tension and compression flanges when the transverse stiffeners are used as connection plates for diaphragms, cross-frames or floor beams. The requirement for positive attachment between transverse connection and flanges is to prevent the unexpected out of plane effect occurring at the web-gap. This unexpected effect could create the distortion-induced fatigue crack at the web-gap and failure the I-beam as the time of cyclic load increases.

The recommendation for exist web-gap of 4 or 6 times of girder's thickness comes from the old steel bridges and special structures. Researcher and designers propose the existence of web-gap to prevent the in-plane effect at positive attachment between transverse connection and flange. If the stiffener is welded to top or bottom flange, the in-plane moment would combine with shear effect at the welding which create the combination of mode I and mode II. This combined mode could damage the bottom flange and quickly fail the I-beam. Therefore, a web-gap is required to prevent the damage of in-plane effect of mode I and mode II.

For bridges built with transverse stiffeners cut short of the tension flanges, fatigue in the web gap was not considered when the bridge was designed. Therefore, the fatigue life of the web gap detail needs to be assessed. To determine the fatigue life of the web gap detail subjected to distortion-induced fatigue, current practice designates the detail as a Category C' detail (AASHTO, 1998) or Category C detail (CSA, 2000) (Fisher *et al*., 1998). The description of the Category C' detail is fillet-welded connections with welds normal to the direction of stress. The Category C' designation and the calculated stress range are then used with the S-N (stress range versus number of stress cycles) curve to determine the allowable number of stress cycles for the web gap detail. It should be noted that the S-N curve and the Category designations were developed for load-induced fatigue not distortion-induced fatigue.

The AASHTO LRFD *Bridge Design Specifications* (AASHTO 2004) do not explicitly classify details susceptible to out of plane distortion. Rather, prescriptive rules are provided for designers to prevent such cracking in bridges. For example, connection plates are to be rigidly attached to all components of a plate girder (i.e., attached to the web and flange, or web and transverse stiffener) to prevent relative movement between elements.

2.3 Mixed-mode fatigue crack growth criteria

Based on applied parameters, stress, displacement and energy concentrated at crack tip, mixed-mode fatigue crack-growth criteria could be classified into three types. The description of the mixed modes of fatigue crack growth should split depending on two main components: the crack length increment and the crack path direction. Some of criteria concentrate on calculation of crack path and crack length under multi-axial loading which is named as mix-mode condition.

Actually, the tests of crack growth under mixed-mode loading have not been standardized yet and, hence, the specimens of different geometries are used. In some part of structures, fatigue cracking is observed in special cases which are caused by the given external loading and the direction of crack growth rather than in the three typical crack modes described by Irwin (usually obtained by the superposition of these loads).

2.3.1 Stress-Based Criteria of Crack Growth:

The basic quantities for all criteria are the near-field solutions for the stress distributions at the crack front. In figure 2.7 shows a Cartesian coordinate system with origin at a point of the crack front.

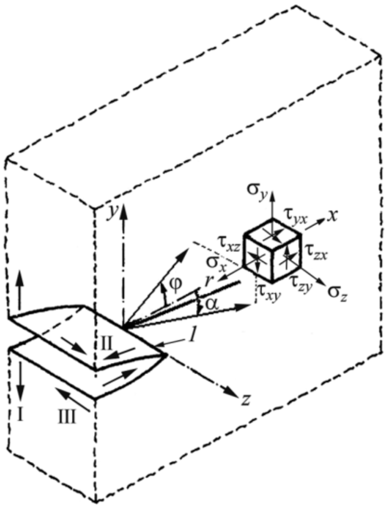

Figure 2.7 Modes of the crack-tip surface displacement and the components of the stress field.

Under uniaxial monotonic loading, crack occurs and propagates when the stress intensity factor K_I close to the crack tip obtains its critical value K_{Ic}. Therefore the criterion could be presented as following:

$$K_I = K_{Ic} \tag{2.5}$$

Under fatigue mixed-mode cyclic loads, according to different criteria,the equivalent range of the stress intensity factor (SIF) Δ Keq is calculated within the limits as following:

$$\Delta K_{I,th} < \Delta K_{eq} < K_{Ic} \tag{2.6}$$

The criteria could be based on the threshold value ΔK_{th} or the critical value K_{Ic}. With advantage of describing the entire history of fatigue cracking in experimental process, the criteria using the critical value are applied more often than other criteria. Some of criteria which is surveyed in this study are based on the critical value K_c, except the criterion proposed by Yates and Miller (1991).

For mixed mode problem under combination of loading, many criterion based on stress intensity factor were proposed. These include the criteria by: Wu (1967), Erdogan and Sih (1963), Yates (1991), Tanaka (1974), Pook (1985), Schollmann et al. (2001), Richard et al. (2001), Forth et al. (2002), Pokluda (2004), Yan et al. (1992), and Bloch and Brown (1993), etc. These criteria base on computation stress field around the crack tip, and propose a K_{eq} for mixed mode combination fracture. For example:

- *Criterion of Erdogan and Sih (1963)* based on the tangential stress. The process of crack growth starts from the crack tip in the radial direction $\varphi = \varphi_0$ perpendicular to the maximum tangential stress $\sigma_{\varphi,max}$ and fracture starts when the maximum tangential stress σ_φ, max reaches the critical value of stresses σ_c (fracture toughness K_{Ic}) equaling to the fracture stress in uniaxial tension.
- *Criterion of Richard, et al. (2001):* The author proposed the generalized failure criterion for three crack modes and the following relation for the equivalent SIF:

$$K_{eq} = \frac{K_I}{2} + \frac{1}{2}\sqrt{K_I^2 + 4(\beta_1 K_{II})^2 + 4(\beta_2 K_{III})^2} \qquad (2.7)$$

where $\beta_1 = \frac{K_{Ic}}{K_{IIc}} = 1.155$ and $\beta_2 = \frac{K_{Ic}}{K_{IIIc}} = 1.0$

- *Criterion of Tanaka (1974*): This criterion includes the following expression for the effective range of the SIF for three cracking modes:

$$\Delta K_{eq,eff} = \left(\Delta K_I^4 + 8\Delta K_{II}^2 + \frac{8\Delta K_{III}^4}{1-\nu} \right)^{0.25} \qquad (2.8)$$

- *Criterion of Forth, et al. (2002):* The criterion includes four relations for the description of fatigue crack growth. An aluminum alloy with semi-elliptic cracks at certain angles was loaded so that all considered crack modes were obtained. The following equations for the determination of ΔK_{eq} were proposed:

$$\Delta K_{eq} = \Delta K_I \qquad (2.9)$$

$$\Delta K_{eq} = \sqrt{\Delta K_I^2 + A\Delta K_{II}^2} \qquad (2.10)$$

$$\Delta K_{eq} = \sqrt{\Delta K_I^2 + \Delta K_{II}^2 + \Delta K_{III}^2} \tag{2.11}$$

$$\Delta K_{eq} = \sqrt{\left(\Delta K_I + \left|\Delta K_{III}\right|\right) + 2\Delta K_{II}^2} \tag{2.12}$$

where A is a material constant.

- *Criterion of Yan, et al. (1992):* The authors proposed the following equation for the range of the equivalent effective SIF for the mixed-mode cracking I and II:

$$\Delta K_{eq,eff} = \frac{1}{2}\cos\frac{\varphi}{2}\left[\Delta K_I(1+\cos\varphi) - 3\Delta K_{II}\sin\alpha\right] \tag{2.13}$$

where φ is the crack-growth direction obtained from the criterion of maximum shear stresses. The discussed criterion is an extended version of the criterion of maximum shear stress for the mixed-mode crack growth.

There are a lot of stress-based criteria of fatigue crack growth comparing to displacement and energy based criteria because it is simple to verify and apply during testing and formulating. First of all, stress-based criteria are based mainly on the stress σ. The parameter K is the determination of the stress field close to the crack tip, and were proved to be very useful to apply in calculating. Especially, it is useful in the case of brittle materials and elastic-plastic materials with small plastic zone to describe crack growth in the threshold range and short cracks and in the beginning stages of long cracks. Besides that, the stress criteria do not get satisfactory results in the case of developing plastic zone at the crack front.

In this literature review, the criteria are presented and relate mainly to the cases under proportional loads. No criterion was found with the stress intensity factor K which is applied to describe the cases of tests under non-proportional loading.

2.3.2 Displacement-based criteria of crack growth

The criteria based on displacements deal with multi-axial fatigue cracking and can be applied solely to the yield point σ_y. Their definition is based on crack-tip opening displacement δ or its range $\Delta\delta$ which firstly were introduced by Wells (1961). It supplies a relationship to the radius of the plastic-strain zone r_p and the crack length in elastic-plastic materials.

Under monotonic loading, the mechanism of crack propagation begins when the crack-tip opening displacement δ obtains the critical value δ_{Ic}. Therefore, the failure criterion is defined as following formula:

$$\delta = \delta_{Ic} \tag{2.14}$$

Criteria based on displacement also exist, such as those by: Panasyuk (1991), Li (1989), Sutton et al. (2000), etc. From the beginning up to now, the displacement-based criteria or the crack-tip opening displacement are not used in wide because there are many difficulties and disadvantages which are encountered in measuring and calculating the crack-tip opening displacements under mixed modes conditions. The number of criteria which using crack opening displacement to compute fracture mechanics is just a few in comparing with stress-based or energy-based criteria.

2.3.3 Energy-based criteria of crack growth

The energy criteria which could be applied in cases of multi-axial fatigue cracking deal mainly with the strain energy density or the J-integral. They could be applied in both elastic and elastic-plastic ranges and. Therefore, energy-based criteria are widely employed in predicting fracture cracking. The equivalent fatigue crack-growth range ΔJ_{eq} under mixed-mode loading is defined in following range:

$$\Delta J_{I,th} < \Delta J_{eq} < J_{Ic} \tag{2.15}$$

Some criteria based on energy are the criteria by: Rozumek and Macha (2006), Sih (1974), Hellen and Blackburn (1975), Hamoush and Reza Salami (1990), Rozumek (2004), etc.

Up to now, the energy-based criteria under mixed-mode fatigue crack condition become more and more interesting at present. Especially, energy failure criteria are applied more widely because new calculation and measuring techniques are now developed quickly and impressively. Among many criteria which is based on energy calculation, the energy approaches employ strain-energy density (in the form of the product of stress and strain) or the J-integral are most famous. The most advantage of the J-integral and the strain energy density in simulating fracture is the available to describe the changes running in the material (within the elastic and elastic-plastic ranges) in the process of crack growth. The approach which was proposed by Sih (1974) is one of the most adopted criteria. Besides that, there are some other methods based on the J-integral for mode I and II that give satisfactory agreement between the experimental and theoretical data (Qian and Fatemi, 1996).

2.4 Existant mixed-mode fatigue crack propagation model

2.4.1 Models using effective stress intensity factors

Fatigue crack growth rate in metals is usually estimated by applying the Paris law, which is first proposed for single mode deformation cases. Initially, Paris law is definite to apply with stress intensity factor if crack propagates continuously. After several studies, the effect stress intensity factor prove to be more useful in predict fatigue crack growth. Therefore, a modified Paris law for mixed-mode loading can be presented in the form of the effective stress intensity factor (SIF) as follow.

$$\frac{da}{dN} = C(\Delta K_{eff})^m \tag{2.16}$$

where C and m are material constants. The curve between $log(\Delta K_{eff})$ and $log(da/dN)$ describes the fatigue crack propagation behavior in range II, or stable propagation stage. The effects of mean stress, loading and specimen geometries are not included in this equation.

With fatigue crack, the effect of stress ratio R $(R = K_{min} / K_{max} = \sigma_{min} / \sigma_{max})$ is important to the results of crack growth, Walker (1970) suggested an equation:

$$\frac{da}{dN} = C\left(\frac{\Delta K_{eff}}{(1-R)^{1-\gamma}}\right)^m \tag{2.17}$$

where C is a constant and m is the slope on the log/log scale.

γ is the material constant obtained at various R.

The value $(1 - \gamma)$ is the weaker effect of stress ratio. From the experiments, Walker (1970) proposed the constant γ for rail steel, aluminum alloy and AISI 4340 steel equaling to 0.82, 0.64 and 0.42 respectively. Therefore, the fatigue crack growth rate of rail steel is less affected by the stress ratio than that of other steels.

Moreover, the effects of crack growth characteristics at low and high levels of range of stress intensity factor (ΔK) are not included in the Walker's equation. The parameter ΔK $(\Delta K = K_{max} - K_{min})$ presented the effect of stress intensity factor range to crack growth rate, especially when K_{max} approaches the critical K_c. In this case, Forman et al. (1967) suggested considering the fatigue crack relationship to Paris law as following:

$$\frac{da}{dN} = \frac{C\left(\Delta K\right)^n}{(1-R)K_c - \Delta K} \tag{2.18}$$

where C and n are material constants. At a given ΔK level, the component $[(1 - R)K_c - \Delta K]$ decreases when the stress ratio R increases and fatigue toughness K_c decreases respectively, in order to increase crack growth rates. Even $K_{max} \rightarrow K_c$, which corresponds to instability, this equation predicts an unbounded value of da/dN.

To include the effect of K_{min}, Donahue et al. (1972) proposed a relationship in the form of Paris law as following:

$$\frac{da}{dN} = K(\Delta K - \Delta K_{th})^m \tag{2.19}$$

where ΔK_{th} is the threshold value of ΔK.

Another important parameter to fatigue crack growth is the sigmoid response. Erdogan and Ratwani (1970) proposed a consideration of sigmoid response by generating fatigue crack growth law as follow.

$$\frac{da}{dN} = \frac{C(1+\beta)^m(\Delta K - \Delta K_{th})^n}{K_c - (1+\beta)\Delta K} \tag{2.20}$$

In the above equation C, m, n are empirical material constants.

$$\beta = \frac{K_{\max} + K_{\min}}{K_{\max} - K_{\min}} \tag{2.21}$$

In this equation, the effect of mean stress on fatigue crack propagation is introduced by using the factor $(1+\beta)$, while the factor $K_c - (1+\beta)\Delta K$ obtained from experimental data at K_{min} level.

In aerospace field, a well-known advanced approach is NASGRO expression. This equation is proposed as follow:

$$\frac{da}{dN} = C(\Delta K_{eff})^n \frac{\left(1 - {}^{\Delta K_0}\!\big/_{\Delta K_{eff}}\right)^p}{\left(1 - {}^{K_{\max}}\!\big/_{K_{Jc}}\right)^q} \tag{2.22}$$

$C(\Delta K_{eff})^n$ is the behavior in the Paris region II, while $\left(1 - {}^{\Delta K_0}\!\big/_{\Delta K_{eff}}\right)^p$ and $\left(1 - {}^{K_{\max}}\!\big/_{K_{Jc}}\right)^q$ are applied in region I and region III respectively.

ΔK_0 is the fatigue threshold.
K_{max} is the maximum stress intensity factor in cyclic load
K_{Jc} is the crack resistance against fracture.
p and q are empirical constants from curve fitting.

Pook and Greenan (1979) studied the crack path propagation and discovered that crack growth was at an angle of roughly 70^{o} in all cases, corresponding to the original crack line even though mode II exist in the applied stress. Therefore, Roberts and Kibler (1971) proposed the equation considering the shear fatigue crack growth as follows:

$$\frac{da}{dN}=\frac{C_1(\Delta K_I)^{n1}+C_2(\Delta K_{II})^{n2}}{\left[\left(\frac{K_{\mathrm{I}max}}{K_{Ic}}\right)^2+\left(\frac{K_{IImax}}{K_{Ic}}\right)^2-1\right]} \tag{2.23}$$

2.4.2. Newman's crack closure model

To relate the effect of crack geometries to fatigue crack growth, Newman (1981) concentrated the crack closure behavior and proposed the following model (as Newman's crack closure model, 1981):

$$\frac{da}{dN}=C(\Delta K_{eff})^n G/H \tag{2.24}$$

Where

$$G=1-\left(\frac{\Delta K_0}{\Delta K_{eff}}\right)^p \tag{2.25}$$

$$H=1-\left(\frac{\Delta K_{\max}}{C_5}\right)^q \tag{2.26}$$

With this equation, the effect of crack length, specimen width and specimen type is presented as a function of the cyclic fracture toughness, as the elastic fracture toughness.

2.4.3. Chen and Keer s' model

Chen and Keer (1991) proposed a model relating the fatigue crack growth to the accumulated crack opening and sliding plastic displacements. There are some assumptions included in this model:

(i) The crack closure and the crack branching effects can be neglected.

(ii) The total accumulated plastic displacement is the vector sum of the accumulated crack opening and crack sliding displacements.

(iii) The tensile and shear stresses in the yield zone satisfy the Von Mises criterion.

Consider the relationship between ΔJ and displacements under small scale yielding condition and the relationship between SIF and displacements, the mixed mode I and II is presented as follows:

$$\frac{da}{dN}=\frac{\pi\Delta K_{eff}^4}{96E\gamma\sigma_{yc}^2} \tag{2.27}$$

where $$\Delta K_{eff} = \left[\left(\Delta K_I^2 + 3\Delta K_{II}^2 \right)^3 \left(\Delta K_I^2 + \Delta K_{II}^2 \right) \right]^{1/8} \tag{2.28}$$

And $$\frac{da}{dN} = \frac{\pi E}{96\gamma} \left(\frac{1+3R_\sigma^2}{1+R_\sigma^2} \right)^{1.5} \frac{\Delta J^2}{\sigma_{yc}^2} \tag{2.29}$$

γ present the effective surface energy for fatigue crack.

R_σ is the ratio of the applied shear stress to tensile stress range.

σ_{yc} is the cyclic yield strength.

The results predicted with this model show the reasonable comparing to experimental data.

2.4.4 Equation using crack tip displacement (CTD) or ΔJ

Forming as Paris law, these equations are presented as following:

$$\frac{da}{dN} = C(\Delta CTD)^m \tag{2.30}$$

$$\frac{da}{dN} = \frac{4}{\pi \sigma_S E} \left[\left(\Delta K_I^2 + 3\Delta K_{II}^2 \right) \left(\Delta K_I^2 + 2\Delta K_{II}^2 + 2\Delta K_I 3\Delta K_{II} \right) \right]^{1/2} \tag{2.31}$$

$$\frac{da}{dN} = C(\Delta J)^m \tag{2.32}$$

Li (1989) suggested using a “Vector Crack Tip Displacement” (CTD), while Dowling and Begley (1976) proposed applying the J-integral approach, as well as Wüthrich (1982), Srivastava and Garg (1988), Chow and Lu (1991). After that, Hoshide and Socie (1987) extended the concept of small cracks under mixed-mode loading to fatigue crack growth rate analyses.

2.4.5 Equation using strain energy density

Sih and Barthelemy (1980) thought the commonly used Paris law is not adequate for mixed mode crack growth problems cause loading parameters, the stress amplitude and the mean stress level are not included in the equation as well as a crack does not grow in a self-similar manner under mixed mode loads. So the using strain energy density to predict fatigue crack is a good approach:

$$\frac{da}{dN} = C_S (\Delta S)^{n_s} \tag{2.33}$$

where ΔS is the strain energy density factor range while C_s and n_s are material constants.

Similar to the Paris law for mode I loading, the constant C_s and n_s can be identified from experiments.

The strain energy density factor is defined as:

$$S = a_{11}k_1^2 + 2a_{12}k_1k_2 + a_{22}k_2^2 + a_{33}k_3^2 \qquad (2.34)$$

and the coefficients a_{ij} *(i, j = 1, 2)* are presented as:

$$16\mu a_{11} = (1+\cos\theta)(\kappa-\cos\theta)$$

$$16\mu a_{12} = \sin\theta\left[2\cos\theta-(\kappa-1)\right]$$

$$16\mu a_{22} = (\kappa+1)(1-\cos\theta)+(1+\cos\theta)(3\cos\theta-1)$$

$$16\mu a_{33} = 4 \qquad (2.35)$$

With $\kappa = 3-4\upsilon$ and $\kappa = (3-\upsilon)/(1+\upsilon)$ for plane strain and plane stress conditions, μ is the shear modulus of elasticity. The angle θ denotes the position of the radius vector, and is measured from a line collinear with the crack.

The k_i is the SIF per constant: $k_i = K_i/\sqrt{\pi}$ with *(I = I, II, III)* (2.36)

In linear elastic fracture mechanics, the strain density density can be rewritten as:

$$\Delta S = 2\left[a_{11}\overline{k_1}\Delta k_1 + a_{12}\left(\overline{k_2}\Delta k_1 + \overline{k_1}\Delta k_2\right) + a_{22}\overline{k_2}\Delta k_2 + a_{33}\overline{k_3}\Delta k_3\right] \qquad (2.37)$$

where $\Delta S = S_{\max} - S_{\min}$; $\Delta k_j = \left(k_{\max}\right)_j - \left(k_{\min}\right)_j$ and $\overline{k_j} = \frac{1}{2}\left[\left(k_{\max}\right)_j + \left(k_{\min}\right)_j\right]$

Lam (1989) discovered that the strain energy density factor range ΔS is not compatible when dealing with the concept of crack closure and suggested an implementation of the concept of ΔS based on contact stress intensity factor concept (Lam and Williams 1984):

$$\Delta S_{eff} = \Delta S[1-g(R)] \qquad (2.38)$$

$$g(R) = [f(R)/(1+R)][(1+R)f(R)-2]+2f(R)$$

with *f(R)* is a monotonic decreasing function with *R*.

2.5 Conclusions

Initially, to prevent the fracture occurred in steel bridges at welding connecting transfer components to the girder tension flange, a web-gap was provided to free the welding between stiffener and flange. Lack of connection creates a weak web gap region susceptible to out-of-plane distortions and fatigue. Current AASHTO (2007) LRFD Bridge Design Specifications require positive attachment between transverse stiffeners and girder flanges. But researchers and designers recommend that the web gap should occur with fixed length relating to girder thickness to prevent the effect of combination of mode I and mode II which is more dangerous to structure. The previous researches concentrated on the stress in the web gap and the parameters that affect distortion-induced fatigue. The assumption on combined mode I and mode III behavior was proposed without details. The fracture mechanics behavior in the web gap under effect of fatigue distortion-induced is unclear. The prediction of the fatigue life at the web gap is not answered.

Many criterion on fracture mechanics have been proposed to predict the crack propagation as well as the fatigue crack growth under mixed mode condition. These criterions could be classified in 3 categories: stress based, displacement based and energy based criterion. Unlike the others, the energy based criteria do not require an equivalent transfer’s value from pure mode to mixed mode, and seem to be more accuracy to solve the fracture problem under mixed mode condition. The advantage of energy based criterion is observed in both crack path prediction and fatigue crack growth. The main question is which one is easier to implement for numerical calculation, and the procedure to simulate with highest accuracy. In the group of energy based criteria, SED criterion with implementation would present as the same form in predicting crack path and fatigue crack growth, while the others are fixed the formula to crack tracking or fatigue crack life.

CHAPTER III

THEORETICAL CONSIDERATION

3.1 General

Earlier studies assumed distortion-induced fatigue crack in the web gaps of steel bridge to be a combination of mode I (bending crack) and mode II (distortion crack). Under mixed mode I and III loadings, crack growth behavior represents a twisted crack. A significant decrease in mode I fatigue crack growth rate can result from the addition of a static mode III load, which has been attributed to a strong mode I crack closure effect due to the applied static mode III load. Also, material deformation has a strong influence on mixed mode I and III crack growth behavior, causing the fracture toughness to depend on the sequence and type of loading. To obtain the solution for fatigue crack at the web gaps, both analytical approach and experimental program are considered:

1) Analytical approach is based on combination of Strain Energy Density (SED) model and modified Paris law for fatigue load. The fatigue life of crack in the web gaps is predicted using finite element method to find down the crack path and the number of cyclic.
2) An experiment is setup to simulate the actual connection of steel bridge that the fatigue crack occurs. In this experiment, the effect of load proportion, crack closure will be considered to establish the relationship between them to fatigue life of distortion-induced crack of the web gaps of steel bridge. The experimental data is used to improve the behavior of distortion-induced fatigue crack at web gap of I-beam and compare with the FEM model.

3.2 Analysis of distortion-induced fatigue crack in the web gap

Previous studies on the fatigue strength of steel bridge details showed that fatigue cracks usually initiate at welded details (Fisher et al, 1978, 1984, 1989). Under out of plane moment, the web gap is observed to have two curves as shown in Figure 3.1. Fracture may be classified into two steps: the crack initiation and the crack propagation.

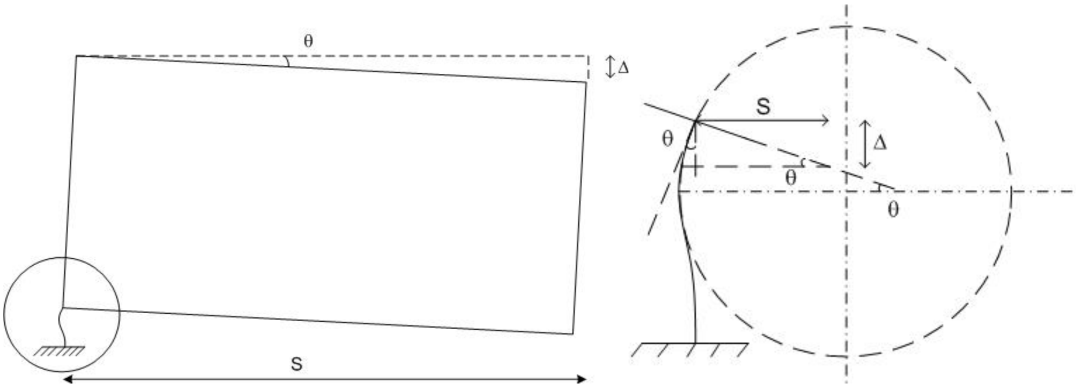

Figure 3.1 Double curvature web gap under distortion-induced.

The stage of crack initiation is crucial but quite complicated. General fracture mechanics program ignore this problem. In fact, it is difficult to determine the location of a new crack. Micro-failure and scratches always create invisible local stress concentration points which are at the origin of failure and cracks. In this research, the crack is assumed to initiate at the weld toe on the girder surface as a semi-elliptical shape across the web thickness. Because our study concentrates on the crack propagation, so the stage with initial crack can be neglected and we focus on pre-existing crack, that is the crack is assumed to occur and become two tip cracks.

The stage of crack propagation can be described as follow: crack begins with horizontal cracks at the web gap, shapes as weld-toe, and then curves depending on ratio between stress out of plane to in-plane and change to vertical cracks in the web as the number of cyclic loading increases. After crack initiates, the behavior of fatigue crack will be assumed to be two crack tips with the different effective of mode I (opening crack) and mode III (tearing crack) as in figure 3.2.

- ***With the crack path:*** mode I will control the whole crack propagation from the initiation in the web gap to the under in-plane loading conditions alone when crack propagate follow vertical line up ward to the fixed flange of beam.
- ***With the crack growth rate:*** mode I and mode III affect to the fatigue life when the cracks follow the horizontal line and the curve changing to vertical line. After the crack propagate as the vertical line, the effect of mode III will disappear, and the crack becomes the pure mode I crack.

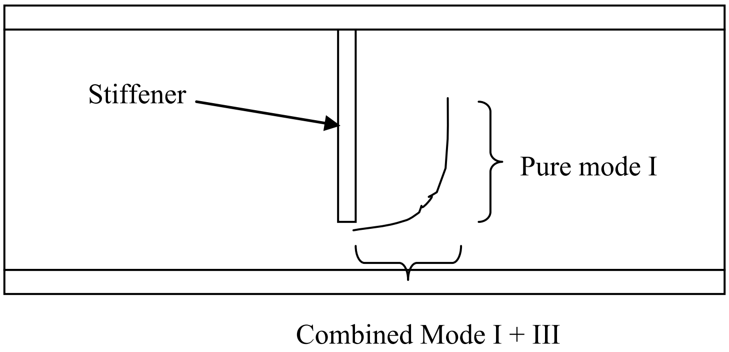

Figure 3.2 Effects of Mode I and Mode III on crack propagation

Initially, crack occurs in tension surface under effect of moment out of plane – M_z – (mode I) and torsion force – V_{yz} – (mode III) as shown in Fig 3.3. The crack grows into the girder as semi ellipse sharp and reaches the other face (compression face). Net section, which is defined as the left area following girder thickness when crack grows to compression face, decreases will lead increasing of opening and torsion stress in net section (section B-B in Fig 3.3 show the change of opening stress in net section). This increase will make the crack easily reach to the other surface even in compression zone. When reaching the compression face, the crack becomes two crack tips and propagates in both faces as shown on section A-A Fig 3.3. In this study, we assume the crack propagates as parallel curve indicating that the increase of crack length of the tension and compression face are the same.

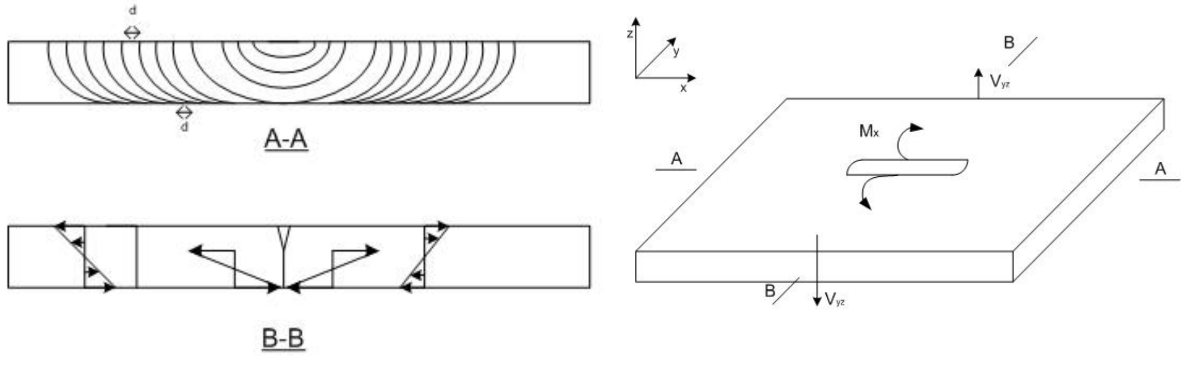

Figure 3.3 Initiation and propagation of crack under out of plane moment and torsion force.

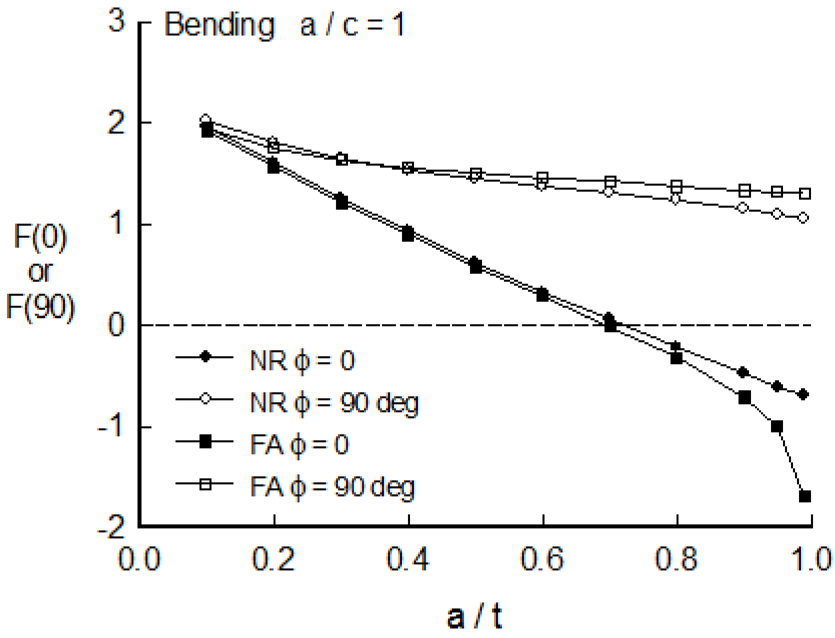

Figure 3.4 Correct factor of stress intensity factor with semi ellipse crack in finite thickness plate (Newman Jr and Raju, 1981)**.**

When semi ellipse crack grow to touch other surface, there are two significant crack tips; one crack tip run along the tension surface and the other runs deeply in the plate. Newman Jr and Raju (1981) considered about the embed ellipse crack in finite plate under bending for both theoretical analysis and FEM as presented in figure 3.4 and appendix A. In this figure, *a/c* represents the deep length of semi ellipse crack to plate's thickness ratio; $\theta = 0^o$ and $\theta = 90^o$ present the position of crack tip along surface and inside the plate, respectively. As shown in figure 3.4, the correct factor of stress intensity factor of crack tip along the surface decreases faster than the factor of crack tip inside the plate when the ellipse grows deeply inside. In other words, the ellipse crack grows faster inside the plate than the surface and quickly touches the compression side.

After becoming two crack tips, the crack continues to propagate following horizontal line under out of plane moment and torsion force until the mode I changes its direction. The effect of out of plane moment decreases far from web gap, and crack changes direction to bending effect from in plane moment. In this state, the direction of crack will grow from horizontal to vertical direction. After crack propagate totally in vertical direction, the in-plane moment will control the fatigue crack and fatigue life as shown in figure 3.5.

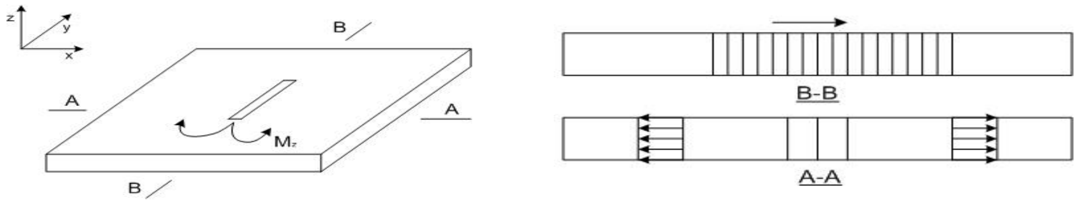

Figure 3.5 Crack propagation under in plane moment.

3.3 Minimum strain energy density criterion (S-criterion)

This criterion was proposed by Sih (1973, 1974), and is based on the local density of the energy field in the crack tip region. The crack is assumed to grow in a direction along which the strain energy density factor, S, reaches a minimum value and fracture occurs when this factor reaches a critical value, S_C. The strain energy density factor, S, can be written as form of stress intensity factor:

$$S = a_{11}k_1^2 + 2a_{12}k_1k_2 + a_{22}k_2^2 + a_{33}k_3^2 \qquad (3.1)$$

with a_{ij} (i, j = 1, 2, 3) are coefficients relating the polar angle.

θ is the angle of crack propagation.

E is elastic modulus.

with $\kappa = 3 - 4\upsilon$ and $\kappa = (3-\upsilon)/(1+\upsilon)$ for plane strain and plane stress conditions, μ is the shear modulus of elasticity.

v is Poisson’s ratio.

$$16\mu a_{11} = (1+\cos\theta)(\kappa - \cos\theta) \qquad (3.2a)$$

$$16\mu a_{12} = \sin\theta\left[2\cos\theta - (\kappa - 1)\right] \qquad (3.2b)$$

$$16\mu a_{22} = (\kappa+1)(1-\cos\theta) + (1+\cos\theta)(3\cos\theta - 1) \qquad (3.2c)$$

$$16\mu a_{33} = 4 \qquad (3.2d)$$

The angle θ denotes the position of the radius vector and is measured from a line collinear with the crack.

The k_i are defined as: $k_i = K_i / \sqrt{\pi}$ with (i = *I, II, III*)

where K_i are stress intensity factors for modes I, II, and III respectively.

The necessary and sufficient conditions for the determination of crack growth directions are based on ***Hypothesis 1*** “The direction of crack propagation at any point along the crack border is toward the region with the minimum value of strain energy density factor S as compared with other regions on the same spherical surface surrounding the point." Thus,

$$\frac{\partial S}{\partial \theta} = 0 \qquad \text{and} \qquad \frac{\partial^2 S}{\partial \theta^2} > 0 \tag{3.3}$$

Simplify the strain energy density criteria for combined Mode I and Mode III, the strain energy density can be rewritten as:

$$S = a_{11}k_1^2 + a_{33}k_3^2 \tag{3.4}$$

In general form of stress field, the strain energy density is expressed as following:

$$\frac{dW}{dV} = \frac{S}{r} = \left(\frac{1+v}{2E}\right)\left[\sigma_{11}^2 + \sigma_{22}^2 + \sigma_{33}^2 - \frac{v}{1+v}(\sigma_{11} + \sigma_{22} + \sigma_{33})^2 + \sigma_{12}^2\right] \tag{3.5}$$

where E is elastic modulus.
v is Poisson's ratio.
r is radius from crack tip.
dW/dV is strain energy density

To apply the SED criterion in FEM for crack path prediction, it's required to modify the computation, which is presented in chapter V (FEM simulation). The most advantage in applying SED factor for crack path prediction is the simple element requirement. In other criteria, singularity or special elements are established in order to track the crack propagation. SED criterion only requires the calculation of all element's strain energy around crack tip for prediction.

3.4 Implementation of SED criterion in fatigue crack growth rate

Sih and Barthelemy (1980) thought the commonly used Paris law is not adequate for mixed mode crack growth problems since loading parameters, the stress amplitude and the mean stress level are not included in the equation as well as a crack does not grow in a self-similar manner under mixed mode loads. Therefore, the strain energy density to predict fatigue crack is a good approach:

$$\frac{da}{dN} = C(\Delta S)^n \tag{3.6}$$

where ΔS is the strain energy density factor range while C and n are material constants.

$$\Delta S = 2\left[a_{11}\overline{k_1}\Delta k_1 + a_{12}\left(\overline{k_2}\Delta k_1 + \overline{k_1}\Delta k_2\right) + a_{22}\overline{k_2}\Delta k_2 + a_{33}\overline{k_3}\Delta k_3\right] \tag{3.7}$$

and $\Delta S = S_{\max} - S_{\min}$; $\Delta k_j = \left(k_{\max}\right)_j - \left(k_{\min}\right)_j$ and $\overline{k_j} = \frac{1}{2}\left[\left(k_{\max}\right)_j + \left(k_{\min}\right)_j\right]$

Lam (1989) found that the strain energy density factor range ΔS is not compatible when dealing with the concept of crack closure and suggested a modification of the concept of ΔS based on contact stress intensity factor concept (Lam and William 1984):

$$\Delta S_{eff} = \Delta S[1 - g(R)] \tag{3.8}$$

$$g(R) = [f(R)/(1+R)][(1+R)f(R) - 2] + 2f(R)$$

with *f(R)* is a monotonic function of *R*.

Then, the fatigue crack growth rate is calculated by Paris law’s implement as:

$$\frac{da}{dN} = C(\Delta S_{eff})^n \tag{3.9}$$

The implement of Paris law with SED factor effect would be useful in computation in FEM simulation. The fatigue crack growth rate is calculate with implement SED factor reveal the capability to predict the fatigue life of crack propagation.

CHAPTER IV

EXPERIMENTAL PROGRAM

Three series of experiments were performed to validate with FEM simulation results. The main idea of experimental program is to obtain the positive deflection between girders and the rigid body (see figure 4.1) to similar the deflection between two neighboring I-beams in steel bridge under cyclic loading. With deflection created in experiment, the girder will be curved out-of-plane at the connection of transfer component (stiffener as in these testing) and the crack occurs due to distortion-induced fatigue effect. Cyclic load is applied to simulate the effect of truck loading on bridge. As number of cyclic loading increases, the crack propagates further and deeper into the web. The experimental details as well as results are described in this chapter.

4.1 Experimental details

4.1.1 Objectives

Based on the real geometries of the steel bridge and ASSHTO 2007, a model is setup to simulate the effect of cyclic load to the initiation and propagation of crack in the web gaps. Based on the assumption that fatigue crack occurs due to effect of mode I and mode III, the model of connection between stiffener and girder are designed to be similar to what occurred in connection of steel bridge that distortion-induced crack happens. The purposes of experiments in this study could be listed as follows:

- To investigate the behavior of distortion-induced fatigue crack at the web gap of I-beam under cyclic load.
- To study the typical of beam failure due to distortion-induced effect.
- To measure the stress field around web-gap, the crack propagation and fatigue crack growth rate in order to validate with FEM models.

4.1.2 Testing setup

The purpose of testing is to study about the behavior of distortion-induced fatigue crack of the web gaps in I-beams of steel bridge. In bridge structures, the stiffener attached to web of I-beam leaves a web-gap close to the top or bottom flange. Due to different deflection between two girders of I-beam under cyclic loads of vehicles, the distortion-induced effect occurs and twists girders at the connection. Besides that, the web-gap is also subjected to bending moment. The combination of different deflection and bending moment results in the fatigue crack at the web-gap. Test is setup to express the combination of in-plane and out-of-plane moment effects. Due to size and capability of cyclic testing machine, small I-beams are designed based on AASHTO 2007 instructions.

The system of testing includes a support beam placing on a steel platform with thickness of 20 cm. The steel platform is thick enough for prevent shapeless under maximum load and laid on the bottom actuator. The pin supports are also laid on support beam and connected by bolts. The distance between two pin supports could be changed and identified depend on each testing beam. A rigid body placing on the steel plate with fix distance to the testing beam is connected to stiffeners by four bolts. The rigid body present the half distance between two girders and supply the identified support point to stiffener as the same problem in real steel bridge. Because the support beam and the rigid body are fixed to steel plate, the relative deflection between the testing beam and support beam will be the same deflection between testing beam and rigid body. All of details of testing system are assembled by bolts and allow to test many kinds of testing beam with different of span length.

The testing machine can supply the cyclic load with combination of top and bottom actuators. Top actuator was fixed during the tests and called the fix actuator. Bottom actuator supply the cyclic load with frequency control and called the cyclic actuator. The machine can supply loading control or displacement control. In this research, the loading control is chosen for all experiments.

The operation of the system can be described as following procedure. When the cyclic actuator moves up and down, the system includes steel plate, support beam, rigid body, pin support and testing beam will have the same displacement. The top actuator is fixed and connected to middle part of testing beam as two loading points on specimen. Testing system will produce the deflection between the specimen and rigid body as the different deflection between two girders in steel bridge. Figure 4.1 and 4.2 show the testing system in design and in experiment.

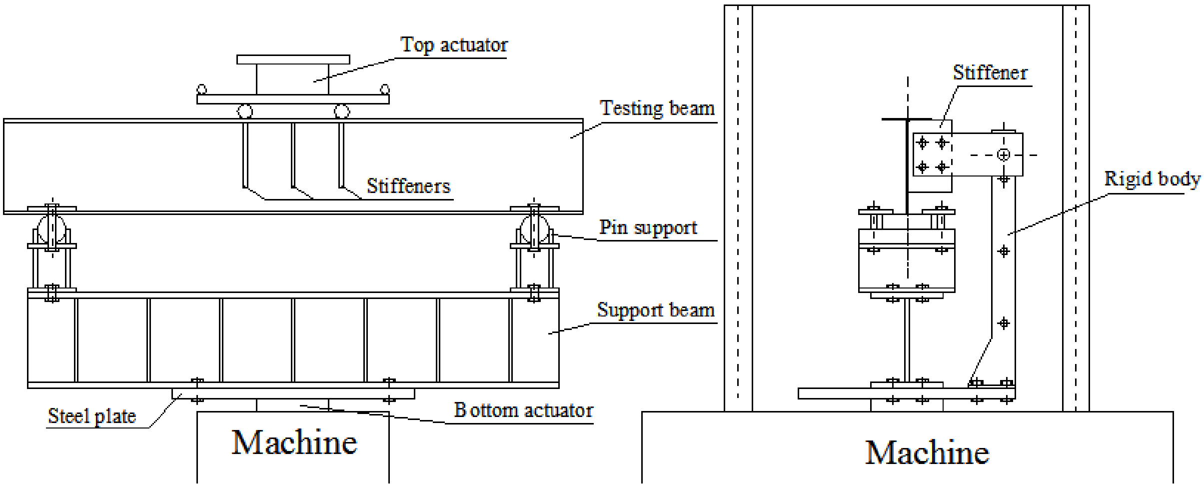

Figure 4.1 Testing system

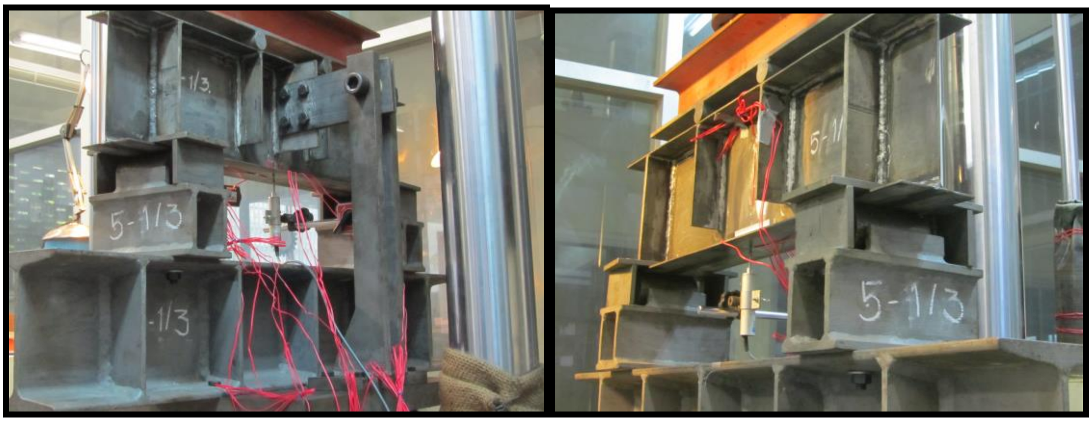

a) Front and back side of testing.

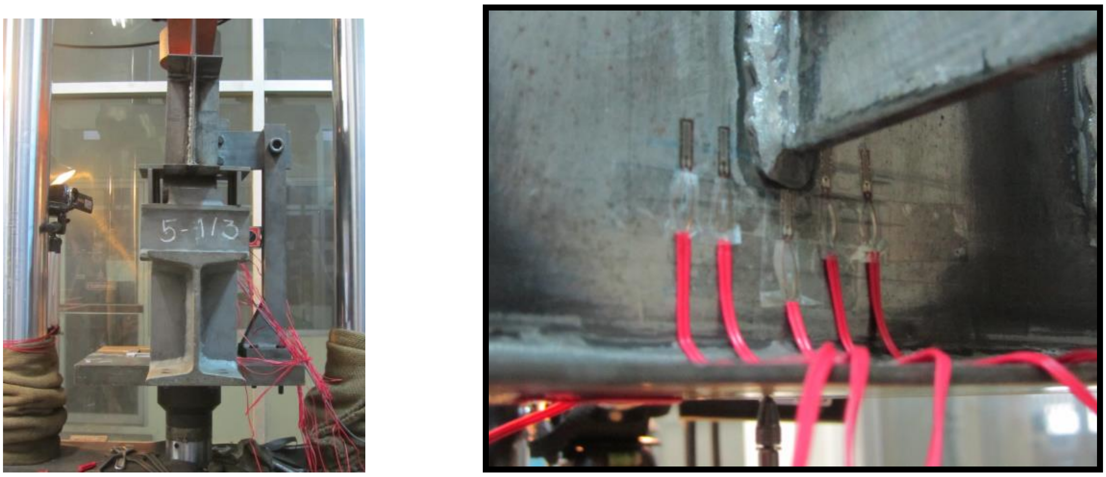

b) Testing on side view and web-gap location.

Figure 4.2 Imagine of experimental program.

There are 3 series of experiments with 9 testing beams. The load was applied on each series cyclic load with the ratio of P_{min}/P_{max} equaling to 0.2. Load range was large enough to produce stress range larger than threshold value for crack to occur and propagate. Load max is also small enough to treat all of details in elastic behavior. Load was applied in 2 points on testing beams to model the case of a simple beam with 4 points (2 points for applied load and 2 points of supporter). In this research, the load applied on each series of specimens can be shown in table 4.1:

Table 4.1: Applied loading in the experimental program.

Series of Specimens	*Load max (kGf)*	*Load min (kGf)*	*Load range (kGf)*	*Stress at bottom range (kG/cm^2)*	*Stress at web gap range (kG/cm^2)*
I	5500	1100	4400	902	1650
II	4000	800	3200	840	1642
III	14000	2800	11200	1128	1710

The cyclic loads applied in experimental programs were strictly followed requirement as:

- Constant amplitude fracture loading.
- Frequency: 4 Hz.
- The stress ratio R = 0.2 ($R = \sigma_{\min} / \sigma_{\max}$)

4.1.3 Specimens

In order to investigate about the behavior of distortion-induced fatigue crack at web-gap of I beam under deflection as in steel bridge, experiments on nine specimens were conducted. The testing I-beam was welding beam instead of hot-roll I-beam. The reason for this choice is that available hot-roll I-beams cannot represent the scale of real steel bridge as AASHTO requirements (the flange's thickness and web's thickness ratio). Thickness of component of specimens is as follows:

- Thickness of flange: 3 mm.
- Thickness of web: 2.5 mm.
- Thickness of stiffener: 5 mm.

The thicknesses of other details are shown in Fig 4.3. Stiffener is located at the middle of the testing specimen and connected to girder by ground smooth welding to prevent the residual stress. Ground smooth welding is also required in other place of specimens such as the welding between flanges and girder. Eliminating residual stress is an important task, because the thickness of flange and web is too thin for assembling with normal welding. If the procedure of doing weld is not strictly applied and the welds are not be grounded smooth one, residual stresses occur unexpectedly and affect the stress field around the welds.

The testing specimens are classified into three series of beams to analyze the effect of geometries on fatigue crack in the web gap. The parameters, that are crucial to distortion-induced fatigue, are varied and they are:

- The different web gap length which affect to stress at the web gap.
- The different span length of beams which affect to in-plane moment to torsion.

Table 4.2 presents the different geometries of three series' specimens in both web-gap length and span length.

Table 4.2: Parameter study of specimens

Series of Specimens	*Number of Specimens*	*Web gap length (cm)*	*Span length (cm)*
I	3	4	100
II	3	2.5	100
III	3	4	60

The details of specimens are shown in figure 4.3:

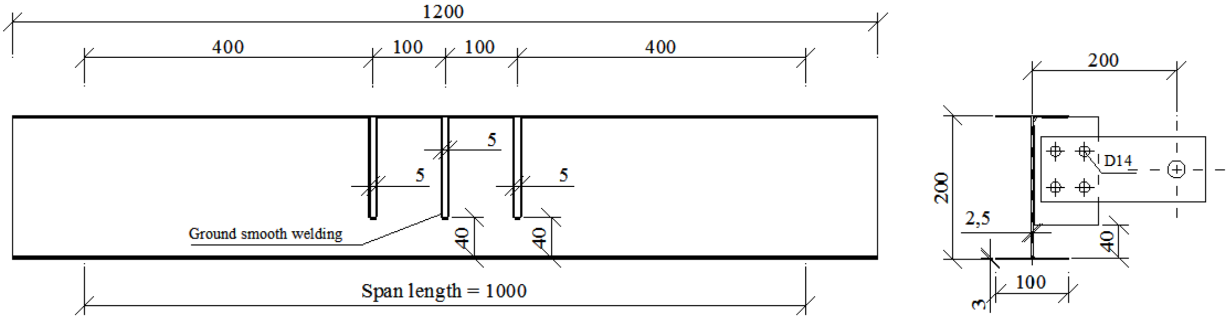

(a) Series I

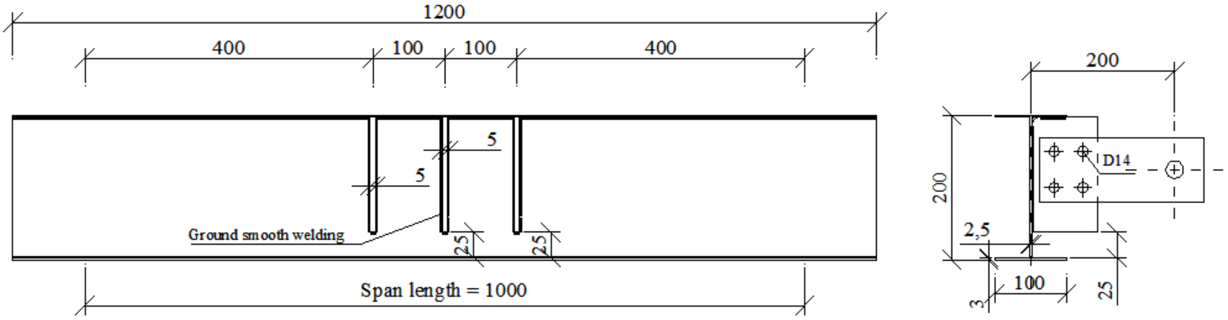

(b) Series II

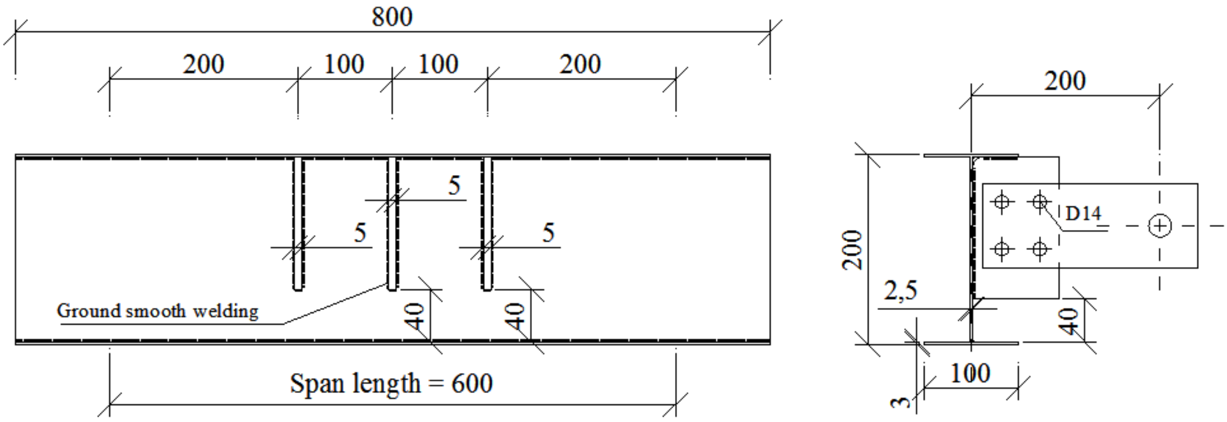

(c) Series III

Figure 4.3 Details of three specimen series

As AASHTO 2007 requirement, web-gap length is chosen to be 4 to 6 times of web's thickness. In these tests, the web-gap length must be large in enough space for placing strain gages (the length of strain gage is about 1 cm). So two values of the web gap length are chosen in this research: 2.5 (cm) and 4 (cm); about 10 to 16 times of the web thickness respectively, which is different from the AASHTO 2007 recommendation.

4.1.4 Material properties

A. *Welding process:*

Fabrication process is important to prevent residual stress and obtain good experimental results. In this process, the quality of welding would determine the quality of specimens. With a good welding methodology, the error would be reduced and specimens reveal the actual behavior of study. Welding methodology in this study employs AWS D1.3 standard for structural welding code sheet steel. This code contains the requirements for arc welding of structural sheet/strip steel including cold formed member hereafter collectively referred to as sheet steel, which equal to or less than 4.88 mm in nominal thickness. The provisions of this code are intended for used sheet steel having a minimum yield point equal or less than 550Mpa (American Welding Society, 2008).

Gas metal arc welding uses an arc between a continuous filler metal (consumable) electrode and the weld pool. Shielding is provided by an externally supplied shielding gas. This process is also known as MIG welding or MAG welding. MIG (Metal Inert Gas) welding means the use of an inert (i.e. non active) gas. MAG

(Metal Active Gas) welding requires the use of an active gas (i.e. carbon dioxide and oxygen). CO2 is a more commonly used shortening of MAG welding gas.

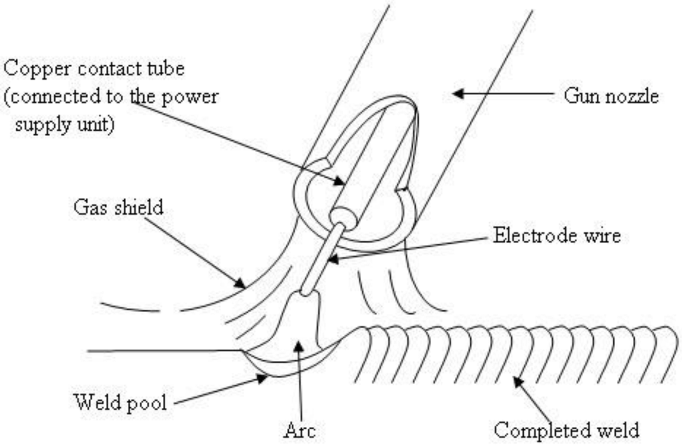

Figure 4.4 Mig/Mag welding method.

The process consists of a DC arc burning between a thin bare metal wire electrode and the work-piece. The arc and weld area are enveloped in a protective gas shield. The wire electrode is fed from a spool, through a welding torch, which is connected to the positive terminal into the weld zone. MIG/MAG welding is the most widely used process in the world nowadays. It is a versatile method that offers a lot of advantages. The technique is easy to use and there is no need for slag-cleaning. Another advantage is the extremely high productivity that MIG/MAG welding makes possible.

The welding properties are presented as table 4.3:

Table 4.3: Welding properties

standard of welding	***AWS D1.3***
Type of current	(DC)
Current (A)	110
Voltage (V)	380
Voltage for welding (V)	380
Sandard of welding rod	AWS A5.18 ER70S-G
Size (mm)	0.9
Strength (Mpa)	48.26
Velocity (mm/s)	1.5
Leg size (mm)	3 - 4

B. Modulus of elasticity and strength of steel:

The steel employed in the testing programs is made from SM400 steel as Thai Standard, with the properties similar to A36 steel. The chemical properties of SM400 are shown in table 4.4:

Table 4.4: Chemical composition of steel SM400 and A36.

Grade	***Chemical composition, % by weight***				
	Carbon max	Silicon max	Manganese	Phosphorus max	Sulfurs max
SM400	0.20	0.35	0.60 to 1.40	0.035	0.035
A36	0.26	0.05	---	0.040	≤0.40

Tension test of three samples is conducted to find out the strength as well as the modulus of elasticity of this kind of steel. The standard for specimens design and testing is ASTM 8370. Figure 4.5 shows the relationship between stress (kG/cm^2) and strain (μm/m) from the tension tests:

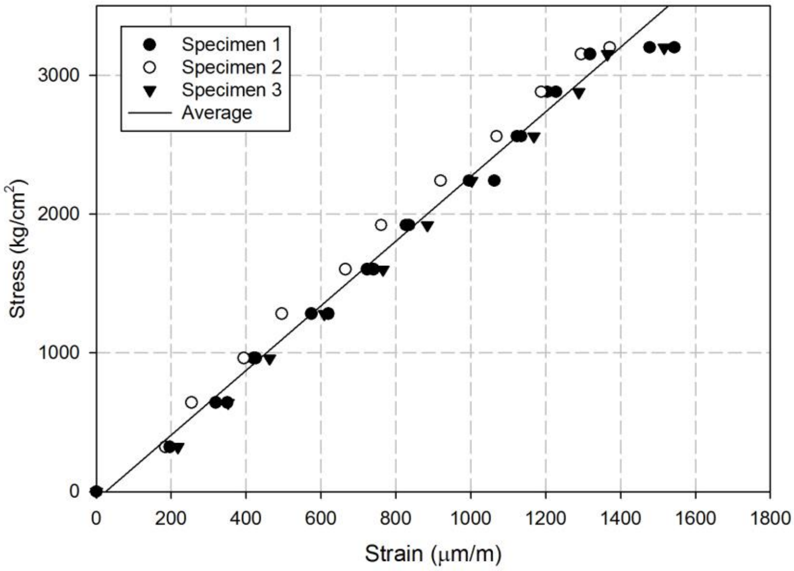

Figure 4.5: Stress – strain relationship of steel samples.

Results from tension test shows that the yield point of steel is around 3200 kG/cm2 and modulus of elasticity is about 2.192E+6 kG/cm2. These values are similar to those of A36 steel in ASTM.

C. C and n material properties

The I-beam specimens in the experiments are manufactured by Siam Yamato, described TIS 1227-2539 SM400 and similar to ASTM A36 as shown in table 4.5.

Table 4.5: Comparison of TIS 1227-2539 SM400 and ASTM A36

Standard	Grade	Strength	
		Yield (Sutton et al.) $N/mm^2(kG/cm^2)$	Tensile $N/mm^2(kG/cm^2)$
TIS 1227-2539	SM400	235 (2,396)	400-510 (4,079-5,200)
ASTM A36	A36	250 (2,549)	400-550 (4,079-5,608)

Fisher et al. (1971) conducted experiments to find the fatigue crack growth rate for A36 steel. The data is re-analyzed by using the SED model to identify the material constant and the *f(R)* function.

The Fisher's data includes 9 specimens in lab air with the ratio of stress from 0.09 to 0.38 and is presented in table 4.6. The geometries of specimens are given in figure 4.6.

Table 4.6: Stress ratio in Fisher's test

Specimen	*Minimum stress (Ksi)*	*Maximum stress (Ksi)*	*Stress ratio*
1	8.96	23.21	0.38
11	2.01	22.01	0.09
12	1.99	18	0.11
13	10	26.01	0.384
15	1.97	21.96	0.0897
17	2	17.99	0.111
18	10.01	25.98	0.385
19	2	17.98	0.111
22	10.01	25.99	0.385

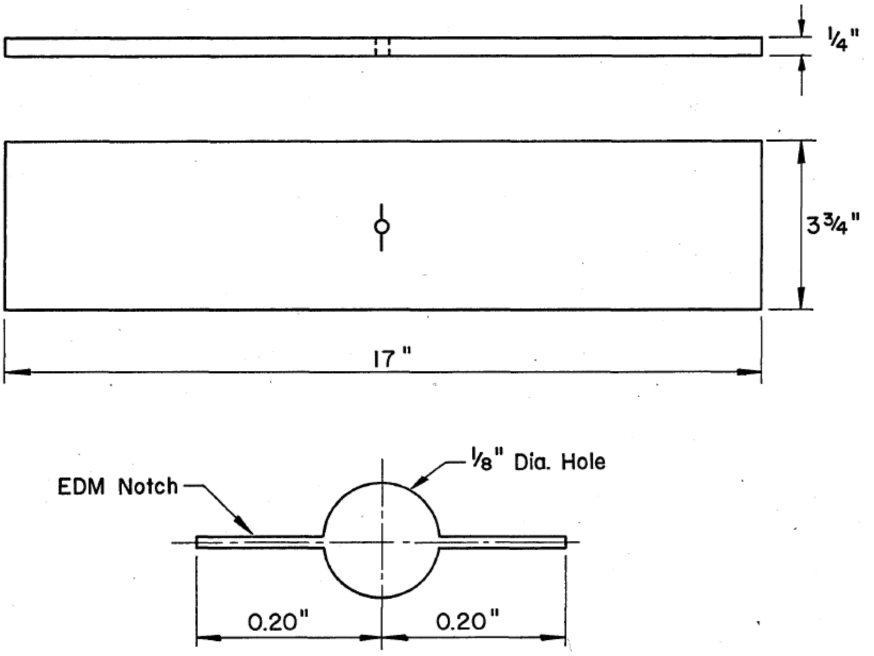

Figure 4.6 Specimen geometries in Fisher's experiment (1971)

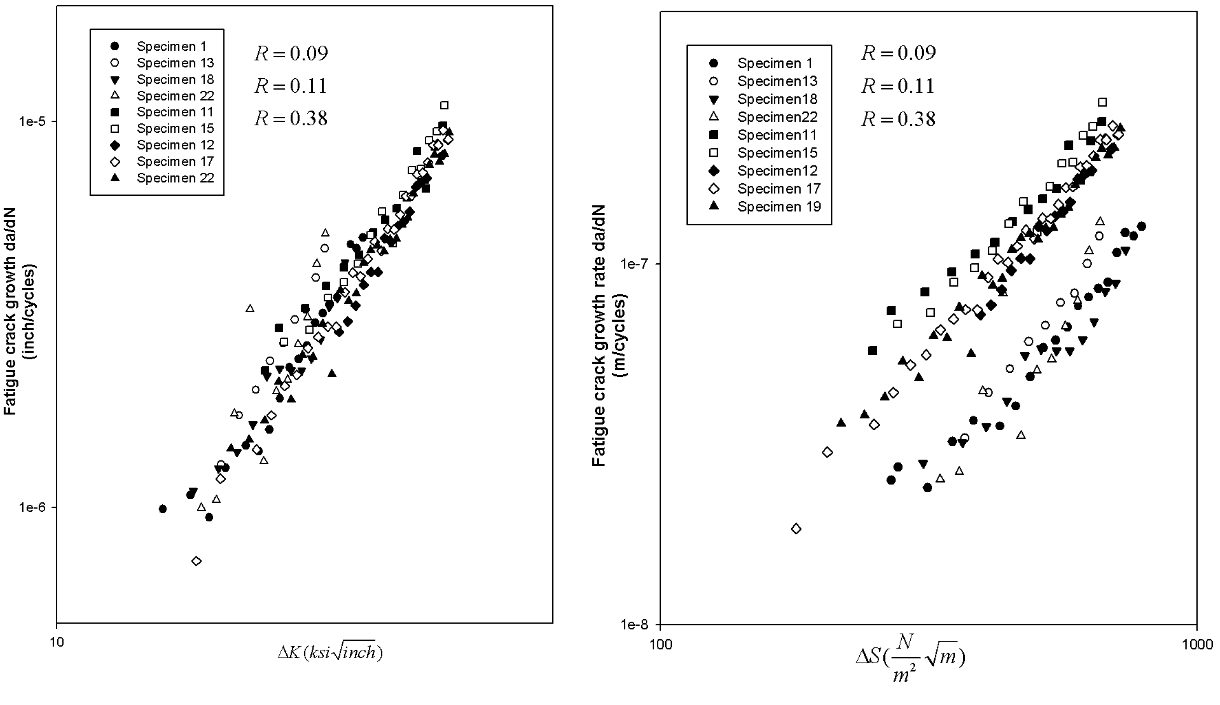

Figure 4.7 *da/dn vs ΔS* and *da/dN vs ΔK* in logarith scale.

It's observed from the Figure 4.6 that *da/dN vs ΔK* yields similar linear relationship for different ratios of stress (*R*). On the figure 4.7, *da/dN vs ΔS* shows different relationship for various values of *R*. Figures 4.7 and 4.8 are presented in log-log scale.

The fatigue crack growth rate between *da/dN* and ΔS_{eff} is shown in Figure 4.7. We can see the linear relationship in logarithm scale. The C and n are calculated from the chart as:

$$C = 5.1E\text{-}11 \left(\frac{m}{cycles} \left[\frac{m}{N} \right]^{n} \right)$$

$$n = 1.64$$

Also we have the $f(R) = 0.49R + 0.54$ with the means square error of 0.945.

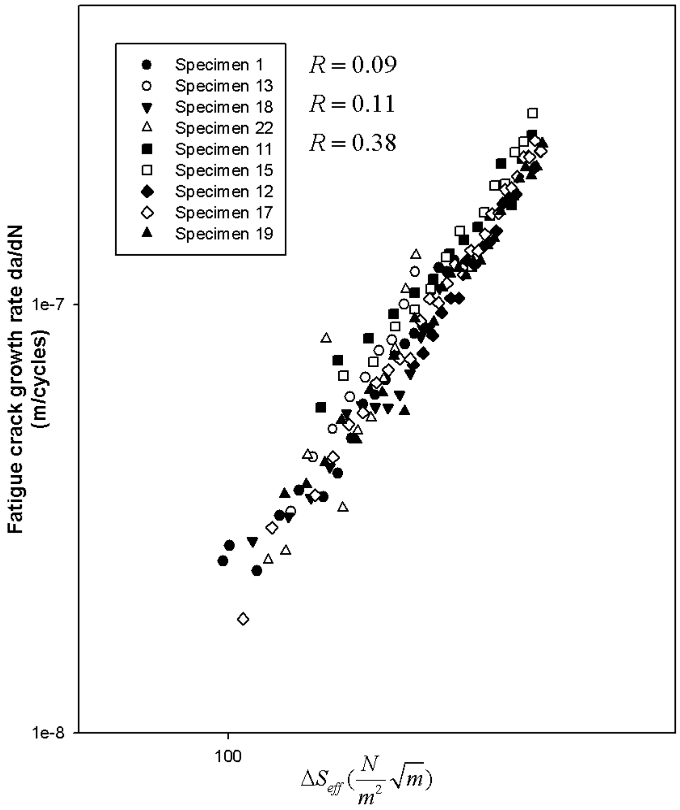

Figure 4.8 *da/dN vs* ΔS_{eff} in logarithm scale.

4.1.5 Test instruments:

a) Strain gage position:

To validate the stress field between testing specimens and FEM model, total 9 strain gages are attached to each specimen. The purpose of each strain gage depends on the position where it is attached on the specimen as follows:

- Strain gage 1, 6 and 7 are used to measure the strain at web gap at front and back side (Figure 4.9).

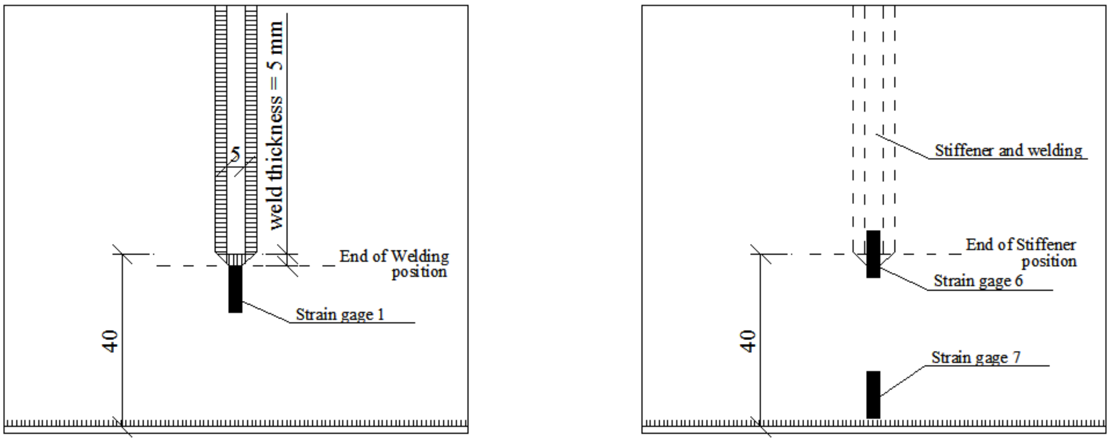

Figure 4.9 Position of Strain gage 1, 6, and 7.

- Strain gage 2, 3, 4 and 5 are used to measure the strain at end of stiffener at front side (Figure 4.10).

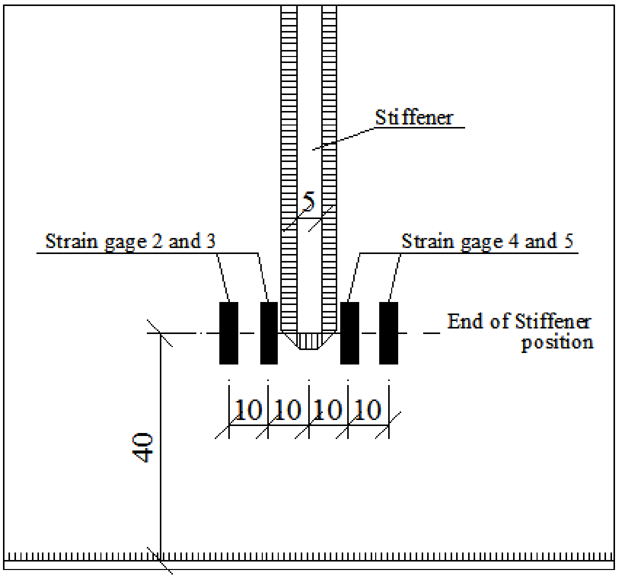

Figure 4.10 Position of Strain gage 2, 3, 4, and 5.

- Strain gage 8 and 9 are used to measure the strain at middle beam of top and bottom flange (Figure 4.11).

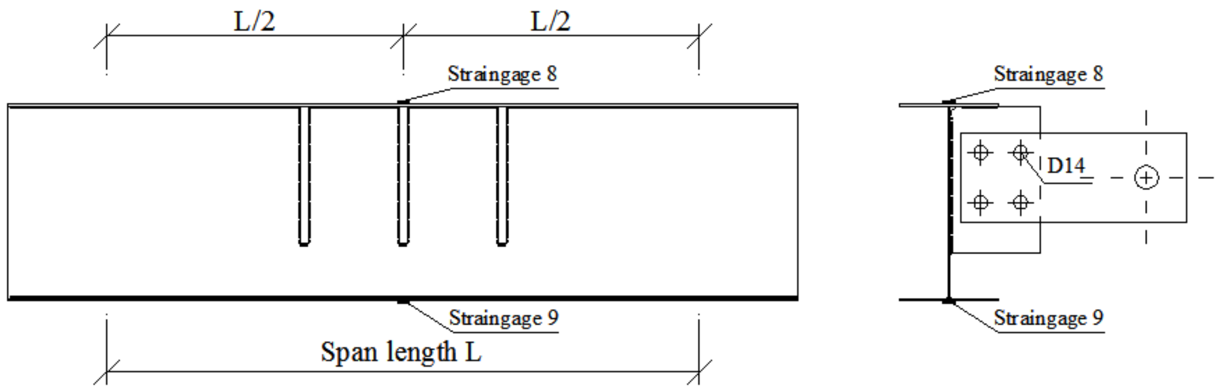

Figure 4.11 Position of Strain gage 8 and 9.

b) LVDT:

LVDT is used to measure the maximum deflection of the testing beam. So it is attached to the bottom flange at middle of specimens. The position of LVDT is shown in Figure 4.12.

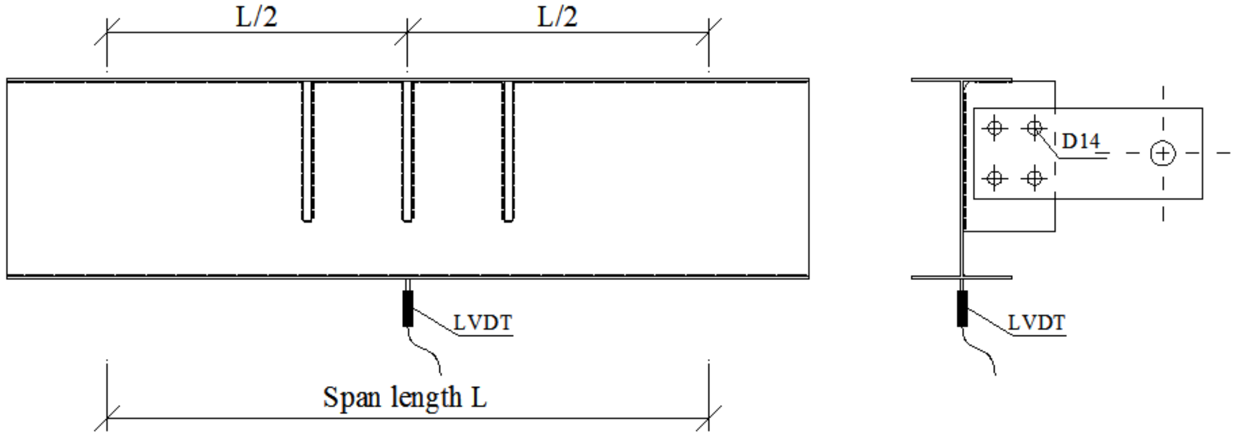

Figure 4.12 Position of LVDT.

4.1.7 Test procedure

- Calibration and testing machine.

- Instrumentation and setup data logger (computer) as well as LVDT.

- Perform constant amplitude fracture load test though P_{max} and P_{min} with fixed frequency and stress ratio.

- Regular monitoring of crack initiation and crack propagation to find the relationships between crack length and number of cycles from stage of crack initiation to specimen failure.

- Stop the test when the specimen gets failure.

4.2. Experiment observation

4.2.1 Specimen series I

A. Specimen S1-1

Specimen S1-1 belongs to series I of specimen with span length equaling to 100 cm and web-gap length equaling to 4 cm. At the beginning, the first crack starts at weld-toe and has shape as welding at the end of stiffener. It grows symmetrically in both sides of stiffener with the same speed. The first crack grows slowly and towards to lower stress field. Second crack originates at the line of the first crack, the same place that the first crack occurs. The last crack grows continuously toward to bottom flange and cause the beam failure. Because this is the first specimen in the experimental program, the testing procedure and the record were not quite good.

There are stresses at bottom flange (G9), LVDT value, and fatigue life left when the test finished. It's unfortunately that the fatigue crack growth rate and other stresses were also lost. The results of specimen S1-1 are presented in table A.1. Figure 4.13 shows the image of specimen S1-1 at stage of failure.

A. Failure of specimen S1-1

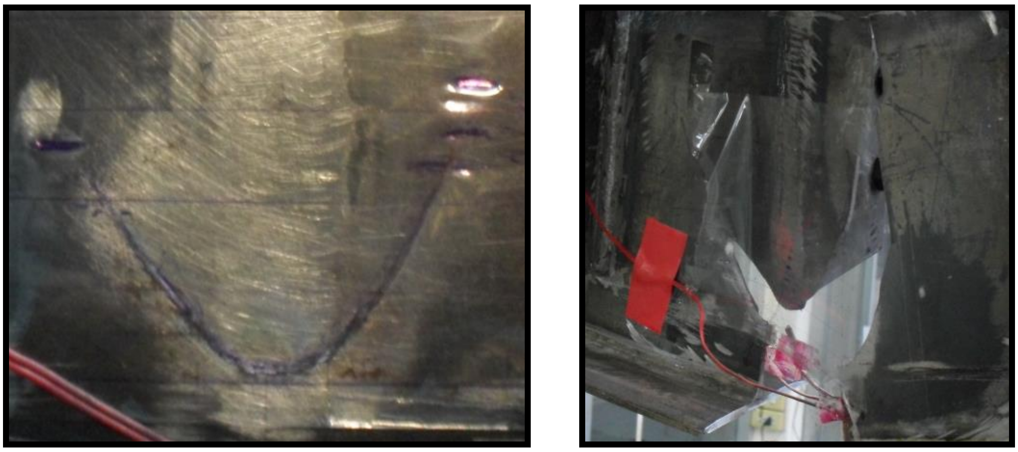

B. Crack before and after failure.

C. Crack surface in propagation.

Figure 4.13 Failure and crack of specimen S1-1.

B. Specimen S1-2:

This specimen belongs to series I of experiment specimen. The total number required for failure is about 3.8 million cycles. The first crack starts at the most critical stress point as the weld-toe by end of stiffener, but is not symmetrical. Crack placed on one side of stiffener goes further from the welding than the other. The second crack occurs at the same position of the beginning of first and runs downward. When the second crack nearly touches bottom flange, the third crack occurs and is located at the weld connecting the girder and bottom flange. The new crack runs quickly in both sides, upward into the web and downward to bottom flange, and destroy easily the specimen. During the time of first crack occurring and propagating, the strain-gages 1, 3, 4, 6 were damaged in order. As shown in figure 4.14, the crack surface at weld-toe gets some scratches which start at front surface and runs to back side of web as parallel curves. The measurement data on this testing are presented in tables B.1.

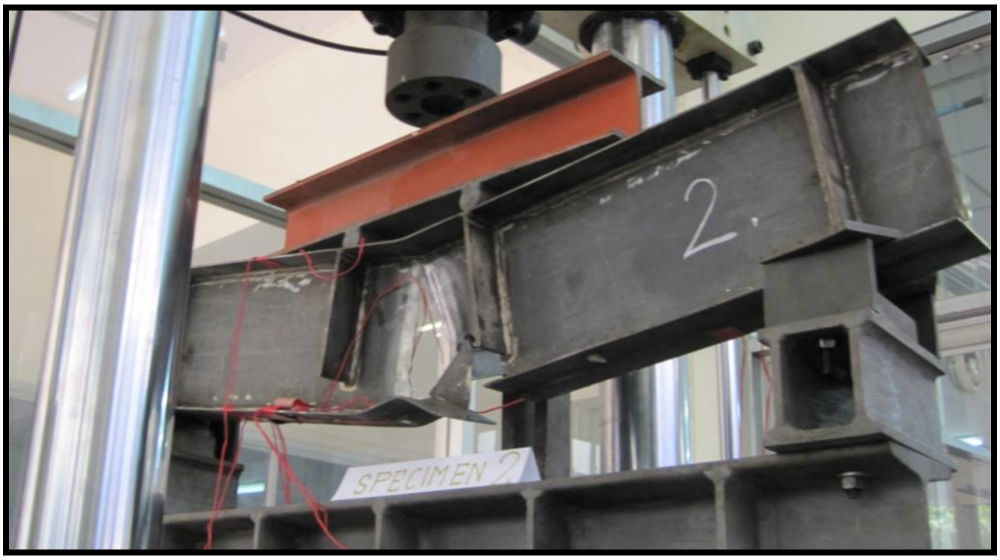

A. Failure of specimen S1-2.

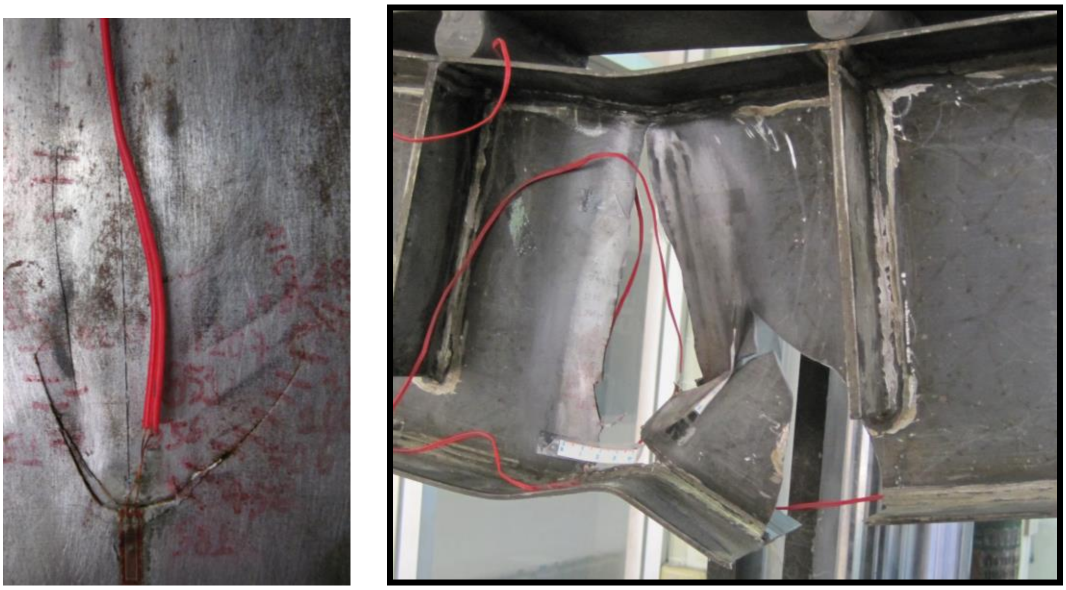

B. Crack before and after failure.

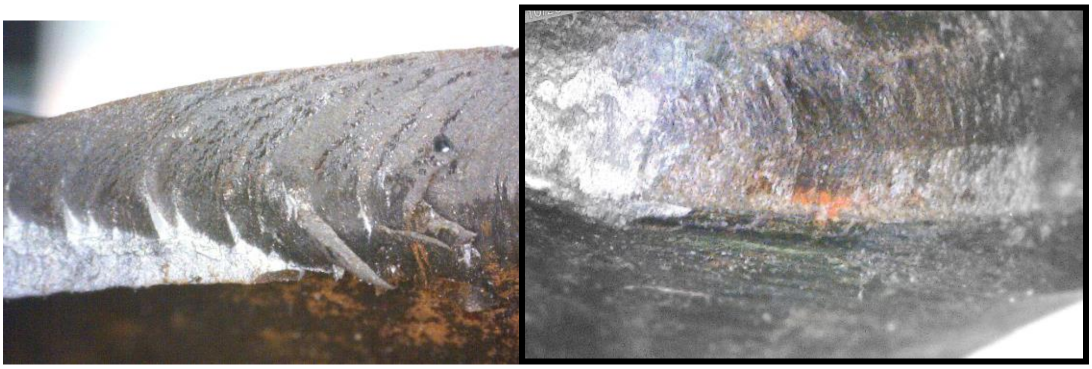

C. Failure and crack of specimen S1-2.

Figure 4.14 Specimen S1-2 at failure stage.

C. Specimen S1-3:

This is the last specimen that is tested in series I of beam. The specimen's crack grows in different way compared to the other two specimens in the same series. The crack initiates at position of weld-toe, but grows in two different directions. One direction is the upward curve as normal. The other goes down and turns to bottom flange. After 1.94 million cycles, the specimen was failed because the crack touches bottom flange and collapses the beam. In this case, there is only one crack occurring in all fatigue life of beam. Therefore, the fatigue life of this specimen is shorter than the life of other two specimens with the same geometries and loading level. As shown figure 4.15, distortion-induced fatigue crack creates scratches as parallel curves that connect both front and back side of web. Figure 4.15 also shows the image of crack at web-gap from side view, which proves that the crack starts at the weld-toe.

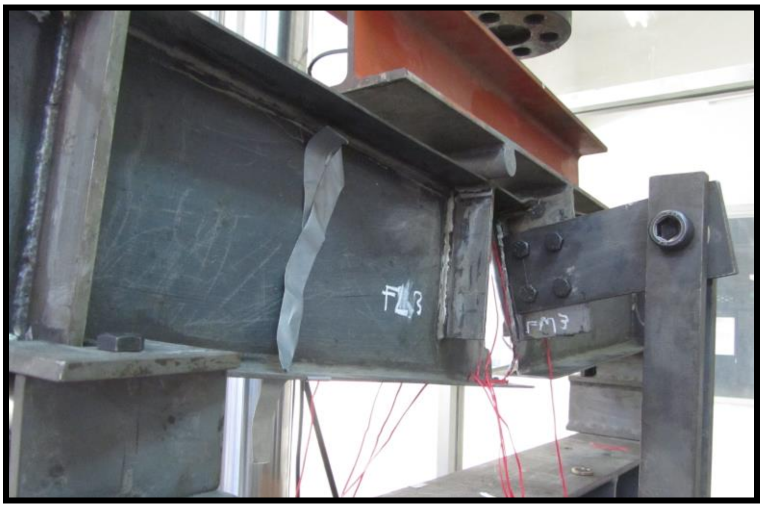

A. Failure of specimen S1-3.

B. Crack before and after failure.

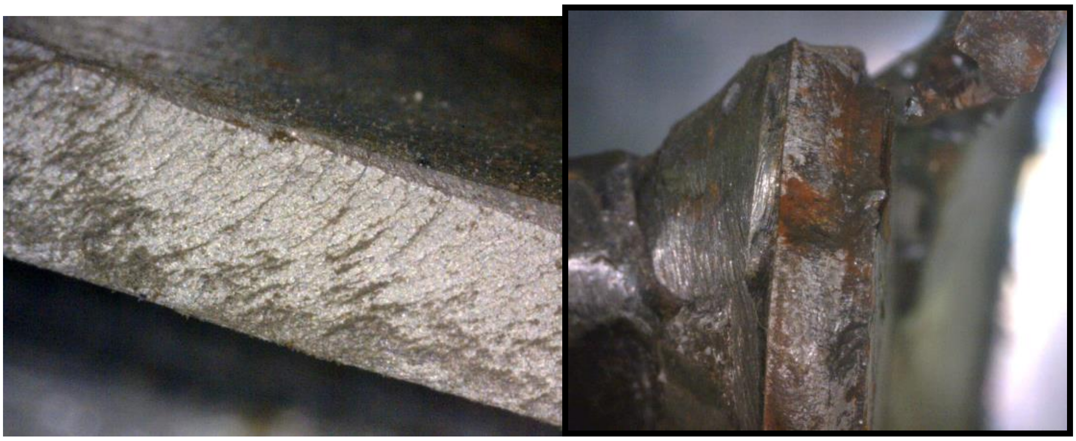

C. Crack surface during growing and at the beginning (weld-toe).

Figure 4.15 Failure and crack of specimen S1-3.

4.2.2 Specimen series II

A. *Specimen S2-1*

Specimen S2-1 belongs to series II of specimen with span length equaling to 100 cm and aim of stiffener equaling to 20 cm. The significant of this series is the short web-gap equaling to 2.5 cm. Because the maximum load level equals to 4000 kGf, it takes a long time for crack to occur at the end of stiffener and weld-toe. The crack goes out of welding as horizontal line for a long propagation before turning in two directions. One crack tip grows upward further to the lower stress field zone and gradually runs slower. The other crack tip tends to move downward and directly to bottom flange. After about 5.3 million cycles, specimen was failed by this crack. In figure 4.16, the crack surface reveals the parallel scratches which are formed during crack propagation. Figure 4.16 also presents the images of specimen S2-1 in damaged shape and details. The results are recorded and presented in table B.2.

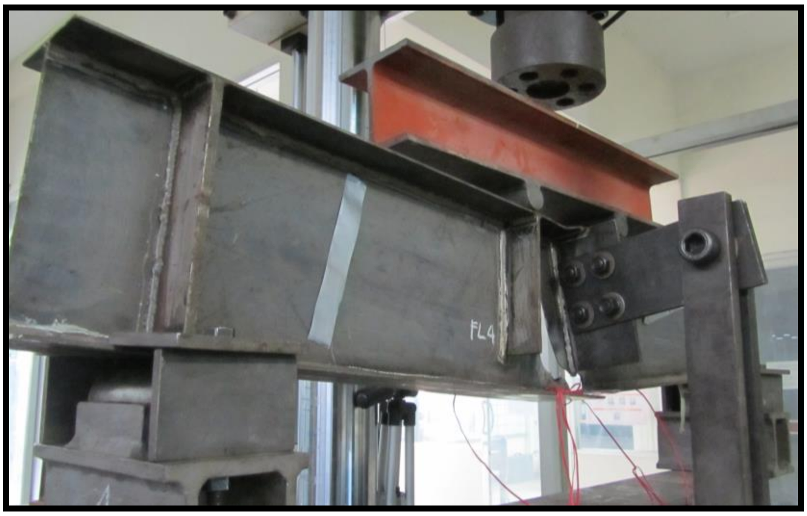

A. Failure of specimen S2-1.

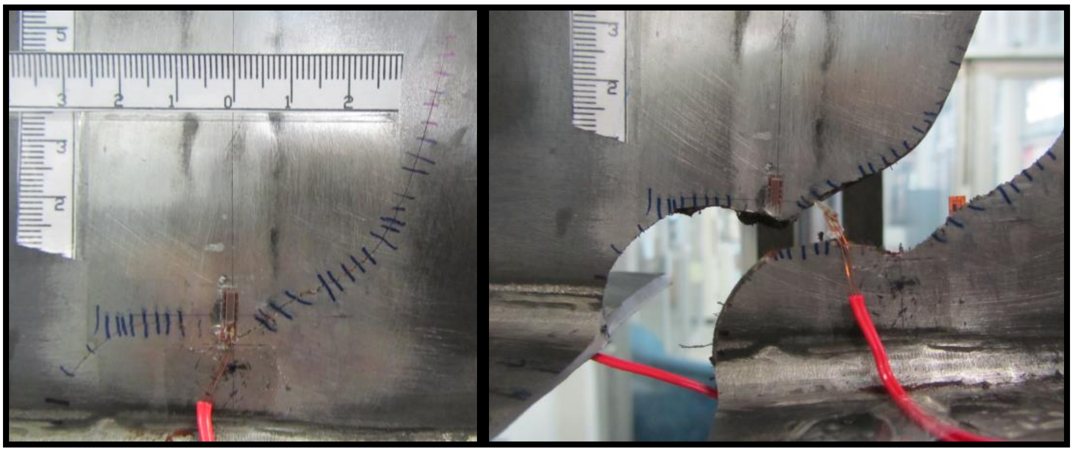

B. Crack before and after failure.

C. Crack surface in propagation, at critical growth and at the beginning (weld-toe).

Figure 4.16 Failure and crack of specimen S2-1.

B. Specimen S2-2

This specimen is classified to series II of specimen with short web-gap. With the low load level, it also takes a long time for crack to occur and destroy the I-beam. In this specimen, the first crack starts at the critical concentrated stress point as normal. The first one grows at both sides of stiffener, runs upward to lower stress field. But one crack tip grows faster than the other. It gets a long propagation and goes close to neutral axis with speed slows down gradually. Located on the line of the first crack under weld-toe, the second crack occurs when the number of cycles of loading is nearly 6.1 million cycles. New crack runs toward bottom flange and collapses the specimens. The total fatigue life of this specimen is around 7.4 million cycles. In this specimen, the semi ellipse crack leaves clearly scratches on the surface of crack as shown in figure 4.17. The scratches are formed as the semi ellipses as stage that crack grows from tension to compression face of web. Other parallel scratches connecting both surfaces of web also exist on crack surface as observed other specimens.

A. Failure of specimen S2-2.

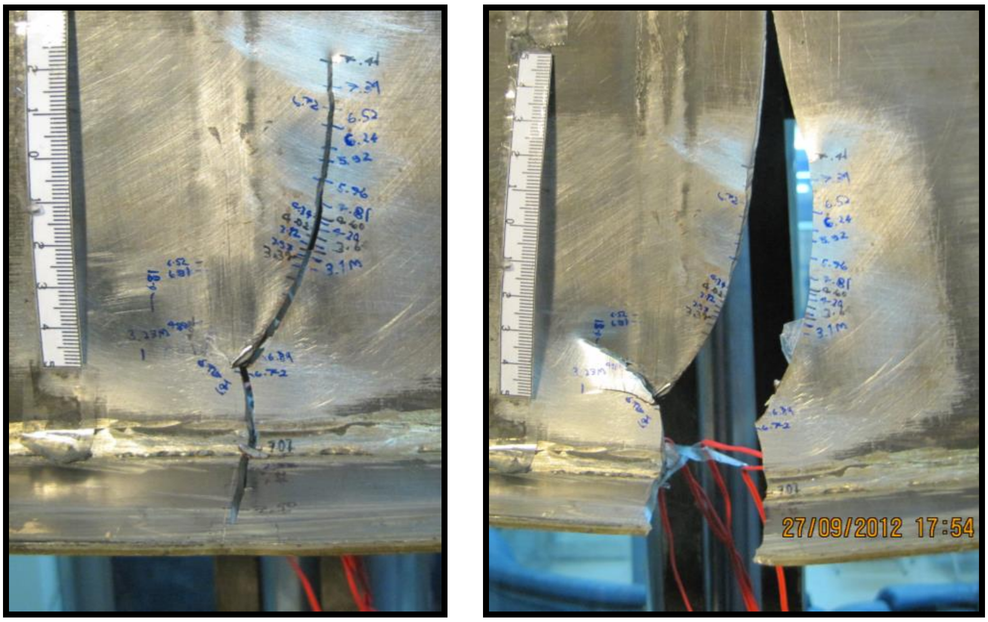

B. Crack before and after failure.

C. Crack surface in propagation, at web-toe and bottom flange.

Figure 4.17 Failure and crack of specimen S2-2.

C. Specimen S2-3

The specimen was tested with the maximum load level equaling to 4000 kGf. With small load level, it’s around 6.7 million cycles for beam failure. The series of collapse is the same to specimen S2-2. The first crack grows upward to lower stress field in both sides of stiffener in symmetry but different fatigue crack growth rates. One crack tip runs faster than the other. Second crack grows from the same position which first crack begins and runs over the weld connecting bottom flange, and destroys the specimen. In this specimen, all data were recorded and presented in table B.2. Figure 4.18 shows the images of specimen failure.

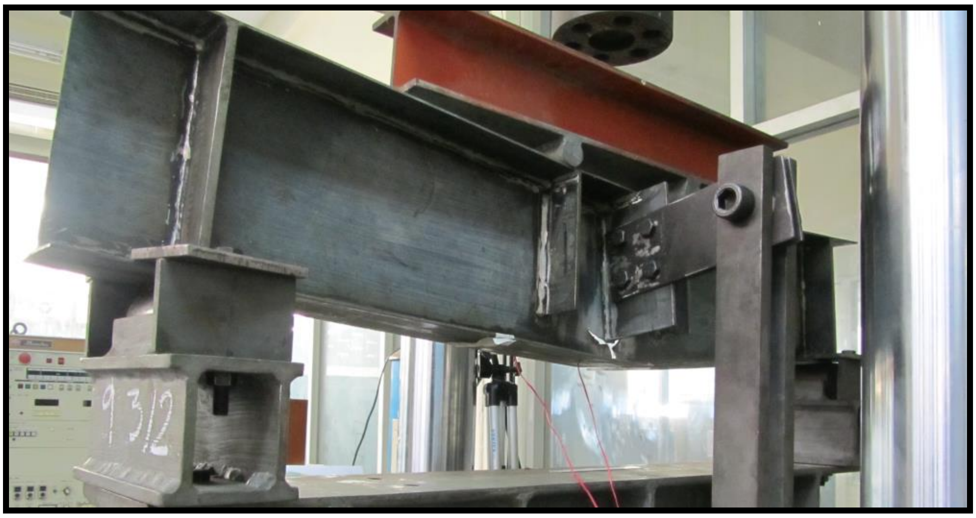

A. Failure of specimen S2-3.

B. Crack on front and back of the girder.

Figure 4.18 Failure and crack of specimen S2-3.

4.2.3 Specimen series III

A. *Specimen S3-1*

Specimen 3-1 belongs to series III of specimen. This series has short span length equaling to 60 cm and web-gap length equaling to 4 cm. Because of short span length, the load level was increased to produce the distortion-induced effect clearly on testing beam. The welding at end of stiffener is the most critical concentrated stress position and the first crack starts from this place. The first crack grows from tension face to compression face of girder and cracks the strain-gages 1, 3, 4 in order. After that, strain-gages 2 and 5 change the value quickly because the crack goes through these strain-gages. The first propagates upward in symmetrical shape to both sides of stiffener. When the first crack grows slowly, the second crack occurs right under weld-toe and begins from first crack line toward the bottom flange. In the last stage, other crack located at welding connecting web and bottom flange suddenly occurs and propagates quickly. Third crack tries to connect to the first one as well as to grow on bottom flange. With a short time from occurring, the third one collapsed the specimen by damaging bottom flange. Figure 4.19 presents the images of specimen failure with three cracks occurring.

A. Failure of specimen S3-1.

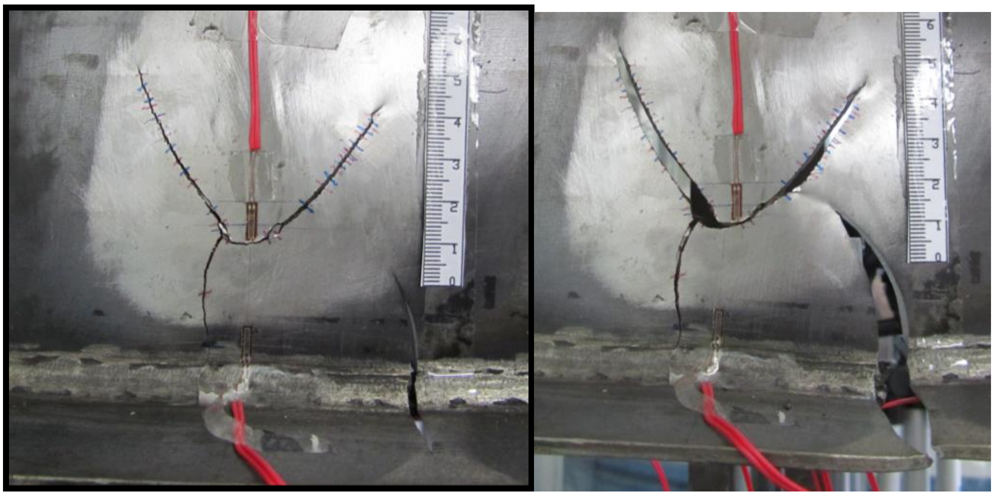

B. Crack before and after failure.

C. Crack surface in propagation and at web-toe.

Figure 4.19 Failure and crack of specimen S3-1.

B. Specimen S3-2:

With the same short span length as specimen S3-1, specimen S3-2 is supported large load level in testing program. The short span length decreases web-gap stress to bottom stress ratio. Therefore the first crack intends to grow upward after becoming two crack tips at weld-toe. In other words, the effect of distortion-induced is not enough to keep the crack to grow as long as horizontal line. It's observed from the crack path of specimen that most of cracks intend to grow along the welding in series III of specimen. In this specimen, the second continues to be the directly reason in beam failure after the first one grows slowly in low stress field. Figure 4.20 shows the stage of specimen 3-2 failure.

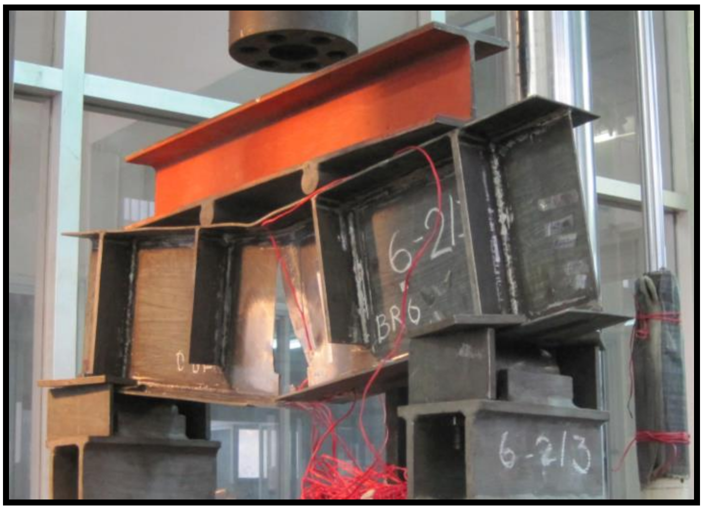

A. Failure of specimen S3-2.

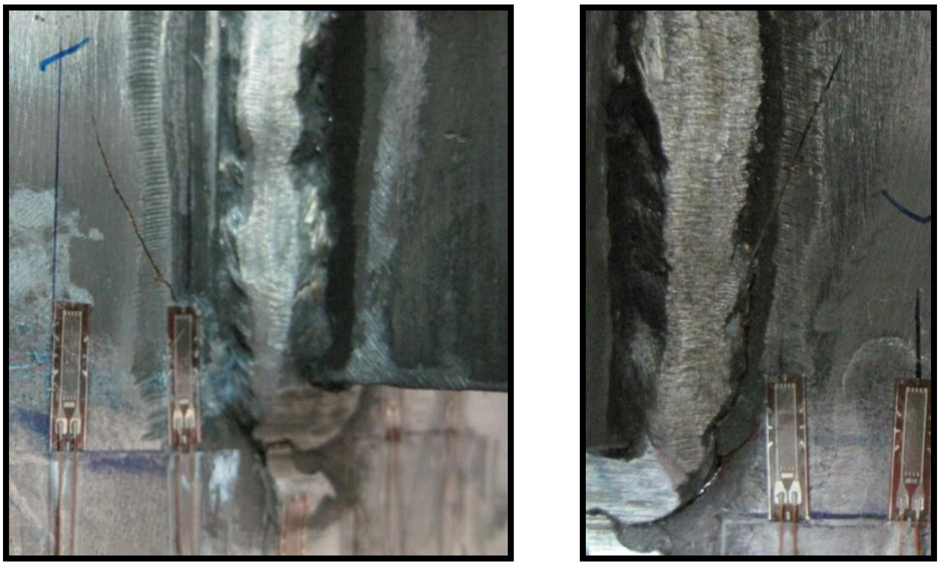

B. Crack occurs from the web-toe.

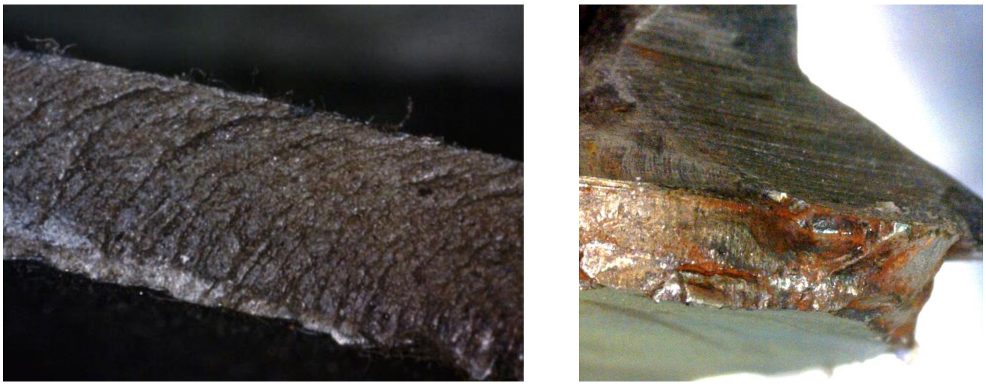

C. Crack surface in propagation and at web-toe.

Figure 4.20 Failure and crack of specimen S3-2.

C. Specimen S3-3:

This is the last specimen in series III with the same typical failure as specimen S3-1. The first crack occurs from web-toe, propagates un-symmetrically and grows toward lower stress field. This crack propagates along the welding for most of fatigue life. s crack occur from the first one’s line and grows downward to bottom flange. But the third one is the crack failing the beam. The third crack located at weld connecting girder and bottom flange propagates in both 2 directions. One end of crack grows toward to bottom flange and becomes the reason for beam failure. The total fatigue life of this specimen is around 1.6 million, which is one of the smallest values of fatigue life in this study. All measurement data were recorded and presented in table B.3 for specimen series III. Figure 4.21 shows the specimen S3-3 in stage of failure.

A. Failure of specimen S3-3.

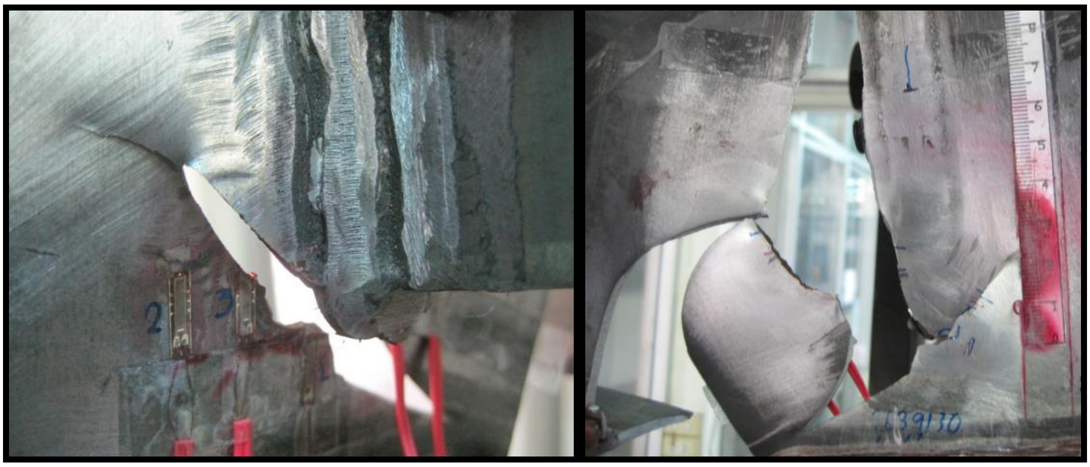

B. Crack on front and back side of girder at failure.

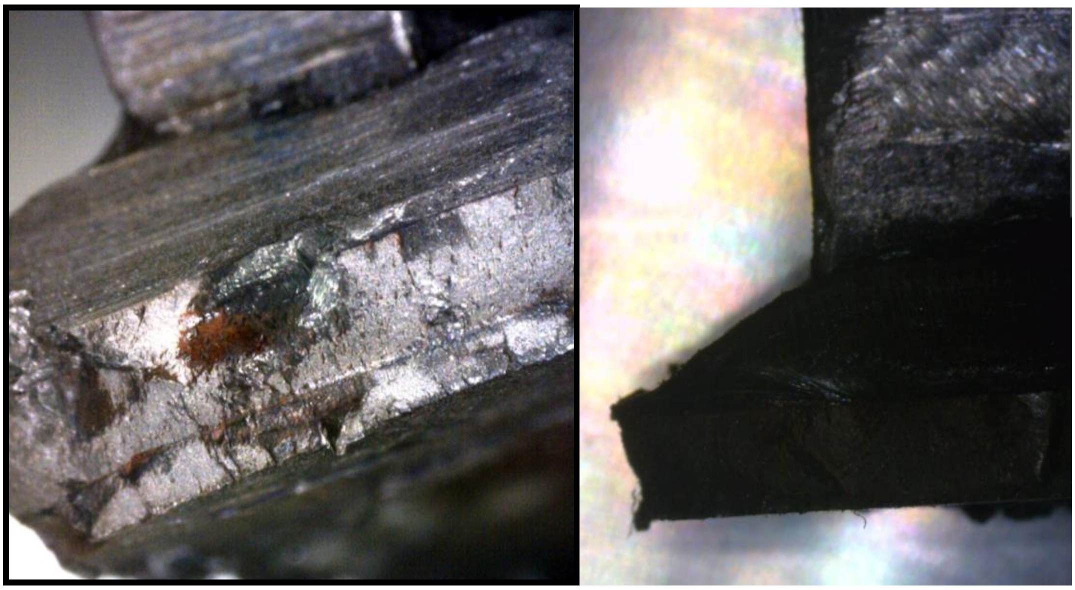

C. Crack surface at web-toe in front and side view.

Figure 4.21 Failure and crack of specimen S3-3.

4.3. Experimental results

4.3.1 Typical beam failure

In 9 specimens, it could be generated in 3 series of beam failure. In most of them, the cracks initiating from the web gap go upward slowly when they touch low stress field, and don’t directly fail the specimen, but they create a great effect to beam failure.

A- Beam fails because a new crack occurs in “weak zone” area:

After crack initiate at the web gap due to the critical zone which influenced by out of plane stress, the crack continues to propagate into lower stress zone. When the stress is small enough, the crack is no longer to propagate further. A “weak zone” area is established between two crack tips. A new crack occurs in this area, mostly in the middle of the beam and close to the position of first crack at the beginning. The second crack occurs and damages the bottom flange in order to fail the specimen. Some specimens show the error of welds with cracks occurring along the welding, but this type of crack not fails the beams. This behavior can represent as typical failure in this research, and can be seen in failure of specimen numbers 1, 6, 8, and 9. The image of this type of failure is shown in figure 4.22 as following.

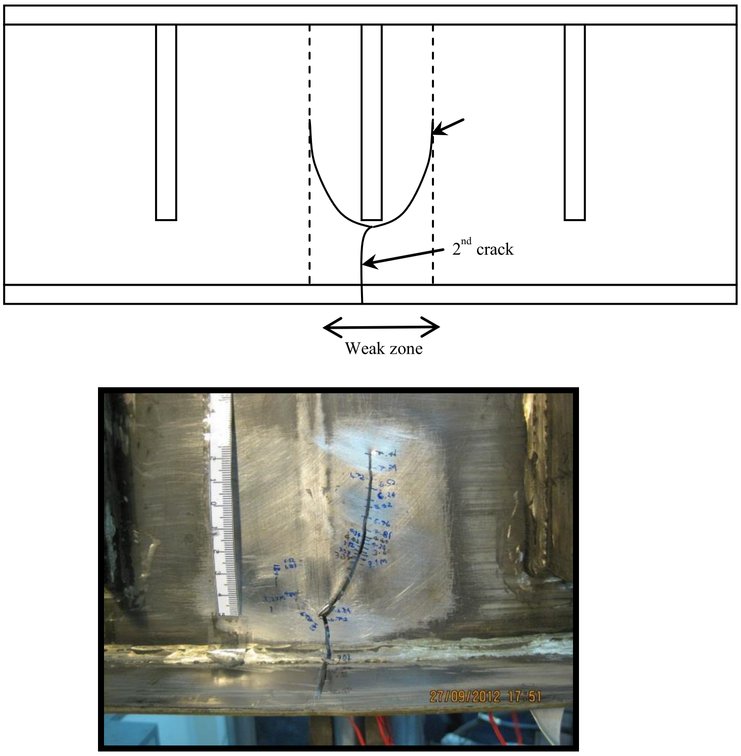

Figure 4.22 Specimen failures with new crack occurring in “weak zone” area.

B- Beam fails because a new crack occurs outside the “weak zone”:

In second, fifth and seventh specimen, the first crack occurs at the web toe and propagates to lower stress zone. Due to small energy in this zone, the crack stops for long time. The second crack also occurs under the welding and begins from line of first crack, propagates toward to bottom flange but do not fail the beam. A new crack occurs at welding of bottom flange and web, outside the weak zone. The third crack tends to move 2 sides at one time; one end goes upward into the web and tries to connect to the end of first crack; the other end moves cross the bottom flange and fails the specimen. The specimen is failed because this crack damages the bottom flange The mechanism failure is shown in figure 4.23.

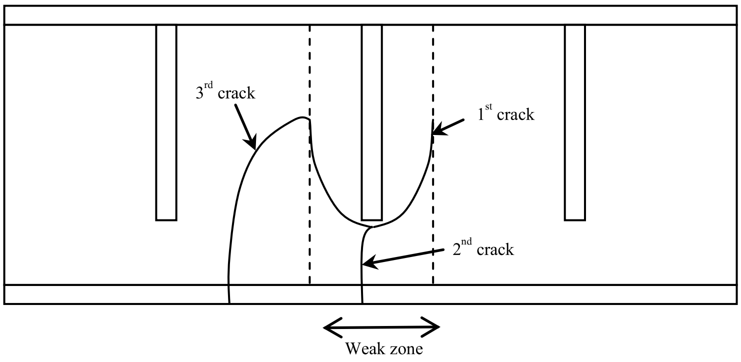

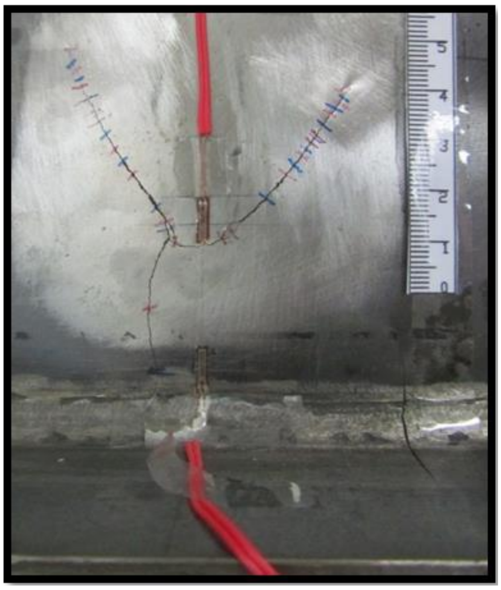

Figure 4.23 Specimen failures with new crack occurring outside the weak zone.

C- Beam fails because crack goes downward:

Observing the third and fourth beams, the cracks initiates at end of weld toe, and goes in different side. One crack tip goes upward as normal and processes to lower stress zone. The other goes downward and propagates to bottom flange. The crack moving to bottom flange will fail the specimens. This behavior occurs in specimens 3 and 4 and is shown in figure 4.24.

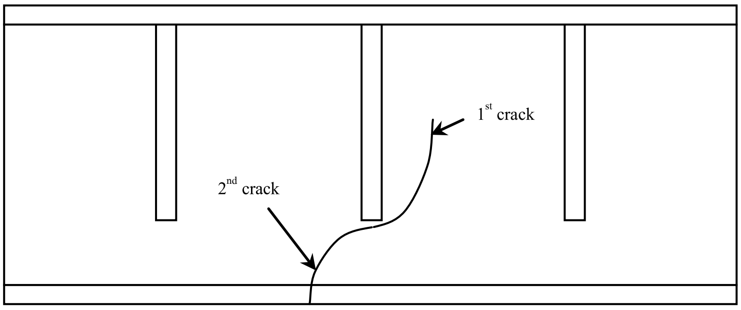

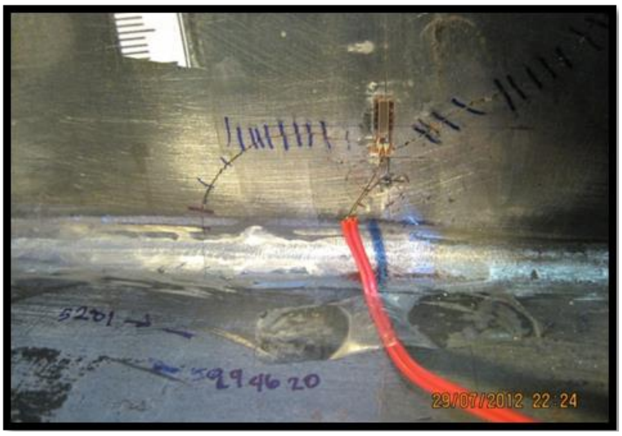

Figure 4.24 Specimen failures with initial crack going downward.

Describing in beam failure for each specimen is shown as in table 4.7:

Table 4.7: Specimens are classified in to 3 types of beam failure.

Specimen	***Series of specimen***	***Number of cycles at failure***	***Type of beam failure***	***Describe in detail***
1 **(S1-1)**	I	3,031,810	**A**	The first crack propagates in symmetric line of both side of stiffener. The second crack occurs at middle of beam, under welding and begins from first crack and fails the beam.
2 **(S1-2)**	I	3,801,220	**B**	The first crack occurs and goes up ward but not symmetric. second crack occurs from line of the first one, slight different from middle of beam, and goes downward. After all, the third crack occurs at welding between web and bottom flange, under load support stiffener, and fails the specimen.
3 **(S1-3)**	I	1,940,140	**C**	Crack occurs at end of welding and goes both side, up and down. The end going down makes the beam fail.
4 **(S2-1)**	II	5,300,040	**C**	Crack occurs at end of welding and goes both side, up and down. The end going down makes the beam fail.
5 **(S3-1)**	III	1,821,520	**B**	The first crack occurs at end of stiffener, symmetrically. When the first crack stops, second crack occurs under welding and begins from first crack, slight different from middle of beam. Other crack begin at weld connecting web and bottom flange, right at boundary of weak zone and fail the specimen.
6	III	1,402,110	**A**	The first crack propagates from end of

(S3-2)				welding of stiffener and not symmetrically. The second crack occurs at middle of beam, under welding and begins from first crack and fails the beam.
7 **(S3-3)**	III	1,595,720	**B**	The first crack occurs and goes up ward but not symmetric. After the first crack stops due to low stress for long time. The second crack occurs at welding between web and bottom flange, outside the weak zone, tries to connect to first crack and fails the specimen.
8 **(S2-2)**	II	7,145,220	**A**	First crack propagates from end of welding of stiffener and not symmetrically. The second crack occurs at middle of beam, under welding and begins from first crack and fails the beam.
9 **(S2-3)**	II	6,771,510	**A**	First crack occurs from the tension side to compression one of the web, it propagates to the lower stress zone and become slowly. The second crack occurs at the first crack, goes toward to bottom flange and fails the specimen.

As shown in table 4.8, there are 2 specimens damaged in type C, 4 in type A and 3 in type B. With 7 specimen’s failures in type A and B, most of them have the second crack beginning from the first crack line. There are 6/7 specimens have second crack under the welding at stiffener, but 4 of them are the reasons for beam failure.

It can be concluded that the first crack appearing under combination of distortion-induced and effect of bending will propagate slowly when it reaches the low stress zone. In case, one of end first crack goes downward to bottom flange, the crack will fail the beam by damaging the bottom flange. When first crack grows slowly in low stress zone, the second crack occurs under the welding, begins from line of the first one and goes downward to bottom flange. As normal, the second crack plays the main role to fail the specimen. In some cases, there are spots in the welding connecting web to bottom flange, the third crack will occur at this position and propagate in both directions. One crack tip goes upward and tries to connect to the first crack; the other propagates to bottom flange and fails the beam by damaging this flange.

4.3.2. The fracture failure:

a) Configuration of crack propagation:

As describe in table 4.7, the failure of beam under combination of distortion-induced and bending moment is classified in 3 types. Actually, if the quality of welds connecting web to bottom flange is in good condition, the third crack will not occur and the second crack is the reason to fail specimens. In other words, the type B of failure become the type A if all of welds are in perfect conditions. The configuration of failure could be described as type A in section 4.3.1 “Typical of beam failure”.

Besides that, the type C of failure occurs whenever the welds around end of stiffener are not symmetrical, and create concentrated stresses at spot of welds. In this case, the problem occurs during fabricating the testing specimens. The welds around stiffener are not quite ground smooth, or there are some scratches on the surface of web. These factors will instruct the crack to grow as gradient of local stress or the way of scratches. So only one crack occurs, propagates downward and fails the bottom flange.

In 9 specimens testing, the progress for crack initiating and propagating can be generated as:

- Crack initiates as the shape of weld toe and grows up ward to the lower stress field.
- The shape of crack depends on ratio of stress in plane and stress out of plane when crack gets out the welding zone.
- The crack propagates until reaching to zone which the stress field is small enough that SED energy couldn’t generate a new crack plane.
- Another crack occurring inside the “weak zone” area depends on the critical stress or spot if they are available in this area. Therefore, this crack would fail the specimen.

The crack propagation progress can be classified in 3 stages:

Stage 1 The first crack occurs on the tension face as semi ellipse crack and grows to compression face of web. The shape of crack is formed as the shape of welding at end of stiffener. After reaching the compression side, the crack becomes two thickness crack tip. This stage is about less than 10% of fatigue life of specimens and shown in figure 4.25.

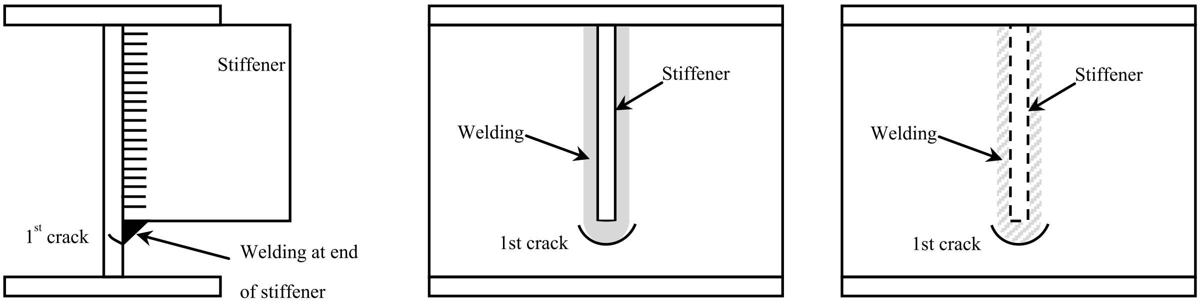

Figure 4.25 Initial cracks in stage 1.

Stage 2 The first crack grows on both tension and compression faces at the same speed and leaves on crack plane parallel scratches. The crack path has the shape as shown in figure 4.26. As the time on growing on web, the crack gradually reaches to lower stress zone. This stage is about 70% fatigue life of specimen. The first crack propagates under effect of combination of mode I and mode III fracture mechanics.

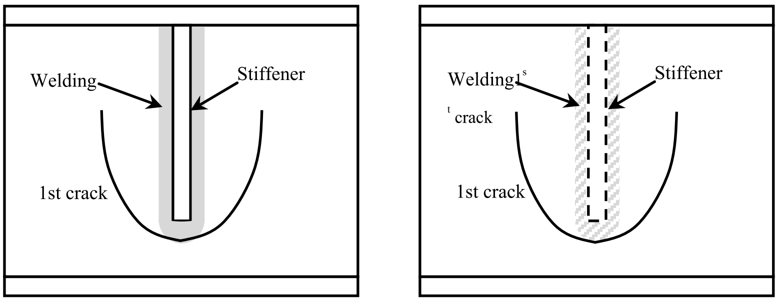

Figure 4.26 First crack propagates in stage 2.

Stage 3 While the first crack grows slowly in low stress zone, a second crack begins from the line of first crack and grows downward to bottom flange as shown in figure 4.27. The second crack occurs due to the spots or scratches of first crack line as well as the critical tension stress under effect of bending moment effect. It is concluded that the second crack is the reason to fail the beam with the effect of first crack. The stage 3 represents in last 20% fatigue life of specimen. The second crack occurs due to the effect of mode I fracture mechanics. Stage 3 process is shown in figure 4.27.

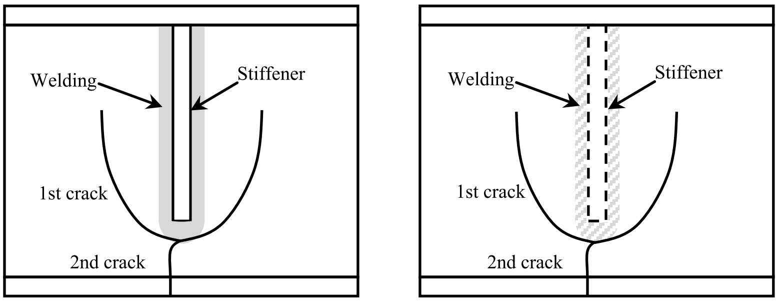

Fig 4.27 The second crack damages specimens in stage 3.

The period for stage 1 and total fatigue life is shown in table 4.8:

Table 4.8: Classifying crack stage in fatigue life

Specimen	***Series of specimen***	***Number of cycles for end of stage 1***	***Number of cycles for failure***
1 (S1-1)	I	---	3,031,810
2 (S1-2)	I	381,120	3,801,220
3 (S1-3)	I	82,140	1,940,140
4 (S2-1)	II	701,500	5,300,040
5 (S3-1)	III	50,530	1,821,520
6 (S3-2)	III	138,930	1,402,110
7 (S3-3)	III	309,790	1,598,720
8 (S2-2)	II	309,330	7,410,000
9 (S2-3)	II	1,008,710	6,771,510

Most of I-beams in steel bridges with the web gap at end of stiffeners grow in 3 kinds of stage as described above. It’s also observed from experiments that the major of fatigue life of these kinds of fracture is in stage 2.

b) Crack surface:

As the typical beam failure, the first crack occurs, propagates and plays the main role in whole of fatigue life. The second crack occurs after the first one “stops” (propagating slowly) for a while, and is the reason for beam failure. In other words, the first crack controls the whole fatigue life and creates the critical condition for the second crack occurring and failing the beam. It could be concluded that the fatigue life of beam with distortion-induced fatigue effect mainly depends on the first crack life.

Considering on crack surface of the first crack line, the crack tip on the tension face grows a little faster than the one in compression face in the zone where crack initiates. When the crack propagates stability far from the end of stiffener, the crack tips on tension and compression faces grow at same speed as well as same position. It's could be observed from the crack surface that there are parallel scratches occurring on surface, from tension to compression side as shown in figure 4.28. This is evidence that the first crack grows as the same speed on both sides of web.

The second crack occurs when the first one reaches to low stress zone. Second crack has short fatigue life and quickly fails the specimen. Due to its characteristic, second crack propagates in a short time and its surface is rough as shown in figure 4.28.

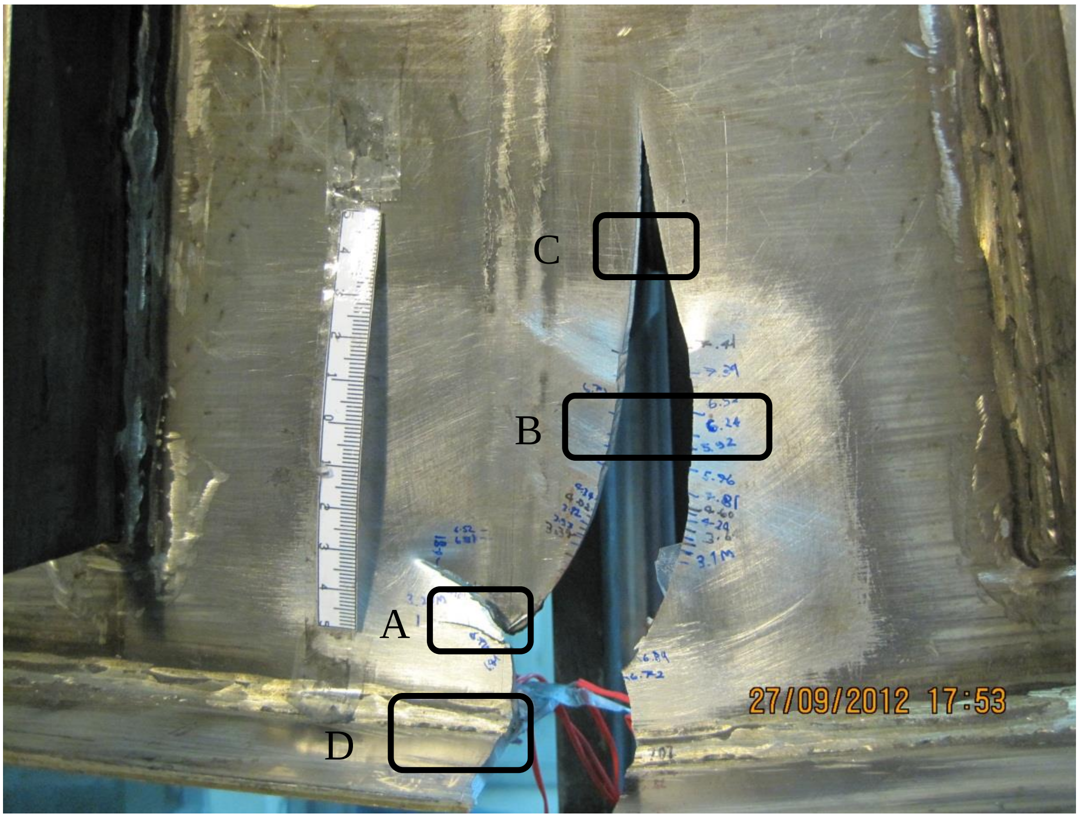

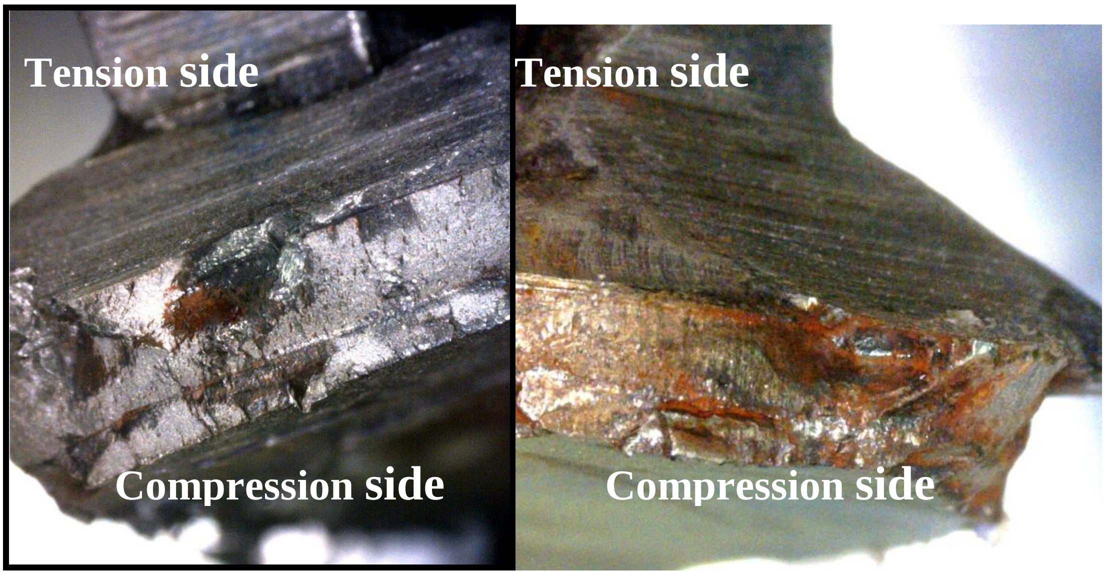

A. First Crack initiate at weld toe

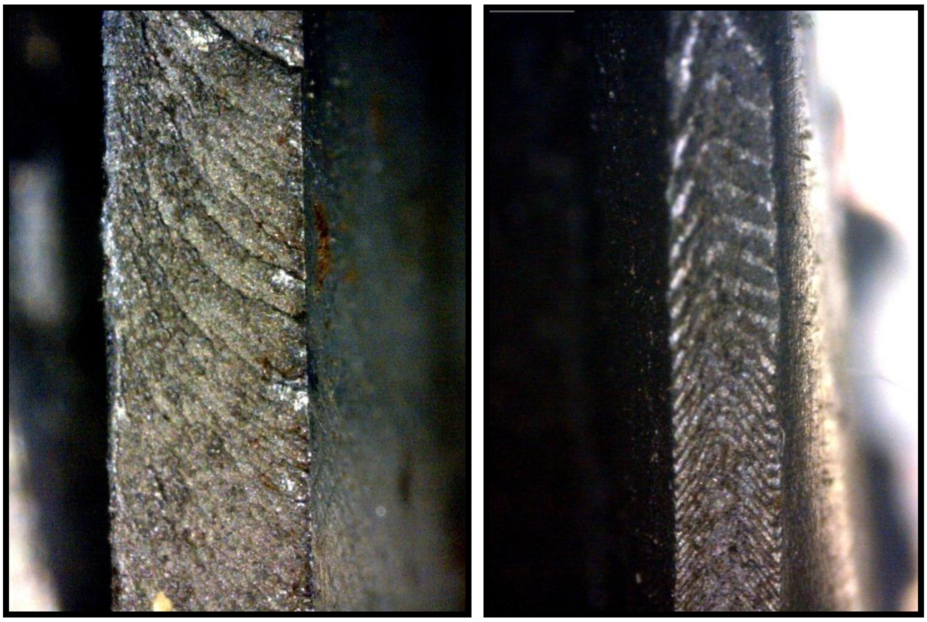

B. First Crack propagation

C. first Crack becomes critical.

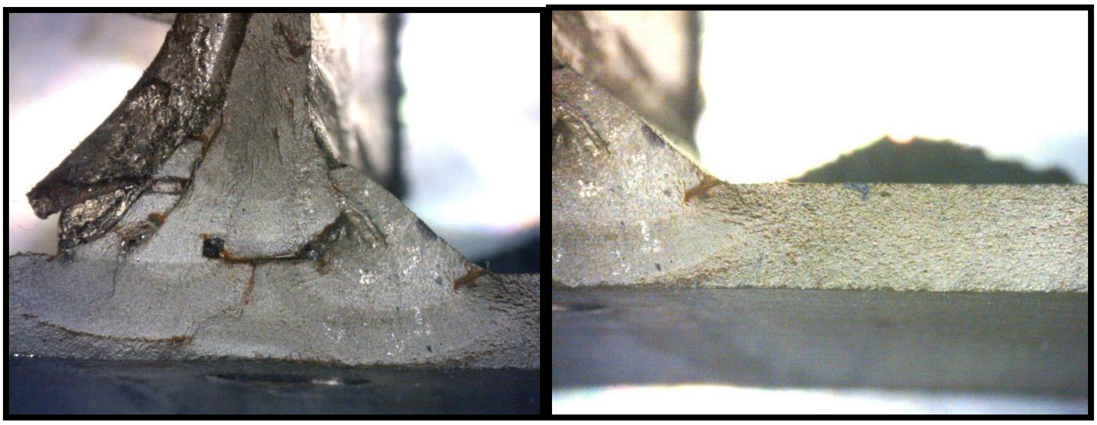

D. Second crack toward to bottom flange and becomes critical.

Figure 4.28 Crack surface of first and second crack

4.3.3. Stress fields

Based on systems of strain-gages and LVDT which is attached to specimens, the stress concentrates around the web gap for both tension and compression faces as well as at middle of the beams. The deflection of each testing beam is also recorded to validate with the data from FEM model. Total 9 strain-gages with positions described in section 4.1.6 were recorded; and they reflect the considering stress fields in this study. The results from strain-gages and LVDT are shown in table 4.10 as following.

Table 4.10: the strain-gages results from data – logger:

SPECIMENS		UNITS	1 (S1-1)	2 (S1-2)	3 (S1-3)	4 (S2-1)	5 (S3-1)
Series of specimen			I	I	I	II	III
Load	Max.	T	5.5	5.5	5.5	4	14
	Mean.	T	3.3	3.3	3.3	2.4	8.4
	Min.(0.2Max)	T	1.1	1.1	1.1	0.8	2.8
Strain-gages	**G8**	μm/m	-	-560	-535	-389	-593
	G9	μm/m	-	556	562	465	662
	G1	μm/m	-	1039	1044	945	1174
	G2	μm/m	-	621	559	250	656
	G3	μm/m	-	1259	814	517	798
	G4	μm/m	-	1095	833	608	709
	G5	μm/m	-	625	552	441	675
	G6	μm/m	-	-1171	-1529	-629	-1239
	G7	μm/m	-	127	596	---	178
Deflection	**LVDT**	mm	-	1.35	1.34	1.05	1.27

SPECIMENS		UNITS	6 (S3-2)	7 (S3-3)	8 (S2-2)	9 (S2-3)	NOTE
Series of specimen			III	III	II	II	
Load	Max.	T	14.0	14.0	4	4	
	Mean.	T	8.4	8.4	2.4	2.4	

	Min.(0.2Max)	T	2.8	2.8	0.8	0.8	
Strain-gages	**G8**	µm/m	-670	-648	-406	-433	
	G9	µm/m	674	658	418	411	
	G1	µm/m	921	955	881	871	
	G2	µm/m	488	788	505	488	
	G3	µm/m	545	1056	560	625	
	G4	µm/m	641	1027	537	621	
	G5	µm/m	500	772	427	485	
	G6	µm/m	-1117	-817	-766	-1420	
	G7	µm/m	-	-	-	-	
Deflection	**LVDT**	mm	1.17	1.17	1.06	1.06	

Figure 4.29 represents the change of strain around web gap which were recorded from strain-gage G1, G2, G3, G4 and G5. In this figure, it could be observed that the strain values collected from the same series of specimens are not quite the same values. There are some errors in these tests due to the shape of welds and the curve of web-gap under cyclic load. The first reason is that stress field around the web-gap is sensitive to the change of shape of welds, especially in a close distance. In this testing, the welding is semi-auto welds and this problem supplies some difference of shapes in each specimen. Basically, the curves of figure 4.29 represent the change of real stress in beam and supply the ideal on behavior of web-gap under loading. The values of strain-gages G2 and G5 as well as G3 and G4 are not quite different (error estimate less than 5%). Therefore, it's concluded that the system of testing is symmetrical. The second problem which influences to the exact of testing results of strain-gage G1 is the curve of web-gap and the length of strain-gage. In these testing, the web-gap lengths are small and present double curves under loading. The maximum of web-gap length is 4 cm and the minimum value equals to 2.5 cm. Comparing with the length of one strain-gage (about 1 cm), it's quite difficult for us to get the same values on strain-gage G1, because the strain values change in a large range inside the length of strain-gage. The strain-gage G1 is also close to welding as well as other strain-gages around weld toe. Shape of welds influences definitely to the local value of strain-gage G1.

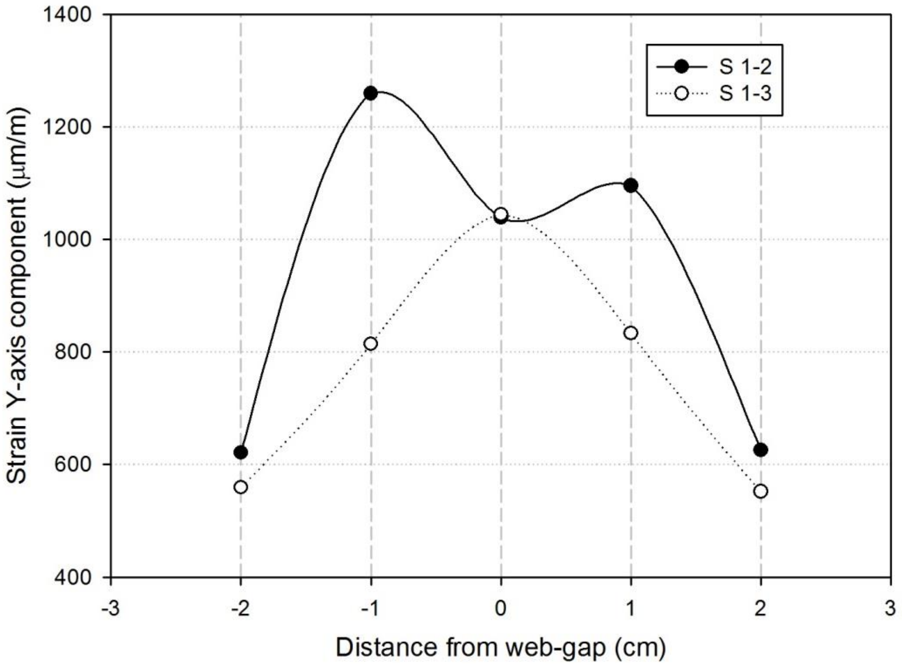

A. Strain-gage value for specimen in series I

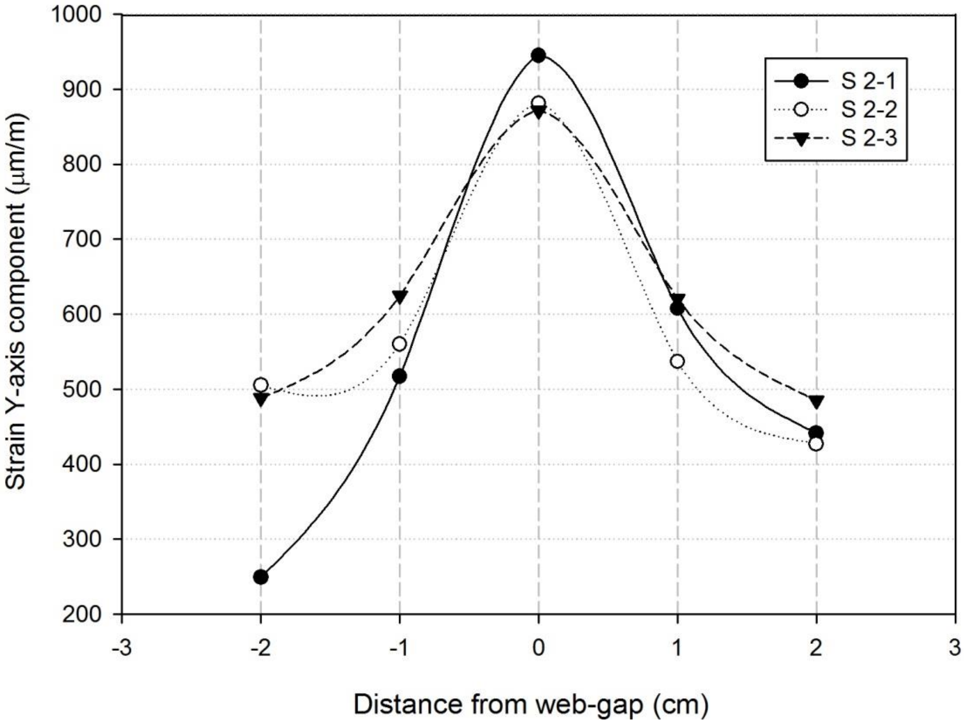

B. Strain-gage value for specimen in series II

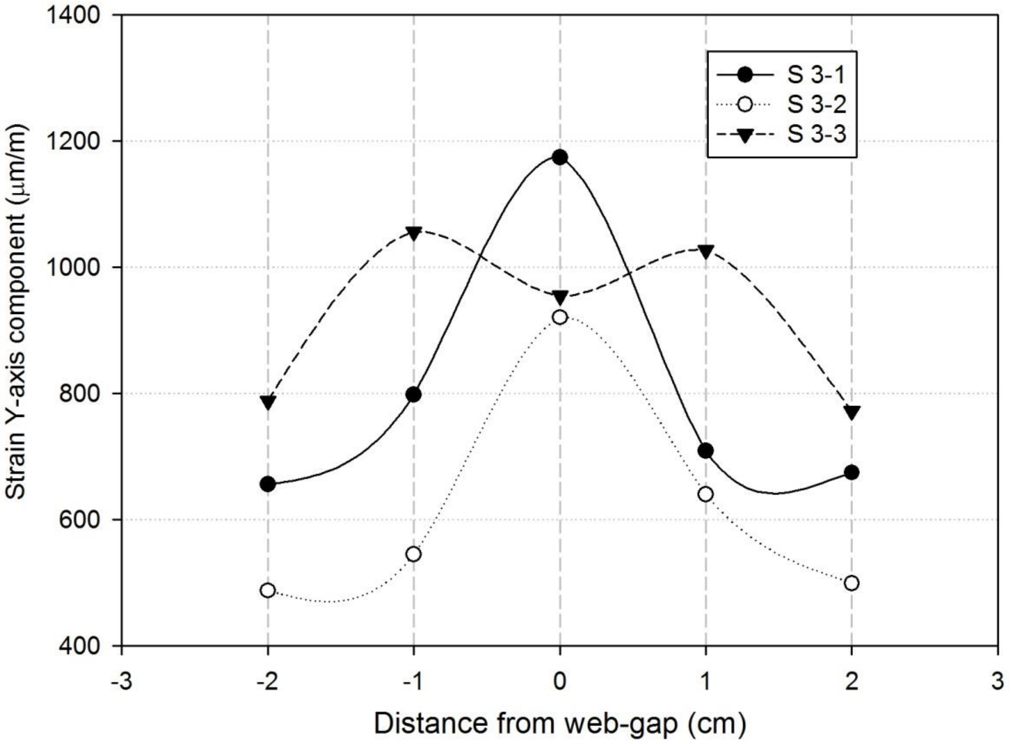

C. Strain-gage value for specimen in series III

Figure 4.29 Strain-gage values from G1, G2, G3, G4, and G5.

In Figure 4.30, the strain data from strain-gages G8 and G9, which are located at middle of beam and attached to top and bottom flange, show the same values in same series of specimens. There a little difference in values comparing values of G8 with G9 for a few specimens due to the attaching strain-gage to beam process. The problem is that strain-gage is not quite parallel to the beam. Errors estimate less than 5% and can be accepted for experimental data. From the values of strain-gages G8 and G9, it can be concluded that the system of testing in this study is symmetrical.

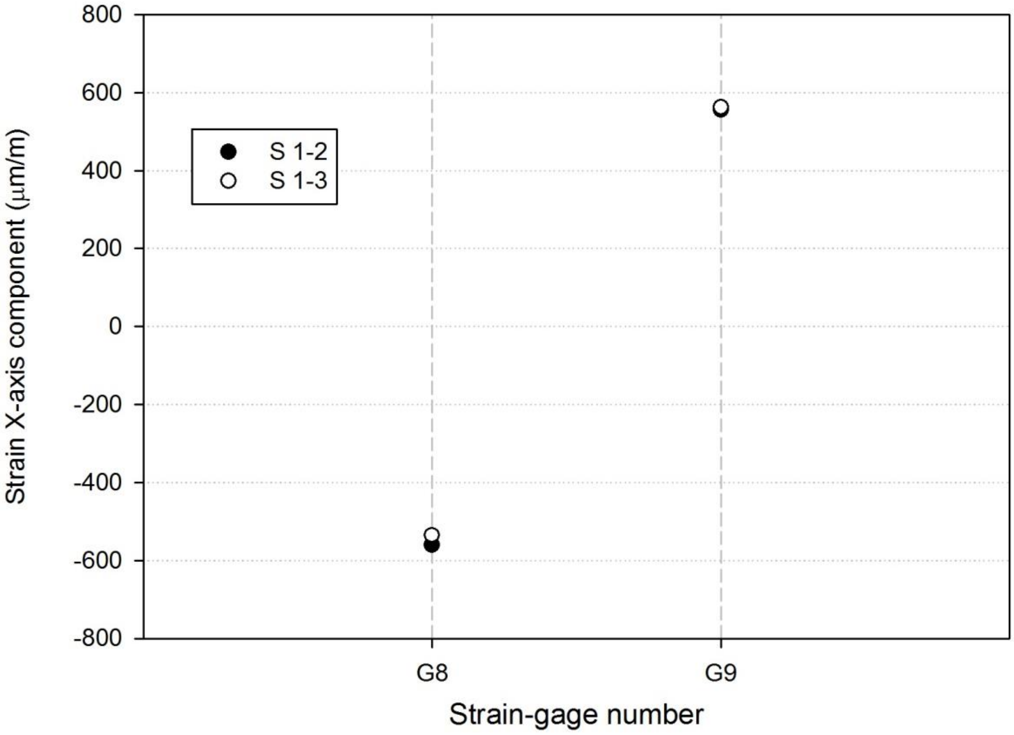

A. Strain-gage value for specimen in series I

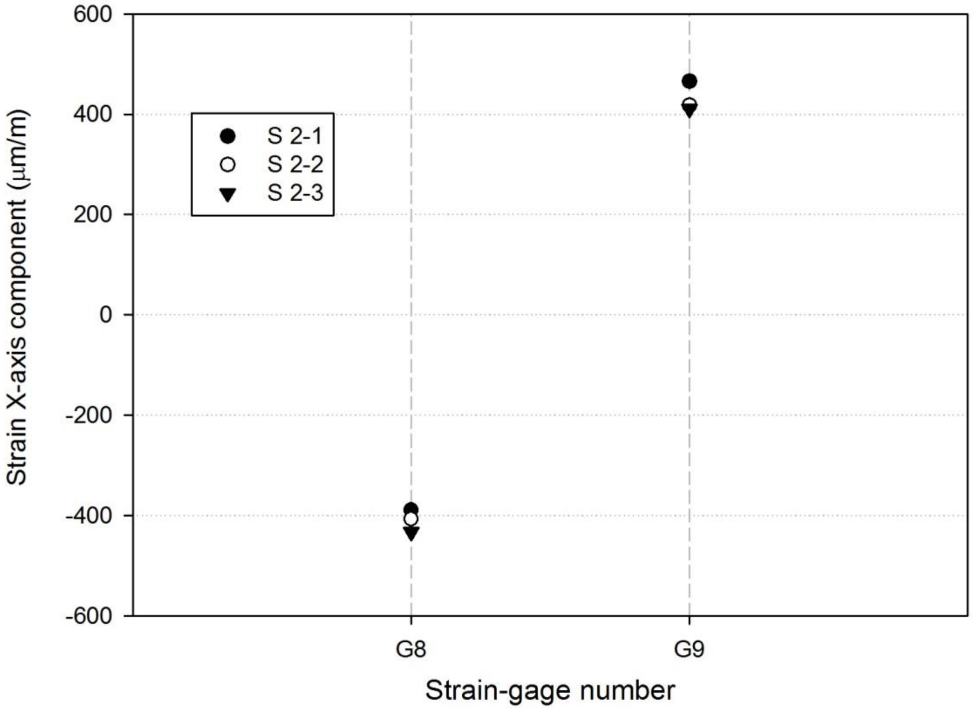

B. Strain-gage value for specimen in series II

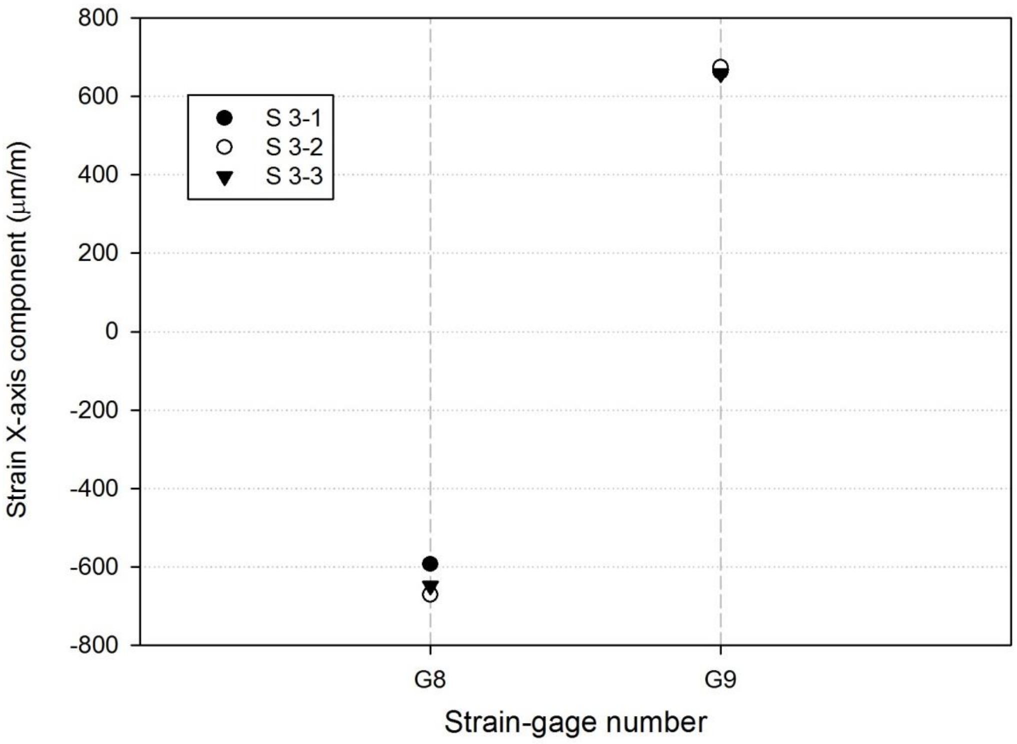

C. Strain-gage value for specimen in series III

Figure 4.30 Strain-gage values from G8 and G9.

Figure 4.31 presents the different of deflection value from experiment.

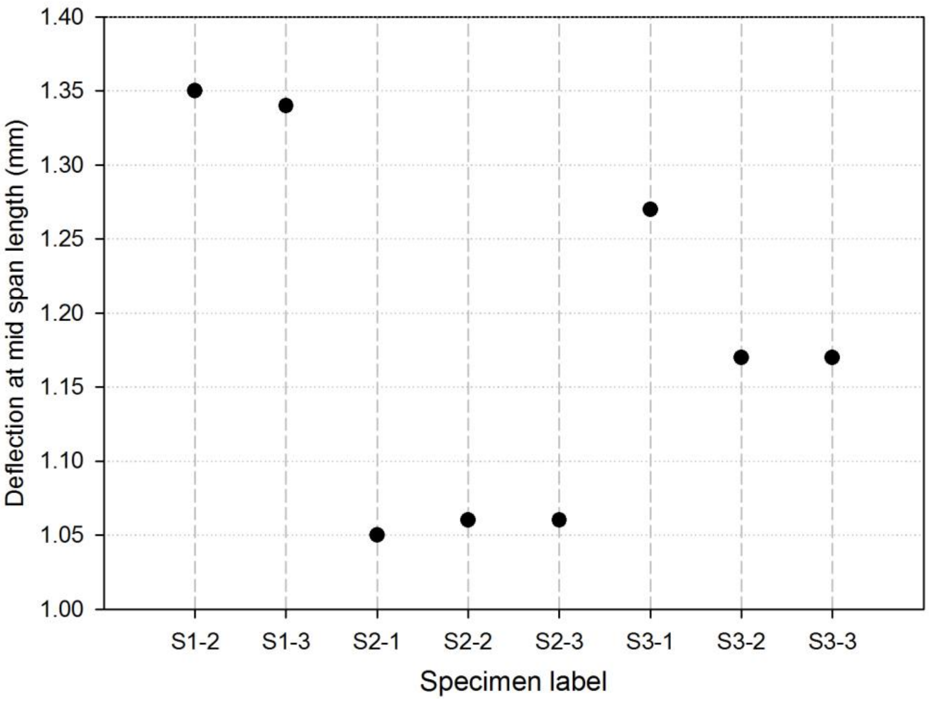

Figure 4.31 Deflection from LVDT in testing program.

4.3.4 Fatigue crack growth

When the crack initiates and propagates in each step of crack size increase, the process of recording is generated. So the fatigue life of crack is recorded and used to compare with finite element model data. The life of crack propagation is recorded by naked eyes without supported technique and has some errors. In this study, the range of error is acceptable for identifying the behavior of distortion-induced fatigue crack. The fatigue crack growth for each specimen is shown in Figure 4.32 and tables C1 to C10 as following:

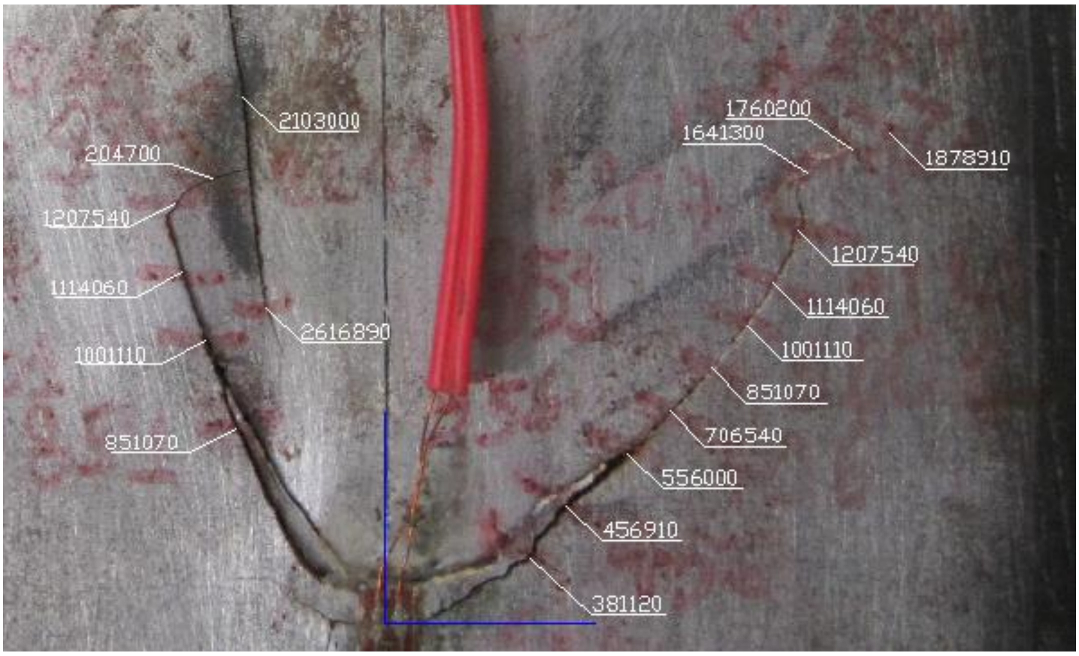

Fatigue crack growth of specimen 2.

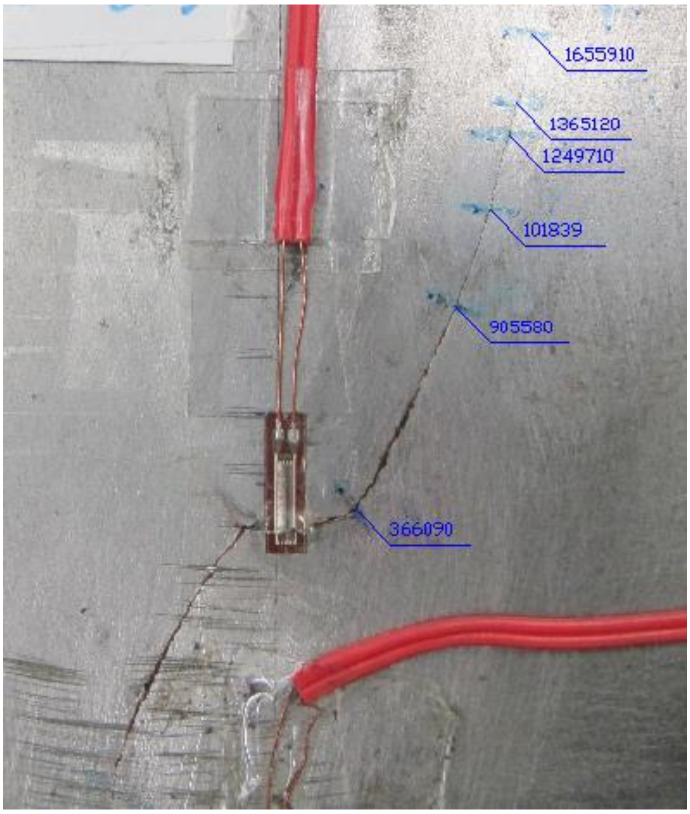

Fatigue crack growth of specimen 3.

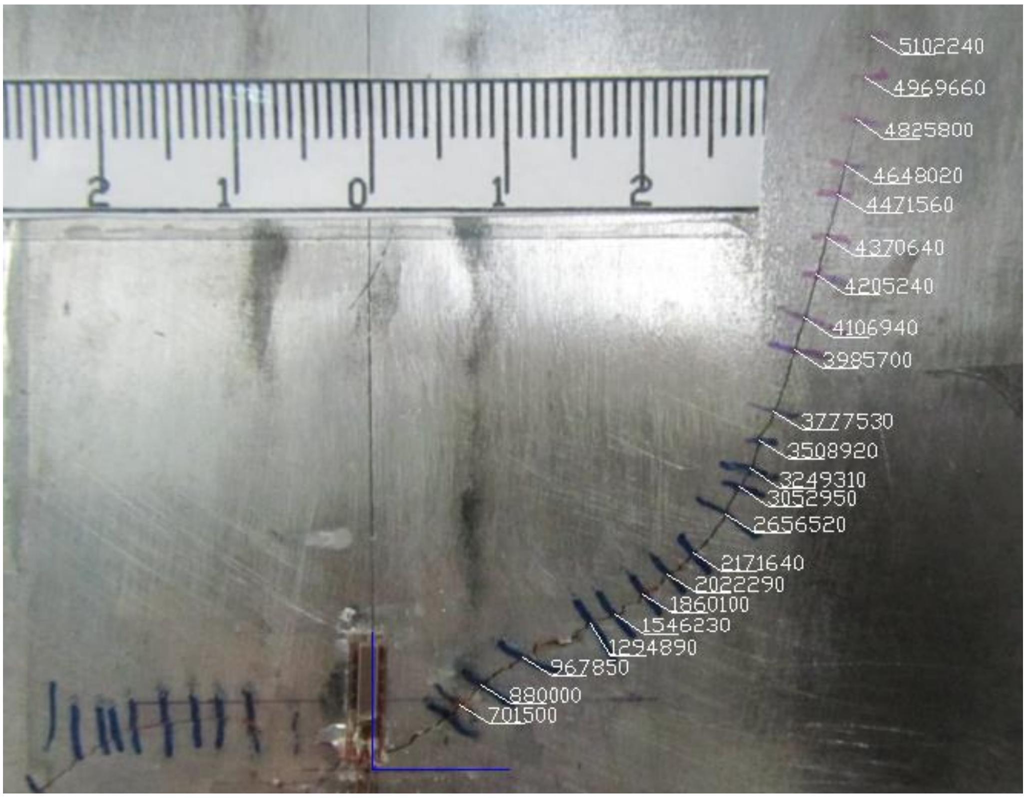

.

Fatigue crack growth of specimen 4.

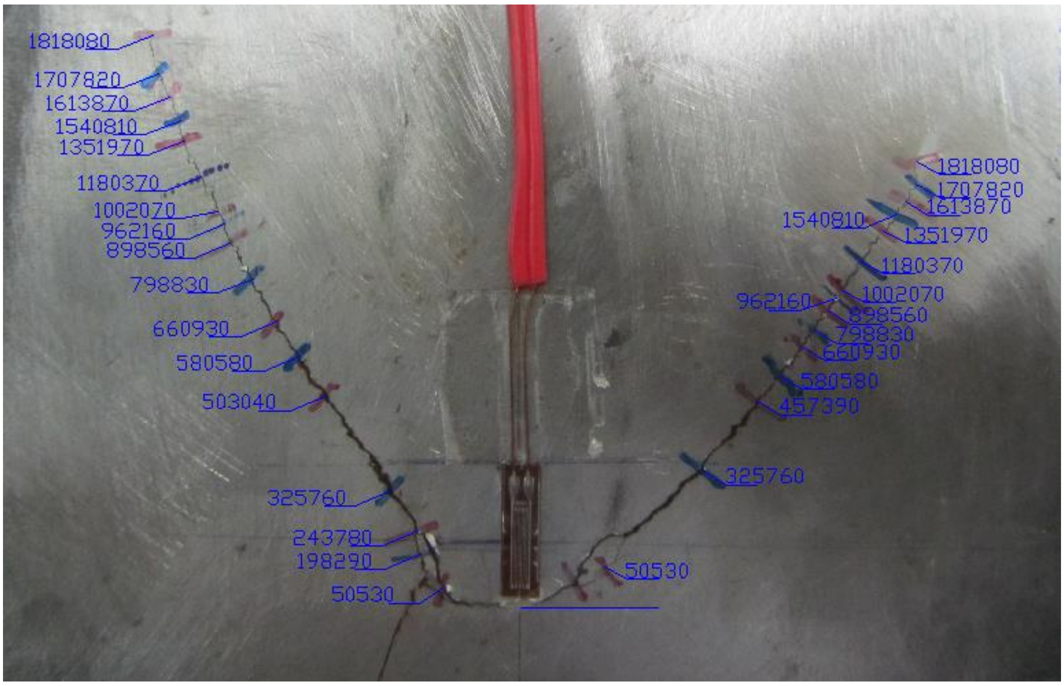

Fatigue crack growth of specimen 5

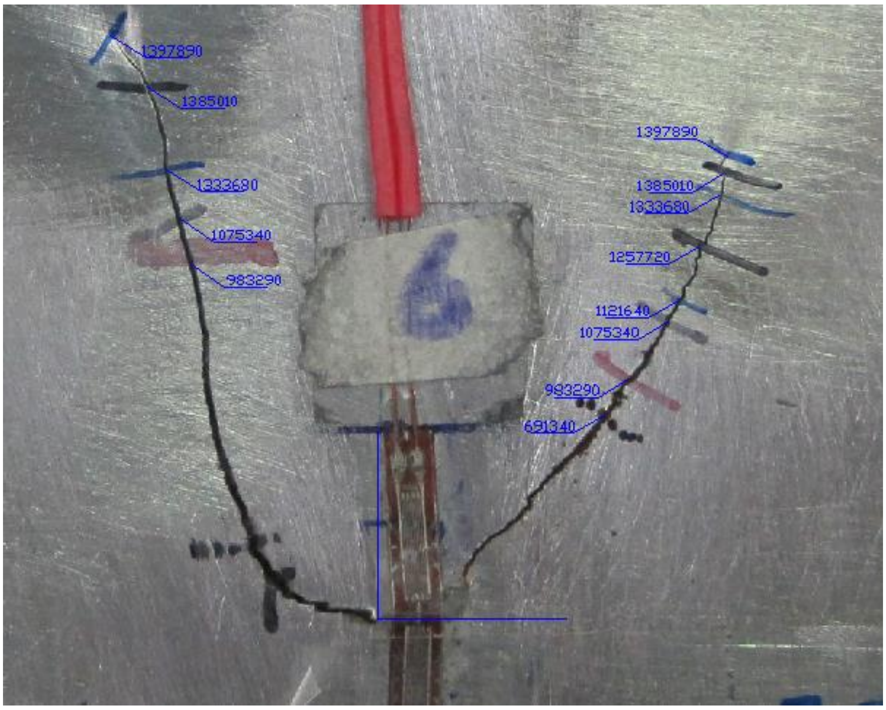

Fatigue crack growth of specimen 6

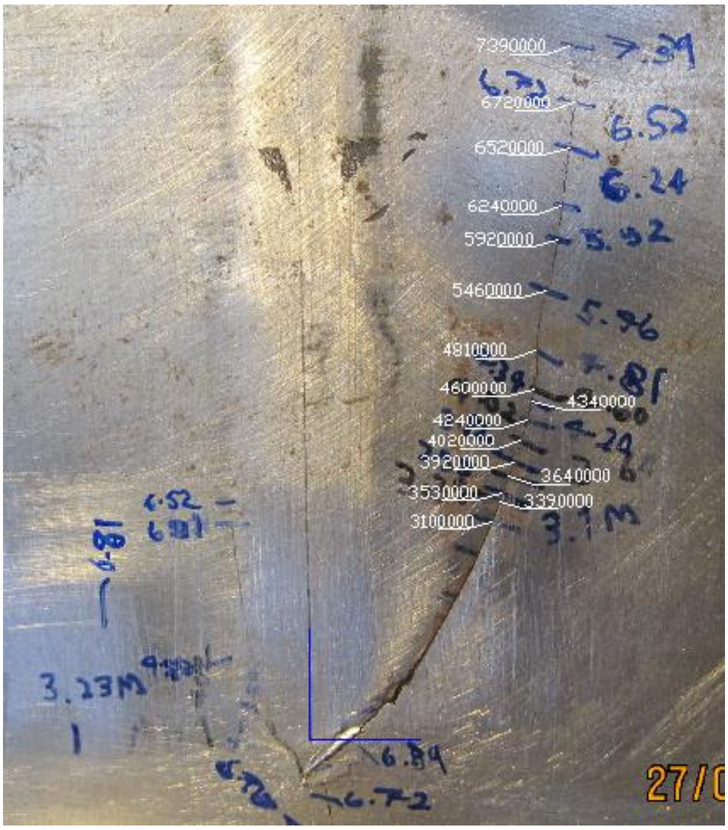

Fatigue crack growth of specimen 7

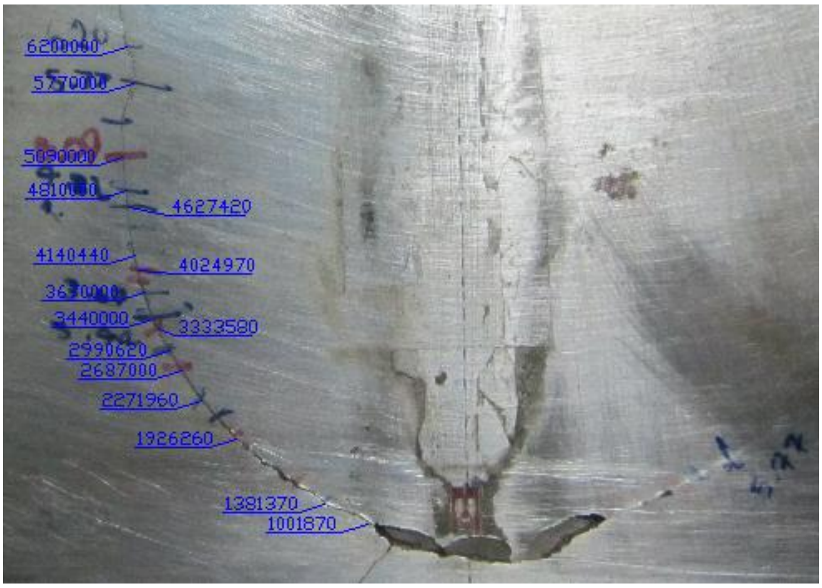

Fatigue crack growth of specimen 9

Figure 4.32 Fatigue crack growth for each specimen.

During the testing specimens, it was unsuccessful in recording the fatigue life of crack propagation of specimens 1 and 7. So there are seven data of fatigue crack growth can be used to compare with FEM results. Anyway, the fatigue life for beam failure can be obtained from all specimens' data. Figure 4.33 presents the fatigue life of beam for all testing specimens. The fatigue life is defined by beam collapse. In figure 4.33, it’s quite obvious that distortion-induced fatigue crack belong to Category C*.

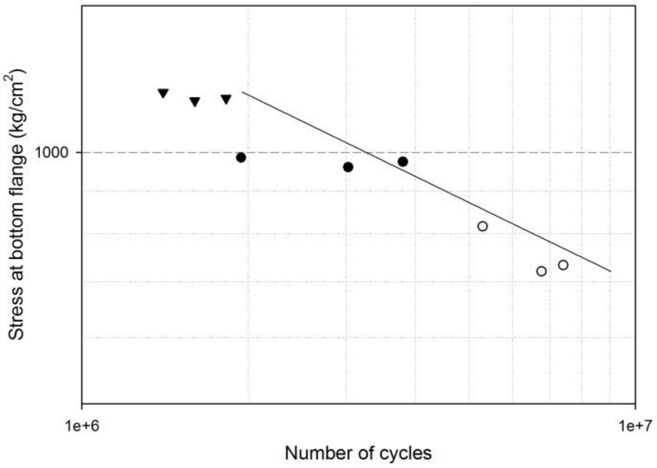

Figure 4.33 S-N curve of 9 specimens.

4.4 Conclusions

In experimental program, tests were conducted to find out the behavior of distortion-induced fatigue crack as well as the results to validate with FEM models. Nine specimens were tested with the same conditions in laboratory. Observations on testing reveal the same assumptions of behavior in Chapter III (Theoretical consideration). The first crack appears at the web-gap on the tension face, grows deeper into the web-thickness as semi-ellipse, and is formed as web-toe. After that, crack grows up to compression face and becomes two crack tips. Crack tip continues to move as horizontal direction and propagates up under effect of mode I and mode III. Bend mark solution reveals parallel scratches on crack surface connecting tension and compression faces. When crack grows close to lower stress zone, it propagates slowly. The second crack starts from the first crack at the position of web-toe, and propagates downward to bottom flange. The beam fails after a number of cyclic loads because the second crack damages the bottom flange. These observations reveal that the typical of beam failure depends on the second crack occurring. Without first crack, the second one could not occur and propagate.

The shape of crack path depends on stress field or energy close to the web-gap. Therefore, the shape of weld is important in distributing stress around critical zone. If the shape of weld-toe has many spot points, it will produce many critical stress points on web. Therefore, the new crack could appear in anywhere of these points. The second crack initiates from one of these critical points. Although loading and geometries are symmetrical, un-symmetrical shape of weld creates trouble around web-gap and makes the crack path to be different in the same series of specimen. These will create difficulty in validation with FEM simulation’s results.

CHAPTER V

FINITE ELEMENT MODELLING

5.1 General

In this study, a finite element study based on elastic fracture mechanics concepts was undertaken to investigate the distortion-induced fatigue crack at the web gap of I-beam. The purpose of FEM model is to simulate the behavior which occurs in pilot testing program in order to analyze stress fields around the web-gap and study the fatigue fracture.

AASHTO code considered in-plane load-induced fatigue progress. But out-of-plane distortion-induced fatigue stresses are still un-answered in AASHTO design code. If in-appropriate finite element analysis or field testing is conducted, the stress field as well as strain energy density around the web-gap would not be determinable because of the complex zone at connection stiffener to girder or flange. It’s required to implement a three dimensional finite element analysis to describe properly out-of-plan distortion-induced effect around the web-gap zone. However the three-dimensional structure intersection, the local geometries, shape of welding, and relative stiffness of detail are not the same to each of bridges. So the finite element model in this study just describes the typical detail of distortion-induced fatigue effect of I-beams of steel bridge.

The whole system of testing was modeled in order to investigate the stress fields as well as the Strain Energy Density of element in crack tip around the web-gap. To accommodate the above purpose, the modeling must be simulated in both two levels, global and local, in three-dimensional structure to describe the behavior occurring in testing.

5.2 Element detail

The FEM analytical procedures of this study are carried out using ANSYS 12.1 (ANSYS, Inc., Canonsburg, Pa.) in structure package option. In these procedures, element SOLID 45 is employed to describe for all computations. SOLID 45 is used for the 3-D modeling of solid structures, and defined by eight or six nodes having three degrees of freedom at each node: translations and rotations in the nodal x, y, and z directions. In case for meshing, SOLID45 could be meshed in eight or six nodes as shown in 5.1.

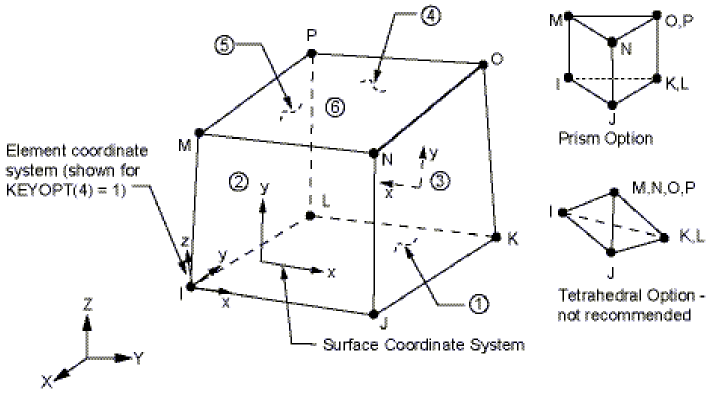

Figure 5.1 SOLID 45 geometries.

All the plate (flanges, girders, stiffeners) and welds are modeled with SOLID 45 elements. The properties of elements are setting with elastic modulus E = 2.192 kG/cm^2 and Poison ratio $\mu = 0.3$ (these properties are obtained from tension tests).

5.3 Loading and boundary conditions

The experimental program represents the typical structure of the distortion-induced fatigue crack at the web-gap detailed in steel bridge. In simulation, a three-dimensional model is constructed with 3D deflection and relative stiffness to investigate the behavior of fatigue crack.

Loads applied on FEM model are line loads with the same values as applied in the experiments. In the experiments, the bottom actuator moves up to create relative deflection and load applied directly on top of beam was transferred from displacement of bottom actuator by "load control" system. In FEM model, the load is applied directly on top of beam and creates the deflection as real structure. Load applied in model is intended to transfer from top of beams to spring supporter and rigid body and create high concentrated out of plan stress at the connection stiffener. Spring supporter supply in-plane reaction and control out of plane rotation. Therefore, Uy and Rx are required for both spring supporters. In experiments and FEM model, the stiffeners simulate a half of out of plane stiffness between 2 neighboring I-beam. The displacements at the middle of stiffener would be just rotation as X axis. So the reactions controlled at this place are Ux, Uy and Uz. The boundary conditions are shown in figure 5.2 and figure 5.3.

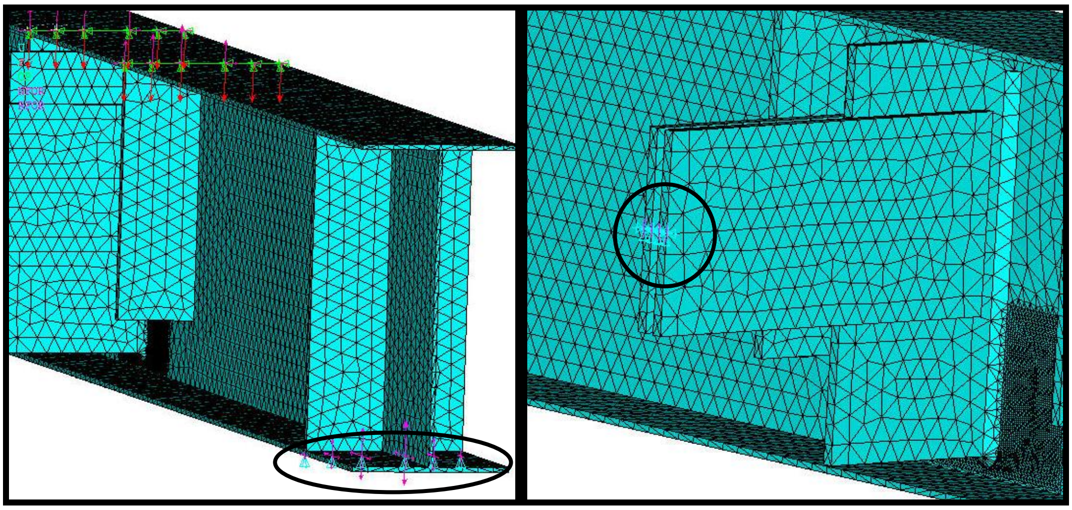

a. Spring supporter at end of model. b. Half of stiffener simulation.

Figure 5.2 Displacement controlling in FEM models.

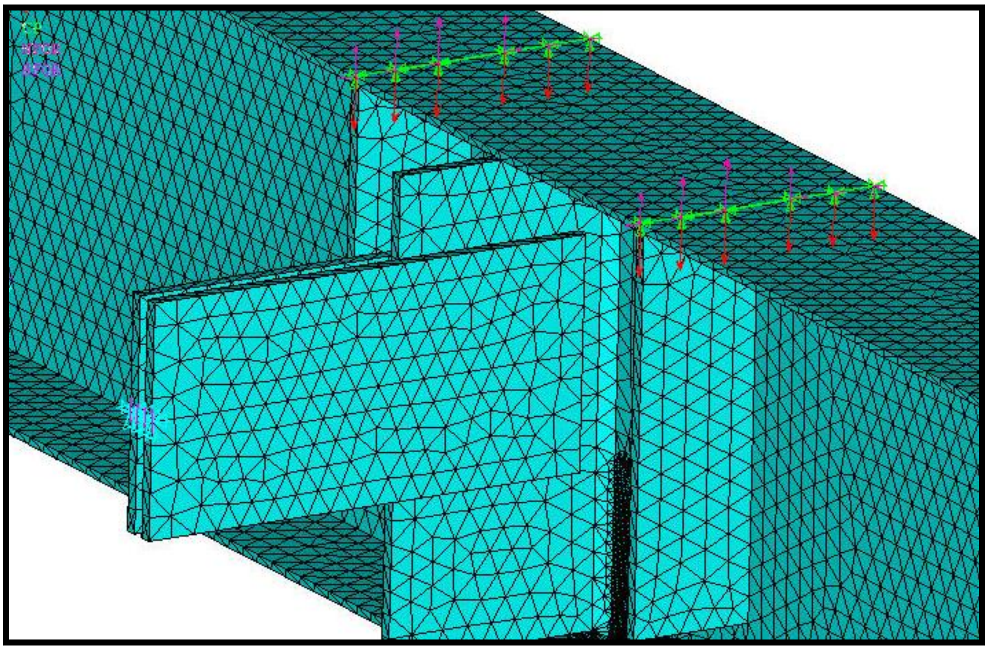

Figure 5.3 Line load applied on model.

In experimental observation, the crack occurred at the web-gap and formed as shape of weld toe. The shape of weld influences to the shape of initial crack and couldn’t be neglected. If the welding connecting stiffener and girder is not modeled in FEM, the stress field couldn’t be determined as in the experiments and lead to error calculation. The geometer of welding which modeled in FEM is the same as the value of 5 cm in testing. However, the welds in experiments are formed by semi-auto method and are not the same shape for all testing beams. This problem leads to the difference between FEM and experimental results. The welding simulated in FEM models begins from the top of stiffener to web-gap and cover the weld-toe as shown in 5.4

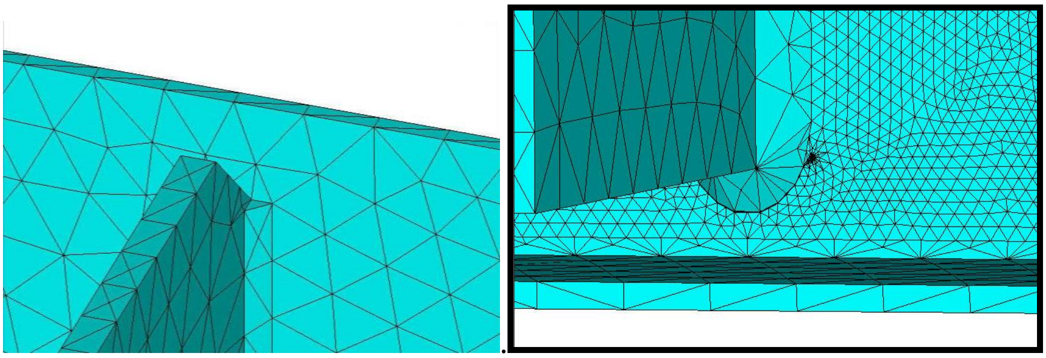

Figure 5.4 Welding simulations in FEM models.

In simulated model, the rotation of top flange is controlled by the line load applied as in experiments. In bottom flange, out-of-plane rotation at middle section of I-beam is freedom and makes curve of girder at web gap position. Although, these loads seemingly act only in plane bending, they also directly create the out of plane through girder deflections. In reality, the girder section along web-gap length deflects downward, curves out of plane. Therefore, this part of web is important in controlling distortion-induced effect under loading. With above boundary condition, the effect of girder reactions is considered in this simulation.

5.4 Initial crack

Initial crack in FEM simulation defends on observation from experiments. As in experiment, the crack occurs at the weld toe where the stress concentrate is maximum, shapes as weld toe, propagates out of welding, and depends on the stress field around weld. The FEM model will try to simulate the same initial crack in testing by setting up an initial crack as shape of weld toe and run out of weld with angle 45^{o} and crack length for 1st step equaling to 0.2 cm. The angle for first step is 45^{o} and not effect to next step of crack propagation, because crack path depends on ratio of bending stress and stress out of plane. The image for initial crack set up in FEM is shown in Figure 5.5. However, the shapes of weld toe in experiments are not the same for all models and the stress field close to weld toe mainly depends on its shape. These problems will influence to predict crack path, especially the path at the beginning.

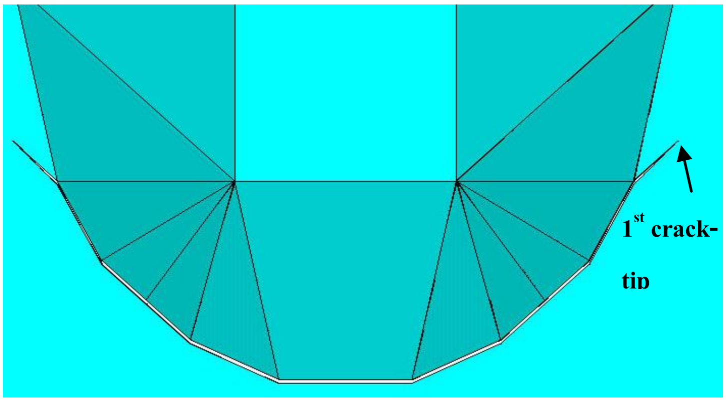

Figure 5.5 initial crack shapes as web toe.

5.5 Ring elements

Figure 5.6 shows the ring elements around a crack tip and the calculated S(θ) curve. Due to slight difference between the values of external ring elements (denoted by “Ext element” in Figure 5.6a) and internal ring elements (denoted by “Int element” in Figure 5.6a), it is recommended that the values for external and internal elements are plotted separately in Figure 5.6b. The values of S(θ) in Figure 5.6b are calculated from FE simulation, in which the accuracy depends significantly on the number of ring elements around the crack tip. Therefore, a suitable mesh refinement around the crack tip is required to yield a good precision.

The values of S(θ) represent some local minimum values around the crack tip. It is suggested to calculate the local minimum of the curve ahead of the crack tip, not the global minimum, i.e. the crack tends to run forward under the guided direction of loading, and the crack will propagate into the area ahead of the crack tip when loading is applied. If the global minimum values are used, the predicted crack might run into wrong trajectories because the crack plane could disturb the SED values of nearest elements in the ring. Bouchard et al. (2003) recommended that the effective range of angle would be between -70° and 70° ahead of the crack tip.

The accuracy of FE simulation from the SED criterion directly depends on the number of ring elements around the crack tip. It should be noted that the number of ring elements is also limited from the aspect ratio of the elements, i.e. the elements in the ring should not have too small vertex angles to yield accurate results. Each element in the ring contains an amount of strain energy, and the local minimum of SED values is then obtained from the $S(\theta)$ curve (see Figure 5.6b). The local minimum could be improved by using a parabola fitting of the three SED values obtained from the element with the minimum SED value and its two neighboring elements. The minimum value of the parabola is then used to represent the local minimum of S(θ) curve. If the technique of the parabola is not used, and all elements in ring around crack tip are taken into account, the predicted crack path appears to be rather inaccurate.

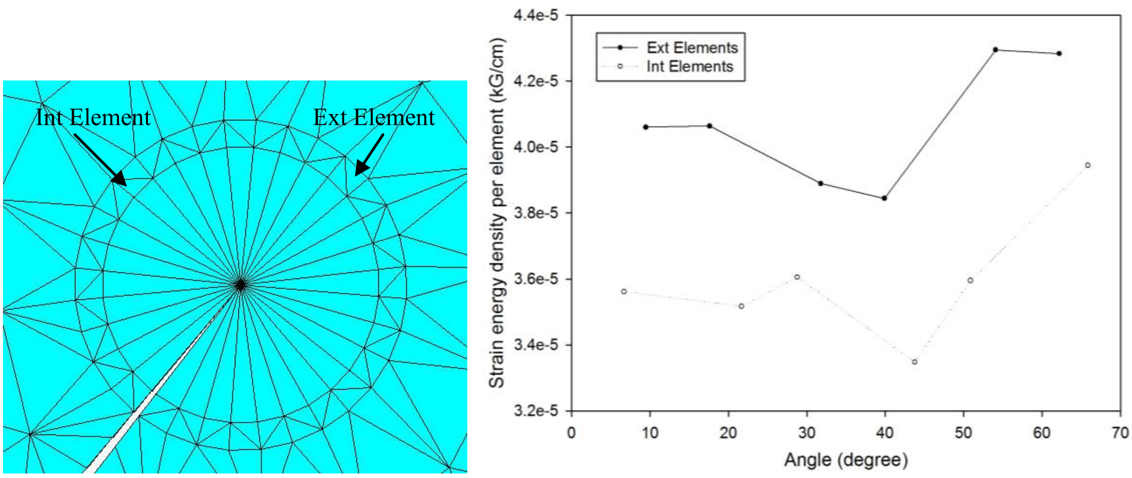

Figure 5.6 (a) Ring elements and (b) calculated *S(θ)* curve for the MSED with the numerical formulation.

To solve a fracture mechanics problem, one of the most crucial steps is identifying the singularity-dominated zone. In the present scheme, the radius of ring elements is recommended to be inside the singularity-dominated zone. This zone is defined as the largest circle, centered at the crack tip, in which the stress intensity factors in the zone do not vary when geometry or applied loading is changed. Different models with different loading, geometry or crack configuration as well as different material properties will result in different singularity-dominated zones. Thus, the singularity-dominated zone must be first identified, and then the ring elements will be placed inside this special zone with conforming mesh around the crack tip.

To identify the singularity-dominated zone, the stress field around the crack tip must be determined. If the meshing is fine enough and the radius of ring elements can capture the singularity dominated zone, the stress field calculated from FEM will be similar to the analytical solution obtained from a classical theory of fracture mechanics, especially in the area closed to crack tip. With coarse meshing and unsuitable shape of ring elements, the stress around the crack tip from FEM cannot simulate the singularity dominated zone as given by the fracture theory. Therefore, it's important to identify the singularity zone in order to capture the conforming fine meshing as well as size of radius of ring elements. In summary, the step to generate ring elements can be performed as follow:

- Generate FE meshing.
- Obtain the stress field around the crack tip.
- Identify the singularity-dominate zone, which is the area where the error between the solution from FEM and the analytical solution is less than 5%.
- Define the radius of ring elements within the singularity zone as well as the conforming meshing.

5.6 Meshing and re-meshing technique

5.6.1 Meshing properties

Each model would be classified in 2 main zones with different size of elements. The inside zone is placed around the web-gap. The out-side zone includes all of plate, excepts the part of inside zone. The purpose of classification is to increase the accuracy in calculating concentrated stress around web-gap zone as well as strain energy density along the crack propagation and it's necessary to apply fine meshing in this zone. The accuracy of stress field in out-side zone is not quite serious and the raw meshing could be applied. In this research, inside element area is 0.2cm^2, while out-side element area equals 1cm^2. The definition of out-sides and in-side zone is presented in Figure 5.7. With this classification, the time for calculation in each step will be reduced due to smaller number of equations in the program, but the accuracy of stress field around the web-gap as well as strain energy density along crack propagation would be reliable.

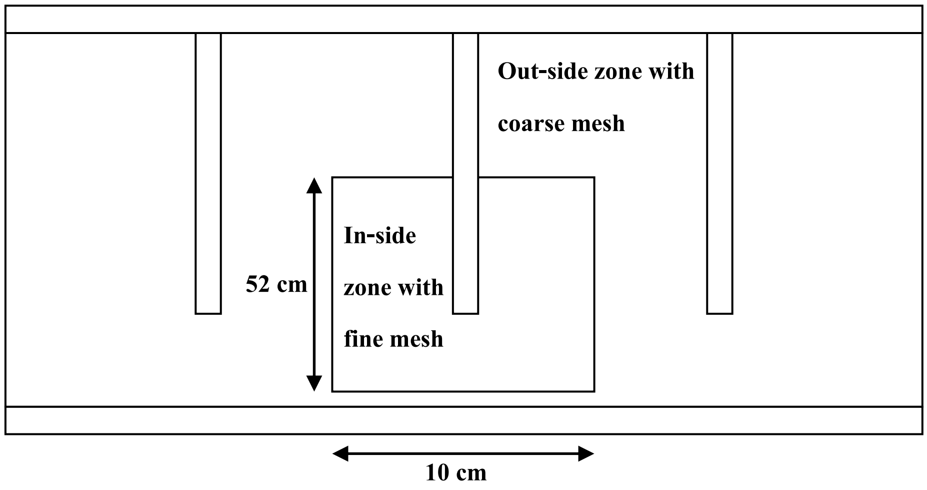

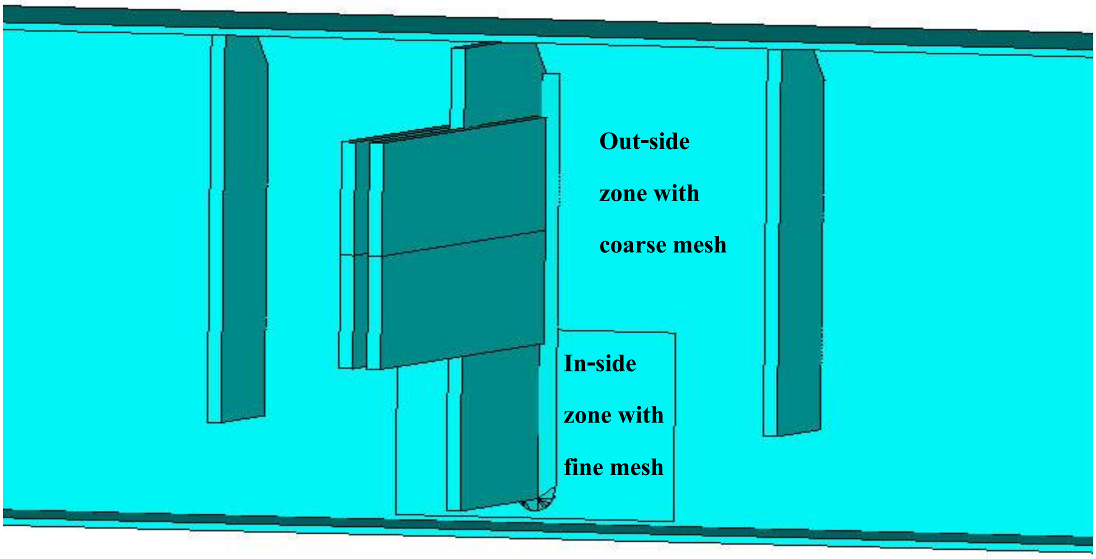

Figure 5.7 Classification of in-side and out-side zone.

Sweep mesh is applied from front to back side of all plate. There are 10 elements along thickness of girder of inside zone. Therefore, the accuracy would be increased in calculation. The plates at out-side zone require one element along the thickness. The number of elements of in-side or out-side zone depend on the geometries in each model. It's around 72000 elements meshing in in-side zone and 55000 elements which are created on out-side zone. With amount number of elements, especially model is classified into 2 zones, the model adjust the requirements for accuracy in calculation as well as the time for calculating.

At crack tip, there is special meshing as describing in section 5.5 (Ring elements). The ring element meshing technique plays important role in this study to supply the minimum strain energy density as well as its value. After one step of increased crack length (crack length increase in each step equals 0.2 cm), the model will be regenerated new meshing with the same strategy as mentioned above. The values required for calculation in each step include Strain Energy Density of each element and the direction of minimum values of elements in ring.

The discrete model described in this study includes two approximations:

- In experiments, the crack in tension and compression propagate at same speech with a little different in position. The crack tip on tension side is slight higher than the other on compression face. This behavior could be observed from parallel curves on crack surface. To simplify the procedure of modeling crack tip, it's accepted to use the assumption that allows the crack tip perpendicular to both tension and compression side. This assumption does not change the crack path and fatigue life of the model.

- In experiments, the shape of welding is not quite symmetrical, Therefore, it influence to the crack propagation line. The crack paths are not the same on both sides of stiffener. In some specimens, crack grows in one side of stiffener. In FEM model, the crack is generated in both sides with same geometries due to symmetry shape of welding. So the crack path in FEM model would be slight difference to the line in experiments.

5.6.2 Ring element radius

Identifying ring element radius is an important step in simulating FEM model in this research. As described in section 5.5, ring element radius is identified from singularity-domestic zone around crack tip. In this study, all models have the same value of girder's thickness, but difference in geometries. Therefore, the singularity-domestic radiuses are not quite difference in values for each model. The results of singularity-zone are calculated from figure 5.8 as following:

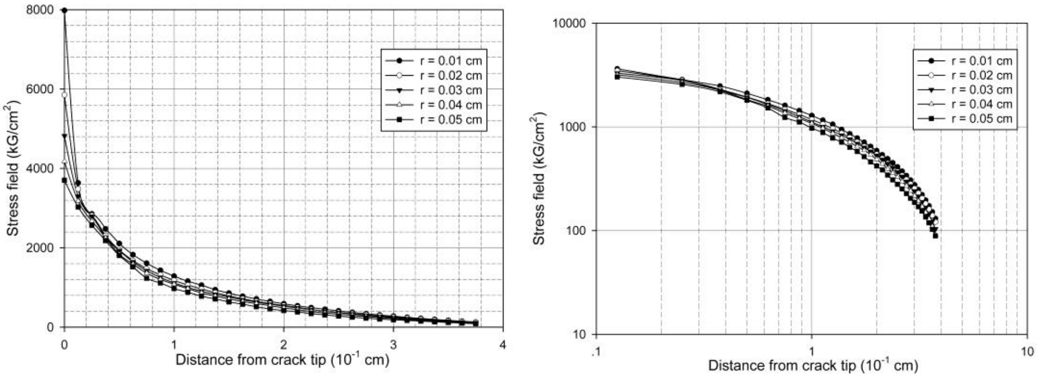

Figure 5.8 stress field at crack tip in linear and log_log scale

As shown in 5.8 in log-log scale stress field at crack tip, we set up a line parallel to the beginning of the slope, it could be observed that the draws of figure change their angles when the curve run out approximate about 0.03 cm on distance axis. It's concluded that the size of singularity-domestic zone is limited to 0.03 cm. Therefore, the radius of ring element is chosen about 0.02 cm for all of models.

5.6.3 Step size

The step size is chosen to guarantee that the crack path is not influenced. If the size of each step of crack propagation is too large, the crack path is not reliable and the values of strain energy density are in-accurate. If the step size is too small, it takes a long time for computation the crack propagation. The step size in this study is chosen about 0.2 cm, depends on comparing three values of step size (0.1, 0.2 and 0.3 cm).

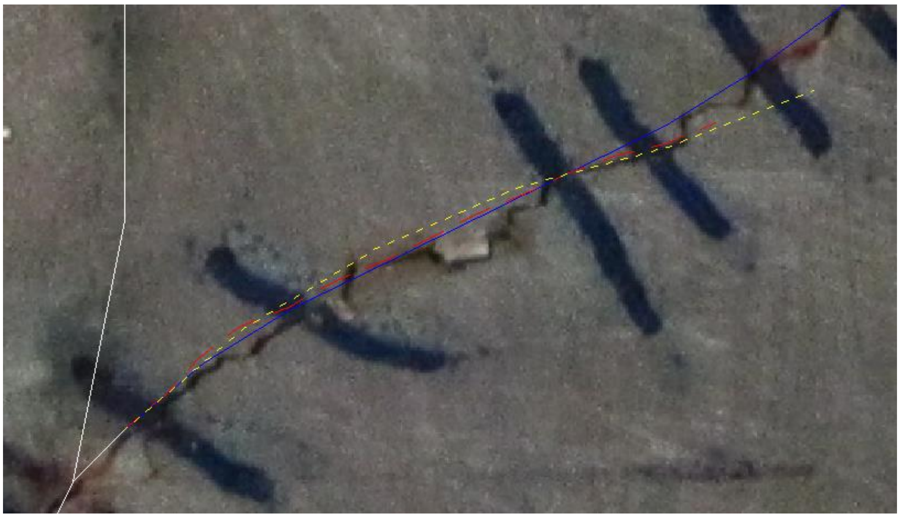

a. Long dash (red) – Step size 0.1cm.

b. Solid line (blue) – Step size 0.2 cm.

c. Short dash (yellow) – Step size 0.3 cm.

Figure 5.9 Comparing crack paths in 3 kind of step size.

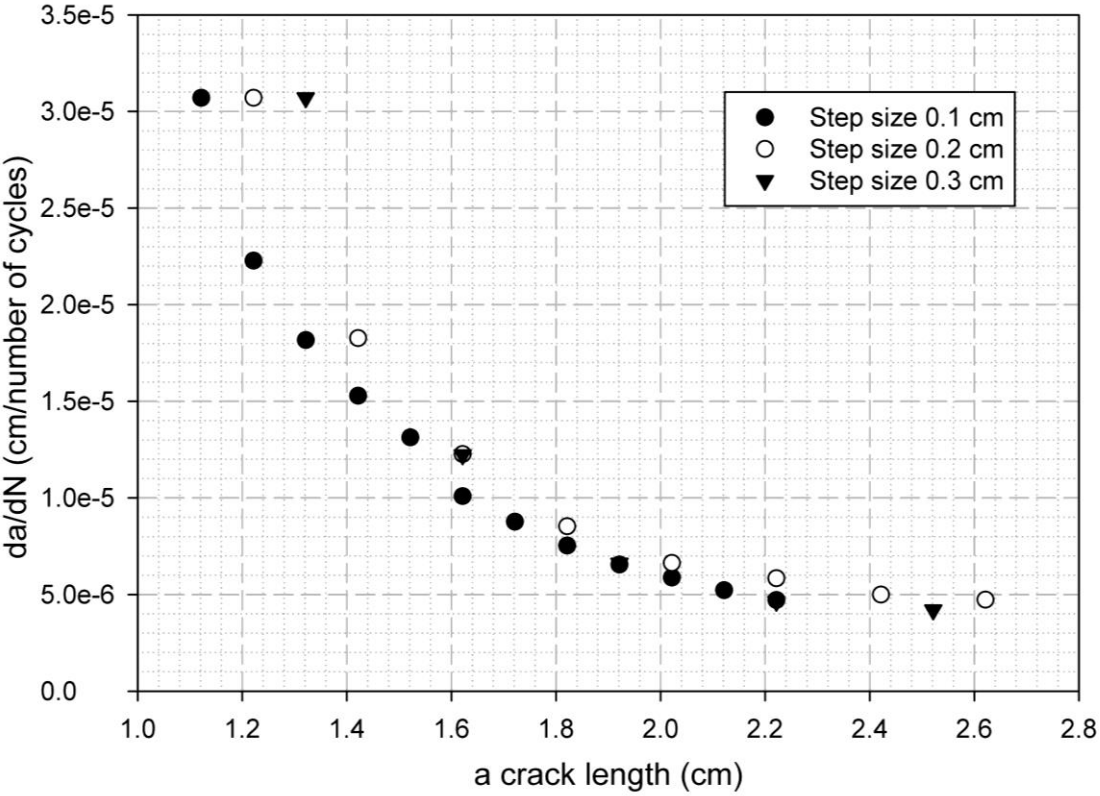

Figure 5.10 Comparing 3 kinds of step size in fatigue crack growth rate.

Figure 5.9 and Figure 5.10 present the comparison of the error from three values of step size in predicting crack path as well as fatigue life. From these figures, the chosen of 0.2 cm step size is reasonable.

5.7 Implementation of SED criterion in FEM

Sih (1974 – 1980) considered that high values of strain energy, *W*, tend to prevent crack growth. Then the crack grows in the direction that minimizes this energy. Let *w* be the strain energy density: $w=\left(\frac{dW}{dV}\right)$, where W is the sum of the volumetric part of the strain energy W_v and the distortion energy W_d. This quantity is proportional to the square of stress, and since the stress has a $1/\sqrt{r}$ singularity at the crack tip (where *r* represents the distance to the crack tip), the strain energy density (*w)* also has a $1/\sqrt{r}$ singularity. Therefore the so-called strain energy density factor, $S = rw$, remains bounded.

Parameter S can be computed using two different techniques:

- ***An analytical formulation***: The strain energy density is inversely proportional to the distance *r* to the crack tip. Then *S* represents the intensity of the local energy field:

$$S=rw=r\left(\frac{1+v}{2E}\right)\left[\sigma_{11}^2+\sigma_{22}^2+\sigma_{33}^2-\frac{v}{1+v}(\sigma_{11}+\sigma_{22}+\sigma_{33})^2+\sigma_{12}^2\right] \qquad (5.1)$$

- ***A numerical formulation***: The strain energy of each element (We) can be calculated from:

$$W_e=\frac{1}{2}[u_e]^T[K_e] \qquad (5.2)$$

where $[u_e]$ is the element displacement vector, and $[K_e]$ is the element stiffness matrix. At each propagation stage, ring elements having the same area are constructed around the crack tip. The strain energy (S) in each ring element is computed and plotted against the angle of the element relative to the crack axis. The direction of crack propagation corresponds to the one with the minimum value of strain energy according to

$$\left(\frac{\partial S}{\partial\theta}\right)_{\theta=\theta_0}=0 \qquad and \qquad \left(\frac{\partial^2 S}{\partial\theta^2}\right)_{\theta=\theta_0}>0 \qquad (5.3)$$

The computation accuracy is quantitatively linked to the number of elements in the ring around the crack tip.

5.8 FEM models

There are total 10 FEM models set up to simulate the distortion-induced effect in this study. These models are not only used to validate the results of experiment data, but also study the effect of parameters to fatigue crack under distortion-induced effect. The I-beam is fixed at both ends as a single beam with simply supported that allows rotation in plane. On out-of-plane side, the I-beam will be fixed at one end supporter to prevent the twisting. Two stiffeners are attached to girder and top flange by welding, and don't weld to bottom flange to allow a small web-gap as the pilot tests. With stiffeners, the I-beam will be divided in 3 parts, and we concentrate the center area where the mixed-mode I + III fatigue crack occurs. The top flange will be subjected to 2 points loading. The load applies on the stiffeners to make the twisting and bending effect. The general image of FEM model is shown in figure 5.11 as following:

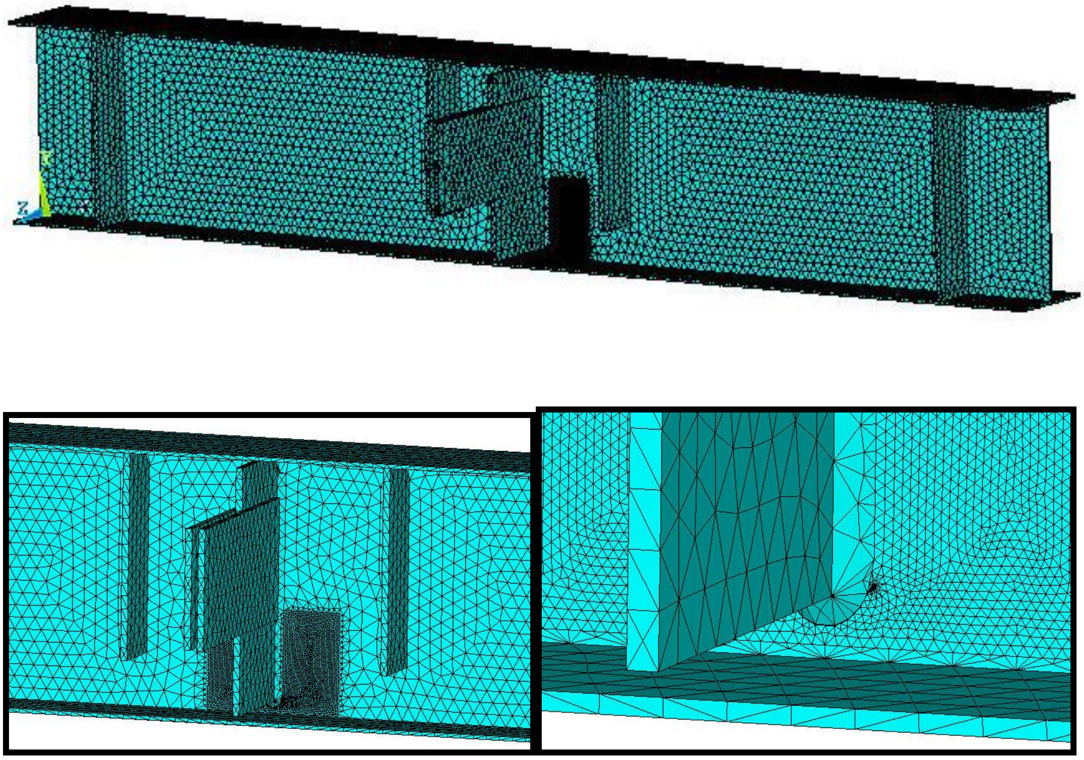

Figure 5.11 FEM model in ANSYS.

Figure 5.12 presents meshing of ring elements around the crack tip.

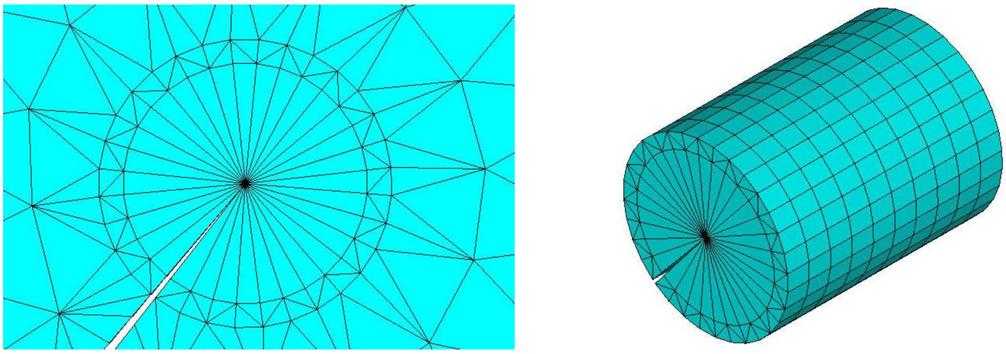

Figure 5.12 Meshing grids as ring elements around crack tip.

In these models, the fatigue distortion-induced crack will occur at the positive moment region of I-beam and propagate in to the web as horse toe shape as crack observed in the experiments. The length of I-beam, distance between two stiffeners, and the length of stiffeners will be changed in difference models to analyze the effect of in-plane moment to torsion to the crack propagation. Other parameters such as web-gap lengths, thickness of stiffener, and thickness of girder would be verified in each model to study the effect to fatigue crack growth. FEM models in this study use solid element and the effect of welding as well as deflection will be included in calculating. Therefore, the accuracy will be more reliable. However, the models are perfectly symmetrical but the testing beams are not quite symmetrical. These problems will influence to the results in validating. There are some assumptions using in these model base on observing behavior on experiments to simplify the calculation. After each step, a new meshing is generated and calculating repeat as the previous. By generating new meshing after each step of crack increases; this procedure could avoid the trouble in transfer from old to new mesh as previous researches.

In summary, the step to calculate in model can be performed as follow:

- Generate FE meshing.
- Obtain the stress field around the crack tip, and strain energy of elements in ring.
- Obtain strain energy of elements in ring as well as elements properties (volumes, coordinates) to identify the minimum values of strain energy and the element get the value.
- Calculate the new direction of crack for generating new crack tip.
- Generate new mesh with crack tip upgraded from computation.

The finite element models are combined with re-meshing technique and numerical formulation to calculate the strain energy density and stress intensity factors, as well as to detect the fatigue crack path. The results from FE models will be analyzed to find out the crack growth rate and predict fatigue life by strain energy density model.

The typical structure chosen for study is three series of I-beam testing in experimental program. These typical structures are implemented from AASHTO design code and applied in testing to confirm behavior in this study. Three series of model have the same I-beam section. The difference geometries are the web-gap length and span length.

In addition to analyze the effect of parameters to fatigue crack path as well as fatigue life, six other series of I-beam are concerned. The studied parameters include the effect of different web-gap lengths, in-plane moment to torsion ratio, thickness of web-gap to thickness of stiffener ratio, and stiffness of web-gap to stiffness of bottom flange. In order to express the difference of above parameters, different value for each model will be varied that include the span length, aim length of stiffener and web-gaps length. The difference of various parameters for each model can be described in table 5.1 as following:

Table 5.1: Cases study in detail.

Model	*Span Length (cm)*	*Aim of stiffener (cm)*	*Web thickness (cm)*	*Web gap length (cm)*	*Stiffener thickness (cm)*	*Height of Stiffener (cm)*	*Flange width (cm)*	*Flange thickness (cm)*
1	100	20	0.25	4	0.5	15.4	10	0.3
2	100	20	0.25	2.5	0.5	16.9	10	0.3
3	100	20	0.25	1	0.5	18.4	10	0.3
4	140	20	0.25	1	0.5	18.4	10	0.3
5	60	20	0.25	1	0.5	18.4	10	0.3
6	60	20	0.25	4	0.5	15.4	10	0.3
7	140	20	0.2	1	0.5	18.4	10	0.3
8	140	20	0.3	1	0.5	18.4	10	0.3
9	140	20	0.25	1	0.35	18.4	10	0.3
10	140	20	0.25	1	0.2	18.4	10	0.3

In table 5.1, models number 1, 2 and 6 use to validate with the results in experiments data.

The reason for these applied cases in research is that the positive deflection between beams under applied loads could create distortion-induced fatigue effect as the actual structure, especially in adjacent beams in steel bridges. The fatigue crack would occur at the web-gap and propagate in positive moment region to the neutral axis. Therefore, the study on distortion-induced moment will be more accuracy and familiar to the problem occurring at web-gap in actual steel bridges.

5.9 FEM results

5.9.1 Torsion distribution along span length

To check the torsion affect along span length, a simple frame were modeled with the same of condition in 3D models.

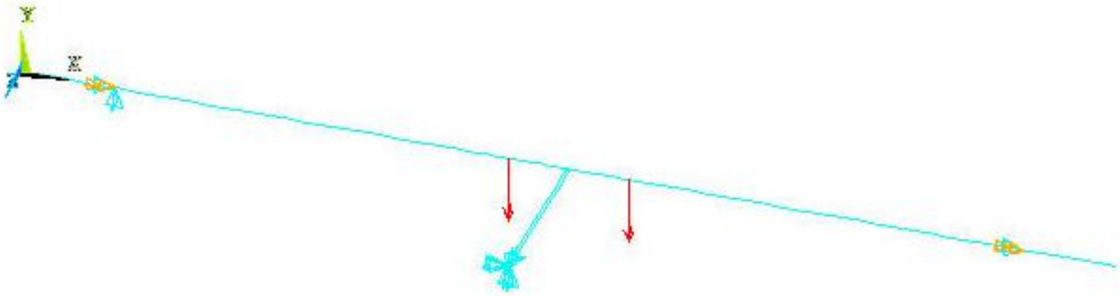

Figure 5.13 Modeling of simple frame

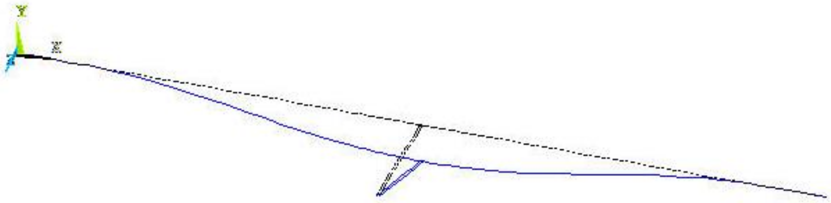

Figure 5.14 Deformation of frame under applied loads

Figure 5.13 shows the applied loads and constraint on simple frame. This frame used to check the distribution of torsion on beam under cyclic loads. The model is restrained as simple frame with pin supported at both ends and displacement controlling at end of stiffener.

- Both ends of frame: $U_x = 0$; $U_y = 0$; $Rot_x = 0$.
- End of stiffener: $U_x = 0$; $U_y = 0$; $U_z = 0$.

The section of beam and stiffener are presented as the actual values in experimental program for specimen series I. Load applied is the same position of experiment series II (Σload = 4 Tf) at two points. There are total 124 elements which are required for this frame modeling. As the result of 3D modeling, the frame is subjected by bending moment and torsion affect as shown in Figure 5.14. From the results of the simple frame, the torsion values are collected and presented in figure 5.15 as following.

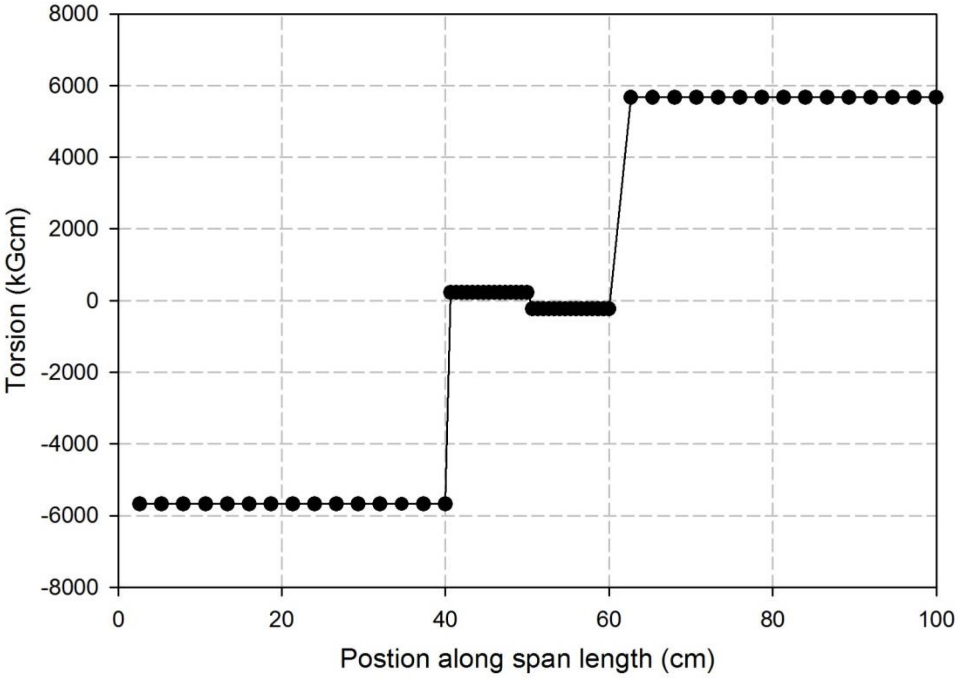

Figure 5.15 Torsion distributions along span length.

Because of restrained out-of-plane rotation at both ends of beam, the twisting gets maximum values at both ends of frame with equaling values. These values unchanged along the frame before dropping suddenly at stiffener whereas loads are applied. The two of stiffeners are used to distribute the concentrated load on top flange into girder as well as keep the web safety from buckling. The torsion value continuously changes once again at middle of beam due to stiffener at this position.

5.9.2 Different between force and displacement control in modeling

From the model 2 (without crack) which is presented for specimens series II. The applied load of 4Tf is presented and results of Y-axis displacement at middle of beam equal 0.94mm. Displacements at load positions are about 0.9535 mm which is used as constraint in displacement controlling model. The other conditions are the same in both force and displacement controlling models. The comparison between two models is shown in table 1. As table 5.2, the different of U_y values are not quite significant for both two models. The maximum different is about 2% and could be neglected. Therefore, the force control could be applied in simulation as well as displacement control. Actually, in both force and displacement controls produce the same effect to the models as well as the specimens. The local different effect is occurred at edges of the top flanges which have a slight different value on stress field.

Other parts of specimens and models have the same mechanism of stress fields as well as strains, even at the web-gap.

Table 5.2: Comparing the different values of displacement between force and displacement control models.

	Force control		*Displacement control*	
	NODE	UY (cm)	NODE	UY (cm)
Nodes at middle of beam (bottom flange)	16243	-0.09574	11375	-0.09486
	16582	-0.09575	11498	-0.09452
	16602	-0.09574	12020	-0.09521
	16693	-0.09575	12135	-0.09408
	16713	-0.09574	12605	-0.09375
Nodes at applied loads	11375	-0.09456	14164	-0.09535
	11498	-0.0951	14184	-0.09535
	12020	-0.09565	14519	-0.09535
	12135	-0.09393	14539	-0.09535
	12605	-0.09376	16108	-0.09535
	14164	-0.09574	16128	-0.09535
	14184	-0.09575	16223	-0.09535
	14519	-0.09574	16243	-0.09535
	14539	-0.09575	16582	-0.09535
	16108	-0.09575	16602	-0.09535
	16128	-0.09574	16693	-0.09535
	16223	-0.09575	16713	-0.09535

Figure 5.16 presents the comparing of stress σ_Y and τ_{YZ} along web-gap length. As discussion in section 5.9.3, these stresses keep the main rule in combination of mode I and mode III. The difference of stress fields around web-gap between force and displacement controlling methods are so small to concern in calculation. So the local stress distribution at location near the stiffener ends should be insensitive to top flange restraint.

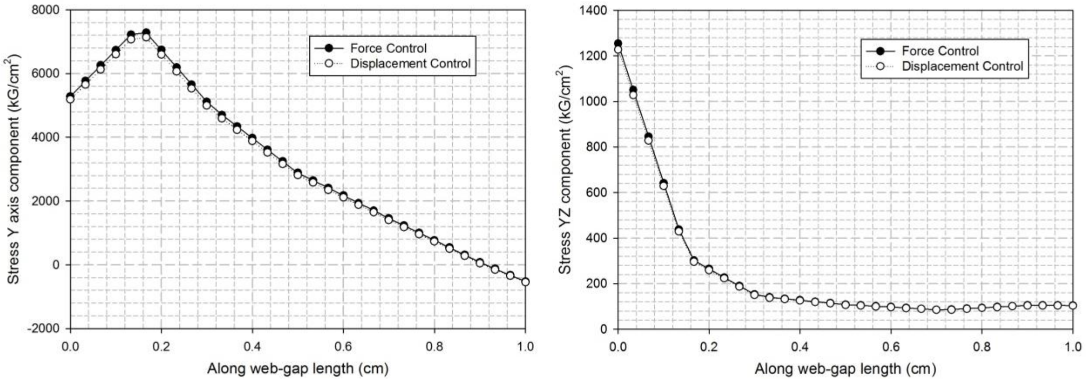

Figure 5.16 Stress σ_Y and τ_{YZ} components along the web-gap length

5.9.3 Principal stress distribution around web-gap

The Mode I is assumed to control the fatigue crack path, and mode III is assumed to contribute to fatigue crack growth rate. The principal stress fields are investigated on modeling at three conditions:

- The modeling without crack occurring (shown in Figure 5.17).
- The modeling with initial crack (shown in Figure 5.18).
- The modeling with “the end” of crack propagation (shown in Figure 5.19).

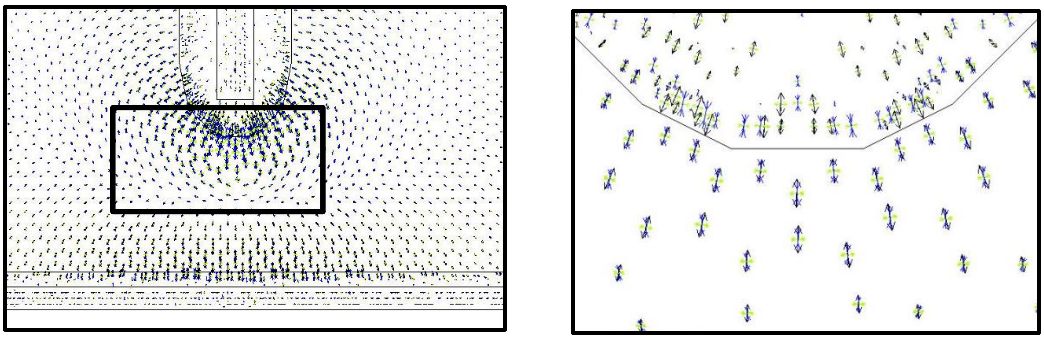

Figure 5.17 Principal stress around weld toe without crack.

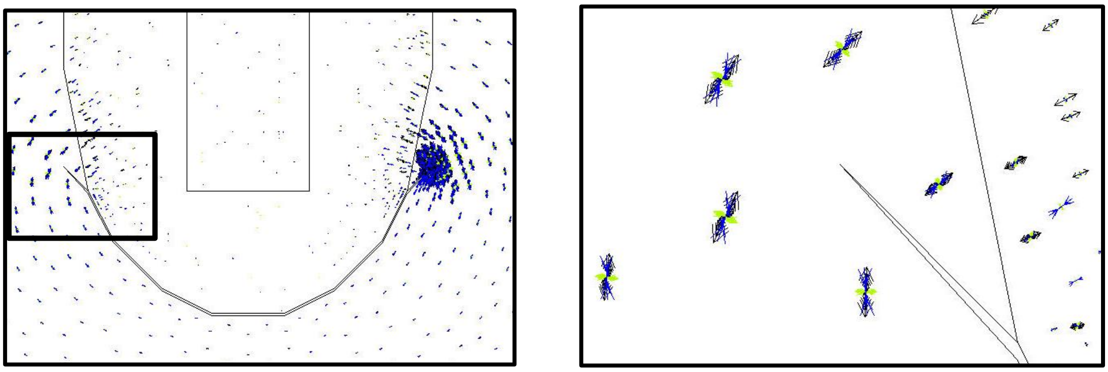

Figure 5.18 Principal stress around crack tip at initial crack stage.

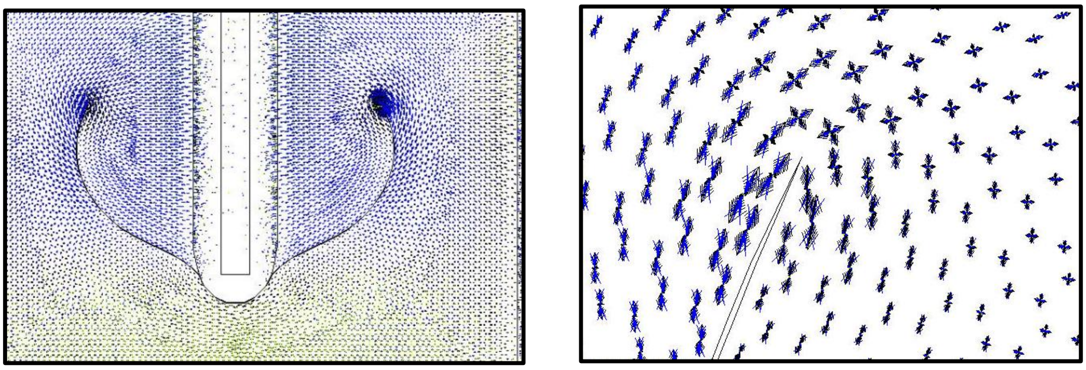

Figure 5.19 Principal stress around crack tip at "the end" of crack propagation.

As shown in Figure 5.17, 5.18and 5.19, the principal vectors perpendicular to the weld toe (model without crack) and crack tip direction. This evident could prove the assumption that the mode I (opening mode) controls the crack direction in all of stage of crack propagation. The stress field around weld toe as well as around crack tips also presents only values of τ_{yz} and σ_y which is subjected by mode III and mode I. Other types of stress also occur with small values which could be neglected (less than 4%). These phenomena are observed on stress field from all of stages of crack propagation. From the investigations of principal stress and stress field, it's concluded that the Mode I control the crack path direction and fatigue crack growth, while Mode III only contribute the fatigue crack growth rate.

As the stress fields of elements around the web-gap from modeling results, the τ_{yz} has much larger value in comparing with τ_{xy} and τ_{zx}. As the present in Chapter III, the mode III effect is presented by exist of τ_{yz}. So the Mode III would contribute to the fatigue growth rate. Samples of stress around web-gap were presented in Appendix E.

5.9.4 SED values along web's thickness

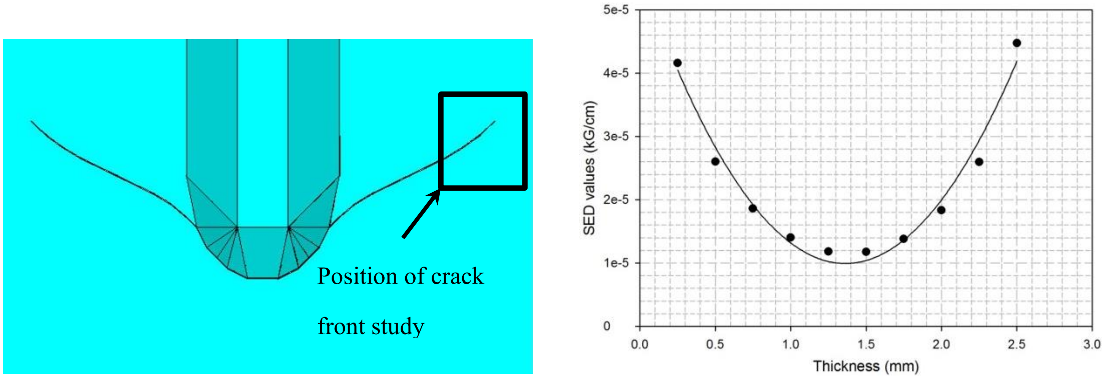

Figure 5.20 SED values along web's thickness.

Figure 5.20 shows the image of SED values along web's thickness in FEM models. The crack tip which is concerned in this investigation deals with the step 10th of model 2 as shown figure 5.20. Obviously, this step is belonging to stage 2 of crack propagation that the crack grows stability father from web-toe. The angle for collecting SED values is the direction that yields the minimum average SED value throughout the thickness of web. As the modeling results, the SED values distribute as parabola as deep of web's thickness. It's proved that the minimum value occurs at middle of web and creates critical condition at this point. This figure of distribution of SED value along the web's thickness could be observed at all the steps of crack propagation in stage 2. In experimental results, the crack front forms as parallel curves with a slight different position of two crack tips at tension and compression faces. This section provides the different observation between the experimental and FEM results in detail of crack front. In global view, the minimum average SED values is required to follow crack propagation which grows in plane with out of plane effect. Therefore, the different view in detail of crack front could be ignored if the angle of minimum average SED values in ring element is the same for both experiment and modeling at each step of crack propagation.

5.9.5 Web-gap fatigue stress

The results of 10 FEM models were analyzed. As expected, significant concentrated stresses were recorded around web toe. The concentration of stress in Y-axis component at the web-gap zone could explain the position and direction of initial crack. Figure 5.21 shows the web gap deformation and stress contour as Von Mises criterion.

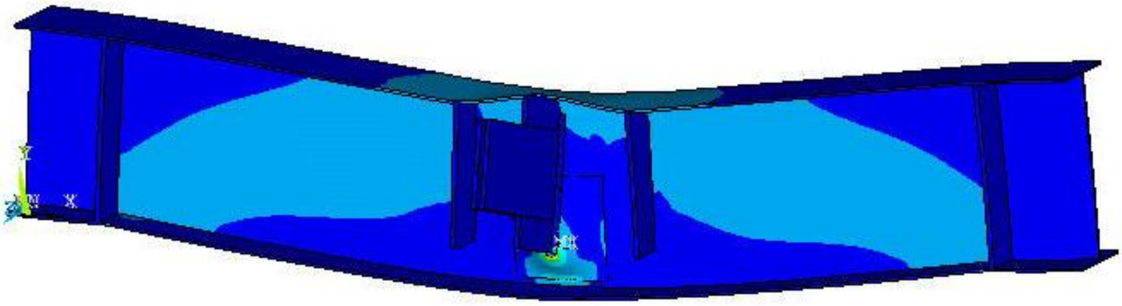

A. FEM model deformation.

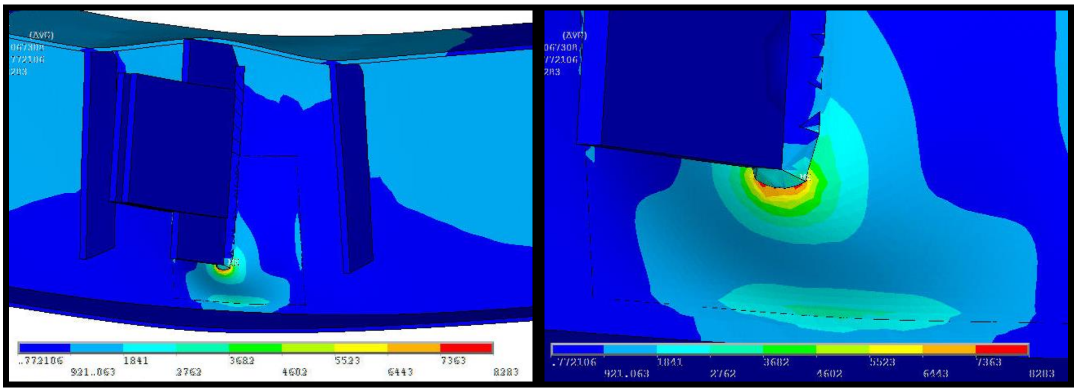

B. Web-gap deformation

Figure 5.21 Stress concentrates at the web-gap

In Figure 5.21, the stress contour forms as shape of weld-toe and decreases its values further from the welding. The director of principle stress at this position is similar to Y direction and could be explained for the crack beginning. In fact, the crack begins at the weld-toe or close to weld toe and propagates out as X-axis. Distortion-induced fatigue effect is the reason for crack occurring but the crack is formed as direction of opening mode.

Figure 5.22 and 5.23 present the range of Y-axis stress at the web gap in ten FEM models as following.

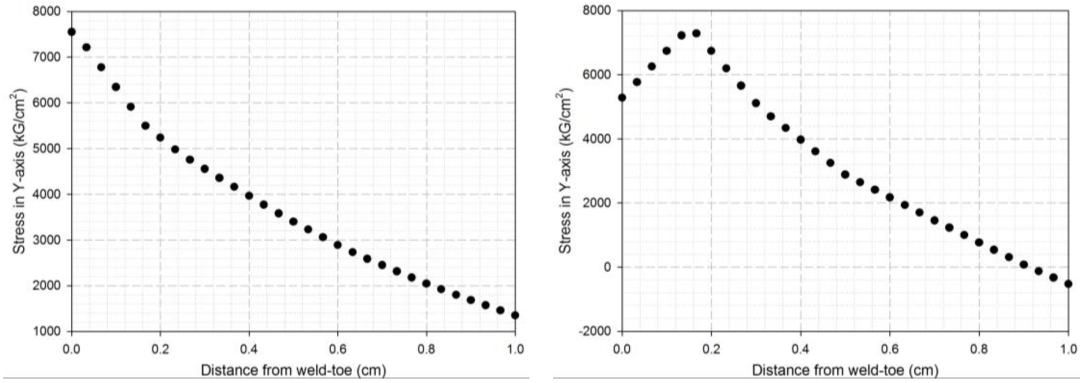

Model 1 Model 2

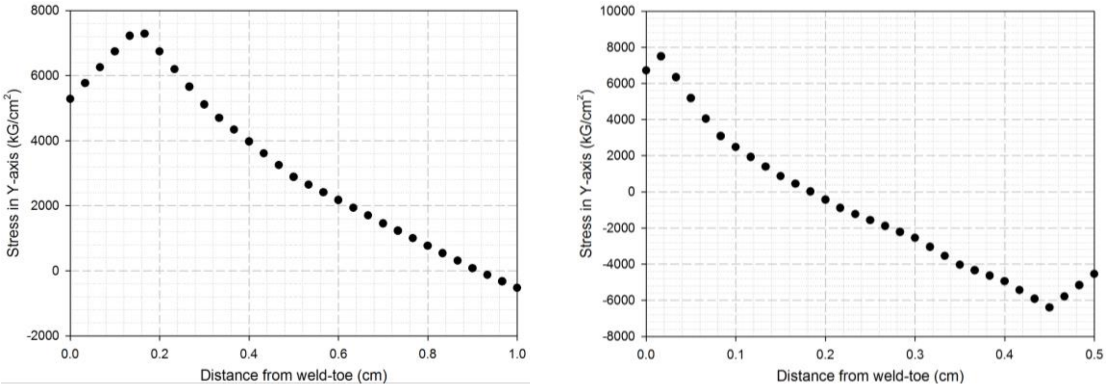

Model 3 Model 4

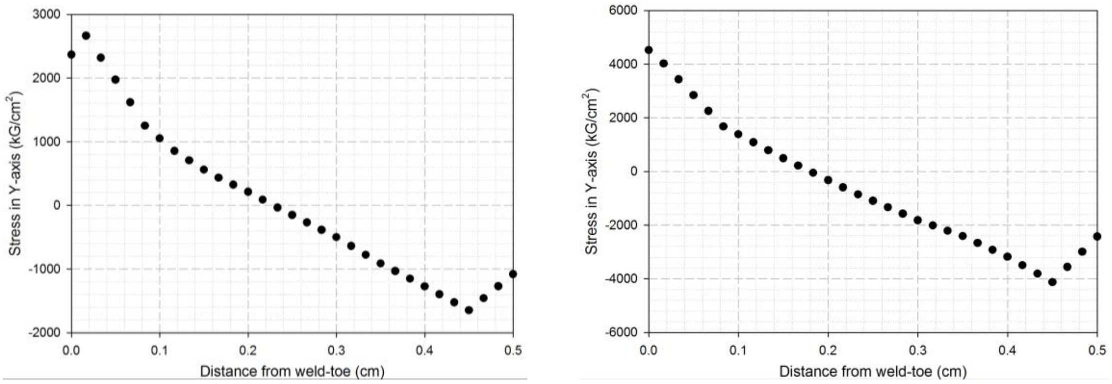

Model 5 Model 6

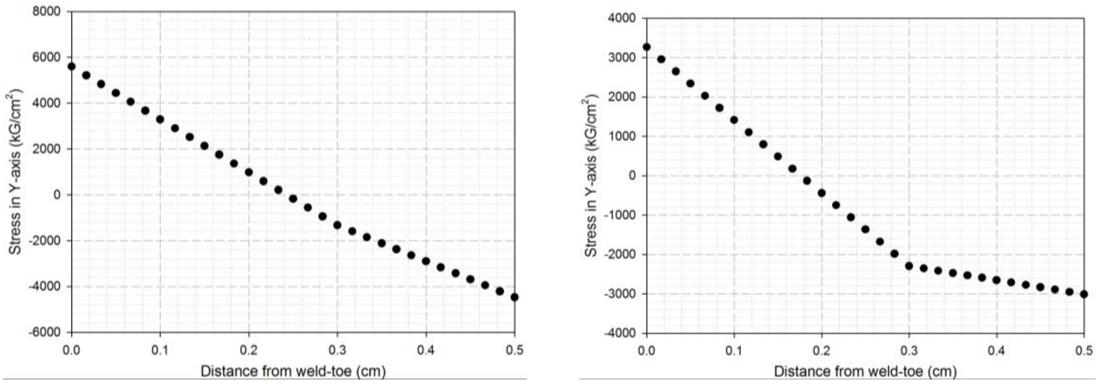

Model 7 Model 8

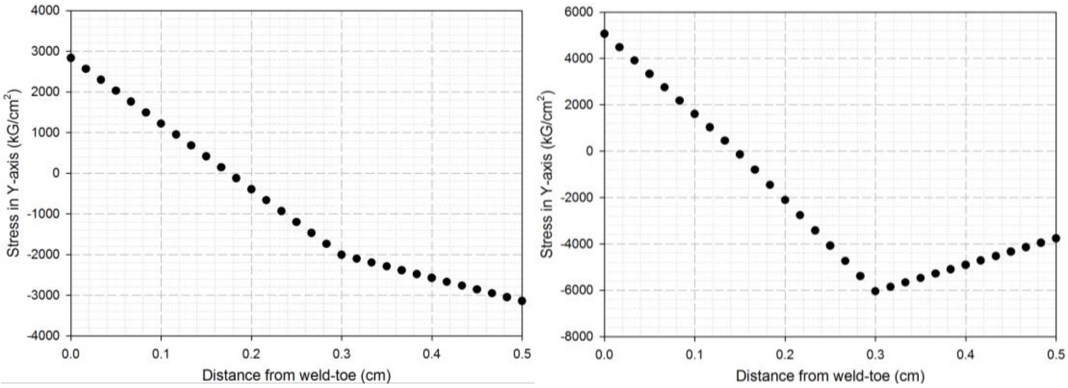

Model 9 Model 10

Figure 5.22 Difference of Stress component Y-axis from weld-toe at the web-gap.

In Figure 5.22, the stress changes its values in a large rank. Therefore, the web-gap gets critical concentrated stress and this position becomes critically to the I-beam. In model 1, the stress decreases continuously from about 7500 kG/cm^2 to 1400 kG/cm^2 in 1 cm length. But in model 2 and model 3, the highest stress does not occur at weld-toe, the critical stress appears at position 0.16 cm close to weld-toe. It's an evident that a curvature occurs close to the weld-toe and curves a part of girder along the web-gap length. Observing the figure on stress at web-gap of model 2, model 3, model 4 and model 5; it's not difficult to recognize the figures of stress values change direction two times. The first time of change occurs at position close to web-toe, and the other is close to bottom flange. In models 4, 5, 6, 7, 8, 9 as well as model 10, figures present the values of stress in length of 0.5 cm, cause wep-gap length of 0.5 cm on these models. Models 4, 7 and 8 have the same geometries with different web-thickness values. Therefore, the gradient stress from weld-toe changes in different type. From figures of models with short web-gap, the models present double curves of web-gap under distortion-induced effect.

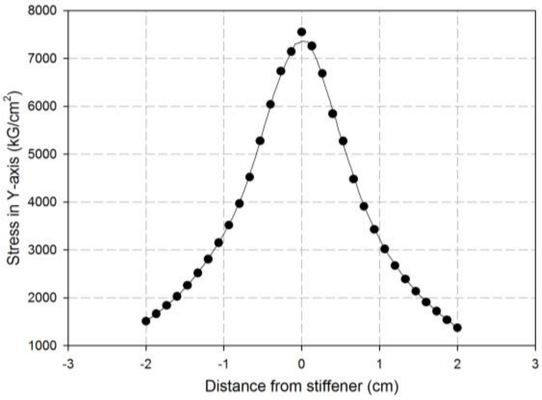

Model 1

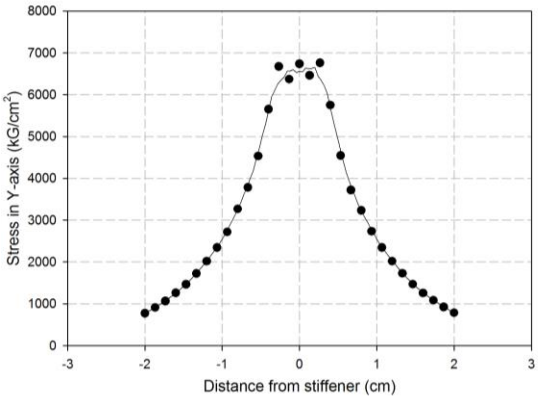

Model 2

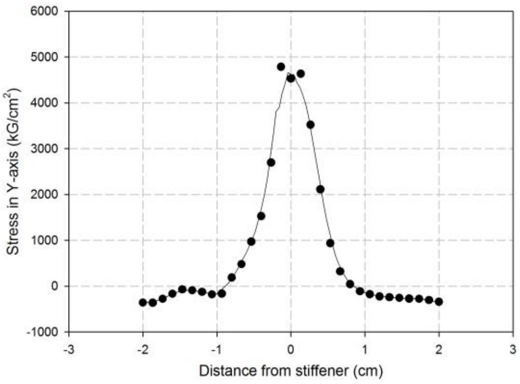

Model 3

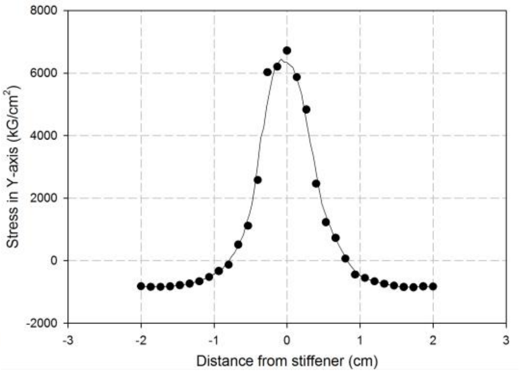

Model 4

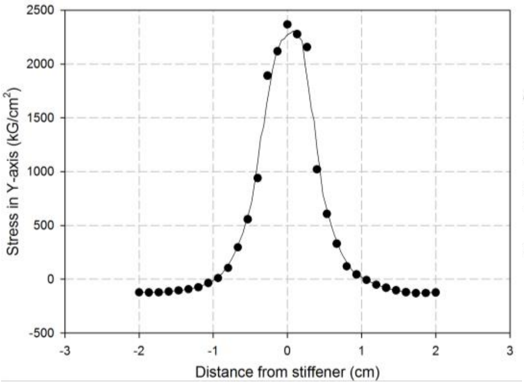

Model 5

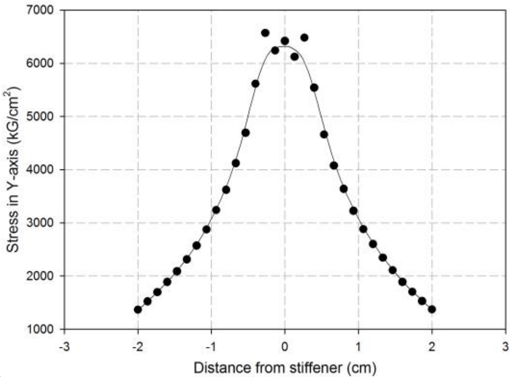

Model 6

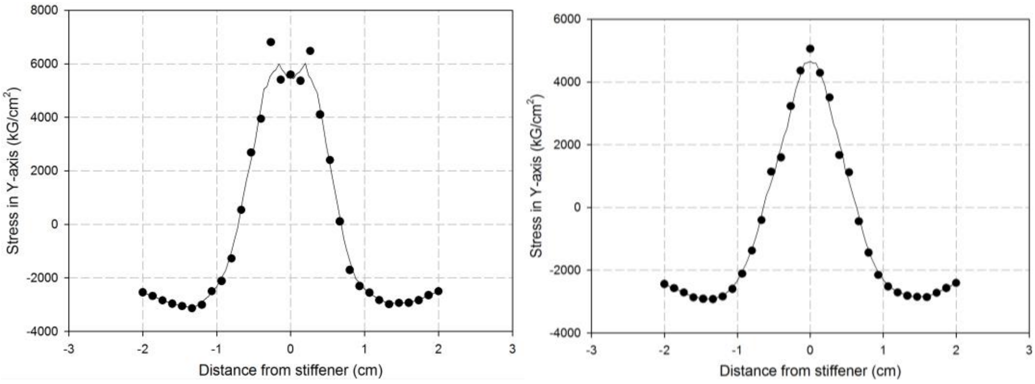

Model 7 Model 8

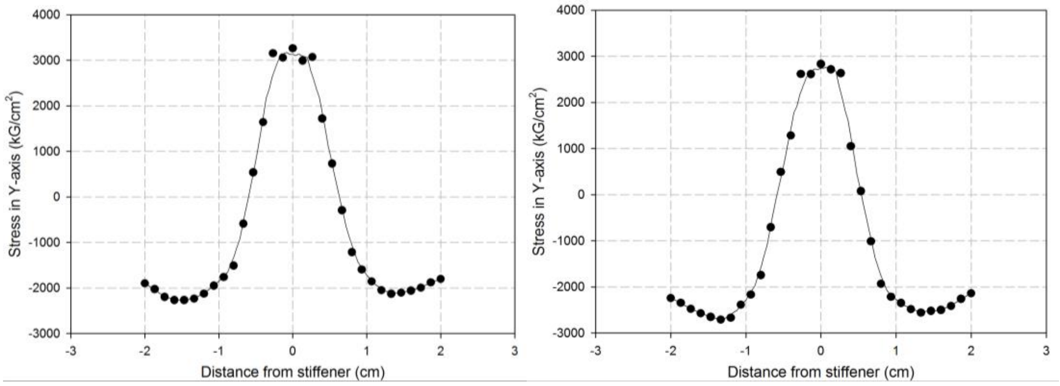

Model 9 Model 10

Figure 5.23 Gradient of stress on the line at end of weld-toe.

As in figure 5.23, the stresses also concentrate at weld-toe and decrease their values quickly further from web-gap. At end of weld-toe, the values of stress depend on the shape of welding. If the shape of welding is smooth and the welding has only one wedge, the stress will have only one highest point at place right under middle of stiffener. In other cases, if the shape of welding gets two sharp points, it will create two critical stresses close to those points. However, these sharp points also play important role to create critical position for the second crack occurring as observation in experiments.

The models 3, 4, 5, 7, 8, 9 and 10 have web-gap lengths of one cm and have stress value decreasing more quickly from end of web-toe than the left models. It’s concluded that the slope of gradient stress depends on the web-gap lengths. With the unchanged other geometries, if the web-gap length is small, the critical zone will be small.

5.9.6 Crack propagation

The purpose of computing FEM model is to predict the crack path under distortion-induced fatigue effect. Applying the SED criterion and meshing technique including ring elements implements, the crack propagations for each model are predicted in this study. Figure 5.24 shows the image of I-beam model with crack propagation.

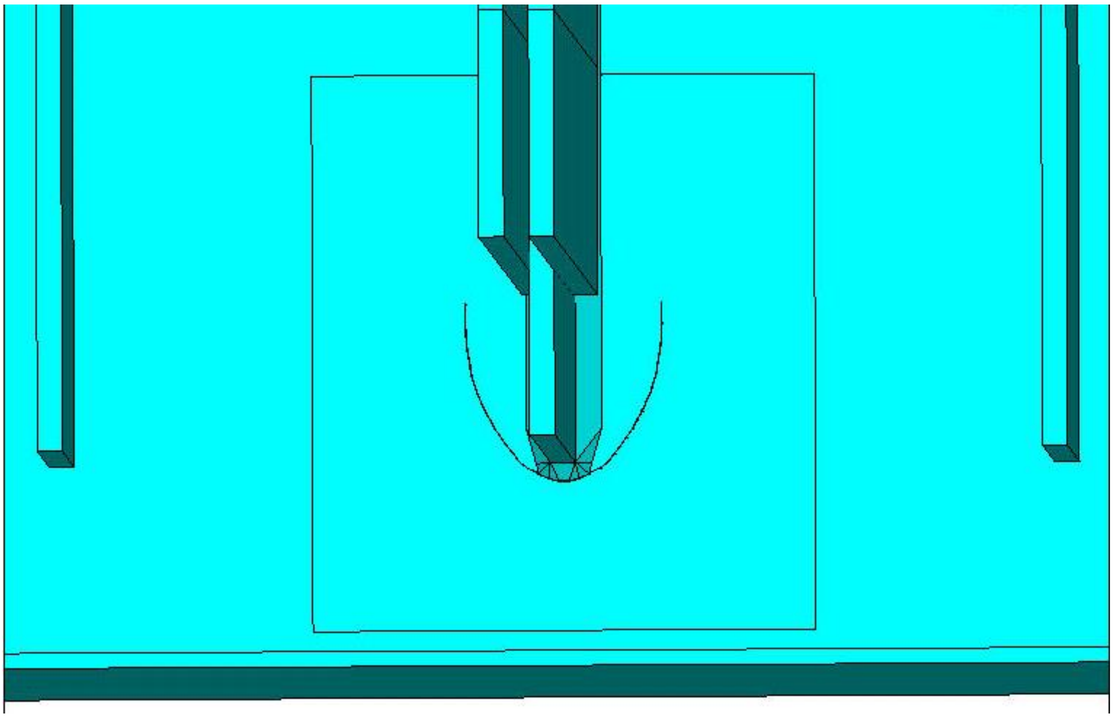

Figure 5.24 Image of predicted crack path in FEM model.

The step size for each model is identified as section 5.6.3 (Step size). The procedure is repeated after each step and continuously. For each model, there are about 20 steps which were generated. And results on crack paths are represented as shown in figure 5.25.

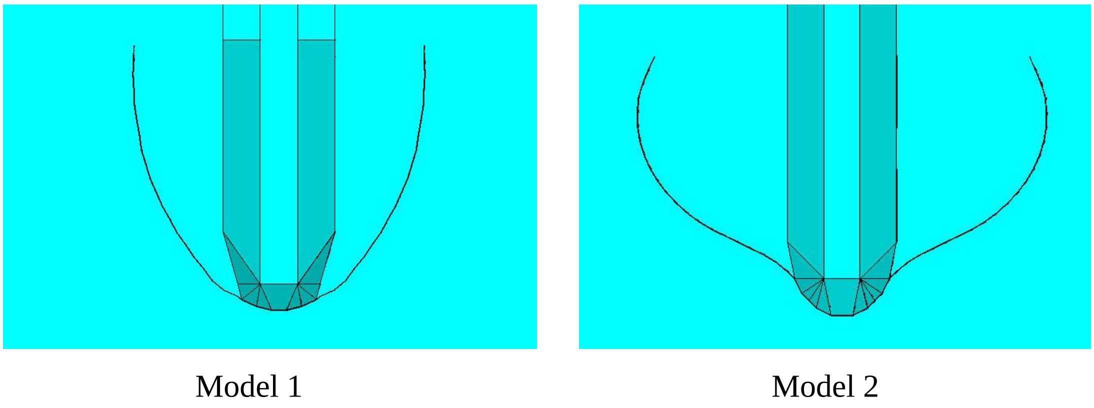

Model 1

Model 2

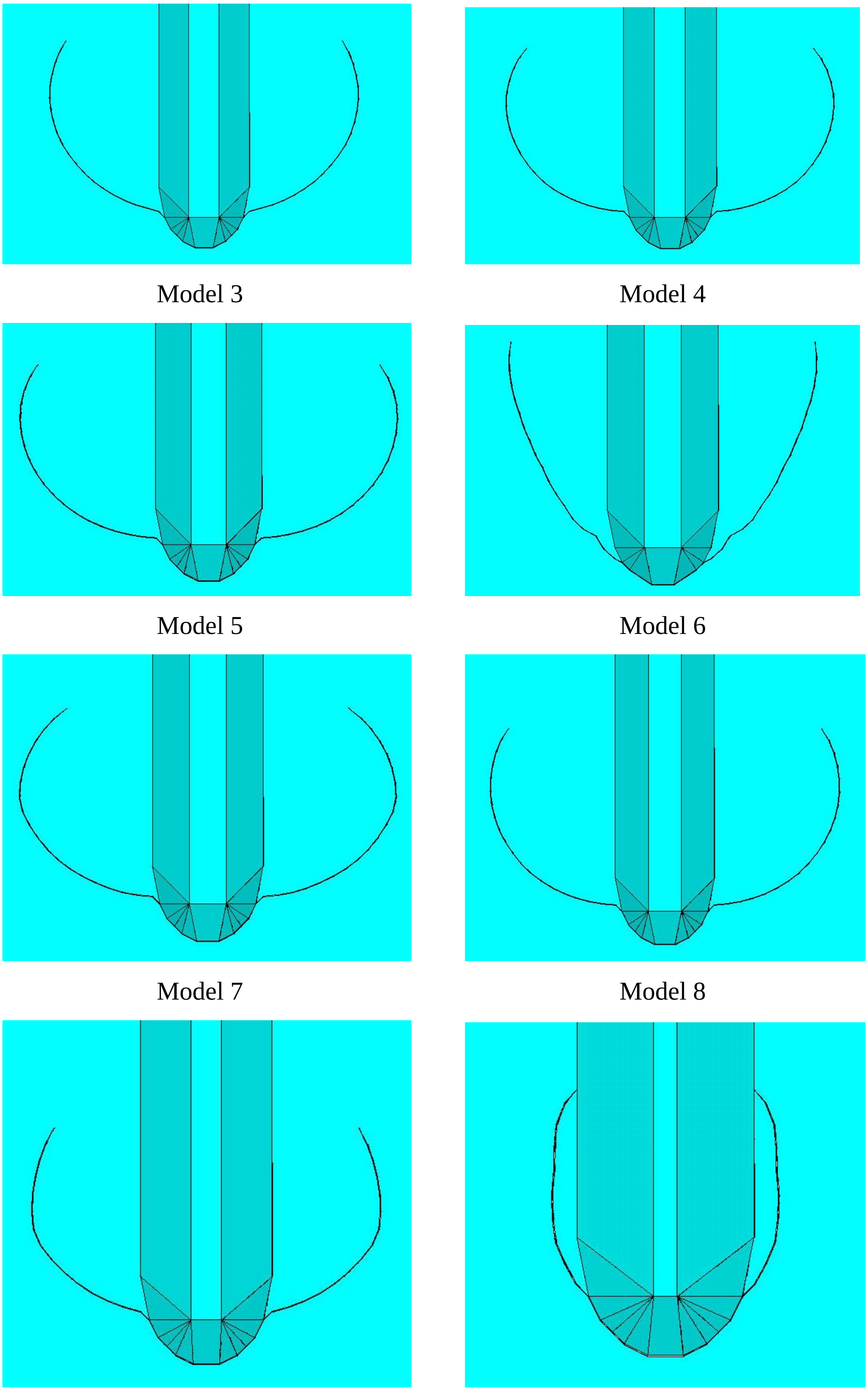

Model 3

Model 4

Model 5

Model 6

Model 7

Model 8

Model 9

Model 10

Figure 5.25 Crack paths obtained from FEM models.

Despite of the same angle and the first length of initial crack, the crack propagation of each model runs out with different paths. Therefore, the crack grows independently for each model and does not depend on the initial crack. The crack path only depends on stress field around crack tip. The shape of weld influences to the local stress field. Therefore, weld also influences to crack path at position close to welding. It will also affect to the accuracy in validating experiment and FEM results.

Table 5.3: Stress at web-gap to stress at bottom flange ratio

	Stress at web-gap (kG/cm^2)	*Stress at bottom flange (kG/cm^2)*	*Stress at web-gap to Stress at bottom flange ratio*
Model 1	7550	1220	6.2
Model 2	7283	784	9.3
Model 3	4525	565	8.0
Model 4	2663	269	9.9
Model 5	7497	698	10.7
Model 6	6934	1511	4.6
Model 7	5594	836	6.7
Model 8	3263	980	3.3
Model 9	5057	992	5.1
Model 10	2833	1102	2.6

Table 5.3 presents the values of stress at web-gap and stress at bottom flange from FEM results. Because this research concentrate on linear elastic fracture mechanics, the stress at web-gap is the maximum critical concentrated stress and in many case its value is larger than yield point. Model 10 have the lowest stress at web-gap to bottom flange ratio, and its slope of crack path is the most strictly. In model 5, with the highest of ratio, the crack propagates far from welding before goes up vertically. Comparing slopes of all models which deal with the effect of ratio, it’s could be recognized that the shape of crack path depends on this ratio. Therefore, we can control the shape of crack path under distortion-induced fatigue effect by applying compatible ratio of stress at web-gap and bottom flange.

5.9.7 Fatigue crack growth rate.

The data from FEM model includes Strain energy density of each element. With the procedure of applying ring element technique described in Chapter V, the direction of crack and the minimum SED value could be identified for each step. Using the implement formula of SED described in Chapter V to find the fatigue life, the process of fatigue crack growth rate could be investigated. These results are necessary for validating theory and experiments to identify the behavior distortion-induced fatigue crack as well as parameters study in next Chapters.

The fatigue crack growth rate is presented in figure 5.26 for each model.

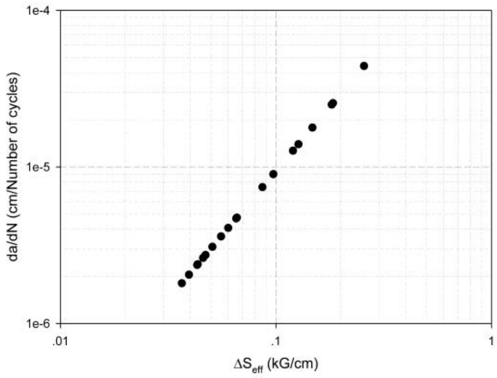

Model 1

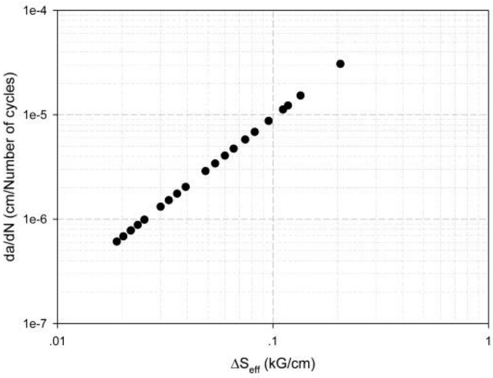

Model 2

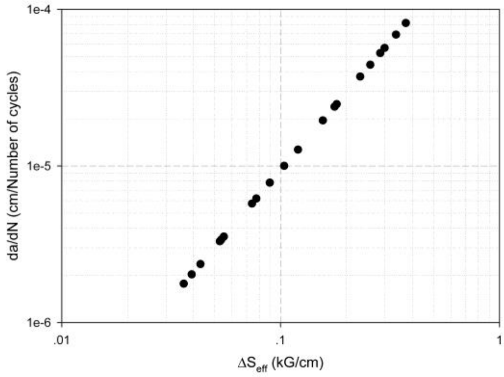

Model 3

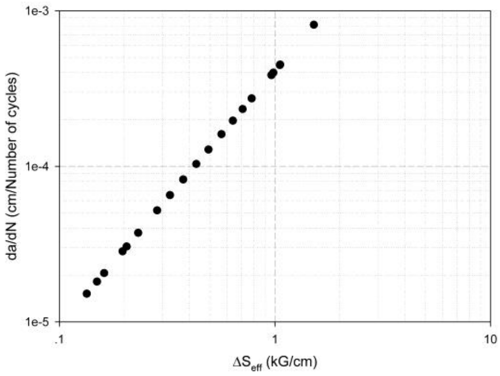

Model 4

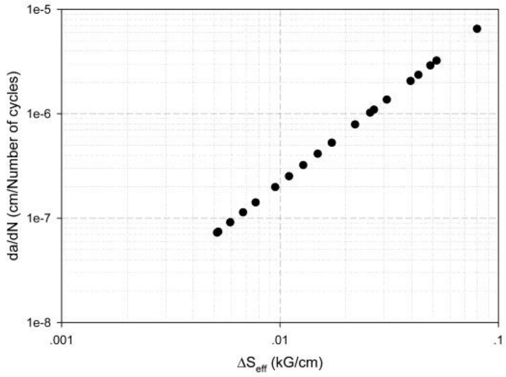

Model 5

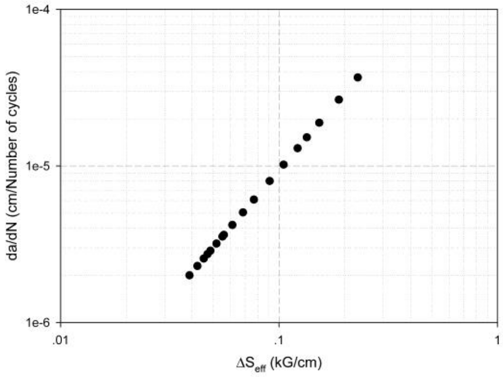

Model 6

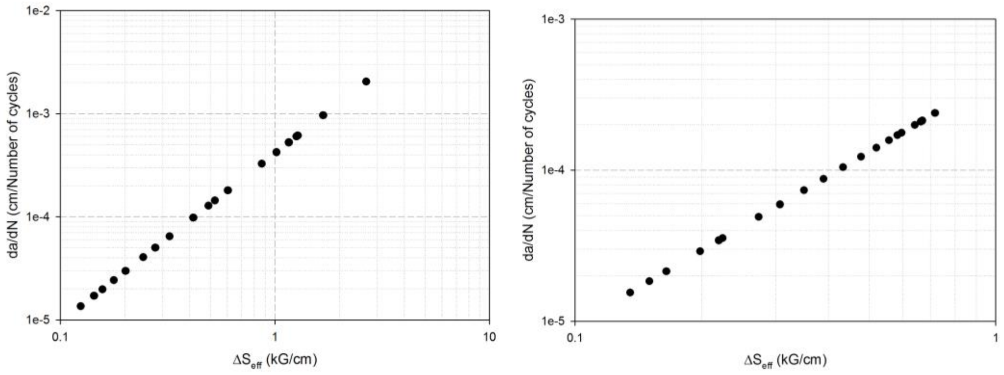

Model 7 Model 8

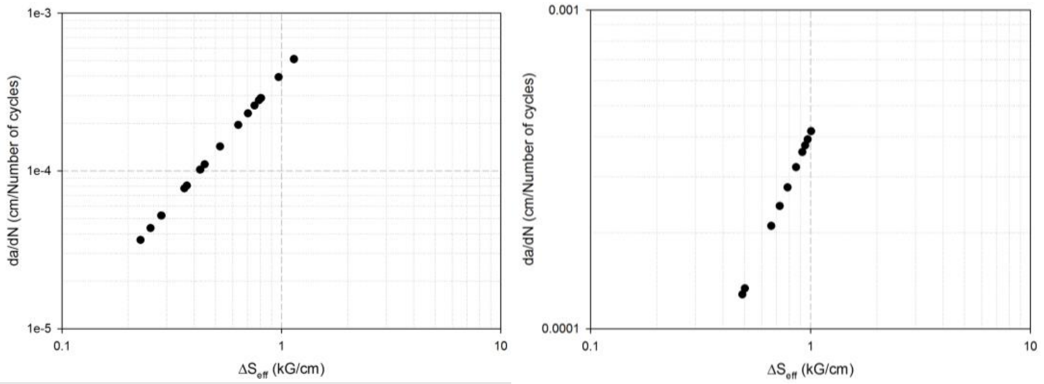

Model 9 Model 10

Figure 5.26 Fatigue crack growth rates from FEM results in log-log scale.

From Figure 5.26, model 5 presents the lowest values of fatigue crack growth rates. The load, which is applied in this model, is only 4000 kGf. Model 5 also has highest in-plane stiffness. Model 4 and 7 is in opposite side with lowest stiffness and the same load applied as model 5 (4000 kGf). Model 7 is worse in resisting distortion-induced effect than model 4 because of its smaller value of web-thickness. The fatigue crack growth rates show the linear relationships of *da/dN* and ΔS_{eff} in log-log scale as Paris law. It is evident that the distortion-induced fatigue crack at web-gap of I-beam propagates in form of stable crack (region II of Paris law). The crack begins with highest fatigue strain energy density and the SED value decreases as crack grows out forward to lowest energy zone. If there is not new branching crack, the fatigue crack will propagate slowly with lower energy up to neutral axis. Figure 5.27 assembles the entire fatigue crack growth to identify the image of distortion-induced fatigue crack.

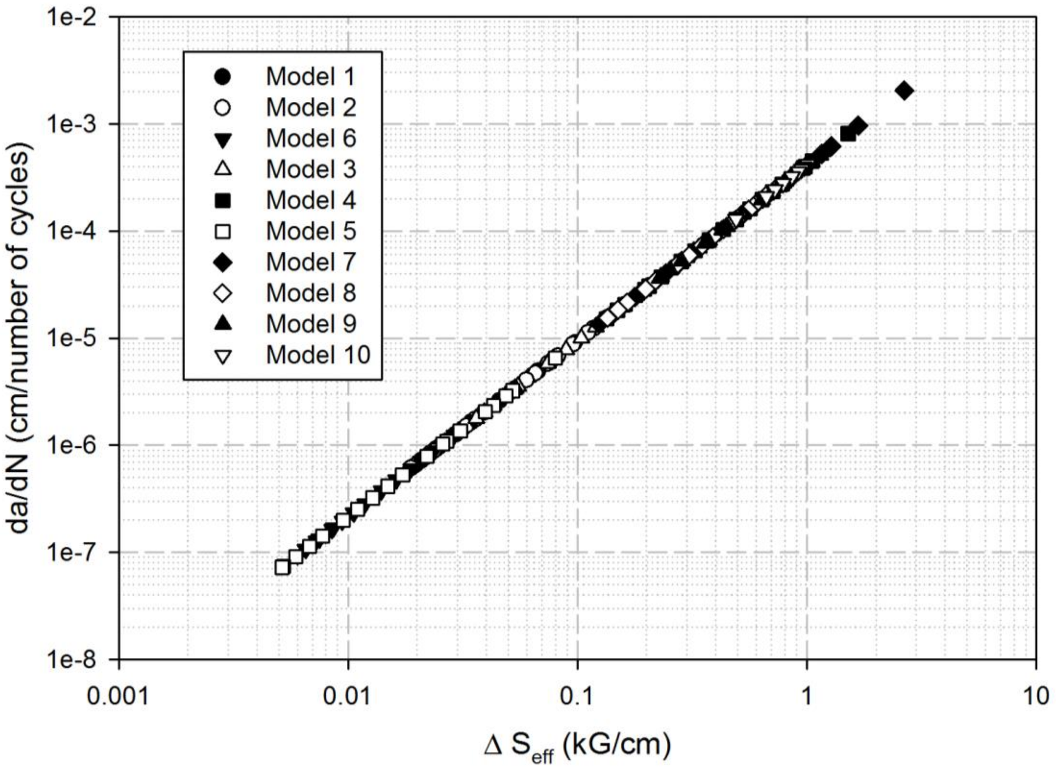

Figure 5.27 Fatigue crack growth rates of all models in log-log scale.

Figure 5.27 presents fatigue crack growth rate of all models in the same applied load, and a comparison is useful to identify which one is best structure in resistance to the distortion-induced. The load which is chosen for this comparison is 4000 kGf and ratio stress equals to 0.2. Figures on models 4 and 7 show the lowest fatigue lifes. Model 4 has short web-gap length equaling to 1 cm which is the longest span length (140 cm). These disadvantage factors create lowest in-plane stiffness and highest concentrated stress at the web-gap. Model 9 and model 10 seem to be better comparing with models 4 and 7 in fatigue crack growth rate. Actually, the stiffener thickness values in model 9 and 10 are smaller than they were in model 4. Therefore distortion-induced fatigue effective zone around web-gap is quite small. As shown in 5.27, stage for crack growing under mode I and mode III combination is shortest, and crack would be quickly influenced by mode I only. In opposite side, model 5 and model 6 have the lowest strain energy density value around web-gap and create longest fatigue life. With the same span length, model 5 has shorter web-gap length than model 6. It could be concluded that the span length controls the fatigue crack better than the web-gap length, and model with short web-gap length will resist more effectually to distortion-induced fatigue effect.

All of models 1, 2 and 3 have the same geometries except values of web-gap length. Model 3 with shortest web-gap length presents worst capability in resisting distortion-induced effect. Although models 1 and 2 also have different values of web-gap length, the fatigue crack growth rates are nearly similar. The web-gap length is effective in resistance to out-of-plane load. But if the web-gap is long enough, the fatigue life will not be quite different.

5.10 Conclusions

FEM simulations investigate the distortion-induced fatigue cracks in stage of stable crack propagation which occupies 70% fatigue life as observation in experiments. FEM does not included investigating stage of initial crack as well as critical crack in this study. As experimental research, the shape of initial crack depends on the shape of web-toe. The critical crack depends on the form of second crack as conclusion from testing program and will be investigated in next researches.

FEM models include some assumptions to simplify the computation: crack tip perpendiculars to compression and tension faces, the crack propagates as symmetrical shape in both sides of stiffener, and the initial crack will be set up as the same properties for all FEM models. These assumptions will lead to slight different results comparing to with experimental data. In this study, these approximates are accepted because it’s quite difficult to control testing program in perfect conditions.

Strain energy density is applied to predict the crack propagation in plane with out-of-plane effect. Implement of SED in Paris law is also applied to predict the fatigue crack growth. The most advantage of applied SED factor in this research is the simple element which is required to practice fracture mechanics. SED criterion wouldn’t require singularity or special element in prediction as other criteria. The solid 45 element (ANSYS program) is enough for prediction both crack path and crack growth rate.

CHAPTER VI

VALIDATION RESULTS

6.1 General

In this study, behavior of distortion-induced fatigue crack at the web-gap of I-beams in steel bridge which assumed to be the combination of Mode I and Mode III from fracture mechanics concepts. To confirm these, experimental programs and FEM simulation were performed to observe the fatigue crack and its mechanism in Chapter IV and Chapter V. In this Chapter, the results from the experimental programs and FEM analysis are compared to verify the assumptions on behavior of distortion-induced fatigue crack.

In experimental program, nine I-beams were tested. The results obtained from testing include: the stress field around the web-gap recorded from strain-gages system; fatigue crack paths and fatigue crack growth rates. Although two specimens didn’t supply all of three above data due to the difficulty in experiments, the obtained results are enough for validations.

In FEM modeling, three models were constructed to confirm three series of specimen in testing. Before validating results from testing and FEM, data from FEM models would be calculated to simulate the same results from the experiments. Because FEM models only yield the stress fields and strain energy density values per elements, it’s difficult to expect the same results between FEM and experiments. Many problems occurring during testing would influence the error of values. For example, the shape of welding for all specimens in the same series as well as in the FEM model is difficult to control, and it will influence the local stress field leading to difference in crack path.

Validation program includes three sections: validation of stress fields, validation of fatigue crack paths, and validation of fatigue crack growth.

6.2 Validation of stress fields

Stress field around the web-gap in experiments is recorded from 9 strain-gages and LVDT. They supply the values of stress which concentrates at weld-toe by strain-gage number 1 to 7 in both front and back faces of specimens. The stresses at top and bottom flanges are also recorded by strain-gages number 8 and 9; and play the important role to classify the category of failure as ASSHTO code. The deflection at the middle of span which represents the relative deflection is recorded from LVDT.

From FEM models, nine positions of stress and deflection are recorded and compared with the experimental results in testing as shown in figure 6.1.

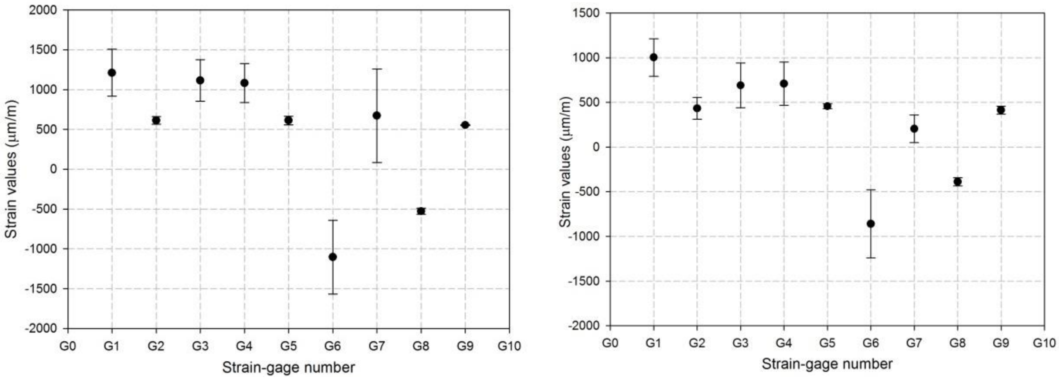

Model 1 – Specimen Series 1

Model 2 – Specimen Series 2

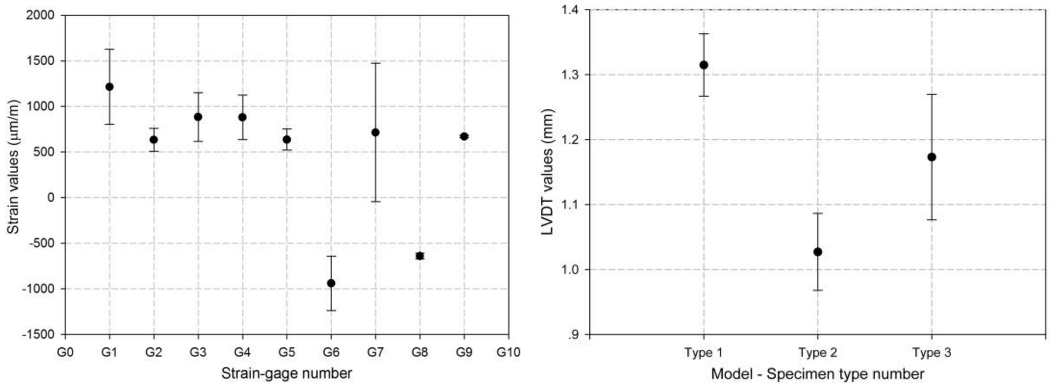

Model 6 – Specimen Series 3

LVDT validation

Figure 6.1 Validation of stress field and LVDT values between FEM and experiments.

Strain-gages number 1, 6 and 7 present the stresses in Y-axis component in the line of middle specimen for both front and back faces. The maximum difference between the values from experiments and FEM model of G1 are about 33%. Under loading, the web-gap is in double curves at two positions, one is close to weld-toe and the other is close to bottom flange. In FEM, the stress range in 1 cm length which is the same length of strain-gage changes large in value as shown in 5.14 in Chapter V. The values in FEM are over the yield point stress, and the plastic zones could be created in testing specimens. In reality, the stress would be limited at the yield point, and the entire plastic zone has the same stress value as the yield point. The values of stress from FEM are the average value of stress in 1cm length and they get lower quantities comparing to the ones from experiments. With values of strain-gage 6, the problem is more complex. Strain-gage 6 locates right at the end of stiffener on the back face. The stress on this location is controlled by the welding quality, the curvature of the web-gap and the edge of stiffener with high concentrated stress. Strain-gage 7 is close to the welds connecting web and bottom flange and covers the second small curve of web-gap. The stress in this position is complicated and varied in a wide range of values. Besides that, the strain-gage is about 1cm in length and records a large change of the stress values. Therefore the difference in comparison in both strain-gage number 6 and 7 is quite large. However, the data from FEM and experiments show the same positive or negative values which present the surfaces in tension or compression at these strain-gages (6 and 7).

Strain-gages number 2, 3, 4, 5 are located in the line of end of stiffener on front side of web and close to weld-toe. The stresses at these positions are influenced by the welds connecting end of stiffener to the web, especially shape of welding. The shape of weld creates local concentrated stress. Therefore, the values of strain-gages 3 and 4 are quite difference when compared with the values from FEM models (the maximum is 48% difference). Strain-gages 2 and 5 are located further from web-toe than number 3 and 4. Therefore, the effect of concentrated stress created by shape of welding is smaller. The errors in values when compared FEM with test are small in strain-gages 2 and 5 (the maximum value is about 19%).

Strain-gages number 8 and 9 are far from the welds, and are not influenced by local concentrated stress which is created by welding as well as the curve of web-gap. The values of these strain-gages in experiments are quite fixed with the same values in FEM models. The maximum error is not over 10%. The same amount of error would be found in validating LVDT values. Comparison implies that the FEM models give a good agreement with the global behavior of experimental results. The problems occur in local view and are quite difficult to control.

Table 6.1: Strain and LVDT values from Experiments and FEM models.

	G1 (μm/m)	G2 (μm/m)	G3 (μm/m)	G4 (μm/m)	G5 (μm/m)	G6 (μm/m)	G7 (μm/m)	G8 (μm/m)	G9 (μm/m)	LVDT (mm)
model 1	1552	655	1271	1318	658	-613	1294	-487	555	1.26
specimen S1-2	1039	621	1259	1095	625	-1171	127	-560	556	1.35
specimen S1-3	1044	559	814	833	552	-1529	596	-535	562	1.34
Model 2	1315	488	1059	1069	472	-620	384	-324	357	0.94
specimen S2-1	945	250	517	608	441	-629	117	-389	465	1.05
specimen S2-2	881	505	560	537	427	-766	112	-406	418	1.06

specimen S2-3	871	488	625	621	485	-1420	-	-433	411	1.06
Model 6	1809	603	1135	1144	600	-581	1251	-646	690	1.29
specimen S3.1	1174	656	798	709	675	-1239	178	-593	662	1.17
specimen S3-2	921	488	545	641	500	-1117	-	-670	674	1.17
specimen S3-3	955	788	1056	1027	772	-817	-	-648	658	1.06

6.3 Validation of crack path

The crack path is recorded from experiments and compared with the crack path which is predicted in FEM models. Before comparison, the images from crack paths of testing are re-scaled to be in the same direction with the ones from FEM models. Three crack paths from FEM simulations are used to compare with nine crack propagations in three series of specimens as shown in figure 6.2.

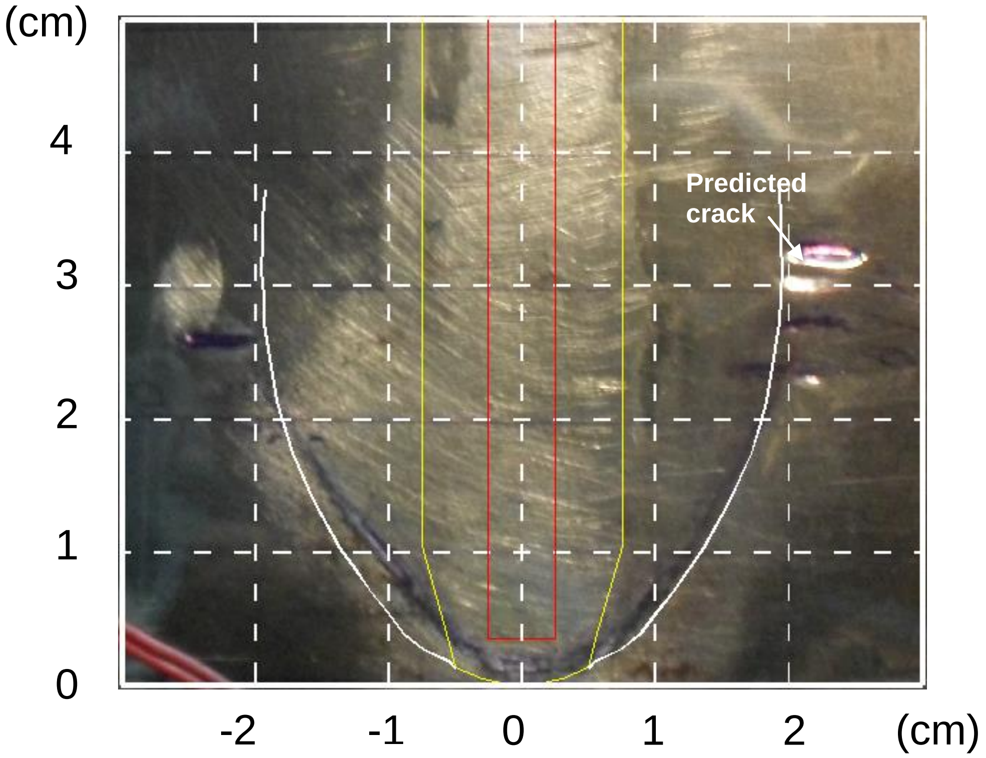

Model 1 and specimen S1-1

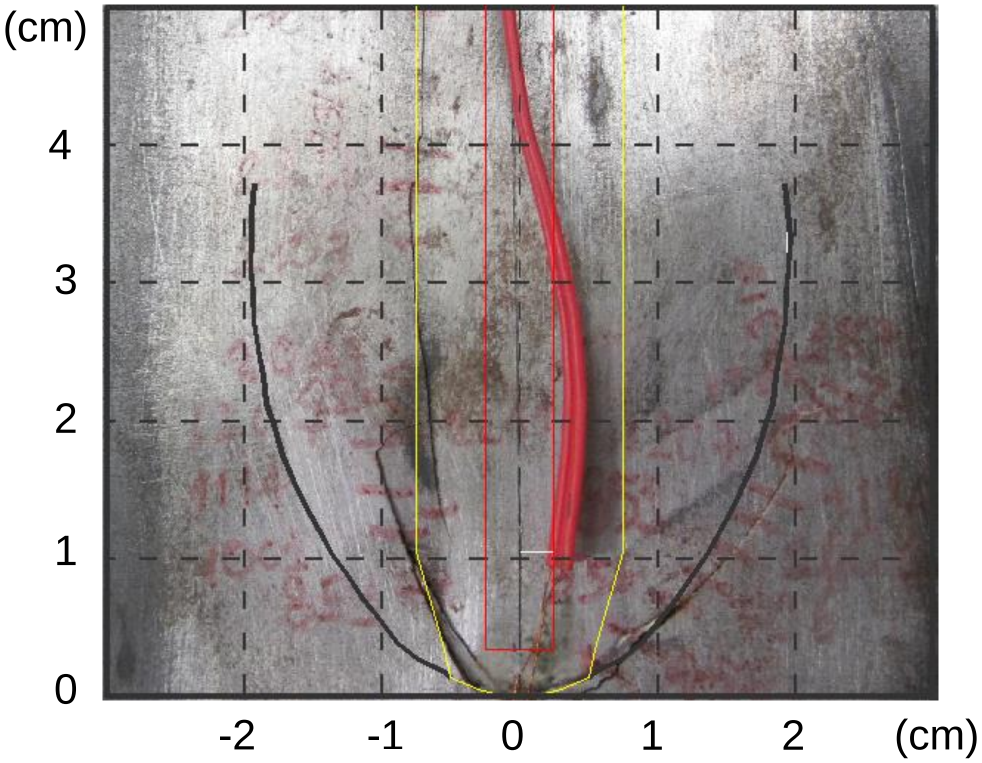

Model 1 and specimen S1-2

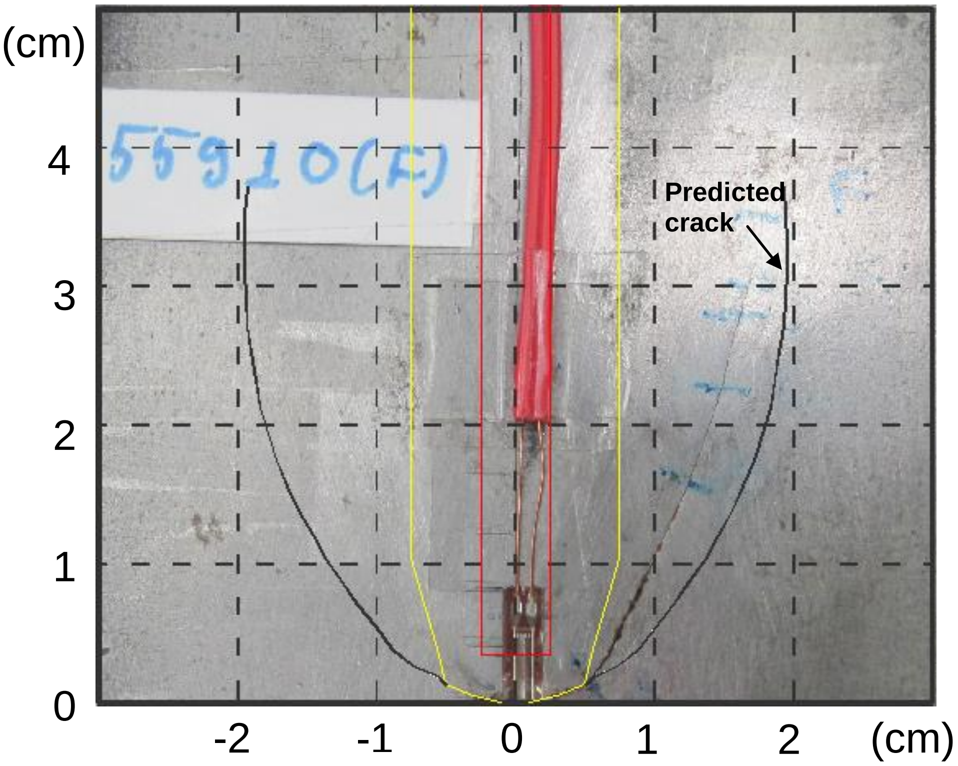

Model 1 and specimen S1-3

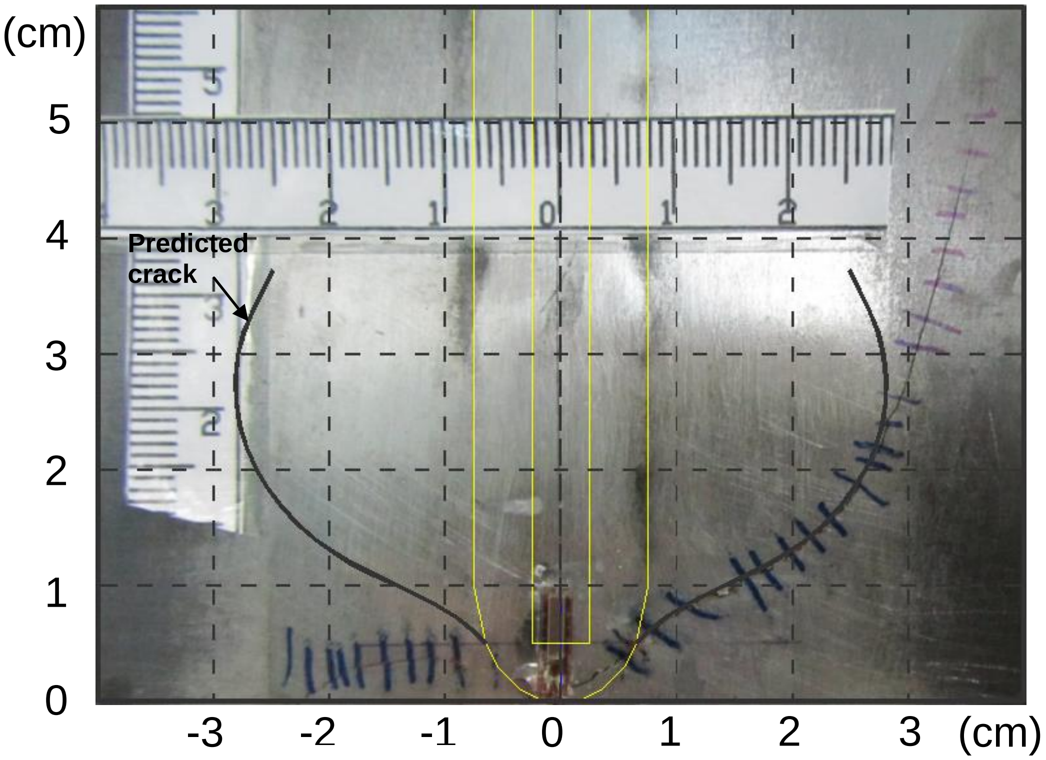

Model 2 and specimen S2-1

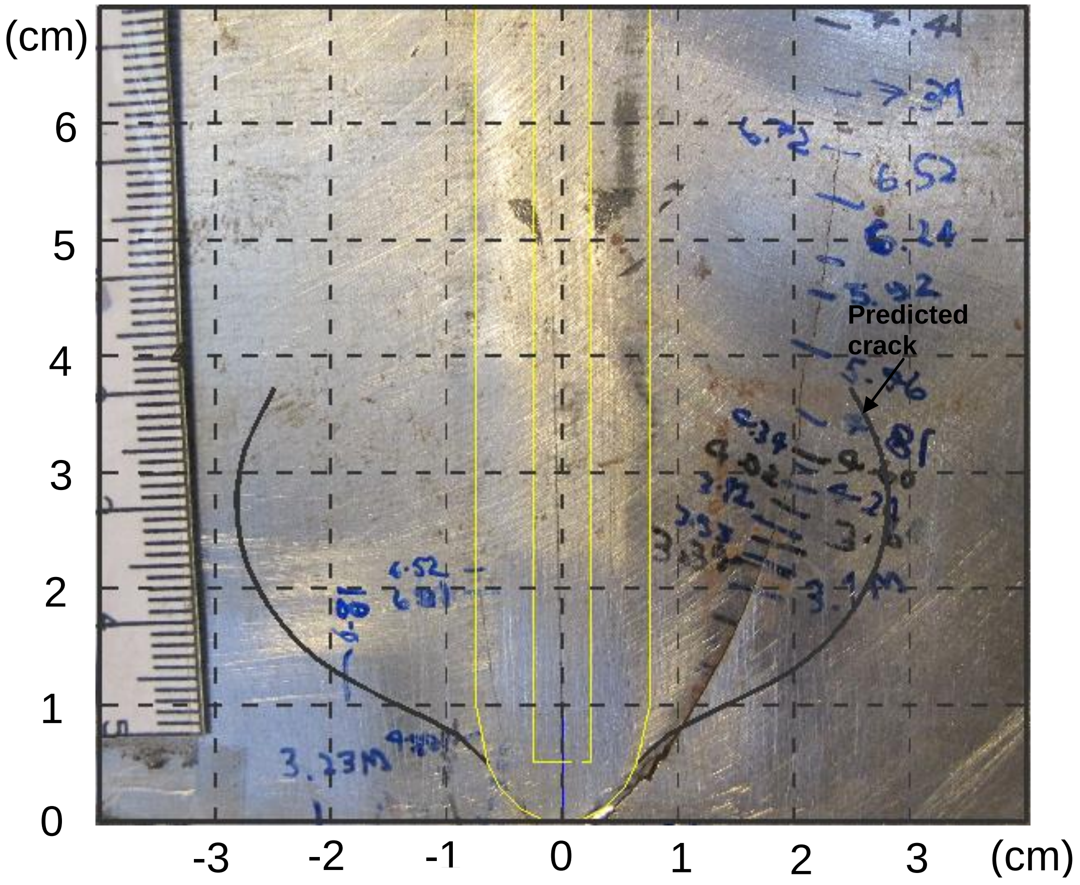

Model 2 and specimen S2-2

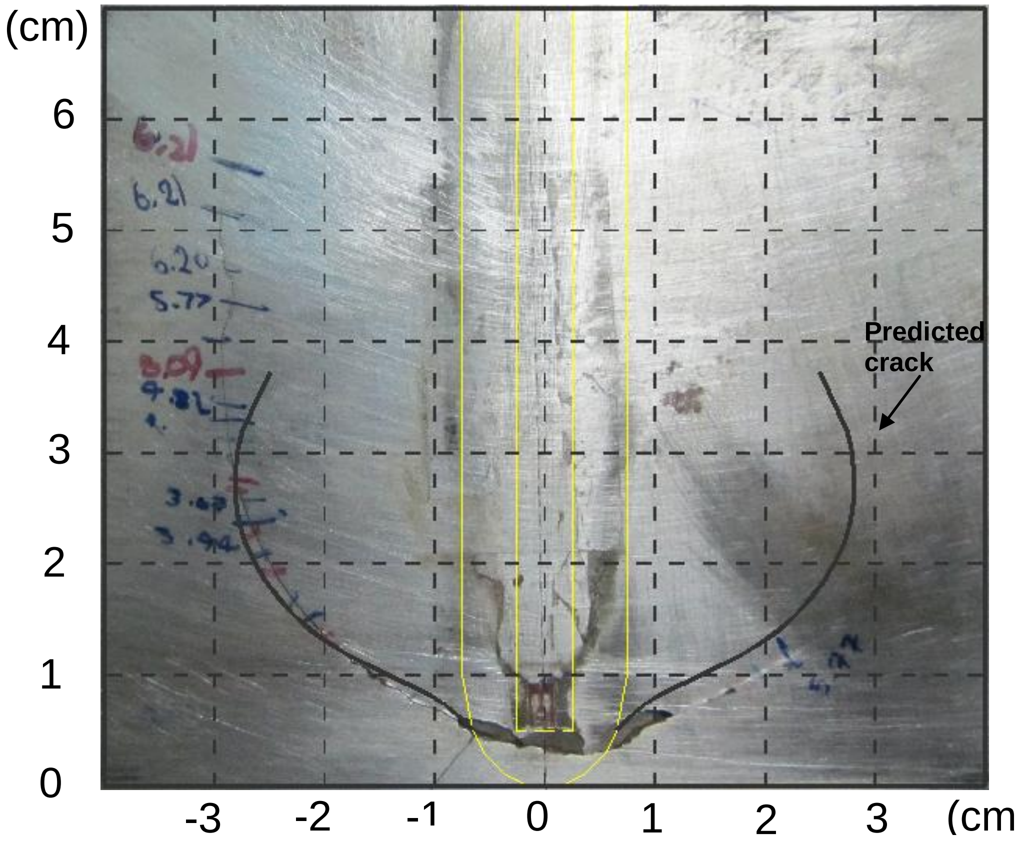

Model 2 and specimen S2-3

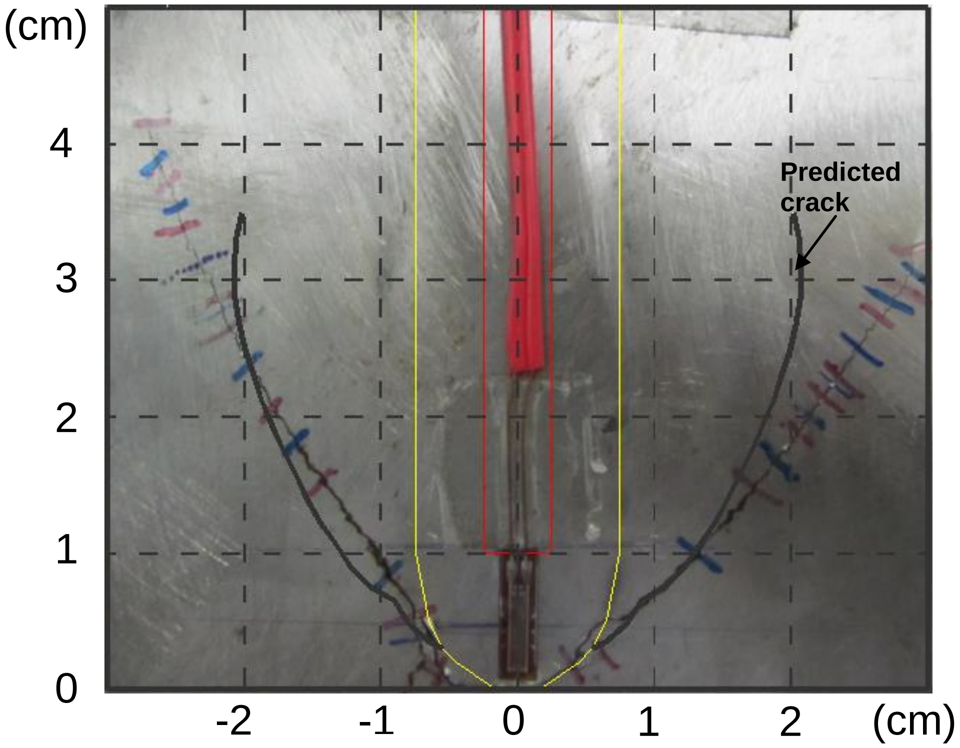

Model 6 and specimen S3-1

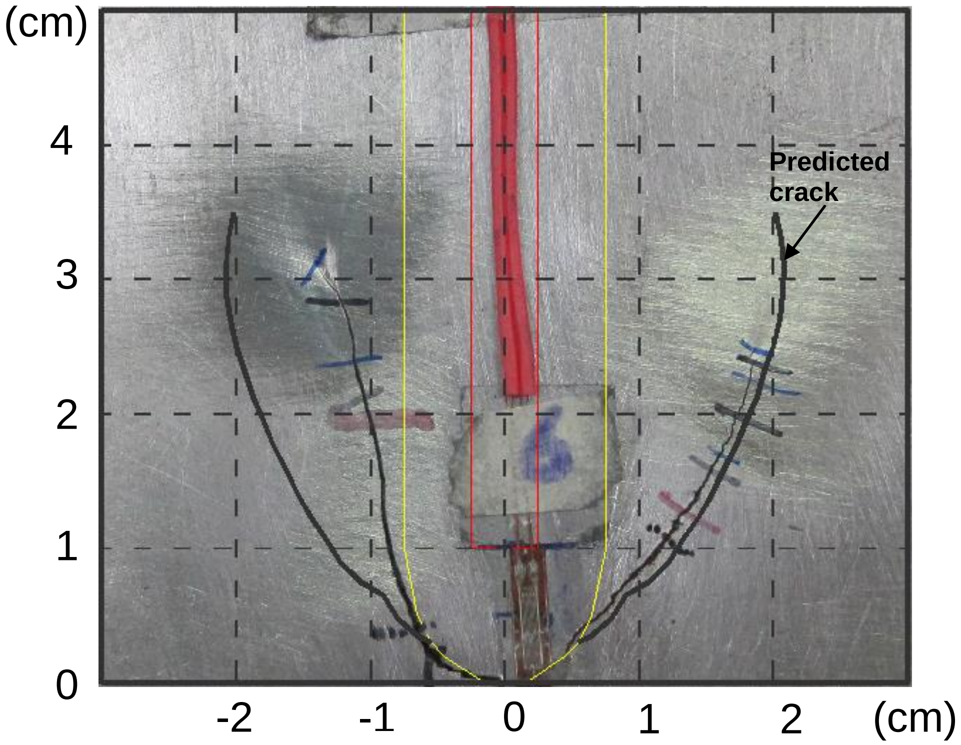

Model 6 and specimen S3-2

Figure 6.2 Comparison of crack paths of specimens and models.

In specimens of series I, the crack path of specimen S1-1 is the most similar one to the crack line which is predicted in model 1. Crack appears at weld-toe and grows up on both sides of stiffener. Crack line of specimen S1-2 shows the effect of un-symmetrical welds to the crack propagation. The height of weld on the right side is larger than on the left side. Therefore, a larger area of concentrated stress was created along the welding on right side of stiffener. It makes the crack path un-symmetrically as shown in figure 6.2. In specimen S1-3, there are small scratches or spots on surface of web which are close to the weld-toe. And these scratches control the crack line to grow down on the left side of stiffener. The crack path becomes un-symmetrically and is different to the crack line which is predicted in FEM model 1.

Validating three crack paths in specimen series II with model 2, the most similar line is the crack on specimen S2-1. In this specimen, the crack on the right side is entirely fixed to the predicted line in model 2 at the beginning. When the crack seems to return towards the welding, there is a concentrated stress zone or scratches which curve suddenly the crack propagation as in figure 6.2. The crack on the left side of this specimen goes down after running horizontally for a long line. The similar results were observed in left side of crack path on specimen S2-3. The crack is not quite fixed to the predicted line due to the shape of left welding along stiffener.

There are two specimens of series III with crack paths which use to compare with model 6. The crack line on the left side of specimen S2-2 is nearly fixed to the predicted crack as shown in figure 6.2. The shape of welding is not symmetrical and creates different concentrated stress zone leading to the un-similar crack paths on both sides of stiffener. The welds along the stiffener are symmetrical and create the symmetrical crack propagation on specimen S3-1. But it seems that the height of weld is larger than the values modeling in FEM modeling. Therefore the crack in the experiment seems to grow further than the predicted crack due to a larger concentrated stress zone.

It's difficult to get the same crack paths in both modeling and experiment. In modeling, the simulation is symmetrical and creates a perfect specimen without spot or scratch. In experiments, the shape of welds is not the same, not only for different specimens, but also for each individual specimen. These welds lead the different crack paths for other specimens in the same series, and even different crack paths on both sides of each individual specimen. However, some crack paths show a good agreement with the predicted crack from FEM modeling. Therefore, if we ignore the effect of different shape of welds, it's concluded that the FEM model could represent the behavior of distortion-induced fatigue crack at web-gap in I-beams of steel bridges.

6.4 Validation of fatigue crack life

Experimental data supply useful information on fatigue crack growths during crack propagation. Assemble these data and compare with the data from FEM in each step of crack propagation, the validations would confirm that the Paris law with SED factor effect is useful in predicting fatigue crack life. The results of comparison are presented in figure 6.3 for all of specimens and models.

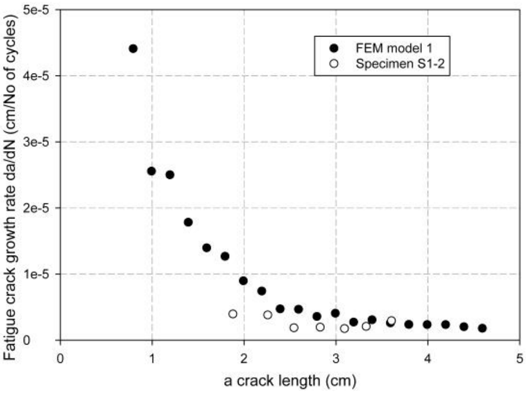

Model 1 and specimen S1-2

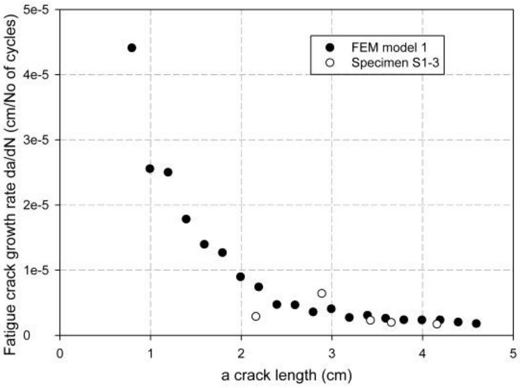

Model 1 and specimen S1-3

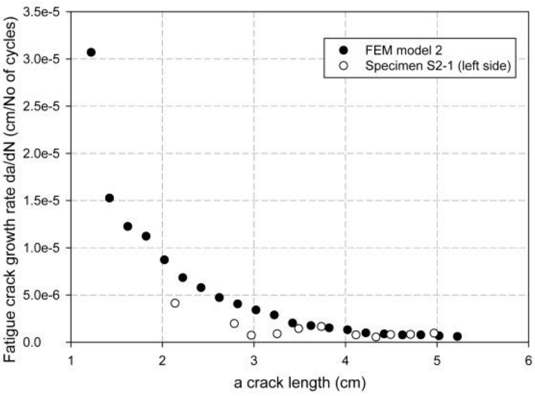

Model 2 and specimen S2-1 (left side)

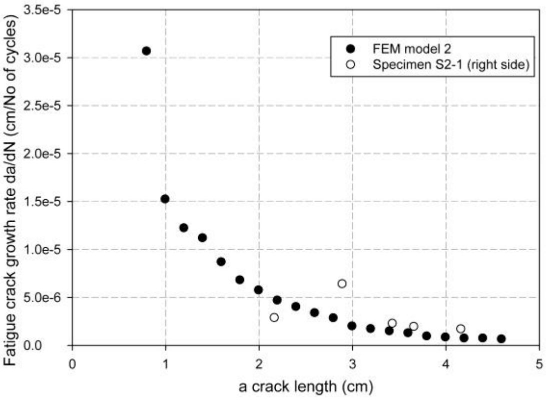

Model 2 and specimen S2-1 (right side)

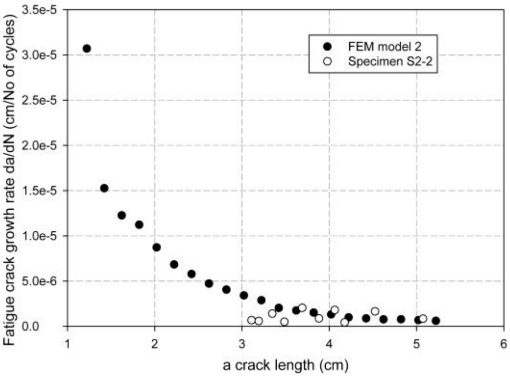

Model 2 and specimen S2-2

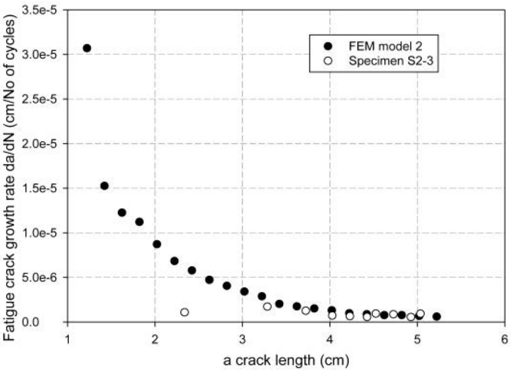

Model 2 and specimen S2-3

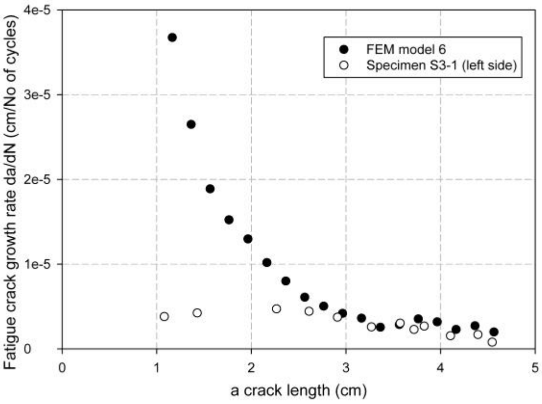

Model 6 and specimen S3-1 (left side)

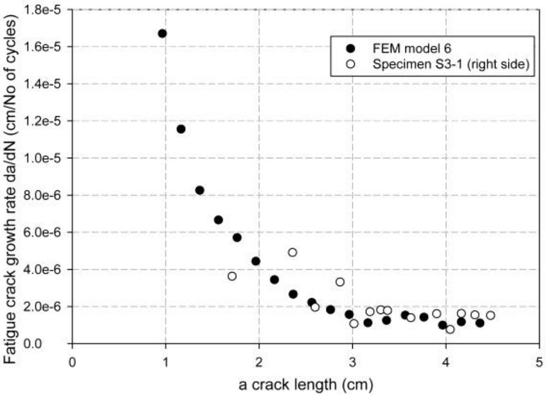

Model 6 and specimen S3-1 (right side)

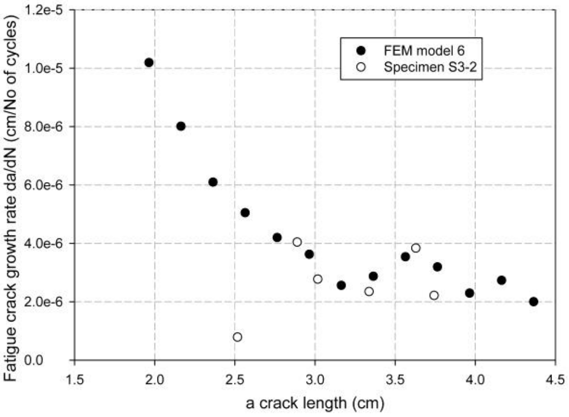

Model 6 and specimen S3-2

Figure 6.3 Validation of fatigue crack growth between experiments and FEM models.

Based on figure 6.3, the values on experiments and FEM models show good agreement. When a crack length is less than 2.5 cm, crack in FEM seems to propagate faster than in those experiments. Actually, the cracks in experiments are recorded and observed by naked eyes without any supported technique. It's difficult to identify micro cracks which already existed. Therefore recorded data is not quite exact at the beginning when the crack goes fast. When the crack obtains stable propagation, the recorded fatigue life is more exact and reasonable as in figure 6.3.

However, the comparison of fatigue crack growth proves that FEM based on SED is good in predicting fatigue crack growth during the time of crack propagation. The agreement in this section is evident that the presented FEM model applying SED factor effect could be used to model and calculate the three dimensional fatigue crack.

6.5 Conclusions

Based on validation of stress fields, crack paths, and fatigue crack growth rates between experiments and FEM model results, it could be concluded that presented FEM model show good agreement when compared with the experimental results. Therefore, the behavior of distortion-induced fatigue crack could be investigated by FEM simulations.

The problems occur in experiments when specimens are not unique. The shape of welding and scratches on surface of web create local concentrated stress zones and influence strongly to crack paths, or even change the crack paths in some cases. These problems lead to difference of crack paths on the same series of specimens as well as the predicted crack. Because of un-symmetrical shape of weld, especially weld-toe, the cracks propagate in different paths on each individual specimen. Therefore, it's quite difficult to request the same crack paths or same local concentrated stress fields on all of specimens. However, the global behavior is reasonable and explainable for distortion-induced fatigue crack at web-gap of I-beams. The initial cracks, the intendant of crack propagation, the failure of I-beam under cyclic load, etc. could be explained from observation from experiments and computation of FEM simulation in this study.

CHAPTER VII

EFFECTS OF PARAMETERS ON FATIGUE LIFE

7.1 General

One of most important tasks in this study is to propose the better structure to prevent or reduce the effect of distortion-induced fatigue crack at the web-gap of I-beam; or to extend the fatigue crack life of I-beam. After implementation of FEM models prove to be appropriate to study on distortion-induced fatigue crack, parameters study were applied to research the effect of different geometries in extending the fatigue crack life.

As in Chapter V, 10 models were established for two purposes: validating with experiments results, and studying about the effect of parameters to crack life. Distortion-induced fatigue crack occurs due to the different deflection between two neighboring I-beams. Crack propagation depends on effect of relative stiffness of stiffener and web-gap, the curve of web-gap under applied load, and the wide of effective zone around weld toe. This study concentrates on the life of crack propagation which grows from the pre-crack at the wed toe to a vertical direction. The parameters which are studied in this chapter include:

- In-plane moment to torsion ratio: torsion moment plays important role in initial crack at weld-toe. If effect of torsion is great, the crack would quickly occur and the life of fatigue crack would decrease. A relative in-plane moment to torsion ratio should be considered to extend the life of crack.
- Change of web-gap length: in this study and previous researches, the increase of web-gap length leads to the decrease of stress at web-gap, that is the main reason for distortion-induced fatigue crack propagation. The shorter of web-gap length leads to larger concentrated stress at the same load level. Therefore, the longer of web-gap length was proposed to reduce the fatigue stress close to weld-toe. A deeper study on this parameter would be useful to obtain the effect of web-gap length to fatigue crack life.
- Stiffener’s thickness to web’s thickness ratio: under effect of loading on I-beam, the web-gap zone is curved in double and a critical stress zone close to weld-toe would be created. The large or small size of curvature controls the wide of effect zone around the weld-toe as well as the crack path. The relative stiffener’s thickness to web’s thickness ratio influences to this curvature.

- Stiffness of web-gap to stiffness of bottom flange ratio: curvature of web-gap zone is also influenced by the relative stiffness of web-gap and bottom flange. This ratio is significant when the bottom flange is restrained. In this research, bottom flange is free from positive constraint and effect of this ratio is not quite large as other parameters. But a study on stiffness of web-gap to bottom flange ratio is considered to understand this effect.

With above cases of parameters study, some of structures will reveal the ability of resistance to distortion-induced fatigue crack.

7.2 Parameter's details and range in study

The web-gap plays an important role in creating concentrated stress at end of stiffener. In this study, 10 models are established to investigate the effect of parameters to fatigue crack at the web-gap under distortion-induced cyclic loading. Due to the validation of experimental data and FEM simulation's results, 3 models (model 1, model 2, and model 6) are set up as specimen's geometries. Model 5 is established as a short beam to study the effect on high I-beam. Other six models' geometries are considered from AASHTO 2007 recommendation on steel bridge design. All models have the same of conditions of constraints with two spring supporters at both ends. In simulation, three-dimensional models are constructed with 3D deflection and relative stiffness. Applied loads on models are cyclic loading with the maximum and minimum loads of 5500 kGf and 1100 kGf respectively. The simulation of 3D models is described as Chapter V (FEM modeling). The geometries in each case study are presented in table 7.1 to 7.4 for four parameters.

- Effects of web-gap length:

Table 7.1: Geometries of models of web-gap length study.

Model	*Span Length L (cm)*	*Aim of stiffener a (cm)*	*Web thickness t_g (cm)*	*Flange thickness t_f (cm)*	*Flange width b_f (cm)*	*Stiffener thickness t_{stf}(cm)*	*Web gap length g_{wg} (cm)*
1	100	20	0.25	0.3	10	0.5	4
2	100	20	0.25	0.3	10	0.5	2.5
3	100	20	0.25	0.3	10	0.5	1

- In-plane moment to torsion ratio:

Table 7.2: Geometries of models for in-plane moment to torsion ratio comparison.

Model	*Span Length L (cm)*	*Aim of stiffener a (cm)*	*Web thickness t_g (cm)*	*Flange thickness t_f (cm)*	*Flange width b_f (cm)*	*Stiffener thickness t_{stf}(cm)*	*Web gap length g_{wg} (cm)*	*Moment to Torsion Ratio*
3	100	20	0.25	0.3	10	0.5	1	5.1
4	140	20	0.25	0.3	10	0.5	1	4.3
5	60	20	0.25	0.3	10	0.5	1	8.5

- Stiffener's thickness to web's thickness ratio:

Table 7.3: Geometries of models of stiffener's thickness to web's thickness ratio.

Model	*Span Length L (cm)*	*Aim of stiffener a (cm)*	*Web thickness t_g (cm)*	*Flange thickness t_f (cm)*	*Flange width b_f (cm)*	*Stiffener thickness t_{stf}(cm)*	*Web gap length g_{wg} (cm)*	t_{stf} / t_g
4	140	20	0.25	0.3	10	0.5	1	2
9	140	20	0.25	0.3	10	0.35	1	1.4
10	140	20	0.25	0.3	10	0.2	1	0.8

- Stiffness of web-gap to stiffness of bottom flange ratio:

Table 7.4: Geometries of models of stiffness of web-gap to stiffness of bottom flange ratio.

Model	*Span Length L (cm)*	*Aim of stiffener a (cm)*	*Web thickness t_g (cm)*	*Flange thickness t_f (cm)*	*Flange width b_f (cm)*	*Stiffener thickness t_{stf}(cm)*	*Web gap length g_{wg} (cm)*	$[(EI)_{web\text{-}gap}/g_{wg}] / [(EI)_{flange}/b_f]$
4	140	20	0.25	0.3	10	0.5	1	5.8
7	140	20	0.2	0.3	10	0.5	1	2.9
8	140	20	0.3	0.3	10	0.5	1	10

To analyze the effect of different parameters to the resistance to distortion-induced fatigue crack at web-gap, all models would have the same of conditions in comparison. The conditions include the model's condition, initial crack and final crack definition which are presented in detail as following:

- Cyclic load: Load which simulates truck load is applied on all models with the maximum and minimum values as 5500 kGf and 1100 kGf respectively. The range of cyclic load guarantees that cracks grow in stable condition.
- Because the crack path is sensitive to the weld that connects stiffener to girder, the shape and size of welds must be the same for all models which have different values of web-gap lengths, girder's thicknesses or stiffener's thicknesses.

- The same initial crack configuration would be set up for all models. The initial crack is set up as shape of weld-toe and grows 0.1 cm with angle equaling to 45^{o}.
- The procedure of crack path simulation is described in Chapter V (Finite element modeling) with the assumption that crack propagates with the same size on compression and tension faces.
- The crack initiates from web-gap as the shape of web-toe and grows up-ward to lower stress field under combination of mode I and mode III fracture. When the crack grows vertically under pure mode I affect, the second crack occurs and the testing beam fails. Because this study concentrates on the first crack propagation, the final crack length would be defined as the time when the first crack becomes vertically.
- Because the number of cycles for crack initiating is different in each model and this research considers the stage that crack grows in stage of stability with pre-crack setup, the stage of initial crack would be ignored. Number of cycles would be counted from the initial crack to final crack which is defined above.

7.3 Effects of web-gap length

This study uses three values of web-gap length with the fixed other geometries for comparison. The web-gap lengths are equal to 4 cm, 2.5 cm, and 1 cm which correspond to 16, 10 and 4 times of web-thickness respectively. In these web-gap lengths, only value of 1 cm corresponds to AASHTO recommendation (web-gap length equals 4 to 6 times of girder's thickness). Table 7.5 presents the number of cycles and different crack path lengths for three models.

Table 7.5: Comparison of "Propagation life" of models with different web-gap length.

Model	*Web gap length (cm)*	*Number of cycles (million cycles)*	*Times*	*Crack path length (cm)*	*Times*
1	4	2.18	26.4	3.6	1.2
2	2.5	0.372	4.5	3.2	1.1
3	1	0.0823	1.0	3	1.0

Web-gap length of 1 cm has shortest fatigue crack life, followed by 2.5 cm and 4 cm respectively. The difference of "propagation life" is quite large for different models with different web-gap lengths. Figure 7.1 presents the comparison of three models for studying effect of different web-gap lengths. As in crack growth rate, the beginning of crack propagation of model 1 is slow and takes a large number of cycles to obtain the same crack length as models 2 and 3. By the end of growth, the “propagation life” of crack in model 1 is at least twice longer than two other models. So the total life of crack in model 1 is great larger than model 2 and 3. Comparing models 2 and 3, when web-gap length increases 2.5 times, the “propagation life” si about 4.5 times difference. Table 7.5 shows that model with larger web-gap length also have longer crack length in growing. It’s concluded that the crack grows further from welding with longer web-gap length. Therefore, the model with long web-gap length could extend the “propagation life”.

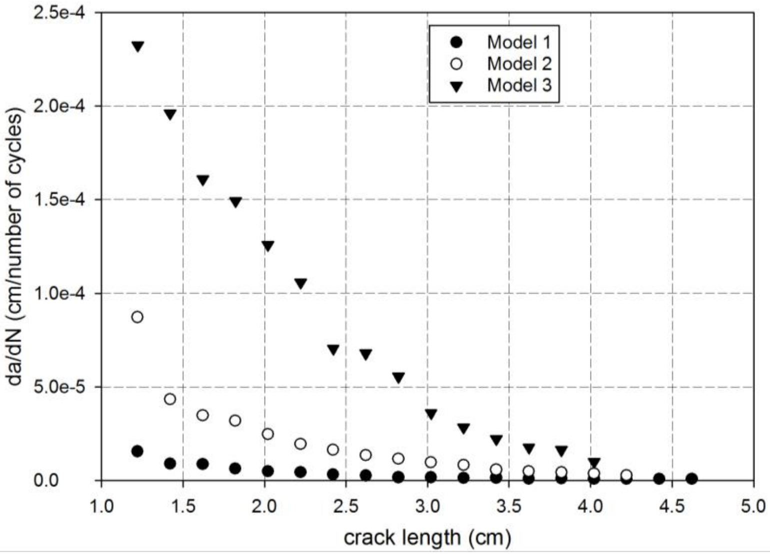

Figure 7.1 Comparison of fatigue crack growth of three values of crack lengths.

The effect of web-gap length to fatigue crack growth is quite important. When the web-gap length is larger, the concentrated stress zone is smaller and leads to larger fatigue crack life as well as longer crack length growth. The short web-gap would lead to the most critical stress which concentrates at the weld-toe; crack easily occurs and the fatigue life of the beam decreases.

7.4 In-plane moment to torsion ratio

In-plane moment to torsion ratio is influenced by the ratio of span length and aim of stiffener, when other geometries are the same. The comparison of this ratio is also studied for finding the better structure in resisting to the fatigue crack under distortion-induced effect. Models 3, 4, and 5 corresponding to the span length of 140 cm, 100 cm, and 60 cm have the same aim of stiffener and would be included in this comparison, whereas the other geometries would be the same for three models.

Table 7.6: Comparison of "propagation life" of different in-plane moment to torsion ratio.

Model	*Span Length L (cm)*	*aim of stiffener a (cm)*	*Moment to Torsion Ratio*	*Number of cycles (million cycles)*	*Times*	*Crack path length (cm)*	*Times*
3	100	20	5.1	0.0824	9.7	3	1.0
4	140	20	4.3	0.00851	1.0	3	1.0
5	60	20	8.5	2.67	313.3	3.2	1.2

Figure 7.2 and table 7.6 show the comparison of in-plane moment to torsion ratio. The resistance to fatigue crack is the most effective when the ratio is equal to 8.5. This ratio shows high resistance to distortion-induced effect with number of cycles close to 2.67 million cycles. Considering the curves of comparison, the effect of in-plane moment to torsion ratio reduces quickly when the ratio decreases from 5.1 to 4.3. The numbers of cycles of "propagation life" are reduced by 9.7 times. When crack length is longer than 3 cm, the fatigue crack growths are not much different. Actually, the crack propagates almost vertically and is influenced by Mode I in this stage. In other words, when the crack length is more than 3 cm, the torsion has no influence on crack propagation. Therefore, the effect of this ratio to resist fatigue strength should be considered in the zone close to web-gap or in high stress field zone. As crack path results of 3 models, the difference is not quite clear for different ratios. All the crack paths seem to be the same with angle and crack length in growing. In fact, the change of in-plane moment to torsion ratio, which is based on changing span length, leads to the different relative deflection that is the main reason for distortion-induced fatigue crack problem. Shorter span length results in decreases of deflection and also prevents the fatigue crack growing on web.

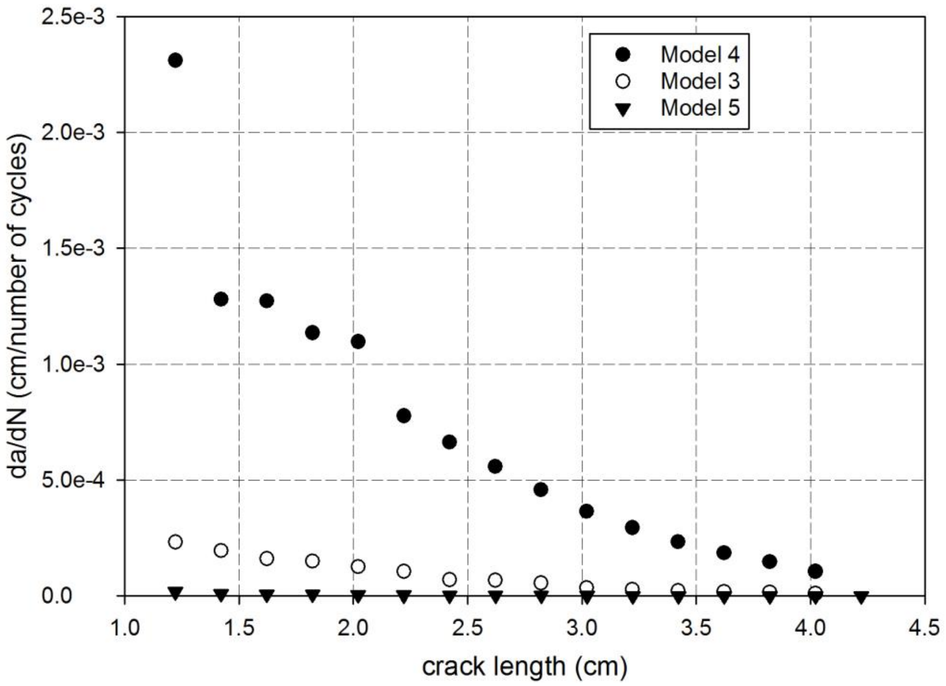

Figure7.2 Comparison of fatigue crack growth of three values of in-plane moment to torsion ratio.

Basically, increase of in-plane moment to torsion ratio leads to the decrease of fatigue crack life. Thus, distortion-induced fatigue crack would be entirely prevented when the ratio is close to one. The fatigue crack life will be serious in case in-plane moment to torsion ratio is large. Therefore, a relative span length and aim of stiffener is more required to identify the ratio in resisting to the distortion-induced fatigue crack.

7.5 Stiffener’s thickness to web’s thickness ratio

In experiments and FEM modeling, there are double curves which occur in the line of stiffener and bend the web-gap. At the location of the highest stress on these curves, the cracks begin from the tension face and grow up to compression face as semi-ellipse. These curves depend on the stiffness of stiffener and web-gap. So it’s necessary to make a comparison of effect of stiffener’s thickness to web’s thickness ratio. Model number 4, 9 and 10 are included in calculating for this comparison with the different values of stiffener thickness (0.5 cm, 0.35 cm and 0.2 cm respectively). The difference of stiffener thicknesses leads to difference of stiffener’s to web’s thickness ratio. Other geometries are the same for all of three models except web-gap length values. Table 7.7 lists the geometries and results of three models.

Table 7.7 Geometries and results calculating for comparison of stiffener's thickness to web's thickness ratio.

Model	*web thickness t_g (cm)*	*Stiffener thickness t_{stf} (cm)*	*t_{stf}/t_g*	*Number of cycle (million cycles)*	*Times*	*Crack path length (cm)*	*Times*
4	0.25	0.5	2	0.00851	25.0	3	3.8
9	0.25	0.35	1.4	0.00432	12.7	2	2.5
10	0.25	0.2	0.8	0.00034	1.0	0.8	1.0

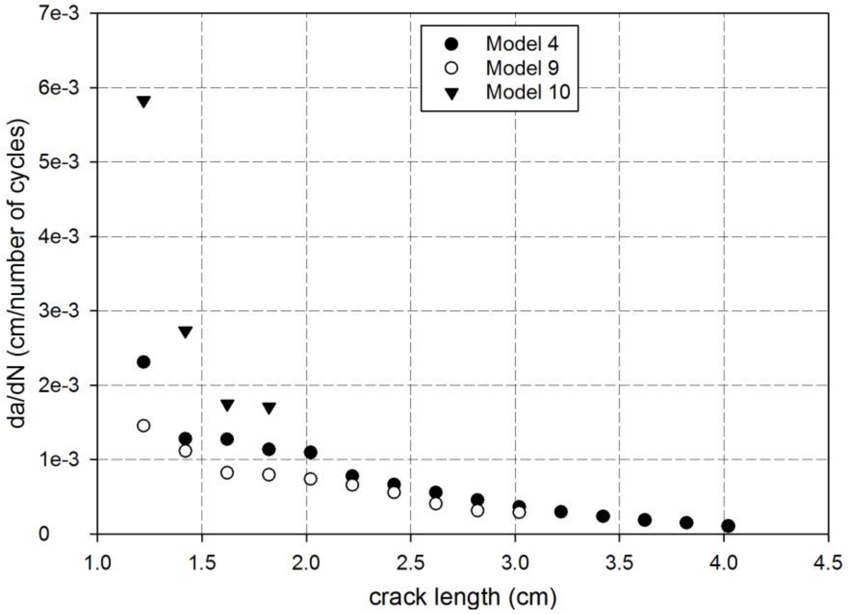

Figure 7.3 Comparison of fatigue crack growth of stiffener's thickness to web's ratio.

Basically, the stiffness of stiffener is much higher than the stiffness of web-gap. This reason could be explained from the curve along the web-gap length under cyclic loading. Figure 7.3 presents the fatigue crack growth comparing the effect of stiffener's thickness to web's thickness ratio. Observing on figure 7.3 and table 7.7, reducing in this ratio would lead to the decrease of fatigue crack growth. When the thickness of girder is higher, the strength of web reduces the curvature of the web-gap as well as the concentrated stress at weld-toe. The effective zone around the weld-toe also decreases. As table 7.7, when the ratio is equal to 0.8, the length of crack propagation is quite short. The crack grows out of weld-toe and turns up-ward immediately. It can be explained that a small effect of distortion-induced to the web-gap couldn't guide the crack further from the welding. The stage for crack growth under combination of mode I and mode III exist in a short time before crack propagates in pure mode I condition. In these models, the strain energy density values are not quite different, and the extension of "propagation life" depends mainly on the length of crack growth. The longer crack length leads to the larger number of cycles loading. Models 4 and 9 have longer crack length propagation values than model 10, and the "propagation life" is extended. In fact, the stiffener's thickness to web's thickness ratio controls the length of crack path to extend fatigue crack life. It's more useful if this ratio could be combined with the change of web-gap length.

7.6 Stiffness of web-gap to stiffness of bottom flange ratio

In fact, the bottom flange could be restrained that contributes to the strain at double curvature of web-gap length. In this research, the distortion-induced fatigue crack is studied at the middle of I-beam without positive constrain at bottom flange. Anyway, the effect of stiffness of web-gap to stiffness of bottom flange ratio still controls the fatigue crack and it's necessary to consider this problem. Three models number 4, 7 and 8 are included in this comparison. The value of web thickness is varied to obtain the different stiffness of web-gap to flange ratios. Other geometries as span length, the aim of stiffener, the thickness of all welding-plate, etc. would be maintained for all models. The flange's thickness to girder's thickness ratio is strictly required as AASHTO recommendation to resist against the effect of buckling in design. Stiffness of web-gap and stiffness of flange include the effect of flange width and web-gap length in calculation as following:

- Stiffness of web-gap: $\left(EI_{web-gap}\right)/g_{wg}$

  where $I_{web-gap}=\dfrac{1}{12}\left(t_{stf}t_g^3\right)$

- Stiffness of bottom flange: $\left(EI_{flange}\right)/b_f$

  where $I_{flange}=\dfrac{1}{12}\left(t_{stf}t_f^3\right)$

Figure 7.4 shows the model for calculate stiffness of web-gap and bottom flange.

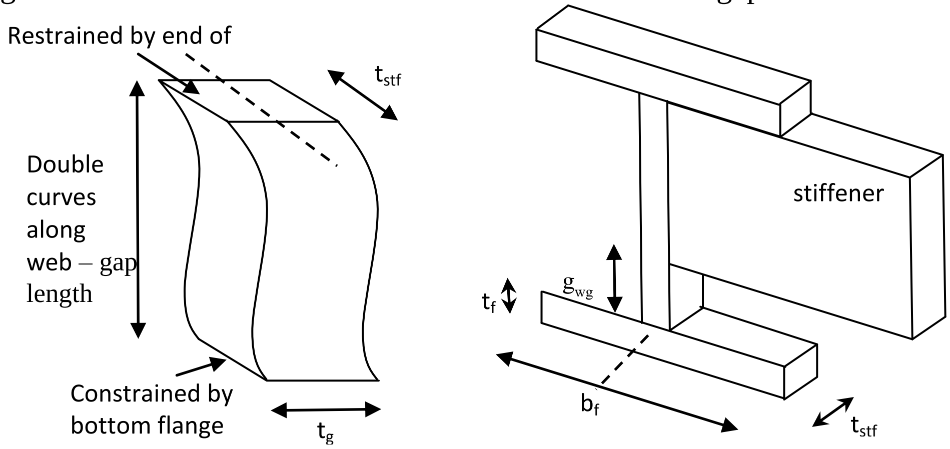

Figure 7.4 Geometries of model for stiffness of web-gap and bottom flange.

The difference of stiffness of web-gap to flange is presented in table 7.8.

Table 7.8 Calculation of stiffness for comparison of stiffness of web-gap to stiffness of bottom flange ratio.

Model	*web thickness t_g(cm)*	*Flange thickness t_f(cm)*	*$[(EI)_{web\text{-}gap}/g_{wg}]$ $/[(EI)_{flange}/b_f]$*	*Number of cycle (million cycles)*	*Times*	*Crack path length (cm)*	*Times*
4	0.25	0.3	5.8	0.0851	1.5	3	1.2
7	0.2	0.3	3.0	0.0550	1.0	2.6	1.0
8	0.3	0.3	10.0	0.00107	1.9	3	1.2

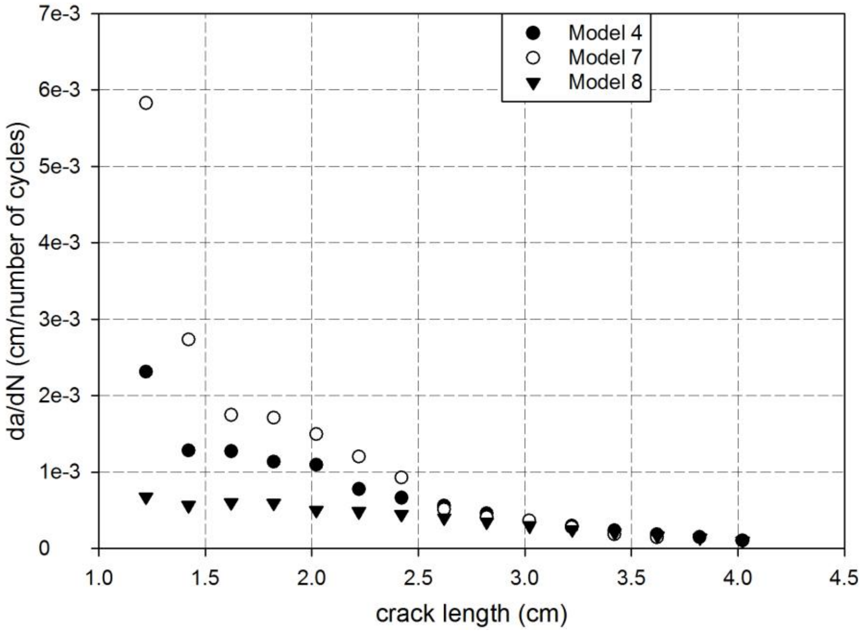

Figure 7.5 Comparison of fatigue crack growth of stiffness of web-gap to stiffness of bottom flange ratio.

Figure 7.5 shows the comparison of three stiffness of web-gap to stiffness of bottom flange ratios. When the value of web-thickness increases, the web-gap has smaller out-of-plane curvature. Therefore, fatigue crack life would be extended. Concentrated stress around the web-gap section is also reduced. Model 8 with the highest value of girder's thickness presents the highest "propagation life" which equal to 1.9 times larger comparing to the "propagation life" in model 7. Model 4 has web-thickness equaling to 1.25 times thicker than model 7. Model 4 also reveals the higher fatigue resistance than model 7 by 1.5 times. The crack length propagation of model 4 and model 8 is also longer than crack path in model 7. So the increase of stiffness of web-gap to stiffness of bottom flange ratio prevents the distortion-induced effect. In addition, the increase of web-thickness also contributes to the values of stiffness of I-beam which leads to smaller value of deflection. However, the effect of this ratio is not quite clear when the bottom flange is free from constraint.

7.7 Conclusions

For the comparisons in this chapter, some parameters of I-beam structure reveal the capability in resisting the distortion-induced fatigue crack at the web-gap. The main idea of these improvements is to decrease the relative deflection of I-beam and curvature along web-gap length as well as to induce smaller concentrated stress around the web-gap. Some parameters show useful effect in extending fatigue crack life.

The most effective parameter is the in-plane moment to torsion ratio. The effect of this ratio is quite significant in resisting fatigue crack propagation. If the detail of web-gap is improved to reduce the value of torsion, the longer propagation life could be obtained. For example, the connection between stiffener and girder or other kinds of transfer components could be studied to eliminate the "local torsion" effect. This comparison reveals the future work to prevent the effect of distortion-induced fatigue crack by improving the detail of web-gap to obtain higher in-plane moment to torsion ratio.

In reducing the effect of distortion-induced fatigue crack, the increase of web-gap length should be considered. It is found that when the web-gap length increases, the smaller concentrated stress leads to a larger number of cycles loading for a girder to crack. ASSHTO recommends a web-gap length with 4 to 6 times of girder's thickness. If the web-gap length equals 4 times of ASSHTO recommendation, the "propagation life" of crack increases 26.4 times. In addition, it's take longer time to create initial crack at web-toe with smaller concentrated stress. It's also the most practical method in resisting distortion-induced fatigue crack at web-gap.

The stiffener's thickness to web's thickness ratio plays an important role in extending the stage of combination mode I and mode III. This ratio couldn't prevent the initial crack at the web-gap, but it can extend the required number of cycles for crack propagation. Although stiffener's thickness to web's thickness ratio proves to be useful for comparison, the weak zone established at the middle of I-beam and second crack is ready to occur.

Less influence than other parameters, the stiffness of web-gap to stiffness of bottom flange ratio has the capability to extend the "propagation life" of crack propagation. Its main rule is to decrease the curvature of web-gap in order to reduce the concentrated stress around the weld-toe. However, this ratio would be more useful in case the bottom flanges or top flanges are restrained from rotation.

It’s difficult to apply all of useful parameters in reality. But some of them reveal the effect and capability in applying for real I-beam of structure. For example, improving the web-gap detail, increasing local web-thickness around weld-toe or increasing the flange-thickness to reduce relative deflection, etc. would be useful in practice.

CHAPTER VIII

CONCLUSIONS

8.1 Behavior of distortion-induced fatigue crack at the web-gap

As observed in experiments and FEM models, the fatigue crack at web-gap under distortion-induced effect is the combination of mode I and mode III.

8.1.1 Initial crack

Web-gap would be double curvatures which depend on web-gap length as well as the ratio of stiffness of stiffener and web-gap. Because of these out-of-plane curves, a concentrated stress zone occurs around the weld-toe which connects end of stiffener to girder. The part of web located at end of weld-toe includes tension face and compression face. Crack begins at the highest concentrated stress point and shapes as weld-toe on tension face as semi-ellipse crack. On tension face, crack expresses as opening crack under Mode I affect. Mode III crack is created by distortion-induced load due to out-of-plane moment which concentrates at web-gap. The role of mode III is to increase the energy for mode I crack propagation from tension to compression face. After touching the compression face, crack becomes two crack-tips crack and continues to grow further from the web-gap in both sides of stiffener.

8.1.2 Crack propagation

Crack propagates from the initial location as horizontal line and gradually changes to vertical direction. Mode I continuously plays the role in crack direction and propagation. Mode III extends the energy to create two crack surfaces and gradually decreases its effect when crack grows in vertical direction. When the crack is totally in vertical line, it becomes opening crack under bending moment. On crack surface, there are curvature scratches between two surfaces of web. These curvature scratches are parallel to each other and disappear when crack becomes unstable one. As the increase of number of cyclic load, the crack grows toward to lower stress field and gradually be slower. The length of crack in horizontal direction depends on out-of-plane to in-plane stress ratio. If the ratio is large, crack will grow in longer horizontal line.

8.1.3 Beam failure

The typical of beam failure could be described as following: after the first crack located from weld-toe touches the low stress field and grows slowly, a second crack located at weld-toe occurs and propagates downward toward bottom flange. The new crack will be responsible for beam failure by failing bottom flange. These problems are serious, because previous researches concentrated on the first crack and tried to stop it in retrofitting the I-beams. In this study, experimental observations propose a series of beam failure which depends on the second crack. Retrofit methods should concentrate on preventing or stopping the second crack.

Other types of beam failure may occur due to a new crack located on the weld connecting web and bottom flange or the first crack which grows downward to bottom to destroy the flange. These types of failure depend on scratches which may be located on welding at connection of web and flange or at the weld-toe. However, the typical failure of I-beam under distortion-induced fatigue crack occupies most of testing specimens.

8.1.4 Sensitive of crack path

Crack path depends on the stress field on web-gap zone and further which created by effect of out-of-plane to in-plane stress ratio. Local stress field close to web-gap also depends on welds, especially shapes of welds. The weld-toe creates local concentrated stress and could change the crack direction in this zone. If the welding is smooth and good quality, the stress field distributes as gradient contour and is different from larger to smaller values of stress. Therefore, the crack prediction would be easy obtained from FEM simulation. If the welding is not entirely in good condition, the crack path would be trouble by local concentrated stress field. Another problem which might influence to crack direction in local zone is scratches. Basically, scratches would reduce the local stiffness of web and guide the crack in propagating as their direction. In some cases, the scratches could re-define the beam failure as presented in section 8.1.3 (Beam failure).

8.1.5 Fatigue life

As experimental data, the beam failures supply the fatigue life of I-beam under distortion-induced fatigue crack at the web-gap. The definition of beam failure is described as the beam is destroyed by crack at bottom flange and crashes down entirely. This definition is un-similar to previous researches which define beam failure as the deflection or crack length obtains an identified value. As in experimental data, we could classify the fatigue life of I-beam under distortion-induced fatigue crack with web-gap detail in Category C*. It’s the same Category with the fatigue life of I-beam with web-gap detail under in-plane effect.

8.2 FEM simulation

8.2.1 Strain energy density study

Sih proposed SED theory to define the behavior in fracture mechanism. In basic, the fracture occurs as the minimum strain energy density direction around the crack tip. Therefore, the MSED is described as a criterion in predicting the crack propagation. SED factor is not enough for identifying the fatigue crack growth rate, if we implement SED criterion in Paris law. SED factor effect would be introduced when we combine SED with impact stress intensity factor which was proposed by Lam. Paris law applying with SED factor effect would be useful in predicting the fatigue crack life as in this study. In fact, the SED factor provides good results in predicting crack path in 2D problems. This study implements the hypothesis 1 of SED factor in solving 3D problems. Actually, the crack in these models is predicted in a plate which includes out-of-plane effect. However, it’s concluded that the SED factor effect could be applied to predict both crack direction and fatigue crack life. The most considerate advantage of SED criterion is the simple applied element. SED criterion would not require singularity or special element in predicting crack growth as other criteria.

8.2.2 FEM implements

FEM models employ solid element and the effect of welding as well as deflection which is included in calculating. The analytical procedures of this study are carried out using ANSYS 12.1 (ANSYS, Inc., Canonsburg, Pa.) in structure package option. FEM models include some assumptions to simplify the computation: crack tip perpendiculars to compression and tension face, the crack propagates as symmetrical shape in both sides of stiffener, and the initial crack would be set up as the same properties for all FEM models. Ring element which is applied in meshing technique is important to identify which element contains minimum value of strain energy. The radius of ring element and step size must be identified as definitely procedure to guarantee the convergence of models. After each step of calculation, a new mesh would be generated to avoid the troubles in transferring the data from old to new mesh as previous researches.

8.2.3 FEM results

With the validation results, the FEM model proves to be able to study about behavior of distortion-induced fatigue crack at the web-gap of I-beam. The crack paths from FEM models which are implemented with SED factor effect calculating is fixed with some crack paths of specimens. The other crack paths are different to the predictions in FEM models due to the effect of welding to the local stress field. Besides that, some scratches existing from fabrication procedure also control the crack to turn into other direction. In reality, I-beam of steel bridge structure also has the same problems which are difficult to control.

With applying SED factor effect in Paris law to predict the fatigue crack growth rate in FEM, simulations present the results which are fixed to crack propagation in experiments. This study concentrates on the stage when first crack propagates in predicting fatigue life. This stage occupies about 70% of total fatigue life of I-beam. And the results in validating for this stage are good for explaining the crack's growth. Observing the fatigue crack growth rate obtained from FEM model's results, we could recognize that strain energy density values decrease when crack propagates in low stress field and closes to neutral axis. It explains that the first crack grows gradually slower as the distance from web-gap increases in experiments.

However, it's difficult to apply the FEM model to predict the second crack, because crack line in prediction is smooth and different to the crack in experiments in local. In testing, the crack path is not too smooth and contains many local crack tips on its line. Therefore, the second crack could begin from these local crack tips and grows downward.

8.3 Parametric study

One of objectives in this study is to find out the influences of parameters on the resistance to distortion-induced fatigue crack at the web-gap. Four parameters were calculated and compared to analyze their useful in applying:

- In-plane moment to torsion ratio is the most effective parameter in resisting to distortion-induced fatigue crack when the ratio decreases. This ratio depends much on span length to aim of stiffener ratio. In reality, it's difficult to apply a short span length for steel bridge. Therefore, this parameter would be not useful in design code.
- The web-gap length shows the good effect in extending the fatigue life. But its effect would be limited when the length is over ten times of web-thickness.
- The stiffener's thickness to web's thickness ratio is useful in extending the crack length in stage of combination mode I and mode III. Comparison proves that the effect to extend the fatigue life would be better if this ratio increases. Actually, the decrease of ratio leads the larger curvature along web-gap length.

Therefore, the stress field would concentrate more around the weld-toe and creates longer crack length growing in horizontal direction. Keep the crack growing in longer line is a strategy but the second crack would occur any time in “weak zone”.

- Stiffness of web-gap to stiffness of bottom flange ratio also proves that it may be useful to be applying in reality. Its main idea is to decrease the curvature of web-gap in order to reduce the concentrated stress around weld-toe. However, this ratio would be more useful in case the bottom flanges or top flanges are restrained from rotation.

Basically, all of above parameters try to decrease the relative deflection or to reduce the curvature along web-gap length. Parametric study reveals some effective methods which could apply to extend the fatigue crack life. An increase of local value of web-thickness around the web-gap could be useful in increasing in-plane stiffness and reducing the curvature of web-gap length. An increase of flange-thickness could be applied in increasing the in-plane stiffness as well as reducing relative deflection. For purpose of reducing the stiffness of I-beam to transfer components ratio, a special detail could be researched to softer the connection between web and stiffener… All of these ideas could be investigated in the future to improve the structure in resisting to distortion-induced fatigue crack at the web-gap of I-beam.

8.4 Recommendation for future works

This study concentrates on analysis of distortion-induced fatigue crack at the web-gap of I-beam in steel bridge. Due to limitation on this study, there are still many works that could be extended from this research, for example,

- The stage of initial crack is known as the growth of semi-ellipse crack. But the procedure to compute this stage is still unclear and required further investigation in order to find out the method preventing initial crack.
- The stage of second crack growth is known as the effect of branching due to the concentrated stress at crack tips on the line of first crack. This crack grows under effect of mode I of in-plane moment. So the time for the second crack occurring and growing is still need for investigation.
- Improvement of the details on the connection between stiffener components and girder is a useful method to extend the fatigue crack growth. This study reveals some effective parameters in resisting the distortion-induced fatigue crack. If the detail study could be studied with applying the effect of

parameters in this study, the web-gap details would be improved for the structure to extend its “fatigue life”.

Reference

American Association of State Highway and Transportation Officials (AASHTO) Bridge Specifications (AASHTO, 1983, 1998, 2007)

Canadian Highway Bridge Design Code (CHBDC) (CSA, 2000)

Berglund, E. M. and A. E. Schultz (2006). *Girder Differential Deflection and Distortion-Induced Fatigue in Skewed Steel Bridges.* Journal of Bridge Engineering 11, No2: 169-177.

Bloch, R. A. and M. W. Brown (1993). *Crack closure analysis for the threshold of fatigue crack growth under mixed-mode I/II loading*. H. P. Rossmanith and K. J. Miller (editors), Mixed-Mode Fatigue and Fracture, ESIS 14, Mechanical Eng. Publ., London(1993): 125–137.

Bouchard, P. O., F. Bay and Y. Chastel (2003). *Numerical modelling of crack propagation: automatic remeshing and comparison of different criteria.* Computer Methods in Applied Mechanics and Engineering 192, 35-36: 3887-3908.

Chen, W. R. and L. M. Keer (1991). *Fatigue crack growth in mixed mode loading.* Journal of Engineering Mater Technology 113(ASME Trans): 222-227.

Chow, C. L. and T. J. Lu (1991). *Cyclic J-integral in relation to fatigue crack initiation and propagation.* Engineering Fracture Mechanics 39, 1: 1-20.

D'Andrea, G. Y. Grondin and G. L. Kulak (2001). *Behaviour and rehabilitation of distortion-induced fatigue cracks in bridge girders*. Structural Engineering Report. Alberta, University of Alberta.

Dexter, R., W. Wright and J. Fisher (2004). *Fatigue and Fracture of Steel Girders*. Journal of Bridge Engineering 9, 3: 278-286.

Donahue, R. J., H. M. Clark, P. Atanmo, R. Kumble and A. J. McEvily (1972). *Crack opening displacement and the rate of fatigue crack growth.* International Journal of Fracture 8, 2: 209-219.

Dowling, N. E. and J. A. Begley (1976). *Fatigue crack growth during gross plasticity and the J-intergral.* Mechanics of Crack Growth ASTM STP 590: 82-103.

Erdogan, F. and M. Ratwani (1970). *Fatigue and fracture of cylindrical shells containing a circumferential crack*. International Journal of Fracture 6, 4: 379-392.

Erdogan, F. and G. C. Sih (1963). *On the crack extension in plates under plane loading and trasverse shear*. J. Bas. Eng., ASTM Trans 85, 1963: 519-525.

Fisher, J. W. (1978). *Fatigue cracking in bridges from out - of - plane displacements*. Canadian Journal of Civil Engineering 5, 4: 542-556.

Fisher, J. W. (1984). *Fatigue and fracture of steel highway bridges*, *Case studies*, Wiley-Interscience.

Fisher, J. W. and P. B. Keating (1989). *Distortion-induced fatigue cracking of bridge details with web gaps*. Journal of Construction Steel Research 12: 215-228.

Fisher, J. W., D. J. Klingerman and K. H. Frank (1971). *Fatigue crack growth in A36 steel, 1971*. p. 411. Fritz Labotory Reports.

Fisher, J. W., G. L. Kulak and I. F. Smith (1998). *A fatigue primer for structural engineers*. National Steel Bridges Allinance (American Institute of Steel Construction, Chicago, IL).

Fisher, J. W., B. T. Yen and D. C. Wagner (1987). *Review of field measurements for distortion-induced fatigue cracking in steel bridges*. T. R. R. 1118. National Research Council, Washington D.C.: 49-55.

Fisher, J. W., B. T. Yen and D. Wang (1990). *Distortion induced cracking in steel bridge members*. Final Report.

Forman, R. G., V. E. Kearney and R. M. Engle (1967). *Numerical analysis of crack propagation in cyclic-loaded structures*. Journal of Basic Engineering 89: 459-464.

Forth, S. C., W. D. Keat and L. H. Favrow (2002). *Experimental and computational investigation of three-dimensional mixed-mode fatigue*. Fatigue & Fracture of Engineering Materials & Structures 25, 1: 3-15.

Fraser, R. E. K., G. Y. Grondin and G. L. Kulak (2000). *Behavior of distortion-induced fatigue cracks in bridge girders*. Structural Engineering Report. Edmonton, Alberta, University of Alberta.

Gross, T. S. (1985). *Frictional effects in Mode III fatigue crack propagation*. Scripta Metallurgica 19, 10: 1185-1188.

Hamoush, S. A. and M. Reza Salami (1990). *Analysing a mixed-mode plane problem by using Jk integrals*. International Journal of Fatigue 12, 5: 441-445.

Hellen, T. K. and W. S. Blackburn (1975). *The calculation of stress intensity factors for combined tensile and shear loading*. International Journal of Fracture 11, 4: 605-617.

Hidayat, M. S. and A. Lenwari (2009). *Effects of Bridge Parameters on Distortion-Induced Fatigue in Multi I-Girder Steel Bridges*. The 1st ASEAN Civil Engineering Conference. Pattaya, Thailand.

Hoshide, T. and D. F. Socie (1987). *Mechanics of mixed mode small fatigue crack growth*. Engineering Fracture Mechanics 26, 6: 841-850.

Jajich, D. and A. E. Schultz (2003). *Mesurement and Ananlysis of Distortion-Induced Fatigue in Multigider Steel Bridges*. Journal of Bridge Engineering 8, No2: 84-91.

Koob, M. J., P. D. Frey and J. M. Hanson (1985). *Evaluation of web cracking at floor beam to stiffener connections of the polar street bridge approaches*, FAI route 70, East St. Louis, St. Clair County, Illinois. Summarized in Tranportation Research Record 1118 (1987).

Lam, Y. C. (1989). *Mixed mode fatigue crack growth and the strain energy density factor*. Theoretical and Applied Fracture Mechanics 12, 1: 67-72.

Lam, Y. C. and J. F. Williams (1984). *The effect of contact stress intensity factors on fatigue crack propagation*. Theoretical and Applied Fracture Mechanics 1, 2: 193-202.

Li, C. (1989). *Vector CTD criterion applied to mixed mode fatigue crack growth*. Fatigue & Fracture of Engineering Materials & Structures 12, 1: 59-65.

Newman, J. C. (1981). *A crack closure model for predicting fatigue crack growth under aircraft spectrum loading.* Methods and Model for Predicting Fatigue Crack Growth Under Random Loading 748 (ASTM STP): 53-84.

Newman Jr, J. C. and I. S. Raju (1981). *An empirical stress-intensity factor equation for the surface crack.* Engineering Fracture Mechanics 15 , 1–2: 185-192.

Panasyuk, V. V. (1991). *Mechanics of Quasibrittle Fracture of Materials [in Russian]*" (Naukova Dumka, Kiev).

Pokluda, A. J. (2004). *Intrinsic thresholds of long fatigue cracks*. XX Symp. on Fatigue and Fracture Mechanics Akdemia Techniczno Rolnicza, Bydgoszcz-Pieczyska, Poland (2004): 327-337.

Pook, L. P. (1985). *The fatigue crack direction and threshold behaviour of mild steel under mixed mode I and III loading*. International Journal of Fatigue 7, 1: 21-30.

Pook, L. P. and A. F. Greenan (1979). *Fatigue crack growth threshold in mild steel under combined loading*. Fracture Mechanics 93 (ASTM STP 677): 671-680.

Qian, J. and A. Fatemi (1996). *Mixed mode fatigue crack growth: A literature survey*. Engineering Fracture Mechanics 55, 6: 969-990.

Richard, H. A., M. Schollmann, M. Fulland and M. Sande (2001). *Experimental and numerical simulation of mixed-mode crack growth*. Proc of 6th Internat. Cof. on Biaxial/Multiaxial Fatigue & Fracture Lisboa, Portugal (2001): 623-630.

Roberts, R. and J. J. Kibler (1971). *Mode II fatigue crack propagation*. Journal of Basic Engineering 93(Trans. ASME): 671-680.

Rozumek, D. (2004). *Application of Δ J-integral range for fatigue crack growth rate in mixed modes I and III*. Proc. of the Seventh Internat. Conf. on Biaxial/Multiaxial Fatigue and Fracture (ICBMFF), DVM, Berlin: 489–494.

Rozumek, D. and E. Macha (2006). *A description of fatigue crack growth in elastoplastic materials under proportional bending with torsion*. Multiaxial Random Fatigue of Machine Elements and Structures. Part IX (Opole University of Technology, Opole, Poland).

Schollmann, M., G. Kullmer, M. Fulland and H. A. Richard (2001). *A new criterion for 3d crack growth under mixed-mode (I+II+III) loading*. Proc of 6th Internat. Cof. on Biaxial/Multiaxial Fatigue & Fracture Lisboa, Poturgal (2001): 589-596.

Sih, G. C. (1974). *Strain-energy-density factor applied to mixed mode crack problems*. International Journal of Fracture 10, 3: 305-321.

Sih, G. C. and B. M. Barthelemy (1980). *Mixed mode fatigue crack growth predictions*. Engineering Fracture Mechanics 13, 3: 439-451.

Srivastava, Y. P. and S. B. L. Garg (1988). *Study on modified J-integral range and its correlation with fatigue crack growth*. Engineering Fracture Mechanics 30, 2: 119-133.

Stallings, I. M., T. E. Cousins, R. K. Rotto and C. B. Reid (1993). *Evaluatino of fatigue cracking in I-65 Mobile delta crossing bridges, volume I: floorbeam - girder connections. F. report*. Alabama Highway Department Research Project**:** 186 pages.

Sutton, M. A., X. Deng, F. Ma, J. C. Newman Jr and M. James (2000). *Development and application of a crack tip opening displacement-based mixed mode fracture criterion*. International Journal of Solids and Structures 37, 26: 3591-3618.

Tanaka, K. (1974). *Fatigue crack propagation from a crack inclined to the cyclic tensile axis*. Engineering Fracture Mechanics 6, 3: 493-498, IN413-IN414, 499-507.

Tedesco, J. W., J. M. Stallings and D. R. Tow (1995). *Finite element method analysis of bridge girder-diaphragm interaction*. Computers & Structures 56, 2–3: 461-473.

Tschegg, E. K. and S. E. Stanzl (1988). *The significcance of sliding mode crack closure on Mode III fatigue crack growth*. Basic Questions in Fatigue 1 ed (Fong and Fields, ASTM, Philadelphia): 214-232.

Walker, K. (1970). *The effects of stress ratio during crack propagation and fatigue for 2024-T3 and 7075-T6 aluminum in effects of environment and complex load history on fatigue life*. American Society for Testing Materials: Philadelphia: 1-14.

Wells, A. A. (1961). *Critical tip opening displacement as fracture criterion*. Proc. Crack Propagation Symp (Cranfield): 210–221.

Wu, E. M. (1967). *Application of fracture mechanics to anisotropic plates.* J. Appl. Mech., ASME Trans 34: 967-974.

Wüthrich, C. (1982). *The extension of the J-integral concept to fatigue cracks*. International Journal of Fracture 20, 2: R35-R37.

Yan, X., Z. Zhang and S. Du (1992). *Mixed-mode fracture criteria for the materials with different yield strengths in tension and compression*. Engineering Fracture Mechanics 42, 1: 109-116.

Yates, J. R. (1991). *Fatigue thresholds under mixed-mode (I+III) loading*. International Journal of Fatigue 13, 5: 383-388.

Zhao, Y. and K. Roddis (2001). *Repair of fatigue cracking due to out of plane distortion*. Journal of Bridge Engineering, ASCE 4, 3: 27-42.

Zhao, Y. and K. Roddis (2003). *Finite Element Analysis of Steel Bridge Distortion-Induced Fatigue*. Journal of Bridge Engineering 8, 5: 259-266.

Zhao, Y. and W. M. K. Roddis (2007). *Fatigue Behavior and Retrofit Investigation of Distortion-Induced Web Gap Cracking*. Journal of Bridge Engineering 12, No 6: 737-745.

APPENDICES

APPENDIX A

Normalized stress intensity factors of semi-ellipse crack in finite thickness plate under tension or bending loads (Newman Jr and Raju 1981)

Only loads which cause mode I deformations were considered. The mode I stress intensity factor K_j for any point along the surface-crack front was taken to be

$$K_I = S_i \sqrt{\pi \frac{a}{Q}} F_i \left(\frac{a}{t}; \frac{a}{c}; \frac{c}{b}; \Phi \right)$$

where the subscript *i* denotes either tension load *(i = t)* or bending load *(i = b)*

Q is the shape factor for an ellipse, is given by the square of the complete elliptic integral of the second kind.

The half-length of the plate *h* was chosen large enough to have a negligible effect on stress intensity *(h/c = 5)*.

Values for F, the boundary-correction factor, were calculated along the crack front for various combinations of parameters with these ranges: $0.2 \le a/c \le 2.0$; $0.2 \le a/t \le 0.8$; and $0.2 \le c/b \le 0.8$

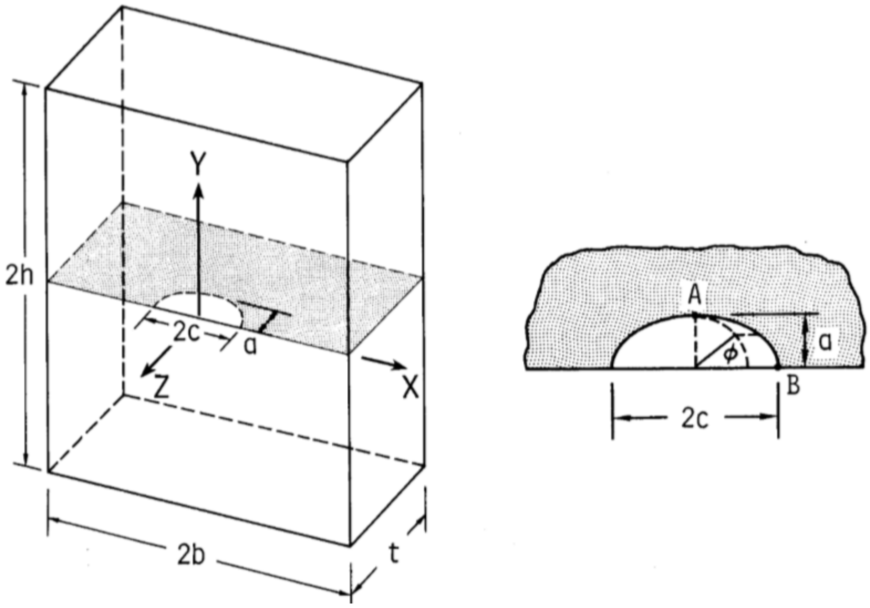

Figure A.1 Surface crack in a finite plate.

Table A.1: Normalized stress intensity factors for a semi-ellipse crack in a finite width plate under tension and bending loads

A/C	$2\phi/\pi$	*C/B*					
		0.6			0.6		0.8
		a/t					
		0.4	0.6	0.8	0.6	0.8	0.8
Tension							
0.2	0.000	0.743	0.941	1.268	1.037	1.465	1.854
	0.125	0.794	0.993	1.289	1.086	1.474	1.833
	0.250	0.903	1.120	1.414	1.214	1.595	1.943
	0.375	1.030	1.278	1.572	1.374	1.752	2.092
	0.500	1.144	1.425	1.720	1.522	1.893	2.216
	0.625	1.243	1.540	1.816	1.636	1.976	2.271
	0.750	1.319	1.619	1.872	1.712	2.016	2.278
	0.875	1.366	1.664	1.888	1.754	2.017	2.253
	1.000	1.381	1.679	1.891	1.768	2.014	2.240
1.0	0.000	1.293	1.445	1.579	1.660	1.853	2.552
	0.125	1.266	1.403	1.512	1.595	1.752	2.334
	0.250	1.210	1.326	1.395	1.487	1.588	2.031
	0.375	1.174	1.272	1.296	1.408	1.449	1.801
	0.500	1.147	1.231	1.239	1.346	1.360	1.632
	0.625	1.127	1.195	1.184	1.294	1.277	1.483
	0.750	1.110	1.165	1.158	1.252	1.232	1.392
	0.875	1.099	1.145	1.137	1.224	1.198	1.330
	1.000	1.095	1.138	1.128	1.215	1.185	1.308
Bending							
0.2	0.000	0.650	0.733	0.834	0.799	0.941	1.153
	0.125	0.646	0.700	0.765	0.763	0.864	1.058
	0.250	0.676	0.700	0.727	0.762	0.824	1.008
	0.375	0.715	0.710	0.695	0.773	0.791	0.968
	0.500	0.739	0.703	0.638	0.766	0.728	0.894
	0.625	0.751	0.679	0.554	0.741	0.637	0.786
	0.750	0.753	0.648	0.455	0.707	0.528	0.660
	0.875	0.752	0.623	0.374	0.680	0.440	0.557
	1.000	0.751	0.613	0.343	0.670	0.406	0.518
1.0	0.000	1.074	1.070	1.058	1.208	1.204	1.574

	0.125	0.999	0.954	0.902	1.079	1.030	1.336
	0.250	0.878	0.780	0.670	0.883	0.772	1.006
	0.375	0.775	0.627	0.460	0.714	0.539	0.721
	0.500	0.686	0.493	0.273	0.566	0.333	0.471
	0.625	0.611	0.382	0.119	0.443	0.164	0.267
	0.750	0.554	0.297	0.00	0.351	0.035	0.113
	0.875	0.518	0.245	-0.075	0.294	-0.048	0.015
	1.000	0.506	0.228	-0.101	0.275	-0.076	-0.019

Appendix B

Table B.1: Testing data on specimens series I

Specimen Series I	***S1-1***	***S1-2***	***S1-3***
G1 (μm/m)	547	1039	1044
G2 (μm/m)	-	621	559
G3 (μm/m)	-	1259	814
G4 (μm/m)	-	1095	833
G5 (μm/m)	-	625	552
G6 (μm/m)	-	-1171	-1529
G7 (μm/m)	-	127	596
G8 (μm/m)	-	-560	-535
G9 (μm/m)	-	556	562
LVDT (mm)	-	1.35	1.34
Number of cycles for failure	3,031,810	3,801,220	1,940,140

Table B.2: Testing data on specimen series II

Specimen Series II	***S2-1***	***S2-2***	***S2-3***
G1 (μm/m)	945	881	871
G2 (μm/m)	250	505	488
G3 (μm/m)	517	560	625
G4 (μm/m)	608	537	621
G5 (μm/m)	441	427	485

G6 (μm/m)	-629	-766	-1420
G7 (μm/m)	-	-	-
G8 (μm/m)	-389	-406	-433
G9 (μm/m)	465	418	411
LVDT (mm)	1.05	1.06	1.06
Number of cycles for failure	53,300,040	7,410,000	6,771,510

Table B.3: Testing data on specimen series III

Specimen Series III	***S3-1***	***S3-2***	***S3-3***
G1 (μm/m)	1174	921	955
G2 (μm/m)	656	488	788
G3 (μm/m)	798	545	1056
G4 (μm/m)	709	641	1027
G5 (μm/m)	675	500	772
G6 (μm/m)	-1239	-1117	-817
G7 (μm/m)	178	-	-
G8 (μm/m)	-593	-670	-648
G9 (μm/m)	662	674	658
LVDT (mm)	1.27	1.17	1.06
Number of cycles for failure	1,821,520	1,402,110	1,598,720

Appendix C

Table C.1: Fatigue crack growth on specimen S1-2

a (cm)	*N (cycles)*	*da/dN (cm/cycles)*
1.58	3.81E+05	
1.88	4.57E+05	3.97E-06
2.26	5.56E+05	3.83E-06
2.54	7.07E+05	1.89E-06
2.83	8.51E+05	1.97E-06
3.09	1.00E+06	1.77E-06
3.33	1.11E+06	2.09E-06
3.60	1.21E+06	2.94E-06

Table C.2: Fatigue crack growth on specimen S1-3

a (cm)	*N (cycles)*	*da/dN (cm/cycles)*
0.59	3.66E+05	
2.16	9.06E+05	2.91E-06
2.89	1.02E+06	6.44E-06
3.42	1.25E+06	2.32E-06
3.65	1.37E+06	1.99E-06
4.16	1.66E+06	1.73E-06

Table C.3: Fatigue crack growth on specimen S2-1 (left of stiffener)

a (cm)	***N (cycles)***	***da/dN (cm/cycles)***
1.77	8.80E+05	
2.14	9.68E+05	4.14E-06
2.78	1.29E+06	1.98E-06
2.97	1.55E+06	7.40E-07
3.25	1.86E+06	8.99E-07
3.49	2.02E+06	1.44E-06
3.74	2.17E+06	1.67E-06
4.11	2.66E+06	7.81E-07
4.33	3.05E+06	5.52E-07
4.49	3.25E+06	8.14E-07
4.71	3.51E+06	8.33E-07
4.97	3.78E+06	9.58E-07
5.44	3.99E+06	2.28E-06
5.68	4.11E+06	2.00E-06
6.01	4.21E+06	3.30E-06
6.30	4.37E+06	1.75E-06
6.62	4.47E+06	3.19E-06
6.84	4.65E+06	1.24E-06
7.18	4.83E+06	1.92E-06
7.50	4.97E+06	2.19E-06
7.81	5.10E+06	2.34E-06

Table C.4: Fatigue crack growth on specimen S2-1 (right of stiffener)

a (cm)	***N (cycles)***	***da/dN (cm/cycles)***
0.59	3.66E+05	
2.16	9.06E+05	2.91E-06
2.89	1.02E+06	6.44E-06
3.42	1.25E+06	2.32E-06
3.65	1.37E+06	1.99E-06
4.16	1.66E+06	1.73E-06

Table C.5: Fatigue crack growth on specimen S2-2.

a (cm)	***N (cycles)***	***da/dN (cm/cycles)***
2.91	3.10E+06	
3.11	3.39E+06	6.79E-07
3.19	3.53E+06	5.85E-07
3.35	3.64E+06	1.41E-06
3.49	3.92E+06	4.96E-07
3.69	4.02E+06	2.04E-06
3.88	4.24E+06	8.75E-07
4.06	4.34E+06	1.81E-06
4.18	4.60E+06	4.34E-07
4.52	4.81E+06	1.66E-06
5.07	5.46E+06	8.46E-07

5.55	5.92E+06	1.03E-06
5.85	6.24E+06	9.43E-07
6.39	6.52E+06	1.92E-06
6.80	6.72E+06	2.05E-06
7.31	7.39E+06	7.68E-07
7.92	7.41E+06	3.04E-05

Table C.6: Fatigue crack growth on specimen S2-3.

a (cm)	***N (cycles)***	***da/dN (cm/cycles)***
1.92	1.00E+06	
2.34	1.38E+06	1.09E-06
3.28	1.93E+06	1.74E-06
3.72	2.27E+06	1.27E-06
4.03	2.69E+06	7.29E-07
4.23	2.99E+06	6.65E-07
4.42	3.33E+06	5.73E-07
4.53	3.44E+06	9.46E-07
4.73	3.67E+06	8.71E-07
4.93	4.02E+06	5.65E-07
5.03	4.14E+06	9.43E-07
5.44	4.63E+06	8.40E-07
5.58	4.81E+06	7.56E-07
5.79	5.09E+06	7.41E-07
6.42	5.77E+06	9.26E-07

Table C.7: Fatigue crack growth on specimen S3-1 (left of stiffener).

a (cm)	*N (cycles)*	*da/dN (cm/cycles)*
0.91	1.98E+05	
1.08	2.44E+05	3.82E-06
1.43	3.26E+05	4.24E-06
2.27	5.03E+05	4.73E-06
2.61	5.81E+05	4.44E-06
2.91	6.61E+05	3.74E-06
3.27	7.99E+05	2.60E-06
3.57	8.99E+05	3.04E-06
3.72	9.62E+05	2.30E-06
3.83	1.00E+06	2.69E-06
4.10	1.18E+06	1.56E-06
4.39	1.35E+06	1.69E-06
4.55	1.54E+06	7.96E-07
4.73	1.61E+06	2.57E-06
4.92	1.71E+06	1.99E-06
5.20	1.82E+06	2.56E-06

Table C.8: Fatigue crack growth on specimen S3-1 (right of stiffener).

a (cm)	*N (cycles)*	*da/dN (cm/cycles)*
0.71	5.05E+04	

1.71	3.26E+05	3.64E-06
2.36	4.57E+05	4.92E-06
2.60	5.81E+05	1.96E-06
2.87	6.61E+05	3.32E-06
3.01	7.99E+05	1.08E-06
3.19	8.99E+05	1.73E-06
3.30	9.62E+05	1.82E-06
3.37	1.00E+06	1.79E-06
3.62	1.18E+06	1.4E-06
3.90	1.35E+06	1.61E-06
4.05	1.54E+06	7.65E-07
4.16	1.61E+06	1.63E-06
4.31	1.71E+06	1.55E-06
4.48	1.82E+06	1.52E-06

Table C.9: Fatigue crack growth on specimen S3-2 (left of stiffener).

a (cm)	***N (cycles)***	***da/dN (cm/cycles)***
2.285	6.91E+05	
2.5163	9.83E+05	7.92E-07
2.8886	1.08E+06	4.04E-06
3.0172	1.12E+06	2.78E-06
3.3372	1.26E+06	2.35E-06
3.6288	1.33E+06	3.84E-06
3.7427	1.39E+06	2.22E-06

Table C.10: Fatigue crack growth on specimen S3-2 (right of stiffener).

a (cm)	***N (cycles)***	***da/dN (cm/cycles)***
0.81	6.25E+05	
2.35	9.83E+05	4.28E-06
2.59	1.08E+06	2.67E-06
2.87	1.33E+06	1.07E-06
3.33	1.39E+06	8.99E-06
3.66	1.40E+06	2.56E-05

Appendix D

Table D.1: Fatigue crack growth on model 1 (maximum load = 5500 kGf, minimum load = 1100 kGf)

STEP	Δs ***(kG/cm)***	Δs_{eff} ***(kG/cm)***	***da*** ***(cm)***	***da/dN*** ***(cm/cycles)***
1	4.97E-01	2.56E-01	0.2	4.41E-05
2	3.56E-01	1.84E-01	0.2	2.56E-05
3	3.52E-01	1.82E-01	0.2	2.50E-05
4	2.86E-01	1.48E-01	0.2	1.78E-05
5	2.47E-01	1.27E-01	0.2	1.40E-05
6	2.33E-01	1.20E-01	0.2	1.27E-05
7	1.88E-01	9.72E-02	0.2	8.99E-06
8	1.68E-01	8.66E-02	0.2	7.43E-06
9	1.28E-01	6.59E-02	0.2	4.75E-06
10	1.27E-01	6.54E-02	0.2	4.69E-06
11	1.08E-01	5.56E-02	0.2	3.60E-06
12	1.16E-01	6.00E-02	0.2	4.08E-06
13	9.13E-02	4.71E-02	0.2	2.74E-06
14	9.82E-02	5.07E-02	0.2	3.09E-06
15	8.90E-02	4.59E-02	0.2	2.63E-06
16	8.40E-02	4.33E-02	0.2	2.39E-06
17	8.36E-02	4.31E-02	0.2	2.37E-06
18	8.36E-02	4.31E-02	0.2	2.37E-06
19	7.65E-02	3.95E-02	0.2	2.05E-06
20	7.09E-02	3.66E-02	0.2	1.81E-06

Table D.2: Fatigue crack growth on model 2 (maximum load = 4000 kGf, minimum load = 800 kGf)

STEP	Δs	Δs_{eff}	***da***	***da/dN***
	(kG/cm)	***(kG/cm)***	***(cm)***	***(cm/cycles)***
1	3.98E-01	2.06E-01	0.2	3.07E-05
2	2.60E-01	1.34E-01	0.2	1.53E-05
3	2.28E-01	1.18E-01	0.2	1.23E-05
4	2.16E-01	1.11E-01	0.2	1.12E-05
5	1.85E-01	9.55E-02	0.2	8.73E-06
6	1.60E-01	8.23E-02	0.2	6.85E-06
7	1.44E-01	7.43E-02	0.2	5.79E-06
8	1.27E-01	6.57E-02	0.2	4.73E-06
9	1.16E-01	5.99E-02	0.2	4.06E-06
10	1.04E-01	5.39E-02	0.2	3.42E-06
11	9.43E-02	4.86E-02	0.2	2.89E-06
12	7.62E-02	3.93E-02	0.2	2.04E-06
13	6.96E-02	3.59E-02	0.2	1.76E-06
14	6.37E-02	3.29E-02	0.2	1.52E-06
15	5.83E-02	3.01E-02	0.2	1.31E-06
16	4.90E-02	2.53E-02	0.2	9.89E-07
17	4.57E-02	2.36E-02	0.2	8.80E-07
18	4.24E-02	2.19E-02	0.2	7.78E-07
19	4.25E-02	2.19E-02	0.2	7.81E-07
20	3.92E-02	2.02E-02	0.2	6.84E-07
21	3.65E-02	1.88E-02	0.2	6.10E-07

Table D.3: Fatigue crack growth on model 3 (maximum load = 5500 kGf, minimum load = 1100 kGf)

STEP	Δs ***(kG/cm)***	Δs_{eff} ***(kG/cm)***	***da (cm)***	***da/dN (cm/cycles)***
1	7.24E-01	7.06E-01	0.2	2.32E-04
2	6.53E-01	6.37E-01	0.2	1.96E-04
3	5.79E-01	5.65E-01	0.2	1.61E-04
4	5.53E-01	5.39E-01	0.2	1.49E-04
5	4.98E-01	4.86E-01	0.2	1.26E-04
6	4.48E-01	4.37E-01	0.2	1.06E-04
7	3.50E-01	3.41E-01	0.2	7.05E-05
8	3.42E-01	3.34E-01	0.2	6.79E-05
9	3.02E-01	2.95E-01	0.2	5.55E-05
10	2.33E-01	2.27E-01	0.2	3.61E-05
11	2.01E-01	1.96E-01	0.2	2.85E-05
12	1.73E-01	1.69E-01	0.2	2.22E-05
13	1.50E-01	1.46E-01	0.2	1.76E-05
14	1.44E-01	1.40E-01	0.2	1.63E-05
15	1.07E-01	1.04E-01	0.2	1.01E-05
16	1.04E-01	1.01E-01	0.2	9.62E-06
17	1.02E-01	9.98E-02	0.2	9.39E-06
18	8.34E-02	8.14E-02	0.2	6.72E-06
19	7.61E-02	7.42E-02	0.2	5.77E-06
20	7.00E-02	6.83E-02	0.2	5.03E-06

Table D.4: Fatigue crack growth on model 4 (maximum load = 5500 kGf, minimum load = 1100 kGf)

STEP	***ΔS*** (kG/cm)	***ΔS_{eff}*** (kG/cm)	***da*** (cm)	***da/dN*** (cm/cycles)
1	2.94E+00	2.87E+00	0.2	2.31E-03
2	2.05E+00	2.00E+00	0.2	1.28E-03
3	2.04E+00	1.99E+00	0.2	1.27E-03
4	1.90E+00	1.86E+00	0.2	1.14E-03
5	1.87E+00	1.82E+00	0.2	1.10E-03
6	1.51E+00	1.47E+00	0.2	7.77E-04
7	1.37E+00	1.34E+00	0.2	6.63E-04
8	1.24E+00	1.21E+00	0.2	5.59E-04
9	1.09E+00	1.07E+00	0.2	4.58E-04
10	9.53E-01	9.29E-01	0.2	3.64E-04
11	8.36E-01	8.16E-01	0.2	2.94E-04
12	7.27E-01	7.09E-01	0.2	2.34E-04
13	6.31E-01	6.16E-01	0.2	1.86E-04
14	5.50E-01	5.37E-01	0.2	1.48E-04
15	4.49E-01	4.38E-01	0.2	1.06E-04
16	3.97E-01	3.87E-01	0.2	8.68E-05
17	3.80E-01	3.71E-01	0.2	8.08E-05
18	3.12E-01	3.05E-01	0.2	5.85E-05
19	2.89E-01	2.82E-01	0.2	5.16E-05
20	2.59E-01	2.53E-01	0.2	4.32E-05

Table D.5: Fatigue crack growth on model 5 (maximum load = 5500 kGf, minimum load = 1100 kGf)

STEP	Δs ***(kG/cm)***	Δs_{eff} ***(kG/cm)***	***da*** ***(cm)***	***da/dN*** ***(cm/cycles)***
1	1.55E-01	1.51E-01	0.2	1.85E-05
2	1.01E-01	9.85E-02	0.2	9.18E-06
3	9.45E-02	9.22E-02	0.2	8.24E-06
4	8.33E-02	8.13E-02	0.2	6.71E-06
5	7.67E-02	7.49E-02	0.2	5.86E-06
6	5.98E-02	5.83E-02	0.2	3.89E-06
7	5.22E-02	5.09E-02	0.2	3.11E-06
8	5.01E-02	4.89E-02	0.2	2.91E-06
9	4.28E-02	4.17E-02	0.2	2.25E-06
10	3.34E-02	3.26E-02	0.2	1.50E-06
11	2.88E-02	2.81E-02	0.2	1.18E-06
12	2.48E-02	2.42E-02	0.2	9.16E-07
13	2.13E-02	2.08E-02	0.2	7.17E-07
14	1.84E-02	1.80E-02	0.2	5.64E-07
15	1.50E-02	1.46E-02	0.2	4.02E-07
16	1.31E-02	1.28E-02	0.2	3.23E-07
17	1.15E-02	1.12E-02	0.2	2.59E-07
18	1.01E-02	9.86E-03	0.2	2.11E-07
19	9.98E-03	9.74E-03	0.2	2.07E-07
20	7.00E-02	6.83E-02	0.2	5.03E-06

Table D.6: Fatigue crack growth on model 6 (maximum load = 14000 kGf, minimum load = 2800 kGf)

STEP	Δs ***(kG/cm)***	Δs_{eff} ***(kG/cm)***	***da*** ***(cm)***	***da/dN*** ***(cm/cycles)***
1	4.45E-01	2.29E-01	0.2	3.67E-05
2	3.64E-01	1.88E-01	0.2	2.65E-05
3	2.96E-01	1.53E-01	0.2	1.89E-05
4	2.60E-01	1.34E-01	0.2	1.52E-05
5	2.36E-01	1.22E-01	0.2	1.30E-05
6	2.03E-01	1.05E-01	0.2	1.02E-05
7	1.76E-01	9.06E-02	0.2	8.01E-06
8	1.49E-01	7.67E-02	0.2	6.10E-06
9	1.33E-01	6.84E-02	0.2	5.05E-06
10	1.18E-01	6.11E-02	0.2	4.20E-06
11	1.08E-01	5.59E-02	0.2	3.63E-06
12	8.77E-02	4.52E-02	0.2	2.56E-06
13	9.40E-02	4.85E-02	0.2	2.87E-06
14	1.07E-01	5.51E-02	0.2	3.54E-06
15	1.00E-01	5.17E-02	0.2	3.19E-06
16	8.20E-02	4.23E-02	0.2	2.30E-06
17	9.12E-02	4.71E-02	0.2	2.74E-06
18	7.54E-02	3.89E-02	0.2	2.00E-06

Table D.7: Fatigue crack growth on model 7 (maximum load = 5500 kGf, minimum load = 1100 kGf)

STEP	Δs ***(kG/cm)***	Δs_{eff} ***(kG/cm)***	***da*** ***(cm)***	***da/dN*** ***(cm/cycles)***
1	9.76E+00	5.04E+00	0.2	5.83E-03
2	6.15E+00	3.17E+00	0.2	2.73E-03
3	4.68E+00	2.42E+00	0.2	1.75E-03
4	4.62E+00	2.39E+00	0.2	1.71E-03
5	4.26E+00	2.20E+00	0.2	1.49E-03
6	3.73E+00	1.92E+00	0.2	1.20E-03
7	3.18E+00	1.64E+00	0.2	9.26E-04
8	2.21E+00	1.14E+00	0.2	5.11E-04
9	1.93E+00	9.94E-01	0.2	4.07E-04
10	1.80E+00	9.28E-01	0.2	3.64E-04
11	1.53E+00	7.88E-01	0.2	2.78E-04
12	1.18E+00	6.11E-01	0.2	1.83E-04
13	1.02E+00	5.24E-01	0.2	1.43E-04
14	8.92E-01	4.60E-01	0.2	1.15E-04
15	7.39E-01	3.81E-01	0.2	8.46E-05
16	6.51E-01	3.36E-01	0.2	6.87E-05
17	5.76E-01	2.97E-01	0.2	5.62E-05
18	5.27E-01	2.72E-01	0.2	4.86E-05
19	5.26E-01	2.72E-01	0.2	4.85E-05
20	4.57E-01	2.36E-01	0.2	3.84E-05

Table D.8: Fatigue crack growth on model 8 (maximum load = 5500 kGf, minimum load = 1100 kGf)

STEP	***Δs*** ***(kG/cm)***	***Δs_{eff}*** ***(kG/cm)***	***da*** ***(cm)***	***da/dN*** ***(cm/cycles)***
1	2.63E+00	1.36E+00	0.2	6.78E-04
2	2.35E+00	1.21E+00	0.2	5.65E-04
3	2.45E+00	1.26E+00	0.2	6.04E-04
4	2.43E+00	1.25E+00	0.2	5.96E-04
5	2.19E+00	1.13E+00	0.2	5.01E-04
6	2.14E+00	1.10E+00	0.2	4.84E-04
7	2.04E+00	1.05E+00	0.2	4.49E-04
8	1.91E+00	9.85E-01	0.2	4.01E-04
9	1.75E+00	9.05E-01	0.2	3.49E-04
10	1.59E+00	8.20E-01	0.2	2.97E-04
11	1.43E+00	7.37E-01	0.2	2.49E-04
12	1.28E+00	6.62E-01	0.2	2.09E-04
13	1.12E+00	5.80E-01	0.2	1.68E-04
14	1.00E+00	5.17E-01	0.2	1.39E-04
15	8.22E-01	4.24E-01	0.2	1.01E-04
16	8.05E-01	4.16E-01	0.2	9.74E-05
17	7.27E-01	3.75E-01	0.2	8.24E-05
18	6.04E-01	3.12E-01	0.2	6.08E-05
19	5.51E-01	2.84E-01	0.2	5.23E-05
20	4.96E-01	2.56E-01	0.2	4.40E-05

Table D.9: Fatigue crack growth on model 9 (maximum load = 5500 kGf, minimum load = 1100 kGf)

STEP	***ΔS*** (kG/cm)	***ΔS_{eff}*** (kG/cm)	***da*** (cm)	***da/dN*** (cm/cycles)
1	4.18E+00	2.16E+00	0.2	1.45E-03
2	3.56E+00	1.84E+00	0.2	1.11E-03
3	2.96E+00	1.53E+00	0.2	8.22E-04
4	2.90E+00	1.49E+00	0.2	7.95E-04
5	2.76E+00	1.43E+00	0.2	7.35E-04
6	2.58E+00	1.33E+00	0.2	6.58E-04
7	2.33E+00	1.20E+00	0.2	5.56E-04
8	1.92E+00	9.92E-01	0.2	4.06E-04
9	1.64E+00	8.46E-01	0.2	3.12E-04
10	1.56E+00	8.07E-01	0.2	2.89E-04
11	1.36E+00	7.01E-01	0.2	2.29E-04
12	1.32E+00	6.83E-01	0.2	2.20E-04
13	1.04E+00	5.37E-01	0.2	1.48E-04
14	9.29E-01	4.79E-01	0.2	1.23E-04
15	8.36E-01	4.32E-01	0.2	1.04E-04

Table D.10: Fatigue crack growth on model 10 (maximum load = 5500 kGf, minimum load = 1100 kGf)

STEP	***ΔS*** (kG/cm)	***ΔS_{eff}*** (kG/cm)	***da*** (cm)	***da/dN*** (cm/cycles)
1	3.70E+00	1.91E+00	0.2	1.18E-03
2	3.56E+00	1.84E+00	0.2	1.12E-03

3	3.47E+00	1.79E+00	0.2	1.07E-03
4	3.37E+00	1.74E+00	0.2	1.02E-03
5	3.15E+00	1.63E+00	0.2	9.12E-04
6	2.88E+00	1.49E+00	0.2	7.88E-04
7	2.66E+00	1.37E+00	0.2	6.89E-04
8	1.85E+00	9.53E-01	0.2	3.80E-04
9	2.43E+00	1.26E+00	0.2	5.97E-04
10	1.80E+00	9.28E-01	0.2	3.64E-04

Appendix E

Stress field around web-gap region.

```
PRINT S    ELEMENT SOLUTION PER ELEMENT

 ***** POST1 ELEMENT NODAL STRESS LISTING *****

  LOAD STEP=     1  SUBSTEP=     1
   TIME=    1.0000      LOAD CASE=   0
  SHELL RESULTS FOR TOP/BOTTOM ALSO MID WHERE APPROPRIATE

  THE FOLLOWING X,Y,Z VALUES ARE IN GLOBAL COORDINATES


  ELEMENT=    7617        SOLID45
    NODE    SX          SY          SZ          SXY         SYZ         SXZ
     184   5829.0      10349.      4072.7      17.049      3044.5     -7.8136
     457   4867.7      9387.4      1829.7      17.049     -669.08      485.08
     458   3336.0      7855.7     -1744.3      17.049     -1072.2     -488.99
     458   3336.0      7855.7     -1744.3      17.049     -1072.2     -488.99
    4500   1306.0      2578.4      384.75     -5.9460      2703.9      5.9487
    4555   344.66      1617.1     -1858.3     -5.9460     -1009.7      498.84
    4553   1974.1      3246.5      1943.7     -5.9460     -731.57     -502.75
    4553   1974.1      3246.5      1943.7     -5.9460     -731.57     -502.75

  ELEMENT=    7618        SOLID45
    NODE    SX          SY          SZ          SXY         SYZ         SXZ
    4500   1310.6      2583.1      395.70     -5.9460      2192.7      7.1892
    4555   1842.8      3115.3      1637.4     -5.9460     -461.06      494.26
    4553   595.34      1867.8     -1273.3     -5.9460     -299.78     -466.25
    4553   595.34      1867.8     -1273.3     -5.9460     -299.78     -466.25
    4499  -2265.2     -3099.3     -2381.8     -3.2862      2375.8     -8.9016
    4556  -1733.0     -2567.2     -1140.1     -3.2862     -277.89      478.17
    4554  -599.78     -1433.9      1504.1     -3.2862     -482.95     -450.16
    4554  -599.78     -1433.9      1504.1     -3.2862     -482.95     -450.16

  ELEMENT=    7619        SOLID45
    NODE    SX          SY          SZ          SXY         SYZ         SXZ
    4499  -448.91     -1283.1      1856.2     -3.2862      2159.6      15.067
    4556  -681.87     -1516.0      1312.6     -3.2862     -674.73      565.21
    4554  -2013.8     -2848.0     -1795.4     -3.2862     -778.27     -599.86
    4554  -2013.8     -2848.0     -1795.4     -3.2862     -778.27     -599.86
    2196  -4487.3     -7439.9     -1202.4     -21.016      2071.2      9.1005
    2469  -4720.2     -7672.8     -1745.9     -21.016     -763.18      559.24
    2470  -3430.6     -6383.2      1263.2     -21.016     -689.82     -593.89
    2470  -3430.6     -6383.2      1263.2     -21.016     -689.82     -593.89

 ***** POST1 ELEMENT NODAL STRESS LISTING *****

  LOAD STEP=     1  SUBSTEP=     1
   TIME=    1.0000      LOAD CASE=   0
  SHELL RESULTS FOR TOP/BOTTOM ALSO MID WHERE APPROPRIATE

  THE FOLLOWING X,Y,Z VALUES ARE IN GLOBAL COORDINATES


  ELEMENT=    7620        SOLID45
    NODE    SX          SY          SZ          SXY         SYZ         SXZ
     184   4925.7      10264.      3776.4      53.782      3216.7     -271.01
     458   4013.3      9351.8      1647.4      53.782     -559.32     -765.95
     183   3603.5      8942.0      691.23      53.782      3369.5     -620.04
     183   3603.5      8942.0      691.23      53.782      3369.5     -620.04
    4500   644.19      1970.7      3.9024      259.32      2813.7     -161.91
    4553  -268.25      1058.3     -2125.1      259.32     -962.32     -656.85
    4432   2555.6      3882.1      4463.7      259.32      3772.5     -729.14
    4432   2555.6      3882.1      4463.7      259.32      3772.5     -729.14
```

```
ELEMENT=    7621        SOLID45
  NODE     SX           SY           SZ           SXY          SYZ          SXZ
  4500   648.88       1975.4       14.851       259.32       2302.5      -160.67
  4553   1123.9       2450.4       1123.3       259.32      -373.09      -618.02
  4432   1584.2       2910.7       2197.2       259.32       1705.2       103.00
  4432   1584.2       2910.7       2197.2       259.32       1705.2       103.00
  4499  -2286.5      -3146.5      -2402.3       17.296       1997.4       569.42
  4554  -1811.5      -2671.4      -1293.9       17.296      -678.26       112.07
  4431   720.64      -139.28       4614.4       17.296       2010.4      -627.09
  4431   720.64      -139.28       4614.4       17.296       2010.4      -627.09
```

BIOGRAPHY

Hung The Dinh was born on Sep 13, 1982 in Ho Chi Minh city, one of the largest cities in Vietnam. He finished his elementary education in Phu Nhuan High school in Hochiminh. Then he continued to study Civil Engineering in Hochiminh City University of Technology (HCMUT), Hochiminh, Vietnam. His undergraduate research focused on Structural Engineering, in the area of building design. In April 2005, he finished his bachelor’s degree and was accepted to become an assistant lecturer in HCMUT. He continues study in master degree in HCMUT from Sep 2005 and finish on Oct 2008. During that time, he was accepted to be lecturer in HCMUT. Then, he got a scholarship from AUN/Seed-net/JICA to continue his study in the Doctoral of Engineering program in Department of Civil Engineering, Falculty of Engineering, Chulalongkorn, Bangkok, Thailand.